La borsa di dottorato è stata cofinanziata con risorse del
Programma Operativo Nazionale Ricerca e Innovazione 2014-202 (CCI 2014IT16M2OP005)
Fondo Sociale Europeo, Azione I.1 "Dottorati Innovativi con caratterizzazione Industriale"

UNIVERSITA' DELLA CALABRIA

Dipartimento di Fisica

Dottorato di Ricerca in Scienze e Tecnologie Fisiche Chimiche dei Materiali

Con il contributo di PON Ricerca e Innovazione 2014-2020

CICLO XXXIV

Innovative hybrid-composite membranes based on 2D materials for desalination of saline waters

Settore Scientifico Disciplinare
CHIM/07 – FONDAMENTI CHIMICI DELLE TECNOLOGIE

Coordinatore: Ch.ma Prof.ssa Gabriella Cipparrone (UNICAL)

Firma [redacted] Firma oscurata in base alle linee guida del Garante della privacy

Supervisore/Tutor: Dott.ssa Annarosa Guglielmi (CNR-ITM)

Firma [redacted] Firma oscurata in base alle linee guida del Garante della privacy

Co-Supervisore/Co-Tutor: Ch.mo Prof. Enrico Drioli (CNR-ITM)

Firma [redacted] Firma oscurata in base alle linee guida del Garante della privacy

Dottorando: Dott. Mirko Frappa

Firma Firma oscurata in base alle linee guida del Garante della privacy

Index

Acknowledgments

This thesis has been executed within 2DMEMPUR PROJECT, which received the financial grant from '***the Italian Ministry of Foreign Affairs and International Cooperation***' within the framework of the Great Relevance International ***Project Italy (MAECI)-China (NSFC) 2018-2020 - New Materials***, with particular reference to ***Two-dimensional systems and Graphene) - MAE00691702020- 06-26***. Many thanks to the Graphene Labs, Fondazione Istituto Italiano di Tecnologia (IIT), Genoa, Italy, for supplying 2D materials dispersant liquid phases and to BeDimensional S.p.A., Genoa, Italy, for accessing related facilities.

Sinopsi

L'acqua è essenziale per la vita di tutti gli organismi viventi e la sua conservazione e uso responsabile è una delle sfide globali che l'umanità dovrà affrontare nel prossimo futuro. Il recupero dell'acqua e dei sali dal mare è la principale fonte e oggi rappresenta un'importante opportunità all'interno della logica della gestione sostenibile. Il riutilizzo dell'acqua è l'uso delle acque reflue trattate per scopi benefici, che aumenta l'approvvigionamento idrico disponibile di una comunità e lo rende più affidabile, soprattutto in tempi di siccità. L'accesso a risorse idriche pulite, comunque richiede urgenti esigenze economiche ed ecologiche a livello globale, sollecitando tecnologie più efficienti. Infatti, a causa del suo consumo di energia, la desalinizzazione dell'acqua di mare è generalmente un processo costoso. Attualmente, il progresso tecnologico ha portato allo sviluppo di una serie di tecnologie che rendono il processo di trattamento delle acque reflue sempre più concreto ed efficiente. Tra di esse, i processi a membrana, rappresentano una valida alternativa grazie ai numerosi vantaggi offerti quali il basso impatto ambientale, l'alta efficienza e i basti costi correlati. La ricerca, nel rispetto dell'ambiente, è sempre più focalizzata sul miglioramento di queste tecniche in termini di produzione e costi. In tal senso sono state sviluppate due tecniche eco-sostenibili basate sull'utilizzo di membrane porose e idrofobiche: distillazione a membrana (MD) e la cristallizzazione a membrana (MCr). Queste due tecnologie non hanno ancora la capacità produttiva per andare a sostituire l'osmosi inversa, che allo stato attuale è il processo leader per la dissalazione. Comunque l'integrazione di questi processi con RO potrebbe aumentare il fattore di recupero vicino al cento per cento. Infatti, oltre ad aumentare la produzione di acqua pulita, è possibile anche recuperare i sali disciolti nell'acqua di mare grazie al processo MCr.

Da qui è nata l'idea di base di questo lavoro, dove si è voluto introdurre diversi materiali innovativi nei sistemi a membrana con l'obiettivo di migliorare e ottimizzare i processi MD/MCr. Nella fattispecie tre classi di materiali sono state prese in considerazione per la preparazione delle membrane polimeriche. Il primo materiale è il Grafene costituito da uno strato monoatomico di atomi di carbonio. La seconda tipologia di materiale proposta fa parte della famiglia dei metalli di transizione e sono dicalcogenuri a Monostrato. Fra i dicalcogenuri sono stati scelti il Tellurio di Bismuto e il Selenurio di Bismuto. Mentre l'ultimo materiale proposto fa parte dei reticoli metallorganici (MOF). Il Grafene e i metalli dicalcogenati sono stati esfoliati mediante la tecnica WET-Jet Milling e forniti dalla BeDimensional S.P.A. mentre il MOF a base di Zirconio [MIL-140B] è stato fornito dalla Nanjing Tech University (Cina). I materiali sono stati utilizzati per la

preparazione di membrane a base di PVDF, caratterizzati e testati in MD e MCr al fine di valutare gli effetti correlati sulla produttività e selettività.

Abstract

Water is essential for the life of all living organisms and its conservation and responsible use is one of the global challenges that humanity will have to face in the near future. The recovery of water and salts from the sea represents the main source and today represents an important opportunity within the logic of sustainable water management. Water reuse is the use of treated wastewater for beneficial purposes, which increases a community's available water supply and makes it more reliable, especially in times of drought. Access to clean water resources, however, requires urgent economic and ecological needs on a global level, urging more efficient technologies. Indeed, due to its energy consumption, seawater desalination is generally an expensive process. Currently, technological progress has led to the development of a series of technologies that make the wastewater treatment process increasingly concrete and efficient. Among them, membrane processes represent a valid alternative thanks to the numerous advantages offered such as low environmental impact, high efficiency and sufficient related costs. Research, respecting the environment, is increasingly focused on improving these techniques in terms of production and costs. In this sense, two eco-sustainable techniques have been developed based on the use of porous and hydrophobic membranes: membrane distillation (MD) and membrane crystallization (MCr). These two technologies do not yet have the production capacity to replace reverse osmosis, which is currently the leading process for desalination. However, integrating these processes with RO could increase the recovery factor close to one hundred percent. In fact, in addition to increasing the production of clean water, it is also possible to recover the salts dissolved in sea water thanks to the MCr process.

Hence the basic idea of this work where we wanted to introduce several innovative materials in membrane systems with the aim of improving and optimizing the MD / MCr processes. In this case, three classes of materials have been taken into consideration for the preparation of the polymeric membranes. The first material is Graphene consisting of a monatomic layer of carbon atoms. The second type of material proposed is part of the family of transition metals and are Monolayer dicalcogenides. Among the dicalcogenides, Bismuth Tellurium and metal organic frameworks (MOF) have been taken in consideration. Graphene and dicalcogenated metals have been exfoliated by the WET-Jet Milling technique and supplied by BeDimensional S.P.A. while the Zirconium based MOF [MIL-140B] has been provided by Nanjing Tech University (China). The materials have been used for the preparation of PVDF-based membranes, characterized and tested in MD and MCr in order to evaluate the correlated effects on productivity and selectivity.

Graphical Abstract

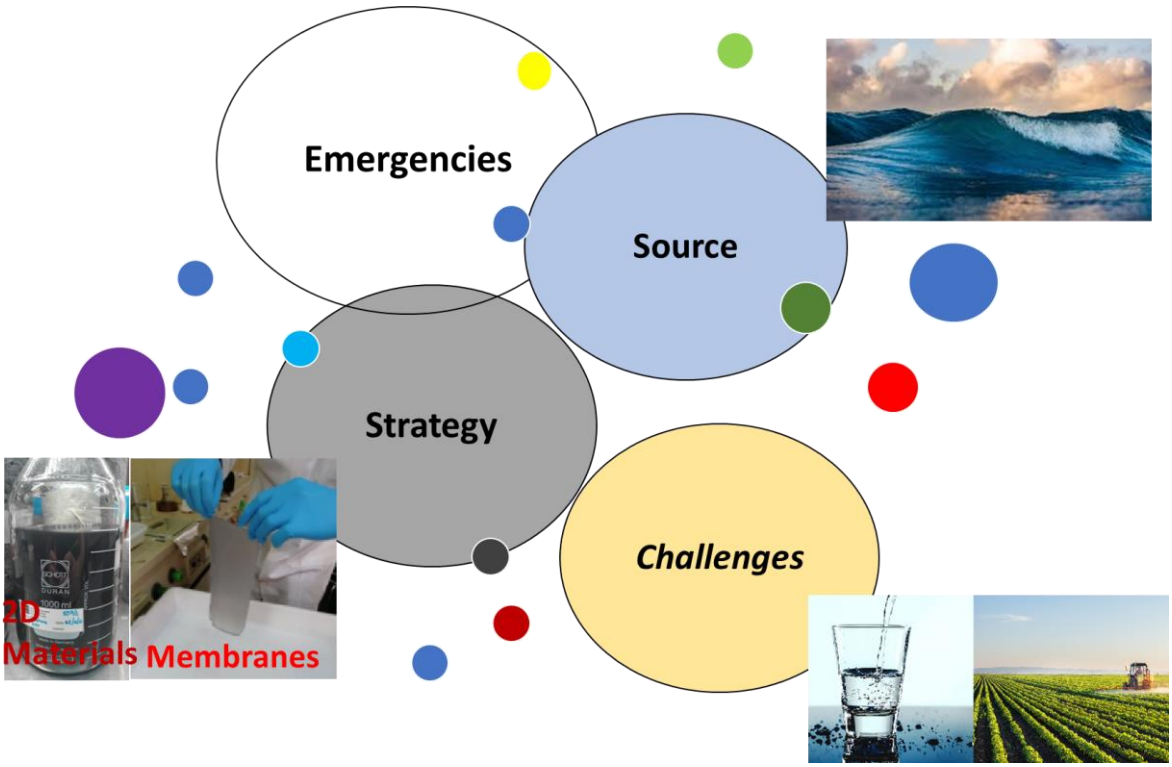

MD/MCR PROCESSES REPRESENT AN ECO-SUSTAINABLE SOLUTION FOR FRESHWATER AND REUSABLE SALTS RECOVERY

Thesis outlines

Water demand is increasing worldwide, while water availability in many regions is likely to decrease due to climate change and socioeconomic development patterns. Due to this increased demand, the need for RO internal brackish water will continue to increase in the future. However, the main limitations to further application of RO inland are the cost and technical feasibility of concentrate disposal. This clearly highlights the need for a more economic and ecological perspective. The development of new eco-sustainable and more productive approaches is fundamental in order to replace or integrate the more traditional ones.

Membrane distillation and membrane crystallization meet the ecological management criteria of natural resources well, because allow us to recovery freshwater from hypersaline streams and salt crystals from natural brine. However, these two operations are not yet competitive on a large scale due to lower productivity and relatively high energy consumption. To this end, the functionalization of membranes to improve performance may be a feasible and interesting way to boost the productivity-efficiency trade-off for these eco-sustainable technologies.

Functional membranes can be designed to improve mass transfer across the membrane, thereby improving water flux and selectivity through controlled kinetics and thermodynamics. In this logic 2D materials, including graphene and chalcogenides compounds, due to their attractive hydrophobic and anti-wetting nature, antifouling properties and selective sorption sites, have been used for the preparation of nanocomposite PVDF membranes and have been tested in MD and MCr devices under different working conditions. Enhancements in productivity, selectivity, thermal efficiency and crystallization kinetics of NaCl have been detected and examined concerning structure-properties relationships. In the specific, the present work is organised into eight chapters:

Chapter 1 starts with a brief introduction on water and the problematic related at this fundamental element.

In Chapter 2 are introduced the Membrane Technologies with particular attention on the membrane process for recovery of water from the sea. The limitations on these processes bring the focus on particular 2D materials for enhancing membrane performance. The state of the art for 2D materials is illustrated in Chapter 3, while Chapter 4 gives indication about materials, equipment and instruments used to carry out the research. More specifically, methodologies and routes used to accomplish the work are described.

Chapter 5 focuses on the preparation of PVDF-based membranes functionalized with 2D materials through a combination of innovative exfoliation technique (Wet-Jet Milling) and the non-solvent phase inversion technique.

All the physic-chemical proprieties on the 2D materials and on the prepared membranes are reported and widely discussed.

In chapter 6 focuses on the application and the performance of functionalized PVDF membranes in membrane distillation while Chapter 7 focuses on the use of the same membranes in the membrane-assisted crystallization process. In the specific Graphene and TMDCs flakes have been studied in PVDF-based membranes. Moreover, pristine PVDF membrane has been also studied in comparison with the functionalized membranes.

Chapter 8 illustrate a preliminary result about the use of MOF as nanofiller for crystallization operations. Preparation, characterization and performance of MOF-enable membranes are explained and analysed.

General highlights of the major results and achievement of the work are reported in the last section of this thesis.

Papers:

M. Frappa, E. Del Rio Castillo, F. Macedonio, A. Politano, E. Drioli, F. Bonaccorso, V. Pellegrini, A. Gugliuzza, High-quality exfoliated graphene for engineered membranes to be used in advanced membrane distillation, Nanoscale Advances, 2020, 2 (10), 4728-4739

M. Frappa, E. Del Rio Castillo, F. Macedonio, V. Pellegrini, E. Drioli, F. Bonaccorso, A. Gugliuzza, Exfoliated Bi_2Te_3 versus Graphene for ultrafast membrane distillation, Water Research, 2021, 203, 117503.

M. Frappa, F. Macedonio, J. Wanqin, A. Gugliuzza, E. Drioli, Performance of PVDF based membrane with 2D materials for Membrane Assisted-Crystallization process, Membranes, 2021, 11, 302.

Book Chapter:

M. Frappa, F. Macedonio, A. Gugliuzza, E. Drioli, Porous membranes for advanced membrane contactors in: Porous Membranes: Breakthroughs in Manufacturing and Applications, (A. Gugliuzza, W. Jin, E. Drioli, Eds), SCRIVENER PUBLISHING-WILEY&SONS, in press

M. Frappa, G. Di Luca, E. Drioli, A. Gugliuzza, Functional few-layered 2D-materials porous membranes for developed water desalination in: submission Porous Membranes: Breakthroughs in Manufacturing and Applications, (A. Gugliuzza, W. Jin, E. Drioli, Eds), SCRIVENER PUBLISHING-WILEY&SONS, in press

Chapter 1

Water as a natural essential and vulnerable resource for life

The Increase in water sources is required in the view of demographic growth and related activities. Waste reuse and water desalination might be necessary to satisfy the supply demand for agriculture, industry and drinking water [1]. World Health Organization (WHO) emphasizes safe and sustainable supply drinking water for the protection of public health to its guidelines [1]. In addition to water scarcity, the quality of water is rapidly growing as a progressive problem. The sustainable developments have also the objective to control of pollution levels. Recent accelerated climate change has exacerbate existing environmental problems in the world and in particular in the Mediterranean Basin where observed precipitation trends are characterized by high variability in space and in time, but climate models clearly indicate a trend towards reduced rainfall in coming decades. The combination of reduced rainfall and warming generates strong trends towards drier conditions. A global atmospheric temperature increase of 2°C is expected to be associated to a reduction in summer precipitation of about 10-15% in southern France, north-western Spain and the Balkans and up to 30% reduction in Turkey. Even if the per capita consumption is high, Italy is considered a country in conditions of water stress and one of those with less availability of water per capita. Most of the population in Italy lives in the temperate zone of the inland and mountainous regions (56.2% vs. 43.8% in the Mediterranean zone) [2]. Limited information is available at a spatial scale on the impacts of climate change in Italy, mainly from the analyses performed at the European or global level with a coarse resolution for Italy. However, the use of high-resolution climate data is pivotal in regions, as Italy, characterized by a significant variability of climatic, pedological, and topographic conditions. Results show that climate change may affect Italian cereal production in the medium to long term periods. Maize is the main affected crop, with yield reductions homogeneously distributed from North to South Italy [3]. Scenarios with 2-4°C temperature increases in the 2080s for southern Europe would imply stronger and more widespread decreases in precipitation of up to 30%. The coupled effect of warming and drought is expected to lead to a general increase in aridity and subsequent desertification of many Mediterranean land ecosystems. Deserts would expand in southern Spain and Portugal, northern parts of Morocco, Algeria, Tunisia, Sicily, southern Turkey and parts of Syria

[4]. Even if the per capita consumption is high, Italy is considered a country in conditions of water stress and one of those with less availability of water per capita. Considering an average consumption of 215 liters, a city of 500,000 inhabitants needs about 110,000 m^3 per day [2]. With the aim to address water scarcity within the Union and moving EU towards a water-efficient and water-saving economy, the EU Commission identified an initial set of policy options to be taken at European, national and regional levels. The Mediterranean Strategy for Sustainable Development (MSSD) 2016-2025 has been adopted as a strategic guiding document for all stakeholders and partners in order to translate the 2030 Agenda for Sustainable Development at the regional, sub-regional and national levels [5]. The MSSD provided an integrative policy framework for securing a sustainable future for the Mediterranean region consistent with the Sustainable Development Goals. One of its targets is the "Target 6.4: By 2030, substantially increase water-use efficiency across all sectors and ensure sustainable withdrawals and supply of freshwater to address water scarcity and substantially reduce the number of people suffering from water scarcity". Ongoing climate and environmental changes, increasing water scarcity and desertification affect agriculture. Limited opportunities to expand the volume of global freshwaters allocated to irrigation means that advanced irrigation technologies, aiming to improve efficiency of existing systems are needed, timely, and are of paramount importance. To combine different local conventional water sources (surface and groundwater) with alternative ones (like reused water or harvested rainwater) is also important for addressing the seasonal scarcity.

Further, main pollution sources are produced by human settlements, industries, agriculture and livestock. About 80% of urban wastewater is not treated before being discharged and heavy metals, solvents and other pollutants are released from industrial activities in significant quantities. Given the large amount of water required, the agricultural sector is one of the main sources of pollution of water bodies. In fact, the constant use of pesticides and fertilizers represents a serious risk for aquatic systems and production activities. Agricultural residues give pollution for about 38% of the European water surface, while in the United States it represents the main source of pollution of waterways. Other factors at high eco-impact are due to the large amounts of water used for irrigation. These high volumes generate phenomena of leaching of the mineral salts naturally contained in the soils. Moreover, different regions of the world present the problems of excessive salinity in water, which alters geochemical cycles with significant impacts on the biodiversity of flora and fauna.

In the last years the agricultural productions have been intensified promoting the increase of agrochemicals. The use of mineral fertilizers has been increased tenfold with large consumption of herbicides and fungicides. The use of crop protection products is now essential to guarantee and sustain the productivity. Livestock farming is a source of organic waste such as manure, pig slurry has BOD levels between 30 and 80 g/L compared to domestic BOD values of 200-500 mg/L; many microorganisms and parasites which survive days or weeks can contaminate water and food; chemical residues, drugs and heavy metals are also a serious danger. Aquaculture is also a source of serious water degradation, in fact anti-vegetative substances, antibiotics and fungicides are commonly used in aquaculture.

European Union (EU) over the years has taken various measures to prevent pollution. Contaminated water and poor sanitation are linked to transmission of diseases such as cholera, diarrhoea, dysentery, hepatitis A, typhoid, and polio. Absent, inadequate, or inappropriately managed water and sanitation services expose individuals to preventable health risks. This is particularly the case in health care facilities where both patients and staff are placed at additional risk of infection and disease when water, sanitation, and hygiene services are lacking. There are many sources of water contamination, including naturally occurring chemicals and minerals (for example, arsenic, radon, uranium, etc.), local land use practices (fertilizers, pesticides, concentrated feeding operations, etc.), manufacturing processes, and sewer overflows or wastewater releases. Toxic substances from farms, towns, and factories readily dissolve into and mix with it, causing water pollution. When the rain falls and penetrates deep into the earth, filling the cracks, crevices, and porous spaces of an aquifer (basically an underground storehouse of water), it becomes groundwater—one of our least visible but most important natural resources.

At sea, tanker spills account for about 10 percent of the oil in waters around the world, while regular operations of the shipping industry—through both legal and illegal discharges—contribute about one-third. Oil is also naturally released from under the ocean floor through fractures known as seeps.

Radioactive waste is any pollution that emits radiation beyond what is naturally released by the environment. It's generated by uranium mining, nuclear power plants, and the production and testing of military weapons, as well as by universities and hospitals that use radioactive materials for research and medicine. Accidentally released or improperly disposed of contaminants threaten groundwater, surface water, and marine resources. In the earlies 2000s has been adopted the EU Water Framework directive (Directive 2000/60/EC) for the protection of aquatic resources and

promoting pollution reduction limiting the release of persistent and bio-accumulative organic toxic substances[6]. According to the EEA report 'European Waters - Assessment of the situation and pressures 2018', a significant improvement of water quality has been fixed by improving wastewater treatment and reducing the runoff of pollutants from agricultural land. Measures have been also taken to allow migratory fish to overcome reefs and restore degraded aquatic ecosystems.

1.1 WATER Quality assessment

Although most European groundwater bodies, such as aquifers, are in good health, only 40% of the monitored lakes, rivers, coastal waters and estuaries achieved at least 'good' ecological status according to the report [7]. Water quality can be expressed through various parameters. The main ones are salinity, nutrients, sediments and the level of contaminants [8]. Conceptually the salinity is the quantity of dissolved salts content in soil or water. Salts are highly soluble in surface and groundwater and can be transported with water movement. Sodium and chloride are the predominant ions in seawater. The concentration of dissolved chloride ions is sometimes referred to as chlorinity. The other main salts dispersed in seawater are composed by magnesium, calcium, and sulphate in different concentrations. The absence of salts leads to the formation of fresh water while when the salt concentration increase different salted water is obtained. Table 1.1 describes the degree of salinity for various salted water.

Table 1.1: *Salinity for water-types*.

***Salinity* Status**	***Salinity (ppm)***	**Use**
Fresh water	*<500*	Drinking and irrigation
Marginal	*500-1000*	Irrigation,
Brackish	*1000-3000*	Irrigation of certain crops; stock
Saline	*3000-10.000*	Livestock
Highly Saline	*10.000-35.000*	Limited use for certain livestock
Brine	>35.000	Some mining and industrial exist

Seawater salinities vary depending on geographical location. In general, seawater, such as that of the Mediterranean Sea, has a total salt concentration of 35g/L (Table 1.2). On contrary, the

seawaters of other regions, as the gulf region in the Middle East, presents a higher the salinity (48 g/L).

Table 1.2: *Mediterranean seawater salt concentration per Liters.*

Salt	***Concentration [g/L]***
NaCl	27.123
$MgCl_2$	3.807
$MgSO_4$	1.658
$Ca\ SO_4$	1.26
$K\ SO_4$	0.863
$CaCO_3$	0.123
$MgBr_2$	0.076

Table 1.3 reports the chemical composition of the Mediterranean, gulf region in the Middle East and dead seawater. These three kinds of seawater present three different salt concentrations. In particular Dead Sea is famous for being the lowest and saltiest catchment area in the world with a salt concentration of 365 g/L.

Table 1.3: *Comparison of chemical composition of three different seawater* [9].

		Mediterranean seawater	**Gulf Region in the Middle East**	**Dead Sea**
Chemical Element	**Chemical symbol**	**Range (ppm)**		
Sodium	Na	10700	11536.00 to 12433.00	40100
Magnesium	Mg	1280	1490.00 to 1543.00	44000
Calcium	Ca	405	378.00 to 404.00	17200
Potassium	K	380	469.00 to 459.00	7650
Strontium	St	10	n.a.	n.a.
Sulfate	SO_4	2700	3200.0 to 3273.00	n.a.
Bromine	Br	65	n.a.	5.300
Chloride	Cl	19365	21933.0 to 22014.00	224000
Organic-carbon	C	23 to 27	8.0 to 8.0	n.a.

Based on the way in which the water is used by man, it is possible to classify waters into:

- **Drinking water**, i.e. waters that has been made such as a result of a purification treatment or spring waters, such as mineral waters. They do not have particular hygienic characteristics and properties favourable to the healthiness of mineral waters. These waters flow spontaneously from natural sources perennial or perforated by man and with hygienic characteristics and original purity (as already mentioned above for the chemical classification). According to the Italian law, which is one of the most rigorous in this regard, "*natural mineral waters are considered to be waters which, originating from an underground aquifer or reservoir, come from one or more natural or perforated springs and which have particular hygienic characteristics and possibly properties favourable to health* [10]". The amount of mineral salts dissolved in the water indicates the fixed residual value of the water. This datum is calculated by bringing the water to a temperature of 180°C and what remains after its complete evaporation represents the fixed residue. This value is expressed in mg/L and the higher it is, the more salts are dissolved in a liter of water. Based on the fixed residue, waters can be classified into:

- minimally mineralized with fixed residue lower than or equal to 50 mg / L;
- oligomineral or slightly mineralized with fixed residue lower than 500 mg / L;
- medium mineral content with fixed residue between 500 and 1000 mg / L;
- rich in mineral salts with a fixed residue greater than 1,000 mg / L.

This type of water is suitable for specific health therapies and can be purchased in pharmacies. In general, those suffering from hypertension or who must favour diuresis should opt for minimally mineralized water or low mineral content water, while sportspeople should prefer medium-mineral water.

- **Industrial waters** are waters which, due to their characteristics, can be used in industrial processes. The main uses of these waters are:

- cooling and chemical processes in the chemical and petrochemical industries
- dilution in the pharmaceutical industries
- production in the agro-food industries
- cooling in the steel industries
- production of printed circuits and components in the electronic industries
- production in the paper industry

Industrial waters are obtained from natural waters subjected to particular treatments (desalination, degassing, etc.), which aim improving the characteristics for industrial use. Industrial waters are usually classified according to two parameters: encrusting power and aggressiveness.

- **Agricultural, zoo-technical and aquaculture waters** are usually surface waters, used in large quantities, probably excessive, in all developed countries. They must be non-polluted waters, because otherwise the pollutants would be fixed by plants or animals, with serious risks for the health of the consumers of these foods. This constitutes the main problem of the user, since the surface waters (rivers, lakes, etc.) are easily altered, if not appropriately purified, by the discharges connected to industrial activities and inhabited centres.
- **Thermal waters,** coming from the subsoil and with specific saline compositions, can be used for therapeutic purposes (hydrotherapy). They are classified in several ways:
  based on the temperature at which they flow from the source they are divided into hypothermal (between 20 ° and 30 ° C), homeothermal (between 30 ° and 40 ° C), hyperthermal (greater than 40 ° C) on the basis of the composition, which is linked to their origin and to the type of rocks with which they have come into contact, they are distinguished mainly in salty or chloride-sodium waters (mainly containing NaCl), sulphurous (containing H_2S and S in various combinations), arsenical-ferrous (containing large quantities of Fe and As), bicarbonate (containing calcium bicarbonate), sulphates (containing various sulphates), carbonic (containing free dissolved CO_2), radioactive (containing radioactive elements, especially radon Rn) , salt-bromine-iodine (containing chlorides, bromides and sodium iodides, of marine origin)
- **Waters for bathing** which must not harm the health of bathers. The quality of the natural waters for bathing is periodically monitored by the bodies in charge (in Italy by the Regions through the ARPA) with the count of the number of Escherichia coli bacteria and intestinal enterococcus bacteria present in 100 ml of water, an index of faecal contamination, which must not exceed specific limit values [11].

Pool waters must have the same values as drinking water and in addition the amount of free chlorine used in water disinfection is determined.

In conclusion, it is important to underline that the process of natural water purification has been, especially in the last century, seriously altered and compromised by industrialization and other human activities, in particular agriculture, in fact the time it takes for the ecosystem to providing

for the complete regeneration and re-accumulation of the water are very long, being linked to very slow and fragile natural processes.

In the last part of human history, two problems concerning the planet's water resources occurred simultaneously:

- water pollution (every year 8 million tons of plastic end up in the water, values that have increased tenfold since 1980, and between 300 and 400 million tons of heavy metals, solvents, toxic sludge and others)
- excessive consumption of water for human activities (global water consumption has grown by 600% in the space of a century)

1.2 Desalination as a way towards water recovery

Water desalination is a practical route to recovery clean and reusable firewater. In this field the membrane technology counts a large number of separation processes, including nanofiltration, reverse osmosis, membrane distillation, and membrane crystallization.

The major sources of clean waters are the oceans and the sea. However to recover clean water from the sea is necessary apply processes to remove the salts contained them. Desalination is the process for removing the saline fraction from waters containing salt, generally from marine waters, in order to obtain water with a low saline content; the water is then often used for food use, but also for industrial use, as cooling water. Drinking water must not be free of salts: both for health reasons and because the addition of certain salts is recommended (however, this is a practice generally carried out downstream of the distillation itself, to allow the addition of the correct salts) and why fully deionized water would be completely tasteless, that is not palatable. A small amount of saline entrainment is therefore left in the treated water, of the order of 25-50 mg /L. The technologies used today in water desalination processes can be classified according to the following main criteria:

- Phase change - in the water to be treated.
- Type of energy involved.
- Process employed.

According to these criteria, the main associated technologies can then be divided as shows in figure 1.1.

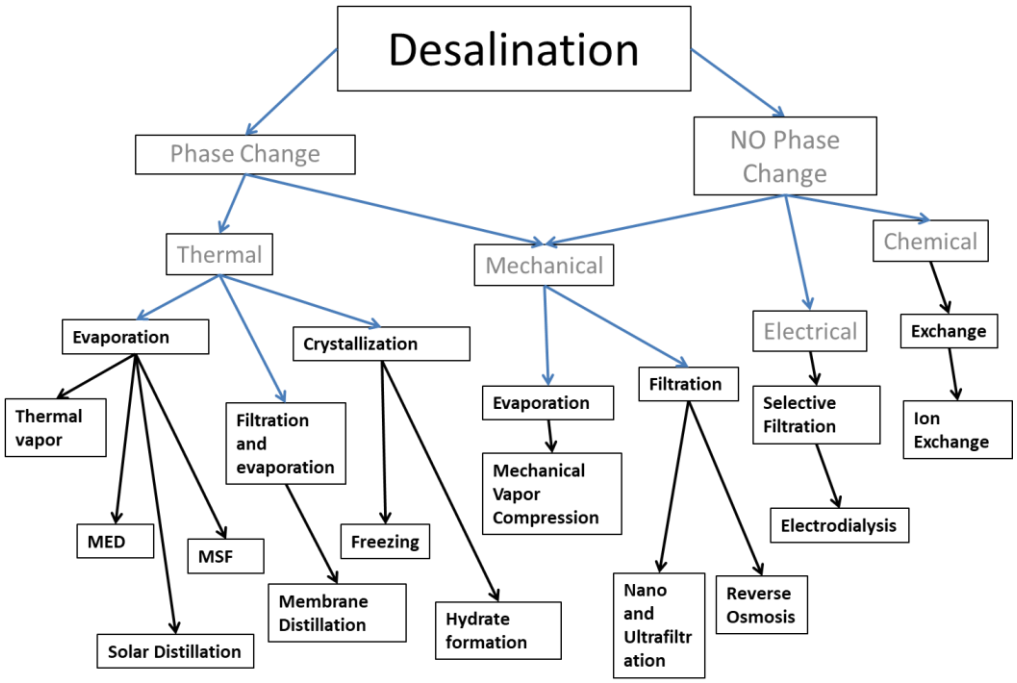

Figure 1.1 *Schematic Processes for desalination.*

As shown in figure 1.1 the first distinction that can be done is between processes based on phase change and processes based on no phase change. A second major distinction that can be made between processes developed for water purification is between processes based on a membrane system and processes that do not use membrane systems. Below there is a brief explanation of non-membrane based systems, whereas in chapter 2 a full description of membrane processes dedicated to water desalination is given

1.2.1 Water recovery with process NO-Membrane based

Multi-effect distillation (MED)

Multi Effect Distillation (MED) is one of the most used desalination process after RO. MED plants are designed with multiple airtight effects. In general, MED unit consists of maintained low pressure where saline water is sprayed. The heat required to cause evaporation of the feed in the next effect is supplied by solar energy or by combustion of fossil fuel. As the pressure and temperature going to decrease, a sequence of evaporation/condensation occurs constantly. The vapour generated inside the first effect is used as the energy source for the next effect and continues in subsequent order along the series of effects. In this way when the feed water is boiling and generating vapour in the same moment the vapour is condensing as fresh water on the other side [12]. The MED process requires heat input and electric power of 0.9 to 1.5 kWhr/m^3. In

general, the cost for large MED systems with a daily production from 91,000 m^3 to 320,000 m^3 ranges between 0.52 $/$m^3$ and 1.01 $/$m^3$ [13]. Furthermore, one advantage of MED systems are representing on its better compatibility with solar thermal desalination. The combination of MED unit with solar system of area 30,000–40,000 m^2 might guarantee a production of 1,00,000 tons of distilled water per year at a cost comparable to conventional methods of desalination [13].

Multi-stage flash distillation (MSF)

Multi stage flash (MSF) is one of the most worldwide desalination techniques used , especially in the Persian gulf and represents about 50% of the total number of large plants [14]. From the 1950s, processes such as MED and multistage flash (MSF) used in the commercial field, involved a series of phases. Seawater or recycled brine flowing inside the tubes is heated by steam exhausted from turbines in heat exchanger, called Brine Heater. The process is composed of a series of elements, called *stages*, where condensing steam is used to preheat the seawater feed. By splitting the overall temperature difference between the hot source and seawater into a large number of stages, the system approaches ideal total latent heat recovery. Operation of this system requires pressure gradients in the plant. Desalination via MSF involves brine heating followed with flash distillation in multiple stages and subsequent heat recovery [14]. The heated vapor is passed through tubes where the cold surface of the tubes allows condensation. The condensed vapor is collected as freshwater while the hot brine flows to other stages. The heat recovery process begins when the absorbed latent heat partially heats the circulating brine to a low temperature, thus saving energy and improving system performance [15]. In the heat recovery stages, the last few stages of MSF, the brine blowdown and distillate are cooled, and the remaining heat is rejected in heat rejection section of MSF. The MSF process requires heat input and electric power of 3.5-4.5 kWhr/m^3. The major disadvantage of MSF plants is the high-energy consumption. Currently, there are facilities where electrical energy generation from solar parks is combined with drinking water production from flash type evaporation plants [16].

Mechanical vapour compression (MVC)

In the MVC process, seawater enters the preheater unit where it exchanges thermal energy with the concentrate and effluents of the produced water. Preheated seawater is sprayed onto bundles of heat exchange tubes, which are at a higher temperature than seawater [17]. Mechanical vapor

compression vacuum evaporators evaporate seawater on one side of the exchange surface, and this is compressed sufficiently to condense on the other side and thus maintain the water distillation cycle; the water vapors are compressed by a mechanical compressor and are pumped into the pipes of the heat exchange beams. The compressed vapor condenses inside the tube, releasing energy, which is transferred to the seawater sprayed on the tube and causes it to evaporate. These small devices are much more reliable and easier to use than reverse osmosis equipment and are virtually maintenance free, making them ideal for supplying fresh water to small towns, remote areas or islands, for example. The specific consumption of these plants is lower than other distillation processes, with an equivalent electrical consumption normally of about 10 kWh / m^3. The major limitation of this type of technology is the maximum size of the volumetric compressors used. Its maximum capacity does not allow a high production of desalinated water [18].

Vapor compression distillation (VC)

Vapor compression distillation (VC) can function independently or be used in combination with another thermal distillation process [19,20]. VCD uses heat from the compression of vapor to evaporate the feed water. VCD units are commonly used to produce fresh water for small- to medium-scale purposes such as resorts, industries, and petroleum drilling sites. The vapors separated in the evaporation chamber EC are brought to higher pressure by the compressor K, driven by the engine M (usually electric, but it can be for example a turbine). Thanks to the increase in pressure, the condensation temperature of the vapors rises, which can therefore condense in the HE exchanger [21]. There are double and even triple effect desalinations of this type, in which the vapor of the last effect, after compression, is sent to the first, doubling (or tripling) the yield in treated water.

Solar distillation (SD)

Solar desalination is generally used for small scale operations. Although the designs of solar distillation units vary greatly, the basic principles are the same [22]. The sun provides the energy to evaporate the saline water. The water vapor formed from the evaporation process then condenses on the clear glass or plastic covering and is collected as freshwater in the condensate trough. The covering is used to both transmit radiant energy and allow water vapor to condense

on its interior surface. The salt and un-evaporated water left behind in the still basin forms the brine solution that must be discarded appropriately [23].

Thermal Vapor Compression (TCV)

Thermal Vapor Compression (TCV) is one of the two technologies used and consists of obtaining distilled water by the same process as multiple effect distillation, but by using a different source of thermal energy [24]. These are thermal compressors (or thermocompressors), which consume medium pressure steam from electricity generation plants (if it is a dual plant, it is process vapor obtained expressly for this purpose). They take part of the vapor produced in the last stage at very low pressure, compress it and obtain an intermediate vapor pressure comparable with the previous ones suitable to contribute to the 1st stage, which is the only one consuming energy in the process [25]. The yield from this type of plant is similar to those from multiple effect distillation (MED) plants; however, their desalination capacity can be much greater by allowing greater adaptability for the input from steam production plants. They are often considered to be the same process, but here they will be treated individually as the energy from the plant is consumed by different equipment [26].

Permeation desalination (PD)

Desalination by permeation is obtained by separation on semipermeable membranes. The characteristics of water and rejection are similar to the previous type; however, it is not possible to achieve total recovery of the aqueous part since membranes by reverse osmosis do not allow the treatment of solid phases, if not by providing an evaporative section [27]. A special case is desalination by electrodialysis. The reverse osmosis type is used for small to large productions in orders of magnitude from 1 to 10 000 m^3 / h and for quality similar to evaporative desalination.

Desalination by ion exchange (IC)

Desalination by ion exchange is obtained by removing the Na^+ and Cl^- ions on resins respectively in the H^+ and OH^- cycle (this obviously applies to all the ions present) [28–30]. Strongly desalinated water is obtained in a single pass; in this case residues of the regeneration of the resins constitute the rejection. The ion exchange type is used for small and very small flow rates, of the order of 1 m^3/h maximum, or to obtain very high purities of the water produced [31].

Combined systems

The implants can obviously be combined; it is a current trend to install a relatively simple reverse osmosis system in series, followed by an evaporated one with the aim of recovering additional

water; a part of the water produced could be further purified by ion exchange demineralization, for example to be able to use it to power a boiler [32].

Reference

[1] V.G. Gude, Desalination and water reuse to address global water scarcity, Rev. Environ. Sci. Biotechnol. 16 (2017) 591–609. doi:10.1007/s11157-017-9449-7.

[2] M.A. Alberti, I. Blanco, G. Vox, G. Scarascia-Mugnozza, E. Schettini, L. Pimentel da Silva, The challenge of urban food production and sustainable water use: Current situation and future perspectives of the urban agriculture in Brazil and Italy, Sustain. Cities Soc. 83 (2022) 103961. doi:10.1016/j.scs.2022.103961.

[3] V. Mereu, A. Gallo, A. Trabucco, G. Carboni, D. Spano, Modeling high-resolution climate change impacts on wheat and maize in Italy, Clim. Risk Manag. 33 (2021) 100339. doi:10.1016/j.crm.2021.100339.

[4] J. Guiot, W. Cramer, Climate change: The 2015 Paris Agreement thresholds and Mediterranean basin ecosystems, Science (80-.). 354 (2016) 465–468. doi:10.1126/science.aah5015.

[5] https://www.medecc.org/wp-content/uploads/2018/12/MedECC-Booklet_EN_WEB.pdf, (n.d.).

[6] P.K. Roy, S. Ray, A. Majumder, Study of Water Quality of Packaged and Municipal Supply Drinking Water With Performance Evaluation of Stand-Alone Filters, in: Bottled Packag. Water, Elsevier, 2019: pp. 63–82. doi:10.1016/B978-0-12-815272-0.00003-9.

[7] C. Galdies, R. Bellerby, D. Canu, W. Chen, E. Garcia-Luque, B. Gašparović, J. Godrijan, P.J. Lawlor, F. Maes, A. Malej, D. Panagiotaras, B.M. Romera, C.E. Reymond, J. Rochette, C. Solidoro, R. Stojanov, R. Tiller, I. Torres de Noronha, G. Uścinowicz, Natașa Vaidianu, C. Walsh, R. Guerra, European policies and legislation targeting ocean acidification in european waters - Current state, Mar. Policy. (2020). doi:10.1016/j.marpol.2020.103947.

[8] G. Walker, I.P. Prosser, Water quality: Land use impacts on salinity, sediments, and nutrients, in: Murray-Darling Basin, Aust., Elsevier, 2021: pp. 109–135. doi:10.1016/B978-0-12-818152-2.00006-1.

[9] V.K. Gouda, I.M. Banat, W.T. Riad, S. Mansour, Microbiologically Induced Corrosion of UNS N04400 in Seawater, CORROSION. 49 (1993) 63–73. doi:10.5006/1.3316036.

[10] https://www.normattiva.it/uri-res/N2Ls?urn:nir:stato:decreto.legislativo:2011;176, (n.d.).

[11] A.H. Farnleitner, G. Ryzinska-Paier, G.H. Reischer, M.M. Burtscher, S. Knetsch, A.K.T. Kirschner, T.

Dirnböck, G. Kuschnig, R.L. Mach, R. Sommer, Escherichia coli and enterococci are sensitive and reliable indicators for human, livestock and wildlife faecal pollution in alpine mountainous water resources, J. Appl. Microbiol. (2010) no-no. doi:10.1111/j.1365-2672.2010.04788.x.

[12] M.C. Garg, Renewable energy-powered membrane technology: Cost analysis and energy consumption, in: Curr. Trends Futur. Dev. Membr. Renew. Energy Integr. with Membr. Oper., Elsevier, 2018: pp. 85–110. doi:10.1016/B978-0-12-813545-7.00004-0.

[13] H. Sharon, K.S. Reddy, A review of solar energy driven desalination technologies, Renew. Sustain. Energy Rev. 41 (2015) 1080–1118. doi:10.1016/j.rser.2014.09.002.

[14] A. Al-Othman, M. Tawalbeh, M. El Haj Assad, T. Alkayyali, A. Eisa, Novel multi-stage flash (MSF) desalination plant driven by parabolic trough collectors and a solar pond: A simulation study in UAE, Desalination. 443 (2018) 237–244. doi:10.1016/j.desal.2018.06.005.

[15] C.S. Bandi, R. Uppaluri, A. Kumar, Global optimization of MSF seawater desalination processes, Desalination. 394 (2016) 30–43. doi:10.1016/j.desal.2016.04.012.

[16] T. Mezher, H. Fath, Z. Abbas, A. Khaled, Techno-economic assessment and environmental impacts of desalination technologies, Desalination. 266 (2011) 263–273. doi:10.1016/j.desal.2010.08.035.

[17] M.A. Farahat, H.E.S. Fath, I.I. El-Sharkawy, S. Ookawara, M. Ahmed, Energy/exergy analysis of solar driven mechanical vapor compression desalination system with nano-filtration pretreatment, Desalination. 509 (2021) 115078. doi:10.1016/j.desal.2021.115078.

[18] Q. Chen, M. Kum Ja, M. Burhan, F.H. Akhtar, M.W. Shahzad, D. Ybyraiymkul, K.C. Ng, A hybrid indirect evaporative cooling-mechanical vapor compression process for energy-efficient air conditioning, Energy Convers. Manag. 248 (2021) 114798. doi:10.1016/j.enconman.2021.114798.

[19] C. Wen, L. Gong, H. Ding, Y. Yang, Steam ejector performance considering phase transition for multi-effect distillation with thermal vapour compression (MED-TVC) desalination system, Appl. Energy. 279 (2020) 115831. doi:10.1016/j.apenergy.2020.115831.

[20] S. Fan, J. Li, Y. Liu, Z. Xiao, Bioethanol production in membrane distillation bioreactor with permeate fractional condensation and mechanical vapor compression, Energy Procedia. 158 (2019) 21–25. doi:10.1016/j.egypro.2019.01.026.

[21] C. Wen, H. Ding, Y. Yang, Performance of steam ejector with nonequilibrium condensation for multi-effect distillation with thermal vapour compression (MED-TVC) seawater desalination system, Desalination. 489 (2020) 114531. doi:10.1016/j.desal.2020.114531.

[22] A.K. Dahayat, A. Somwanshi, B. Patel, Economic analysis of conventional single slope solar distillation plant for different climates in India, Mater. Today Proc. (2022). doi:10.1016/j.matpr.2021.12.479.

[23] C. Li, X. Zhou, Y. Xiao, T. Zhang, M. Ye, Inhibition of typical phenolic compounds entering into condensed freshwater by surfactants during solar-driven seawater distillation, Sci. Total Environ. 815 (2022) 152694. doi:10.1016/j.scitotenv.2021.152694.

[24] M.A. Farahat, H.E.S. Fath, M. Ahmed, A new standalone single effect thermal vapor compression desalination plant with nano-filtration pretreatment, Energy Convers. Manag. 252 (2022) 115095. doi:10.1016/j.enconman.2021.115095.

[25] S. Zhou, X. Liu, K. Zhang, S. Shen, Investigation and optimization for multi-effect evaporation with thermal vapor compression (MEE-TVC) desalination system with various feed preheater arrangements, Desalination. 521 (2022) 115379. doi:10.1016/j.desal.2021.115379.

[26] B. Shahzamanian, S. Varga, J. Soares, A.I. Palmero-Marrero, A.C. Oliveira, Performance evaluation of a variable geometry ejector applied in a multi-effect thermal vapor compression desalination system, Appl. Therm. Eng. 195 (2021) 117177. doi:10.1016/j.applthermaleng.2021.117177.

[27] X. Wang, W. Qin, L. Wang, K. Zhao, H. Wang, H. Liu, J. Wei, Desalination of dye utilizing carboxylated TiO2/calcium alginate hydrogel nanofiltration membrane with high salt permeation, Sep. Purif. Technol. 253 (2020) 117475. doi:10.1016/j.seppur.2020.117475.

[28] B. Smitha, S. Sridhar, A.A. Khan, Solid polymer electrolyte membranes for fuel cell applications - A review, J. Memb. Sci. (2005). doi:10.1016/j.memsci.2005.01.035.

[29] Y. Mei, C.Y. Tang, Recent developments and future perspectives of reverse electrodialysis technology: A review, Desalination. 425 (2018) 156–174. doi:10.1016/j.desal.2017.10.021.

[30] C. Zhang, J. Song, T. Huang, H. Zheng, T. He, Increasing lithium extraction performance by adding sulfonated poly (ether ether ketone) into block-copolymer ethylene vinyl alcohol membrane, J. Chem. Technol. Biotechnol. 95 (2020) 1559–1568. doi:10.1002/jctb.6350.

[31] T. Xu, C. Huang, Electrodialysis-Based separation technologies: A critical review, AIChE J. 54 (2008) 3147–3159. doi:10.1002/aic.11643.

[32] S. Xiao, Q. Guan, W. Zhang, L. Wu, Optimal scheduling of the combined power and desalination system, Energy Reports. 8 (2022) 661–669. doi:10.1016/j.egyr.2021.11.253.

Chapter 2

Membrane Technology: a suitable strategy for water desalination

2.1 Membranes and membrane filtration: general concepts

Traditionally, a membrane is defined as a barrier that separates two phases and allows selective transportation of species under the influence of a specific driving force and according to suitable mechanisms (Figure 2.1).

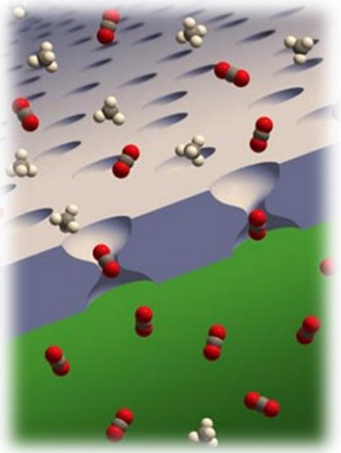

Figure 2.1 *Selective transportation of species under the influence of a driving force.*

The driving force can be a difference of chemical or electrical potential between two sides of the membrane. Depending on the kind of driving force it is possible to obtain different membrane processes. Pressure-driven membrane processes such as microfiltration (MF), ultrafiltration (UF) and nanofiltration (NF) are widely used in membrane purification applications. Because of the driving force, solvent or water passes through the membrane together with small molecules, while the molecules larger than the membrane nominal pore size are rejected. Going from MF to NF the size of membrane pores becomes smaller (from 10 µm in MF to 2 nm in NF) and consequently also the dimension of the particles rejected decreases. Denser membranes are used in reverse osmosis (RO) applications where the pore size is in the order of a few nm. RO membranes are used when low molecular weight solutes such as inorganic salts or glucose have to be separated from the solvent. RO membranes require high pressures to operate (ranging from 15 to 80 bar) and they are often applied for the desalination of brackish water or seawater. In concentration-driven

processes, on the contrary, dense membranes are used. The transport across the membrane occurs by the dissolution and adsorption of a target molecule through the membrane material. The affinity between the polymer and the permeating molecule is therefore of primary importance in order to achieve the separation. The chemical gradient formed by the difference in concentration between the two sides of the membrane represents the driving force in this type of membrane separation. Pervaporation, gas separation and vapour permeation are among the membrane separation processes based on the concentration difference [1].

The membranes are generally allocated in suitable supports, to which the supply and discharge connections are also connected, so as to form modules that, in turn, can be connected according to the requirements of the desired separation process (fig. 2.2).

At the industrial level, where hundreds or thousands of square meters of membrane are required, membranes are assembled together in order to form modules with different configurations. There are basically 3 types of configuration: flat, spiral, and hollow fiber membranes. Schematically they are shown in Figure 2.3. For each configuration the properly modules are necessary.

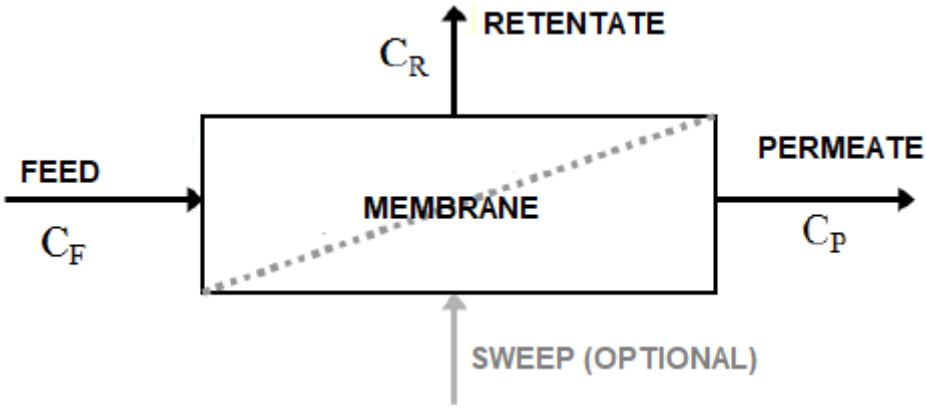

Figure 2.2 *Separation mechanism of a generic membrane.*

Plate and frame modules were one of the first modules developed by the industry. In this configuration, flat-sheet membranes and permeate spacers are layered with spacers forming feed flow channels and clamped together between two end plates (Fig. 2.3). The feed is forced across the permeate that is collected through a central permeate collection manifold. In spiral-wound configuration, flat sheet membranes are wound like an envelope with feed spacers around a central collection tube. The feed is pumped into the space outside the envelope and the permeate is, then, collected inside the envelope and directed to the central tube.

Tubular membrane modules are used for hollow fibre, capillary and tubular membranes. Hollow fiber membrane modules are made up of several tubular membranes arranged in parallel in two types of configuration. In the shell side configuration, the feed is in contact with the external fibre

surface. Thus, the permeate passes through membrane walls and exits through the open fibre ends where it is collected. In the second configuration, the feed is circulated through the lumen of the fibres and the permeate is collected on the shell side.

Processes based on the pressure driven are reverse osmosis (RO), nanofiltration (NF), ultrafiltration (UF), microfiltration (MF), pervaporation (PV) and membrane gas separation (GS). The concentration gradient driven membrane processes are dialysis and membrane extraction, while an electrical potential driven membrane process is electrodialysis (ED).

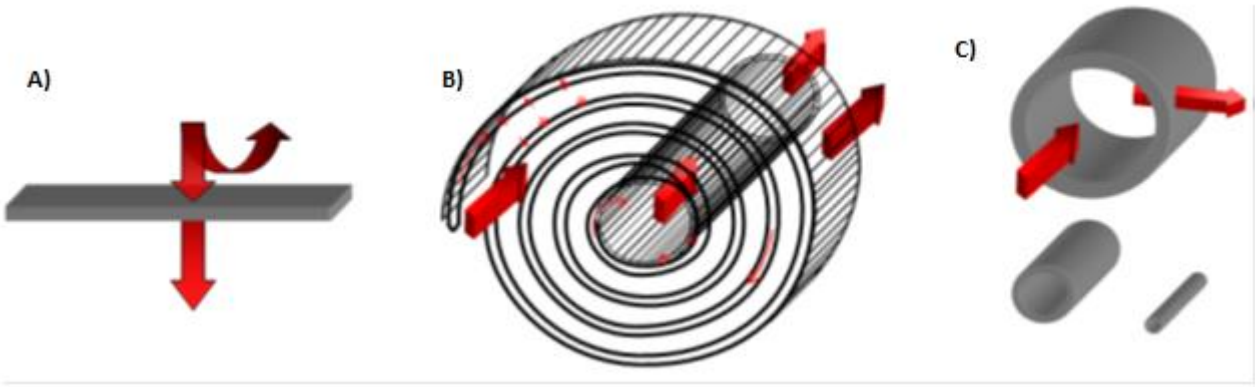

Figure 2.3 *Different membrane configurations. A) flat sheet, B) spiral and C) hollow fiber configurations.*

Membranes have a multitude of characteristics, but the first distinction that can be made is about their synthetic or biological nature. The biological membranes include liposomes and phospholipid vesicles, which, in recent years, are gaining great importance in separation processes, especially in medicine and biomedicine. Synthetic membranes are artificially produced, and in general, can be homogenous or heterogeneous, symmetric or asymmetric in structure, solid or liquid, can carry a positive or negative charge, or can be neutral or bipolar [1].

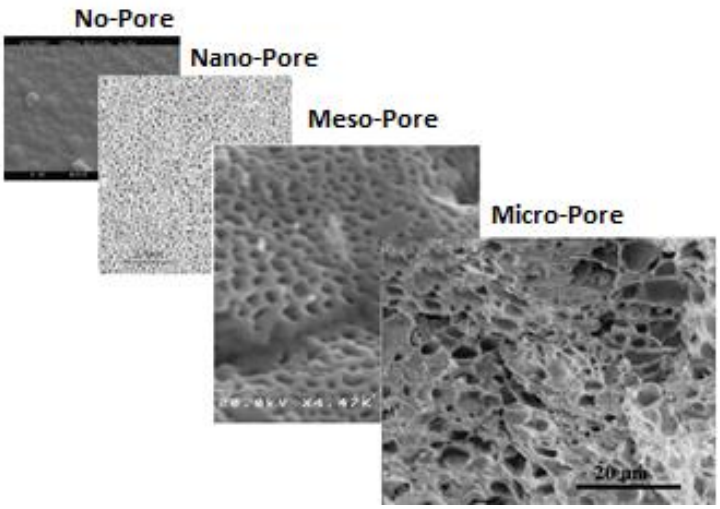

Figure 2.4 *SEM Pictures from Dense to microporous membranes.*

Membranes can be made of polymers, metals, inorganic compounds, carbon, ceramic and liquids (Figure 2.5). The polymeric membranes (fig. 2.6), unlike the previous ones, have the characteristic of having a low production cost and a relative simplicity of preparation. In principle, all polymers can be used to form a membrane and, considering the huge variety of polymeric materials available, polymeric membranes therefore possess an enormous variety of properties, thus finding application in various fields.

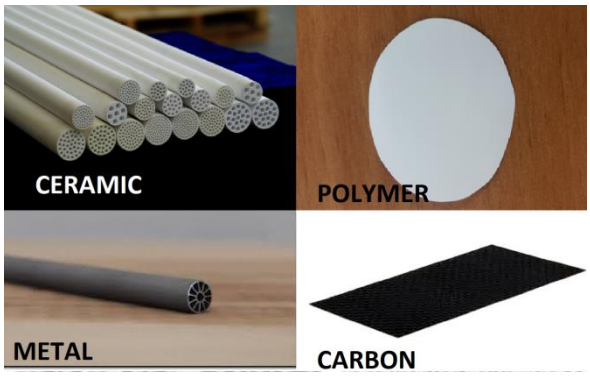

Figure 2.5 *Such examples of different membrane materials: ceramic, polymer, metal and carbon.*

Polymeric membranes are the most widely used on an industrial level both for their low cost and ease of workability. Although a large number of novel polymers have been developed at a lab scale, so far less than twenty have been used as materials for industrially established membranes. They include cellulose, polyvinylidene fluoride, polyethersulfone, polypropylene, polyethylene, polyacrylonitrile, polyamide, polyimide, etc. (Figure 2.6). These polymers have different properties also dependent on the preparation method which make the corresponding membranes suitable for different separation processes (from gas separation to filtration, etc.) [2,3].

The commercial application of membranes started since 1960s. One of the most important discoveries in the membranes field has been that of Loeb and Sourirajan [4]. They developed the first asymmetric integrally skinned cellulose acetate reverse osmosis membrane. The concept of a thin skin layer of separating barrier on the top of a highly porous polymer support is associated with a much lower pressure drop than symmetric membranes. This development stimulated the interest about membrane based separation techniques, either in industrial processes or in academic field.

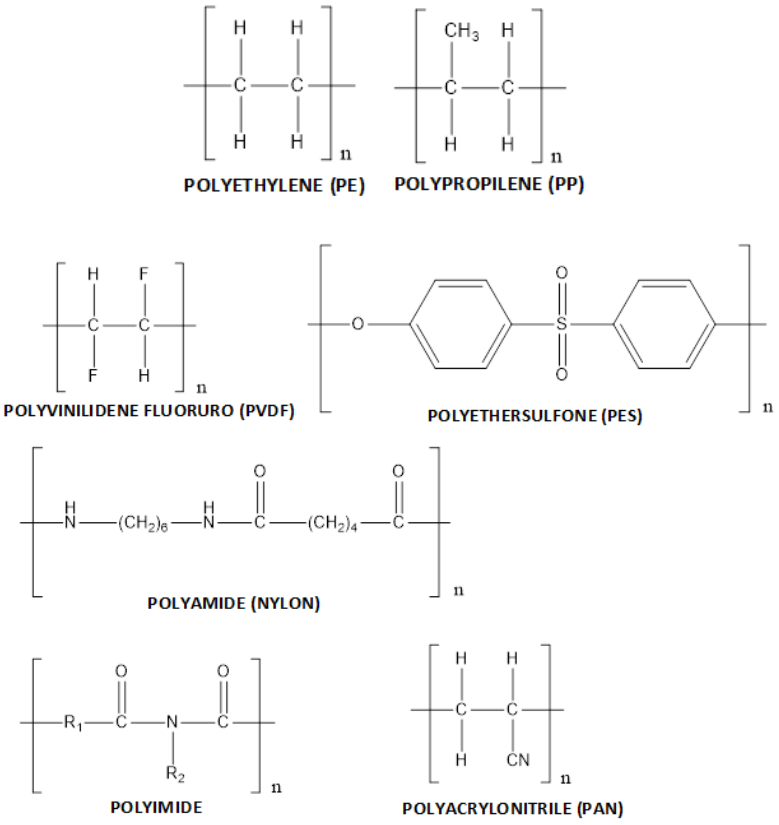

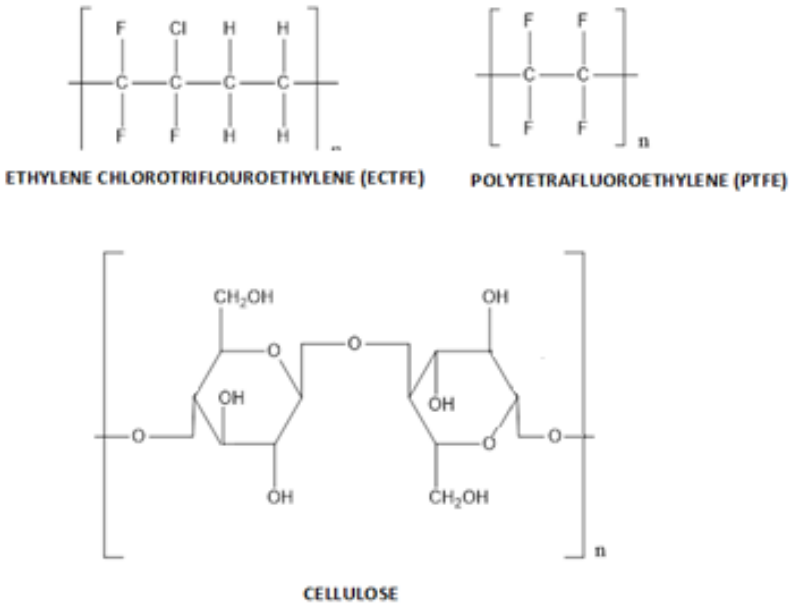

Figure 2.6 *Chemical structures of some polymers used for membrane production.*

2.2 Membrane preparation

Mainly two categories of techniques are distinguished for the preparation of synthetic polymeric membranes [1]. The techniques based on traditional phase inversion and the techniques that are breakthrough for strategy and ability to control morphology and chemistry on scale. For the first category, the polymer must be soluble in a suitable solvent or in a mixture of solvents. A polymer is precipitated in a state-controlled manner through several different techniques:

• *Evaporation of the solvent, (EIPS):* it is the simplest technique for preparing membranes through phase inversion (fig. 2.7). With this method, the polymer is dissolved in a suitable solvent and a homogeneous solution, is spread on a support, such as a glass plate. The solvent is then left to evaporate in an inert atmosphere at a controlled temperature and humidity, thus obtaining a dense and homogeneous membrane.

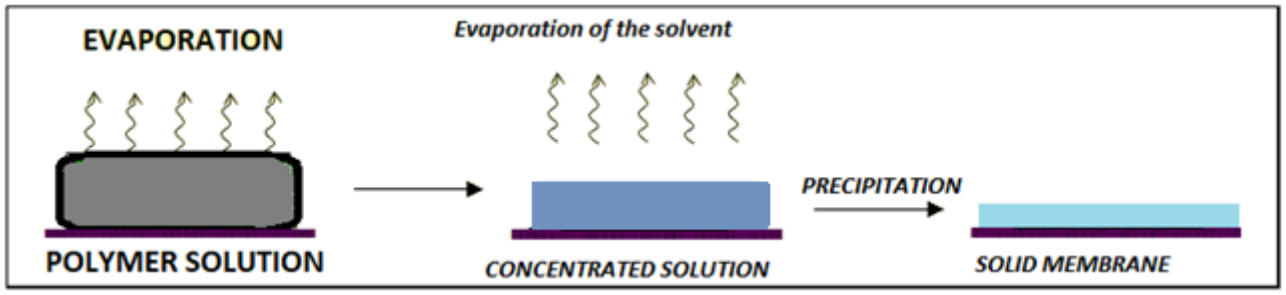

Figure 2.7: *Schematic representation of the evaporation of the solvent induced phase inversion process.*

• *Thermally Induced Phase Separation (TIPS):* is the technique used for those polymers that are not soluble in common solvents at room temperature and require high temperatures to be solubilized (fig. 2.8). In fact, it is based on the phenomenon of non-solubility at low temperatures. The polymer is dissolved in the appropriate solvent at a high temperature and the solution is spread at a high temperature on a special support where it is cooled in a controlled way. The thermal gradient induces the non-solubility of the polymer with its consequent precipitation and formation of the membrane. With this technique it is possible to prepare porous and symmetrical membranes or porous and asymmetrical membranes if the solvent does not evaporate completely. Finally the solvent is extracted or evaporated in an oven.

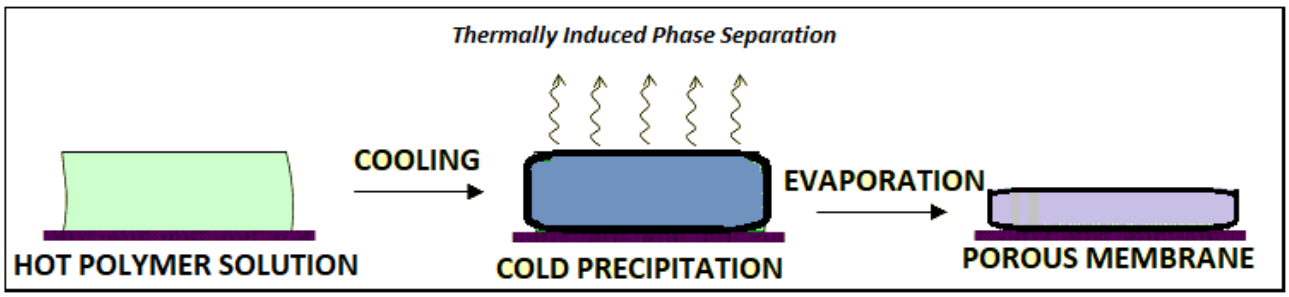

Figure 2.8: *Schematic representation of the thermally induced phase inversion process.*

• *Vapor Induced Phase Separation (VIPS):* is a technique in which a spread film, consisting of a polymer and a solvent, is put into contact with a vapor atmosphere, where the vapor phase is represented by a non-solvent for the polymer, saturated with the solvent (fig. 2.9). The high concentration of solvent in the vapor phase prevents the evaporation of the solvent from the film. The formation of the membrane is given by the penetration (diffusion) of the non-solvent, usually water, into the spread film.

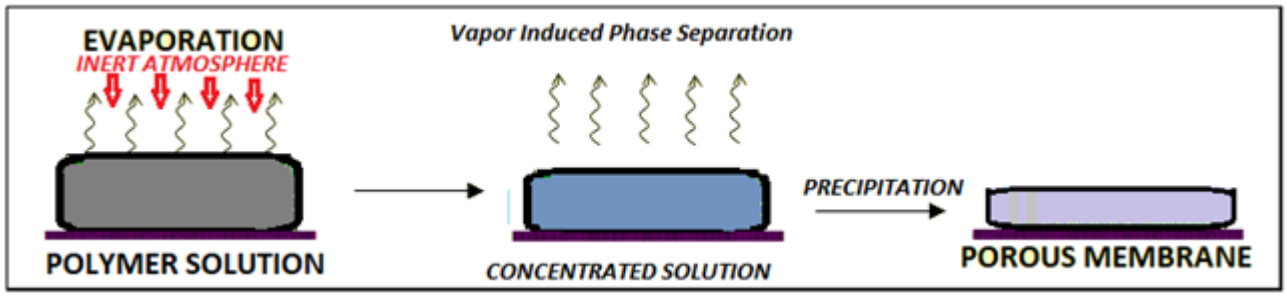

Figure 2.9: *Schematic representation of the vapor induced phase inversion process.*

• *Non-solvent-induced phase inversion (NIPS):* The polymeric solution, spread on a suitable support, is immersed in a coagulation bath containing a non-solvent (fig.2.10). Precipitation occurs due to the exchange between solvent and non-solvent in the coagulum bath. The formation of the first solid states slows down the diffusion of the non-solvent inside the "bulk" of the membrane,

resulting in the formation of porous structures. Composition and temperature of the casting solution and of the clot bath, as well as the time of exposure to air before immersion, and time of immersion in the clot bath decide the final morphology of the membrane. It is one of the most commonly used techniques for the production of commercial membranes, including those dedicated to water desalination.

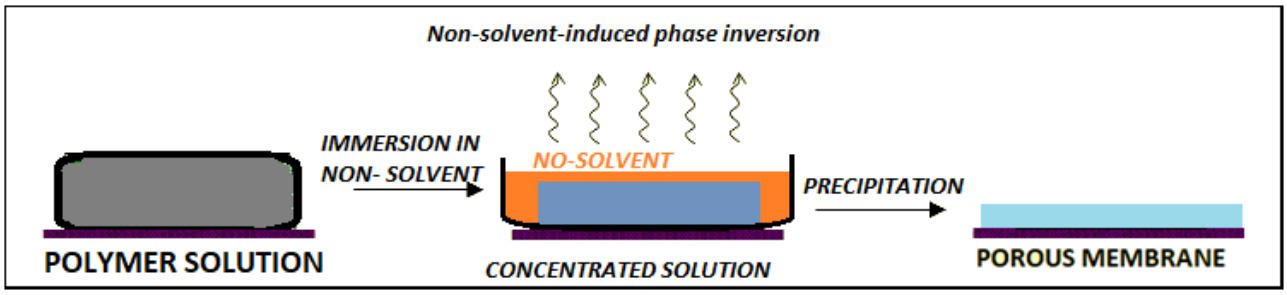

Figure 2.10: *Schematic representation of the non-solvent induced phase inversion process.*

Other traditional manufacturing techniques include:

- *Sintering*: It is a relatively simple technique and is used for the preparation of porous membranes starting from powders. These are pressed and then brought to high temperatures, very close to the melting temperature of the polymer. Only the outer part of the powder becomes molten, while the central part remains solid. Under pressure, the surfaces join together causing the particles of the powder to join together to form the membrane. The pore size of the membrane depends on the size of the initial dust particles and their distribution. This technique is suitable for non-soluble polymers, and for materials with high thermal, mechanical or chemical stability.
- *Extrusion*: This is the fastest and simplest technique for preparing dense membranes. The polymer or inorganic material is brought to a high temperature in an extruder, i.e. in a tank with an orifice on the side. The polymer is made to exit from it at high pressure with the desired shape, which depends on the geometry of the extrusion head, the rheology of the solution and the speed of collection and stretching of the film produced.
- *Etching*: A film of polymeric material is bombarded with high-energy particles from a source. These particles damage the polymeric material in different points, and since the source must be fixed, the number of damage depends on the speed of movement of the film and the intensity of the radiation. Subsequently, the damaged film is immersed in an acid or basic solution, with the aim of removing the damaged material and forming perfectly cylindrical pores. The pore diameter is a function of the immersion time in the corrosive bath.

A second category of membranes is that realized according to more sophisticated featured manufacturing strategies. These breakthrough methodologies include:

- *Lithographic technique that* is a technique proposed especially for making polymeric surfaces with a regular structure with a precise geometric order. The main feature of lithography is the mechanical reproduction of certain images. At the nanometer level (lateral size between the size of a single atom and about 100 nm), lithography can be used in the fabrication of advanced semiconductor integrated circuits or nano electromechanical systems (NEMS). Lithography can also be performed by using a support [5] on which the polymer solution is placed, making the final result with certain structures and properties. Patterns are created by mechanical deformation of the impression strength and subsequent processes. The main disadvantage of this process is the high cost of making molds with dimensions of the order of the nano as well as the difficulty in obtaining a large resolution. On a larger scale, the creation of well-made surfaces turns out to be more efficient and easer.

- *Phase separation micro-molding (PSμM) that* is a highly specialized manufacturing process that produces extremely small, high-precision thermoplastic parts and components with micron tolerances [6]. The process starts in a tooling department where a mold is created that has a cavity in the shape of the part desired. Thermoplastic or resin is rapidly injected into the cavity, creating the component or part at high speed. The combination of micro-molding and phase separation techniques turn out to be another approach to create nanostructures with hierarchical ordered morphology. It can be seen as an evolution of the traditional phase reversal. A polymer is precipitated from a solution assuming a desired configuration similar to traditional phase inversion. The final configuration can be flat, cylindrical or spherical. The solidification process begins with the transition from a liquid to two liquid phases: one rich in polymer, the other rich in solvent. The first solidifies forming a solid network; the second generates pores or voids in the matrix [7].
- *Colloidal templates for Membrane Preparation that uses* polymeric nanocapsules as colloidal particles composed of a shell or membrane, which is mechanically very strong and separates the internal cavity from the outside medium thus creating a barrier for various substances that can be encapsulated therein [8]. Scientists found that monodisperse colloidal spheres can self-assemble into arrays of periodic spheres, called colloidal crystals,

in a hexagonal arrangement under well-controlled experimental conditions using drop-coating, spin-coating, dip-coating, electrophoretic deposition and self-assembly at the interface liquid / gas. Moreover, in the large hollow spaces, substances such as drugs and biomolecules can be encapsulated and released in a controlled manner, which makes the polymeric nanocapsules attractive devices for drug delivery, cancer and gene therapy, protecting enzymes, etc. [9]. The synthesis of monodisperse colloidal spheres offers the opportunity to extend their applications. Membranes with morphological features of high structural order at nanometric scale may be achieved according to colloidal template method. Colloid crystalline particles are three-dimensional close-packed crystals of sub-micrometer spheres working as imprinting agents, whose long-ranged ordered structure is replicated in a solid matrix, thus yielding materials with ordered pores. Colloidal crystal structures with this ordered architecture, are of great interest for the tissue engineering wherein the availability of arrays for cellular proliferation is requested to promote the optimum environment for a good adhesion and consequent cells proliferation [10].

- *Self-assembly copolymers that exploits* the ability of some materials to spontaneously form ordered aggregates [11]. This allows having nanostructures, even complex ones, depending on the intrinsic structure and chemistry of the molecules involved. The components most present in these types of assemblies are: lipids, proteins, carbohydrates and nucleic acids; molecular crystals; liquid crystals; semi-crystalline and separate phase polymers. In the case of membranes, the ability of polymers to self-assemble on a nanometric scale is exploited. Different techniques are used in these processes. The two main strategies that have been used by the researchers:

  - Use block polymers, which give rise to a cylindrical morphology with expedients, such as to ensure that the cylindrical domains are oriented perpendicularly to the thin dimension of the film.

  - Use a block polymer with a bi-continuous morphology (i.e. a gyroid phase), which obviates the need for alignment [12].

- *Breath figure for bio-inspired high-defined membranes that has been* developed in the context of bio, innovative and bio processes in the preparation of micro-porous membranes [13]. This technique allows obtaining membranes with ordered pore geometry. The basic idea in the development of BF has been born from the observation of the common phenomenon of fog formation that is formed when water vapor comes into

contact with a cold surface. During this event, the condensation water droplets tend to rearrange themselves into an ordered geometry that resembles honeycomb patterns. BF allows the formation of rearranged droplets in well-defined geometries. This ability can be exploited to model the formation of pores in polymer films with simple and inexpensive techniques. The condensation of water droplets on the surface of dilute polymeric solutions containing immiscible or partially miscible solvents also allows easier recovery of the solvent at the end of the process. Furthermore, water is a widely available non-toxic templating agent, so the general approach can be considered as an environmentally friendly production technology. Despite the simplicity with which droplets can be formed, the mechanism that controls the formation of BF geometry can be very complex and not perfectly unique. This may depend on the polymeric materials and solvents used, but also on changes in the surrounding experimental conditions, which make the management of water droplet dynamics somewhat difficult [14].

2.3 Membrane technology for water desalination

Membrane desalination processes represent a reliable route for improving water quality at reduced costs and low environmental impact. The results achieved to date confirm the potential of Micro and Ultrafiltration in the removal of suspended solids and colloidal species. Nanofiltration is used to reduce water hardness and limit fouling in subsequent distillation processes [15-17].

Among the different processes introduced in the previous paragraph the common factor present in such of them is the Membrane-based systems. Membrane technologies represent interesting solutions to the production of freshwater. In fact, the growing global demand for water makes membrane processes the principal source of water with desalination and wastewater treatment. Figure 2.11 displays the percentage of the different membrane based technologies used in desalination processes. The technology that dominated this field is represented by Reverse Osmosis (SWRO), able to produce more than 100 million m^3/day of fresh water in 2020 from seawater, brackish water and wastewater [18]. This process, over the last few decades, became successful because it has the highest water recovery factor with respect to any other conventional distillation process [19,20]. Obviously, the membrane characteristics affect the performance of the process as well as the temperature and concentration of feed.

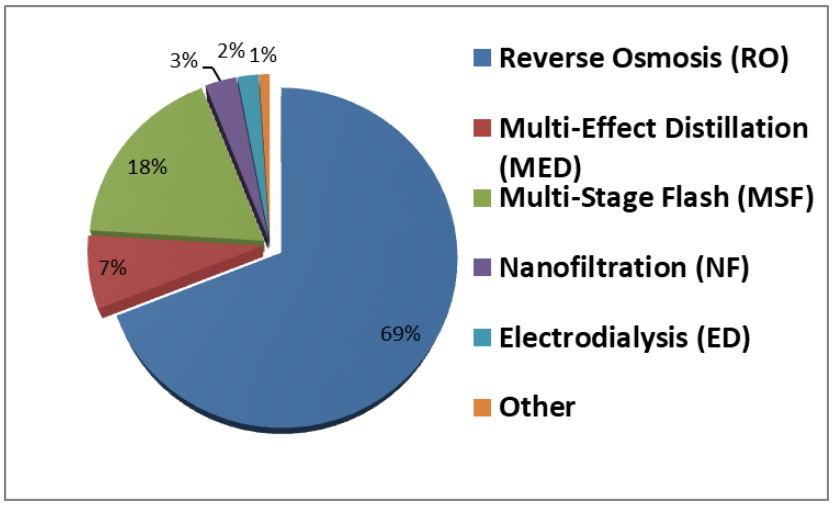

Figure 2.11 *Percentage of the most desalination techniques used based on the productivity of fresh water in 2019. Reprinted with permission from [21].*

Many desalination methods have been developed, some of which (not based on membrane processes) have been briefly introduced in chapter 1. On contrary the Membrane techniques are often evolutions or hybridizations of the main techniques. This category includes direct osmosis (FO), nanofiltration (NF), freeze desalination (FD) and hybrid approaches.

In accordance with the "process intensification" strategy, the future will focus on greater production capacity, energy and raw material savings, an increase in plant safety, an improvement in automation and control devices, and a reduction in overall dimensions of equipment and costs, to mitigate the environmental impact. Potentially, membrane operations have all the characteristics mentioned. This potentially makes them the technologies of the future by replacing conventional energy-intensive techniques, enabling selective transport and increasing the efficiency of numerous processes. Furthermore, the creation of compact membrane systems, capable of carrying out the operations of traditional process units, today represents a real prospect.

Another challenge is membrane performance improvements in various membrane-based applications. For example, numerous studies have been conducted to improve membrane performance and stability in FO and PRO applications. However, progress is still not good enough for commercialization. If a suitable membrane can be fabricated for these applications, the FO and PRO processes will succeed RO as the next generation of the commercial desalination process. In other words, a suitable membrane should be manufactured and developed for its commercial applications. Furthermore, the world is also facing challenges in terms of environmental

protection, water demand and energy regeneration. With desalination technologies, producing freshwater and generating energy can be realized in one application within a few decades. Even though there are some limitations at present, these issues can be addressed during the development of the science and engineering. For the next generations of humans, it should be accomplished to increase the total volume of freshwater supply, harvesting valuable resources, and generating energy in simply designed desalination applications. The requirements of process intensification are well satisfied even when membrane engineering is applied to the agro-food industry (fruit juice treatment) and the similar concept is now also being investigated in the petrochemical industry. In the production of ethylene via thermal cracking, membranes are proposed for the separation of gases, the production of oxygen enriched air, the removal of hydrocarbons and acid gases from wastewater and furnace effluents, and the elimination of coke from the water for Microfiltration [22-24].

2.3.1 Nanofiltration (NF)

Nanofiltration is a membrane process for the removal of divalent ion. This implies that the separation process is based on the charge of the solute and the molecular size of the unfilled solute. The selectivity of the NF membrane for solute rejection depends on the charge and size of the solute. This aspect differentiates NF from RO in which all solutes are rejected, also requiring a lower working pressure than RO. However, NF is not suitable for seawater desalination, but can preferably be used as a pre-treatment unit in a hybrid method. NF membrane devices are specifically designed to eliminate viruses from contaminated sources. In most cases, the working parameters such as flow rate, temperature, membrane nature, virus load and filter area are optimized for efficient and reproducible elimination of the virus in question. Furthermore, exclusion of the virus from contaminated water based on other existing techniques than NF membrane techniques can be costly and time-consuming. The main applications of NF are in water treatment for the production of drinking water, as well as in waste water treatment and also in reuse. NF can be used to treat all types of water including groundwater, surface water and wastewater or as a pre-treatment for desalination.

2.3.2 Electrodialysis (ED)

Electrodialysis (ED) and Electrodialysis Reversal (EDR) processes are driven by direct current (DC) in which ions flow through ion-selective membranes to electrodes of opposite charge. Similar in principle to electrolysis, the ED have different compartments for the positive and negative electrodes [25]. This is the opposite compared to water in pressure-driven processes as outlined

above. In EDR systems, the polarity of the electrodes is reversed periodically. Ion-transfer (perm-selective) anion and cation membranes separate the ions in the feed water. These systems are used primarily in waters with low total dissolved solids (TDS). Desalination through ED occurs via a direct current from an external source applied through the electrodes in a brine solution containing ion-selective membranes, which are connected in parallel to form channels. When the electrodes are charged, the negative salt ions move through the anion-permeable membrane towards the anode and vice versa the positive salt ions move the other way through the cation-permeable membrane to the cathode. These movements of ions create the separation of concentrated brine, allowing the formation of fresh water. In general ED is used for desalination of brackish water with low concentration of salt (with total dissolved solid (TDS) <5000mg/L) operating at 85–90% recovery. The largest EDR plant is built in Barcelona, Spain, which guarantees 200,000 m^3/day of drinking water.

To calculate the energy consumption for ED plant, it is fundamental to consider two components: The energy of separation and the energy of pumping. The first can be approximated as requiring 1 kWh/1000 usg per 1000 ppm of salt removed. This energy requirement varies significantly with temperature and is stated reflecting typical ambient conditions of 18–22°C. The energy of pumping is approximately 2 kWh/1000 usg of water produced. The energy consumption of EDR at 75% recovery and 25 °C has been shown to vary between 0.49 kWh/m3 at 1000 mg/L TDS and 1.75 kWh/m3 at 5000 mg/L TDS [26].

2.3.3 Forward Osmosis (FO)

Forward osmosis FO is the opposite process of the Reverse Osmosis, in which the natural osmotic pressure existing across the membrane is used to draw water from the less concentrated side of the membrane to the more concentrated solute. Compared to RO, where saline water is pushed through a membrane, instead, forward osmosis (FO) uses osmotic pressure generated from a natural salt concentration gradient as the driving force through a membrane. For this work, there is the feed water – often seawater – on one side and membrane and then a draw solution on the other side. The diluted solution is then processed to separate the product from the reusable draw solution. The process of desalination when using FO is complete only with the addition of a fresh-water recovery unit. Hence FO is best used as a pre-treatment unit for other desalination methods such as RO. At difference of RO, which is not indicated for desalting highly saline waters, a hybrid FO system is ideal for desalination of high-salinity feed water. Moreover, an FO hybrid method

consumes less energy than RO. Other advantages of FO over RO include high water recovery and minimal fouling [27]. The major limitations of FO are the high energy requirement when used as standalone method of desalination and the limited choice of draw solute.

2.3.4 Reverse Osmosis (RO)

Actually, growing global demand for water makes membrane filtration the prominent technology in desalination and wastewater treatment; the global cumulative contracted capacity is dominated by Reverse Osmosis (SWRO), where the Global capacity is now more than 100 million m^3/day [28], with an increase of 6.8% per year in the last decade, equivalent to an annual addition in fresh water production of 4.6 million m^3/day. Membrane desalination technologies account for more than 90% of all desalination plants [29]. RO uses semipermeable membranes with excellent separation performance and good chemical stability [30]. The water to be treated is pushed into the membrane module by a pump, which exerts a pressure higher than the osmotic pressure of the feed water so as let pure water pass through the membrane, while the remaining part comes out with a high salt concentration, due to the retention of all the components that do not cross the membrane. The separation takes place thanks to diffusion and dissolution mechanisms, which intervene in varying degrees and allow action up to ionic level. The performance of the membrane depends on the membrane structure, membrane material as well as on temperature and concentration of feed. As a matter of fact, feed osmotic pressure increases with the growing of the feed temperature and concentration parameters as indicated by the following Van t'Hoff's law (valid for dilute solution):

$$\pi_s = \frac{n_s}{V} RTi \qquad (2.1)$$

where π_s is the osmotic pressure, n_s is the total amount of moles of solutes in solution, R the ideal gas constant, V the volume of solvent and i Van t'Hoff's coefficient.

Current state-of-the-art SWRO plants consume between 3 and 4 kWh/m^3 and emit between 1.4 and 3.6 kg CO_2 per cubic meter of produced water [31-34], depending strongly on the fuel used to produce the electricity. The thermal desalination technologies, less efficient, generally emit between 8 and 20 kg CO_2/m^3, with the exception of stand-alone MED at 3.4 kg CO_2/m^3. As small as these numbers may appears through a global lens, they can be large in regional grids and ecosystems. In term of costs, energy consumption is one of the main cost components in RO desalination [35-37] even if concentration polarization and membrane fouling are the 'Achilles'

heel' of this membrane process. Concentration polarization is the result of the selective transport of some species through the membrane. Retained species accumulate in front of the membrane and might cause the creation of a concentration gradient between the solution at the membrane surface and the bulk. This leads to a back transport of the material accumulated at the membrane surface by diffusion. The direct consequence of concentration polarization is the reduction of both water flux and rejection. Membrane fouling is due to the dissolved, colloidal or biologic matter that can accumulate at the membrane surface, building a continuous layer that reduces or inhibits mass transfer across the membrane. For efficient RO desalination, an adequate pre-treatment, supplying high quality feed water is essential. Notable examples of very productive and large seawater reverse osmosis (SWRO) desalination plants are the ones in Israel (such as the Sorek SWRO desalination plant), United States (such as the Carlsbad Desalination SWRO Plant in San Diego County), Oman (such as the Al Ghubrah plant or the Barka IWPP expansion –both SWRO), United Arab Emirates (for example the Al Fujairah IWPP expansion). Despite the enormous success of membrane desalination technology, improvements are still required in terms of desalted water cost, higher productivity (that means higher water recovery factors), better water quality and enhanced eco-sustainability of the desalination process. The further improving of SWRO desalination processes require high-permeability and/or antifouling membranes. Recently, the application of nanotechnology and biotechnology to membrane fabrication has heralded a new generation of RO membranes, whose water permeabilities potentially surpass conventional polymeric membranes by several orders-of-magnitude. Examples can be found in the carbon nanotube- (CNT) and other carbon-based membranes (like graphene and graphene oxide), as well as in inorganic membrane, mixed matrix membranes and biomimetic membranes. These are emerging as developed membranes with superior permeability, durability and selectivity in particular for water purification.

2.3.5 Membrane distillation (MD)

Membrane distillation (MD) is a membrane contactor-based process dedicated to water treatment, including water desalination. Freshwater can be recovered from saline streams with a theoretical salts and non-volatile components rejection of 100%. As mentioned, This process works at low operating temperatures with respect to conventional distillation columns, reduced concentration polarization with respect to pressure-driven membrane processes and low

operating pressure with respect to reverse osmosis (RO). This process involves mainly two-phase changes of water: evaporation and condensation. The first one occurs at the liquid/vapour interfaces (i.e., feed side); successively, the water vapour passes through no-wetted pores of hydrophobic membrane and, then, condenses at the opposite side of the membrane (i.e. permeate side). In the last 30 years MD received a constantly growing interest of about researcher in the entire world. As shown in Figure 2.12, the number of publications in the early 90' was only a few tens, while in 2020 the publications arrived to 700, confirming the large interest in this new eco-sustainable process for water desalination.

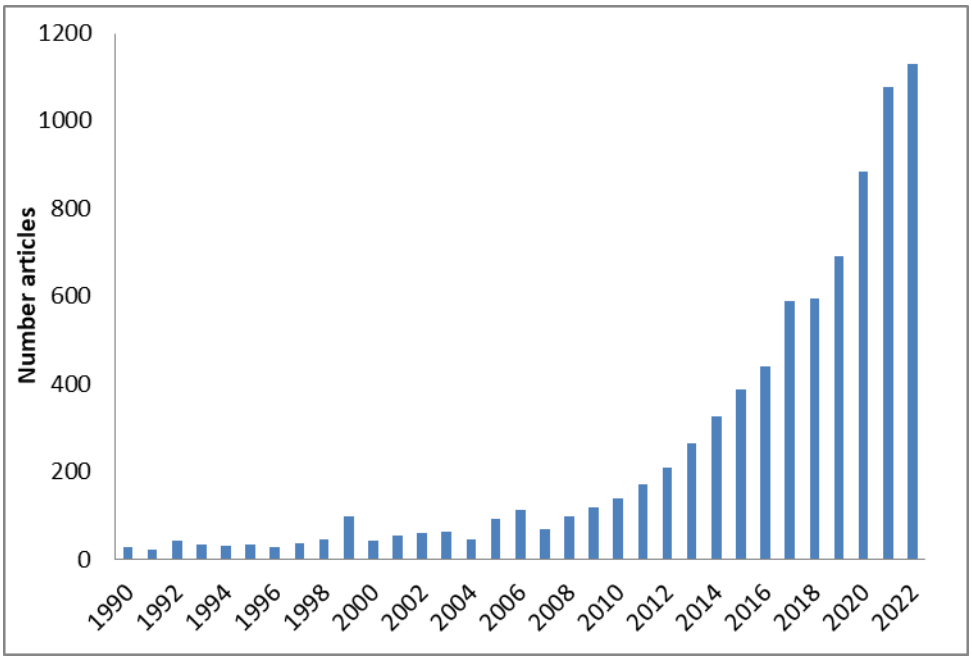

Figure 2.12 *Number of membrane process articles in the last 30 years through August 2022: font ScienceDirect .*

Depending on the approach used to induce water evaporation and condensation, different MD basic configurations can be assembled (Figure 2.13). Hereafter, a short description of more classical and recent configuration-types is given:

A) **B)** **C)**

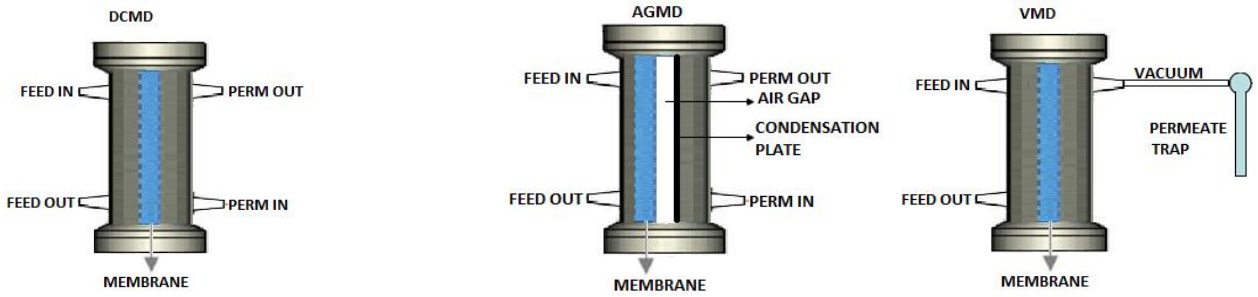

D) **E)** **F)**

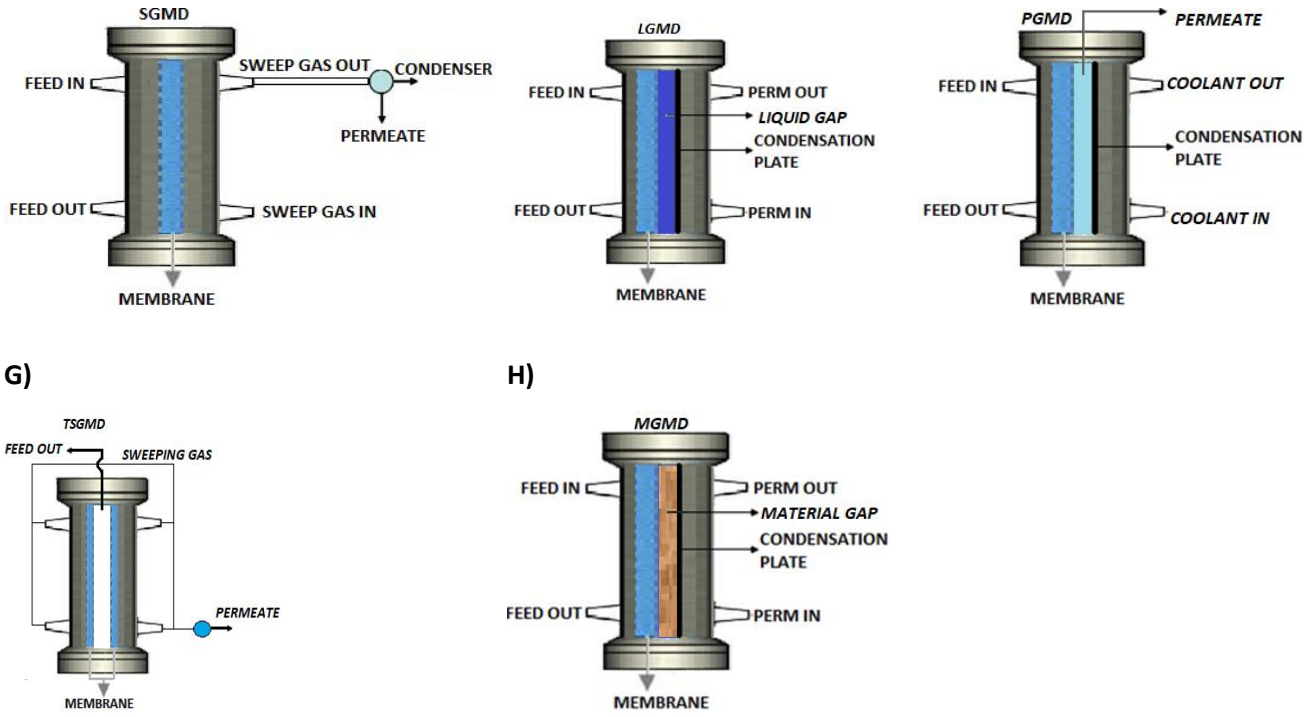

Figure 2.13: *MD configurations schematic setup: A) direct contact membrane distillation DCMD, B) air gap membrane distillation AGMD, C) vacuum membrane distillation VMD and D) sweep gas membrane distillation SGMD, E) liquid gap membrane distillation LGMD, F) permeate gap membrane distillation PGMD, G) thermostatic sweeping gas membrane distillation TSGMD and H) material gap membrane distillation MGMD.*

1 *Direct contact membrane Distillation* (DCMD) is obtained when the saline solution faces the feed side while a cold pure water solution is circulated tangentially to the permeate side of the membrane. A difference of temperature or concentration across the membrane induces the necessary vapour pressure difference to promote transport through the membrane [38].

2 In *Air Gap Membrane Distillation* (AGMD) an air gap is interposed between the membrane and a cold condensing surface placed inside of the membrane module. The air gap helps in increasing the conductive heat transfer resistance, thus decreasing the amount of heat lost by conduction through the membrane [39,40]. The heat loss is indeed one of the most critical issues of membrane distillation, as detailed hereafter.

3 *Vacuum Membrane Distillation* (VMD) required the application of vacuum or a low pressure at the permeate side and an external condensers in order to condense the vapor water and collect the permeate [41-43].

4 In *Sweep Gas Membrane Distillation* (SGMD) a gas, such as air or nitrogen, sweeps the permeate side of the membrane carrying the evaporated molecules outside the membrane module for condensation in place of the vacuum used in VMD [15,42,44,45].

5 *Liquid Gap Membrane Distillation (LGMD)* is a merging of DCMD and AGMD configurations (Figure 2.13). In fact, LGMD show the same aspect of AGMD with the difference of the gap kept filled by a stagnant cold liquid solution, frequently the produced distilled water (as DCMD [46].

6 *Permeate Gap Membrane Distillation (PGMD)* includes a third channel by an additional non-permeable foil with the separation of the distillate from the coolant. In general, the coolant can be any other liquid, such as cold feed water. One significant advantage of PGMD is the efficient heat recovery system. The presence of the distillate channel reduces sensible heat losses due to an additional heat transfer resistance and reduces the temperature difference across the membrane, which slightly lowers the permeation rate.

7 *Thermostatic sweeping gas membrane distillation* (TSGMD) combines SGMD and AGMD to minimize the temperature of the sweeping gas (Figure 2.13). In fact, usually, the temperature of sweeping gas may be increased close to the membrane module due to the heat transfer from the feed side through the membrane to the permeate side [47]. The presence of the cold wall in the permeate side reduces the increase in the sweeping gas temperature resulting in an enhancement of the driving force and the water production rate as a consequence [47].

8 In *Material gap membrane distillation* (MGMD) the gap between membrane and condensation plate is filled with materials such as polyurethane (sponge), polypropylene mesh, sand and deionized water [48]. In terms of heat transfer MGMD show performance comparable to the DCMD mainly due to the high heat loss through conduction. The heat developed in the materials at higher temperatures decreases the mass transfer during the MGMD process, a possible reason for the reduction in the percentage flux enhancement [48].

In all cases, the success of the separation depends on the capacity of the membrane to keep stable and durable interface between two phases and subsequently constant mass transfer. The trans-membrane flux is measured according to the following equations:

$$J = B * (P_F - P_p) = B\Delta P \tag{2.2}$$

$$B \propto (r^a \varepsilon)/(\delta\tau) \tag{2.3}$$

where B is a membrane distillation coefficient which depends on the membrane morphology, *r* is the nominal pore size of membrane, *a* is the exponent of r in the range of 1 to 2 (a=1 for Knudsen diffusion, a=2 for viscous flux), τ is the pore tortuosity and δ is the membrane thickness.

The understanding of heat and mass transfer phenomena in MD allows identifying membrane characteristics for enhancing MD performance.

Regardless of the MD configuration used, water and solute (if the solute is volatile) evaporate from the liquid-vapour interface on the feed side of the membrane, diffuse and/or convect across the membrane, and are either condensed or are removed from the membrane module as vapour on the permeate side.

For what concerns heat transfer, heat is first transferred from the heated feed solution of uniform temperature T_f across the thermal boundary layer to the membrane surface at a rate $Q = h_f \cdot \Delta T_f$.

At the surface of the membrane, liquid is vaporized and heat is transferred across the membrane at a rate $Q_V = h_V \cdot \Delta T_m = N \cdot \Delta H_V$ (where N is the rate of mass transfer and ΔH_V is the heat of vaporization). Additionally, heat is conducted through the membrane material and the vapour that fills the pores at a rate $Q_m = h_m \cdot \Delta T_m$ where $h_m = \varepsilon h_{mg} + (1- \varepsilon) h_{ms}$ (ε is the membrane porosity, h_{mg} and h_{ms} represent the heat transfer coefficients of the vapor within the membrane pores and the solid membrane material, respectively). Conduction is considered a heat loss mechanism, because no corresponding mass transfer takes place. Total heat transfer across the membrane is $Q = Q_V + Q_m$. Finally, as vapour condenses at the liquid-vapor interface, heat is removed from the cold-side membrane surface through the thermal boundary layer at a rate $Q=h_p \cdot \Delta T_p$

Moreover, the pores play a relevant role in heat transfer as well. For a feed with a certain temperature T_f, the heat is first transferred from the heated feed solution of transfer across the thermal boundary layer to the membrane surface at a rate, which can been expressed as:

$$Q = h_f \cdot \Delta T_f. \qquad (2.4)$$

Where h_f is the calor latent of feed and ΔT_f is the difference of temperature existing on the two of membrane. The surface of the membrane liquid is vaporized and heat is transferred across the membrane at a rate $Q_V = h_V \cdot \Delta T_m = N \cdot \Delta H_V$ (where N is the rate of mass transfer and ΔH_V is the heat of vaporization). Additionally, heat is conducted through the membrane material and the vapour that fills the pores at a rate

$$Q_m = h_m \cdot \Delta T_m \qquad (2.5)$$

where h_m represents the heat transfer coefficients of the vapor within the membrane. Conduction is considered a heat loss mechanism, because there is no corresponding mass transfer. The total heat transfer across the membrane is measured by the addition of the previous by following:

$$Q = Q_V + Q_m \tag{2.6}$$

After the passage of vapour across the membrane, on vapor-liquid inteface will take place the condensation, where heat is removed from the cold-side membrane surface through the thermal boundary layer at a rate $Q=h_p \cdot \Delta T_p$ (Fig. 2.14).

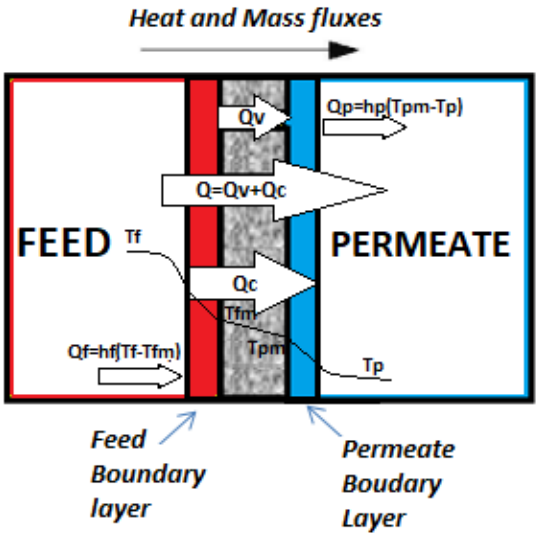

Figure 2.14: *Representative scheme of heat and mass transfer in MD process.*

A MD process limit is represented on the heat transfer across the boundary layer because a large quantity of heat must be supplied to the membrane surface to vaporize the liquid. For this reason the properly choice of membrane materials with low resistance of mass transfer and low thermal conductivity to prevent heat loss across the membrane are fundamental. In fact, in MD, the polarization of the concentration does not significantly affect the driving force of the process and therefore it is possible to reach high recovery factors and high concentrations (refs). In addition with MD and/or RO processes it is possible to increase the recovery factor with potential zero brine production transforming the traditional problem of disposal of the brines into a potential new profitable market [49,50].

Another important concern is the polarization phenomenon related mainly to fluid dynamics. One way to reduce it is the generation of mixing and turbulence in the flow, thus reducing the thickness of the boundary layer. With the terms polarization phenomena is possible to define two types: temperature polarization coefficient (TPC) and concentration polarization coefficient (CPC).

These are used to quantify the heat and mass transport resistance in the boundary layer with respect to the total transfer resistance of the system:

$$TPC = \frac{T_{fm} - T_{pm}}{T_f - T_p} \quad (2.7)$$

$$CPC = \frac{C_{Bm}}{C_{Bbf}} \quad (2.8)$$

where T_{fm} is the temperature of the feed at the membrane surface, T_{pm} is the temperature of the permeate at the membrane surface, T_f is the temperature of the feed in the bulk, T_p is the temperature of the permeate in the bulk, C_{Bm} is the concentration of the non-volatile solutes at the membrane surface whereas C_{Bb} is the concentration of the non-volatile solutes at the bulk feed. The increase temperature of a MD system will cause more heat to flow from the higher to the lower temperature region, leading to high temperature difference. A decline in permeate flux results from the resistances imposed on heat transferred from bulk feed and bulk permeate, caused by the formation of thermal boundary layers on the feed and permeate sides of the MD module. The increased concentration of non-volatile compounds next to the membrane surface would have the influence of reducing the transmembrane flux due to the establishment of concentration polarization (CP) layer at the feed side that acts as a mass transfer resistance to the volatile molecule species (water).

Coefficient polarization phenomena might be strongly reduce the performance of membrane operations because decrease the mass flux and/or separation performance. This is due to the accumulation to retained material and to a depletion of permeating components in the boundary layers adjacent to the membrane.

To reduce them, there are two options: 1) increasing the flow rates (even if this increase has not to produce an operating pressure above the liquid entry pressure (LEP) for preventing wetting); 2) including the spacers for promoting turbulence [51]. In fact, when the hydrostatic pressure on the feed side of a MD membrane exceeds LEP (eq.2.9)**,** liquid penetrates the pores and is able to pass through the membrane (wetting). To recovery this aspect, the membrane must be completely dried and cleaned. LEP equation is defined by the Laplace equation (eq.2.9) as the relation between the membrane's largest pore size (r_{max}) and operating conditions and geometric factor determined by pore structure (B).

$$LEP = (-2\,B\,\gamma_L\,cos\theta)/r_{max} \quad (2.9)$$

where B is a geometric factor determined by pore structure, γ_L the liquid surface tension and θ is the liquid/solid contact angle. When the hydrostatic pressure on the feed side of a MD membrane exceeds LEP, liquid penetrates the pores and is able to pass through the membrane. Once a pore

has been penetrated it is said to be “wetted” and the membrane must be completely dried and cleaned before the wetted pores can once again support a vapor-liquid interface.

Suitable membranes for MD

The choice of a membrane for a given MD application is a compromise between a low thermal conductivity obtained from thicker membranes and/or low thermal conductive materials, a high permeate flux obtained from membranes with low resistance to mass transfer and a high porosity, a narrow distribution of a large number of pores to provide large interfacial area, high resistance to wetting and high factor of separation. The physical properties of the membrane have certain effects on both permeate flow and thermal efficiency. Materials with higher thermal conductivity coefficients exhibit lower permeate flow and reduced thermal efficiency.

Today the membranes available on the market do not meet all MD requirements fully. The identification of new materials for making membranes suitable for membrane distillation separation is hence a crucial factor. Table 2.1 summarizes some of the highest measured MD performances of some flat sheet and hollow fiber membranes made with different types of materials and processed with NaCl solutions. For example hydrophobic membranes, PTFE represents an ideal material for the production of MD membranes since it has one of the highest hydrophobic characteristics among polymers and also one of the best chemical resistance and thermal stability. The fundamental disadvantage of PTFE lies in its difficult machinability due to the impossibility to use conventional melt processing methods making it necessary to use expensive methods. Other polymers such as PP and PVDF have been employed in the preparation of membranes for filtration purposes. These membranes have been also used for various MD applications. The PP membranes preparation is however too expensive because they are prepared by the melt extrusion technique followed by stretching or the thermal separation process of the phase, which requires the dissolution of the polymer at a high temperature in less common solvents. PVDF dissolves at room temperature in a variety of solvents and therefore porous membranes can be easily produced by phase separation process (i.e. phase inversion), simply by immersing the film of the cast solution in a coagulating bath (i.e. non-solvent, often water). In this case, the porosity of the membrane is "controlled" by the additives (ie pore forming agents) in the casting solution.

Table 2.1 *Membrane distillation performance.*

Membrane	Feed	Config.	Feed and Perm flow rate and temperature [ml/min]	Feed and Perm temperature [°C]	Flux. [LMH]	Rejection [%]	Ref.
PVDF (hollow fiber)	10g/L NaCl	DCMD	450; 125	81.6; 19.8	13,17		[52]
PVDF-H (hollow fiber)	10g/L NaCl	DCMD	450; 125	85.4; 16.6	14,21		[52]
PVDF-E (hollow fiber)	10g/L NaCl	DCMD	450; 125	81.4; 19.6	7,51		[52]
FAS grafted Al2O3	20g/L NaCl,	DCMD	0.03; 0.03	80; 20	19.1	99.5	[53]
GVHP	3g/L NaCl	DCMD	22.7-52.7; 12-42	480	~3	~100	[54]
M1 (PVDF-Hollow fiber)	35g/L NaCl	DCMD	60; 15	500; 100	<1	99.99	[55]
M3 (PVDF-Hollow fiber)	3,5 wt% NaCl	DCMD	60; 15	500; 100	21,8	99.99	[55]
PVDF	35g/L NaCl	DCMD	40-70; 20	3.7; 2.9 m/s	31-38	99.99	[56]
MD080CO2N	35 g/L NaCl	DCMD	25-70; 15	3300; 1620	0.83	100	[57]
PTFE, flat sheet	*11*–58 g/L NaCl	DCMD	*55; 20*	*500*	*7.94*	99.9	[58]
PTFE, flat sheet	*11*–58 g/L NaCl	VMD	*55*	*500*	*10.08*	99.9	[58]
PDMS-PVDF	*20g/L*	VMD	*10*	*50*	*15.4*	99.9	[59]
PDMS-PVDF	*20g/L*	DCMD	73; 25	*900; 225*	18.9	99.8	[59]
PVDF (hollow fiber)	35 g/L NaCl	VMD	*85*	*900; 225*	22,4	99.9	[60]
CM-L (ceramic PMSQ tubular aerogel)	58g/L NaCl	VMD	300	47,5	1,3	99.9	[42]
CM-S ceramic	58g/L NaCl	VMD	140	50	20	99.9	[42]

Alumina hollow fiber							
AD60/PVDF hollow fiber	36 g/L NaCl	VMD	2000	70	10	99.9	[61]
PVDF/AC hollow fiber	100g/L NaCl	VMD	0.010m/s	70	54,9	n.a.	[62]
Electrospun PVDF	1g/L Lead solution	AGMD	1500	60; 10	18.6	99	[63]
PVDF ES15-0	1g/L Lead solution	AGMD	850	60	19	84.2-72.7	[64]
Commercial, Vladipor	14.67–88 Ni	AGMD	1250	60; 20	6.5-4.3	n.a.	[65]
PP hollow fiber	25g/L NaCl	AGMD	2000	80; 25	1.85	99.9	[66]
TF450	30g/L NaCl	AGMD	2416-3416	71-30	2.05-50.25	97.22-99.98	[39]
PVDF GO-APTS 0.3	35g/L NaCl	AGMD	n.a.	85; 20	6.4	99.9	[67]
PVDF/Graphene mixed matrix membrane	RO brine from CSG produced water: 14 g/L	AGMD	n.a.	60; 20	20.5	99.9	[68]

2.3.6 Membrane crystallization

Membrane crystallization (MCr) is emerging intensive technique for the recovery raw materials from high-concentrated brine

Membrane assisted crystallization (MCr) is an extension of MD where the continuous evaporation of volatile components from the feed (with a high concentration of solute) generates a supersaturation of the solute. In figure 2.15 are shown the schematic representation of membrane crystallization set-up with the separation process. This phenomenon, with a simultaneous separation and purification of chemical species from the solution, allows the solute to precipitate in an orderly way, forming well-defined crystals [19,69]. The surface structure of the membrane yields heterogeneous nucleation because it may trap solute molecules in its cavities, thus leading to a localized supersaturation, which assists nucleation and crystals formation at supersaturation

conditions [49,70,71]. Traditionally, crystallization is a separation process, based on the limited solubility of a compound in a solvent at a certain temperature, pressure, etc. A change of these conditions to a state where the solubility is lower will lead to the formation of a crystalline solid. Although crystallization has been applied for thousands of years in the production of salt and sugar, many phenomena that occur during crystallization are still poorly understood. Above all, the nucleation and growth mechanisms of crystals and the complex behaviour of industrial crystallizers remain elusive. One reason is the lack of adequate tools to measure and monitor crystallization processes. On the other hand, the demands for constant product quality (purity, crystal size, etc.) are continuously increasing, thus creating great interest in crystallization research. Membrane-assisted crystallization has been evaluated to provide important advantages against traditional crystallization due to easy scalability and good control of crystal nucleation growth [25]. This process arises, in fact, from the need to produce substances in the solid crystalline state required in various sectors of industry, technology and scientific research. The solid crystalline state makes these products more stable for storage and more functional to manage by users, where morphology is the dominant feature with a consequent safe interest in countless applications [19].

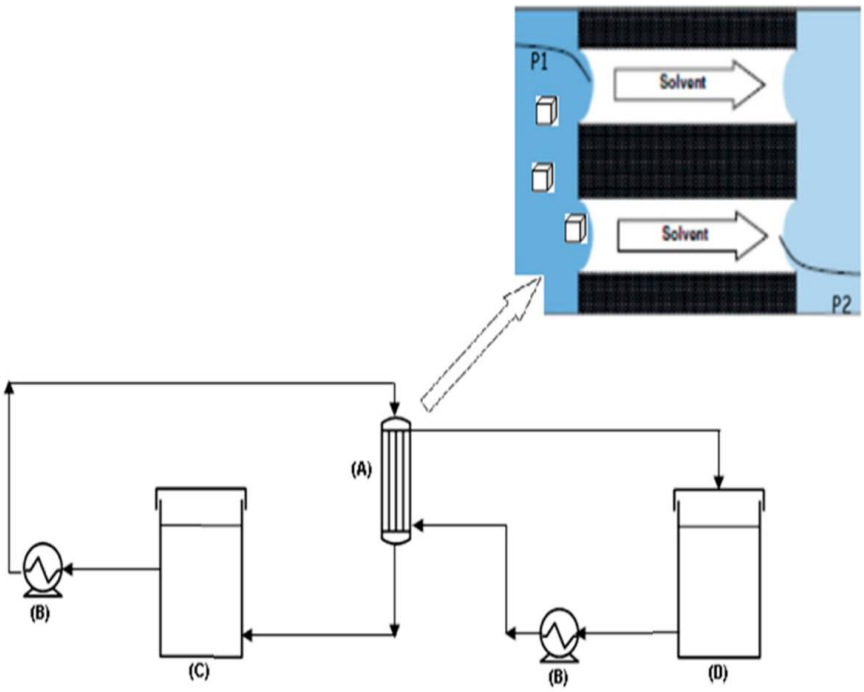

Figure 2.15 *Schematic representation of a DCMCr unit comprising (A) membrane module, (B) pump, (C) crystallizer tank and (D) permeate tank. [5] Open access.*

The crystallization has been applied in food, pharmaceutical, chemical and environmental divisions [49,70]. Other applications are the fabrication of organic semiconductor single-crystals based

devices and photonic crystals, or medical advancement by rationale design of new structure-based drugs. This is because the solid state makes these products more stable for storage and more functional to be managed by users. In some technological fields, such as in microelectronics, in nonlinear optics and in sensing, the solid state is the basis in the realization of single semiconductor crystal devices; furthermore, crystalline materials experience a wide diffusion in heterogeneous catalysis, in the controlled release of active substances and, more generally, in the nanotechnology. As regards research in the medical field, single crystals or crystalline powders are required through a rational strategy of drug design and the development of materials based on the structure. Generally, the crystalline properties have a significant impact compared to their effective use. In the case of crystalline powders, the morphology of the crystals is the dominant feature. During production, preferred crystal forms are required, for example for more efficient filtration of particle recovery from parent solutions by filtration for improved compressibility when producing tablets and for optical behaviour in the case of pigments.

The technique is based on MD process where the evaporation of water from a solution in contact with a hydrophobic membrane causes a concentration of the solution to reach super-saturated conditions. The operational principle is based on the vapor pressure gradient created by a different temperature or concentration across a microporous hydrophobic membrane [72-74]. Fig.2.16 shows the SEM picture of the PVDF commercial and an optical microscope picture of cubic sodium chloride crystals formed by Membrane Crystallization.

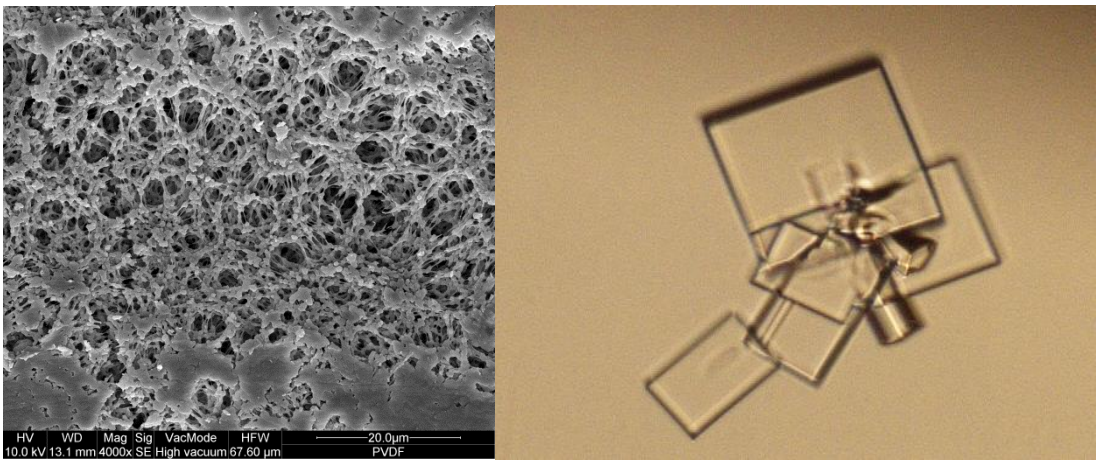

Figure 2.16 *SEM picture of PVDF commercial membrane and NaCl Crystals recovered from feed solution. Picture from optical microscope with magnification 20X.*

The principal advantages of MCr is the control of the crystallization process in order to minimize deposition and growth of crystals on the membrane and to maximize the crystal production by

choosing a broad set of available kinetic trajectories in the thermodynamic phase diagram. This can be done through the choice of membranes with specific chemical–physical properties and through the choice of the process parameters - temperature, concentration, flowrate, etc., which enable the solvent evaporation rate to be controlled thereby leading to the production of crystalline morphologies and structures.

In general, the different polymorphic forms of the same substance are considered different materials, with their characteristic physical, chemical and biological properties, making each of them a different and patentable drug. In the case of proteins, large crystals (100 mm at least in two dimensions) are required with high order in their crystal lattice for the determination of the structure at the atomic level by X-ray diffraction analysis [75,76,85]. Other, but not less important, applications have been developed for the treatment of waste water for the recovery of high purity silver [77] or sodium sulphate [78], CO_2 capture [24,79,80], nanotechnology, such as the synthesis of $BaSO_4$ and $CaCO_3$ particles [81,82], or the recovery of antibiotics [83] or of polyestyrene microparticles [84].

The solid-crystalline state is useful for its more stability for storage and more functionality to be managed by users. For this reason the solid-crystalline phase are utilized in several field of industry, technology and scientific research or as additives for cosmetics, hygiene and personal care, pharmaceuticals, fine chemicals, pigments and foods [86]. In organic semiconductor field, the crystalline phase is utilized for the preparation of single-crystals based devices and photonic crystals due to experience a wide diffusion in heterogeneous catalysis. MCr might be applied for the preparation of new structure-based drugs in medical devices. In fact, the crystal forms are required to obtain the highest surface-volume ratio and greater catalytic efficiency [76,87]. The different polymorphic forms of the same substance, in some case, are considered different materials, with their characteristic physical, chemical and biological properties. This aspect is fundamental in pharmaceutical industry where is possible to make different and patentable drugs with the different polymorphic shape of a single crystal [88,89].

Different materials (such as silver [77], sodium sulphate [90], sodium chloride NaCl [91,92], lithium chloride [70] or polyestyrene microparticles [93]) can be recovered from water treatment with high level of purity by using MCr. In conventional crystallization methods it is more difficult to realize an appropriate control of crystallization [94]. Based on MD concepts, heat and mass transport through membrane can be described if the overall system is not in thermodynamic equilibrium [95-99]. The mass transport, as has been introduced from Cui et al. [74], can be

explained in three steps. 1) Diffusion in feed boundary layer; 2) transfer through the membrane pores*; 3)* passage to permeate boundary layer. In order to analyse the mass transfer in boundary layer the Dusty Gas Model (DGM) may be applied. This describes the mass transfer in porous media through four possible mechanisms: a) viscous flow; b) Knudsen diffusion; c) molecular diffusion; d) surface diffusion. Considering the simplest configuration (direct contact configuration, DC) the molar trans-membrane flux J' can be determined as follow [74,95,100]:

$$J' = \frac{\varepsilon P D_{ij}}{\tau \delta R T} ln \left(\frac{p_a^{2} - \frac{2r}{3}\left(\frac{8RT}{\pi M_i}\right)^{1/2} + PD_{ij}}{p_a^{1} - \frac{2r}{3}\left(\frac{8RT}{\pi M_i}\right)^{1/2} + PD_{ij}} \right) \quad (2.10)$$

where J' is the molar trans-membrane flux, ε is the porosity, *P* is the total pressure, D_{ij} is the diffusivity, τ is membrane tortuosity, δ is membrane thickness, *R* is ideal gas constant, *T* is temperature, *r* is pore size, M_i is molecular weight, p_a^1 and p_a^2 are the partial pressure of air at feed and membrane surface, respectively [96,101-103]. From, eq. 6.3.1 is possible to observe how the trans-membrane flux is proportional to membrane porosity (ε), and inversely proportional to membrane thickness (δ). This confirms how the membrane morphology strongly influences the membrane crystallization performance. After the crystallization, the critical size of crystals n^* is described by the following relation [104]:

$$n^* = \frac{32\pi v_0 \, \sigma^3}{3(k_B T)^2 ln^3 S} \quad (2.11)$$

where v_0 is the molecular volume, σ is the interfacial energy, *T* is temperature, k_B is Boltzmann's constant and *S* is the supersaturation. From eq. 2.11 it is possible to establish how at high operating level of supersaturation, the crystals size tends to increase in size. Therefore, in order to optimize the process are fundamental the proper choice of membrane chemical-physical properties and process parameters [74].

Several authors have studied the impact of crystallization technology on crystal morphology. In general, crystals formed through membrane crystallization result in sharper edges than crystallization with conventional cooling. Membrane distillation-crystallization therefore appears to be competitive in terms of crystal morphology compared to conventional technologies [70,105,106]. There are several variables that can be tuned in membrane crystallization to control crystal morphology. For example, evaporation rate and temperature are just some of the key factors that influence the formation of some polymorphic forms compared to others. In table 2.2

different membranes used in crystallization are reported. Here is possible to observe how the different membrane structures and the operating condition might be influence the crystallization in terms of size, nucleation rate and other. For these reason the proper choice of membrane materials, and the consequent their characteristics are fundamental in crystallization.

Table 2.2. *Characteristics and performance of membranes used in membrane crystallization.*

Membrane materials	**Config.**	**Feed**	**Pore size [µm]**	**Porosity [%]**	**Flux [L/m^ 2*h]**	**Lowest Coefficient of Variation**	**Crystals Pictures**	**Ref.**
PVDF/Hyflon AD40H_010	DCMCr	5,3 M NaCl	0.1	74.06	1,78	35	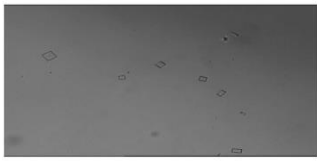 AD40H_010 membrane	[74]
PVDF/Hyflon AD40H_022	DCMCr	5,3 M NaCl	0.22	75.11	2	34.41	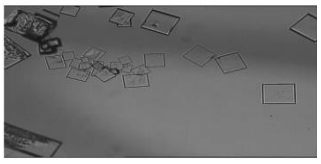 AD40H_022 membrane	[74]
PVDF/Hyflon AD40H_045	DCMCr	5,3 M NaCl	0.45	78.91	2,54	38.71	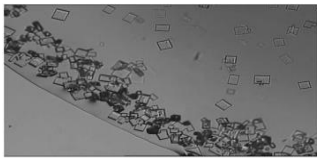 AD40H_045 membrane	[74]
ceramic PMSQ aerogel	VMCr	5,5M NaCl	0.333	23.3	0,22	26.7	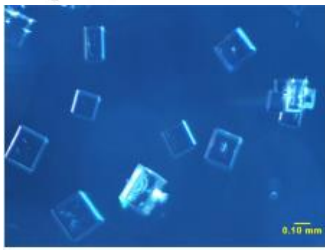	[42]
ceramic Alumina	VMCr	5,5 M NaCl	0.22	55	16,5	32.28		[42]
PVDF	DCMCr	100 g/L NaCl + acid humic	0.45	n.a.	15	n.a.	n.a.	[107]
PVDF	DCMCr	260 g/l NaCl and 2M Na2So4	0.22	70	20	10.1	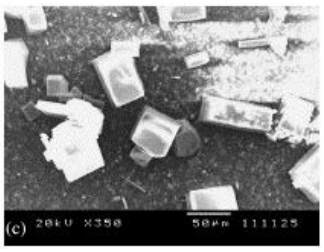	[91]

							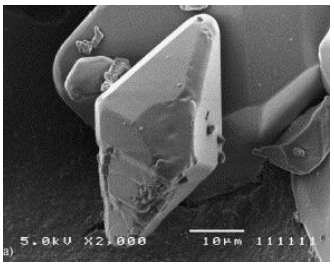	
PVDF	DCMCr	264g/L NaCl	0.228	78.27	20	30	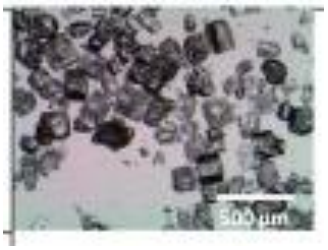	[108]
PP	DCMCr	Waste water	0.2	73	83.4	34	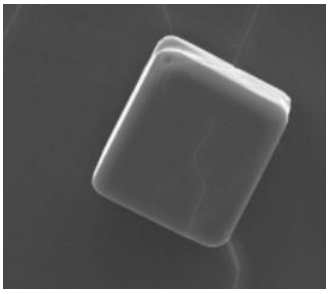	[109]
PTFE-PP	DCMCr	water from the Great Salt Lake	0.22	70	≈30-45	n.a.	n.a.	[110]

2.4 From passive to interactive membranes: new strategies to overcome current limitation of MD and MCr

As aforementioned, membrane processes play a primary role in water separation and purification thus guaranteeing good results in water recovery [57,111]. RO is the most process used in water recovery by desalination but at the same time it is not free from defects or disadvantages. The Water recovery factor (%) of RO with seawater as feed has been lower than 50% (where the recovery factor is the ratio between the flow rate of the permeate and the flow rate of the feed water). Moreover, the discharge of inadequately treated waste water in many developing countries contributes negatively to pollution and to the degradation of limited water resources. As a result, salted water desalination can be one of the ways to increase fresh water production. Economics is one of the most important factors determining industrial decisions. Water is the cheapest product on earth, yet sometimes the cost of water is too high for certain consumers. In

general, it is difficult to analyse and compare the costs of the current desalination plants and technologies because the cost of desalted water depends on many factors, such as the location of the plant, its capacity, the salinity and quality of the feed water available at the selected site, and the energy cost at the site under consideration. Moreover, thermal desalination is generally more cost-intensive than RO desalination, although the cost of desalination was declining over time. In table 2.3 are reported the capacity and the energy consumption of the main process utilized in water recovery.

Table 2.3: *Operating conditions, capacity and energy consumption of the main process for water recovery.*

Process	Energy Consumption (kWh/m^3)	Operating condition	Feed	Separation process	Membrane type	Capacity	Ref
MSF	14-25	90-110 °C	seawater	Thermal process	-	< 20 milion (m^3/day) (cumulative in the world)	[112,113]
MED	7-25	60-75 °C	Seawater (limit 70g/L)	Thermal process	-	< 10 milion (m3/day) (cumulative in the world)	[112,114]
BWRO	0.5–3	17-20 bar	brackish water	Pressure driven	Poliamide, Cellulose acetate	> 40 milion (m3/day) (cumulative in the world)	[112,115,116]
SWRO	3–6	52-69 bar	seawater(limit 70g/L)				
MD	671-699	Feed temperature= 40–80°C; Possibility to work with Solar energy (of about 7 kWh/m^2)	Seawater; Brackish water, reclamation of wastewater and the treatment of various industrial wastewaters	difference of vapour pressure	Hydrophibic porous membranes made of Polymeric or Ceramic materials,	120 (kg/day)	[117]
ED	0.49-1.75 (brackish) 10–25 (seawater)	18–22°C	Brackish water with a salinity of 1000–5000 mg/L; Seawater	Non-Pressure driven	electricity and specialized membranes to separate ionic substances	350 (kg/day)	[25,118]
NF		feed pH > 1–3, feed	River water; Brackish water or inland	pressure-driven separation	Hydrophilic porous membrane	10 (kg/day)	[119]

		pH < 9–11, and a maximum operating temperature commonly between 40° and 50 °C.	water; Seawater; Brine or concentrated seawater	processes to remove most of the suspended or un-dissolved ingredients like suspended solid, inorganic and organic compounds	made in Polymeric or Ceramic Materials		
FO	0.11	No necessary high temperature	MBR and conventional activated sludge (CAS) effluent, sewage, seawater and landfill leachate	Difference in chemical potential of water between two solutions separated by a semipermeable membrane.	Dense Polymeric Membranes	n.a.	[69]

The merging of RO with other membrane process as MD and MCr might be increase the recovery factor near the 90%, but in the future this might be not enough. In addition to these problems, desalination, and similar process, involves serious concerns about the potential environmental impact. In fact, although desalination plants produce large volumes of clean water, they also produce almost the same amount of concentrate (i.e. brine) and consume energy. The costs of disposal of this brine represent a cost that varies from 5% to 33% of the total cost of desalination [114], depending on the type of treatment of disposal and concentration of brine. Moreover, the brine disposal costs of the internal plants are higher than those of coastal plants [120]. However, these additional problems do nothing more than encourage the research of this sector with the development of innovative technologies for the exploitation and re-use of the brine. Thanks to these technologies it is able to produce renewable energy, produce salts and chemicals for the industry [12]. For these reason some aspects of the research need to be well addresses [120], including:

1. Development of novel membrane materials and polymer chemistry for the development of membranes that are highly resistant to chemicals low resistance to mass transfer, energetically efficient and reducing the overall cost of processes.

2. Development of water treatment systems coupled with renewable energy sources in order to allow significant reduction in energy consumption.
3. Recourse to membrane pre-treatment in order to (i) decrease costs associated with plant footprint, RO membrane replacement costs, and chemical costs, and (ii) increase recovery and permeate flux related to lower fouling rates.
4. Enhancement of transport mechanisms and improvement of module design (e.g., further research in the transport properties of polymer, carbon- and carbon-nanotube based, zeolite, and mixed-matrix membranes).

Efficient separation and purification techniques for membrane processes are indicated to replace those traditional energy-consuming techniques. Polymeric membranes can perform this by differentiating molecules and with high permeability. Moreover, the polymeric materials could guarantee further improvements also through modifications or functionalization of the polymer already widely used in the preparation of the membranes [19,121]. Membrane technologies require improvements in terms of operation cost, higher productivity (that means higher water recovery factors), better water quality and enhanced eco-sustainability of the desalination process. In literature, new research has been developed, including composite porous hydrophobic/hydrophilic membrane prepared using fluorinated surface modifying macromolecule (SMM) and polyethermide [123]; CF4 plasma surface modification of hydrophilic membranes into hydrophobic ones [124]; preparation of nanotube-structured TiO2 surfaces with superomniphobic characteristics [125]; fabrication of hybrid graphene/PVDF membranes [126]. Graphene has attracted considerable attention in recent years for water treatment and purification processes as it improves the membrane properties and adds functionalities such as anti-fouling properties [126, 127]. Graphene possesses many interesting properties for MD application such as high hydrophobicity, ion selectivity and water vapor transport, good thermal stability and mechanical properties [128,129]. The possibility of cheaper synthesis of large area of graphene as recently reported makes it more interesting for modern use [70]. Graphene shows great potential as filler material and is ought to be explored. In addition to graphene, two dimensional (2D) materials of atomic thickness represent the next generation membrane materials with extraordinarily high permeability. 2D membranes with well-defined transport channels and ultra-low thicknesses have demonstrated exceptional performance for liquid and gas separation applications. The unique atomic thickness of the membrane offers ultra-low resistance to mass transport. The potential

materials for 2D membranes include zeolites, mixed-organic frameworks, graphene, molybdenum disulfide etc. The current main challenges for the commercial scale implementation of these membranes include limited available techniques for exfoliating the high aspect ratio and intact nanoporous monolayers from bulk crystals, drilling of the pores with required characteristics (uniform, high-density, large-area, subnanosized) in membrane matrix and scaling up of these atomic scale membranes into real scale separation devices [71]. The potential of membrane crystallization is addressed from an intensification and integration point of view, with particular attention to present and future applications, i.e. green economy and value-added production.

However, the development and application on an industrial scale of membrane crystallization technology requires facing and overcoming the following problems:

- Development of proper membranes for MCr application: as for MD, development of new material/membrane preparation methods with extended life, with stable hydrophobic character, with properties tailored for this technology (in terms of pore size, porosity, thickness, thermal conductivity, surface roughness, etc.).
- Technology transfer to industry: application and testing of the technology on industrial-scale and valuation of benefits/advantages/drawback with respect to conventional process.

Reference

[1] M. Mulder, Basic Principles of Membrane Technology, Springer Netherlands, Dordrecht, 1996. doi:10.1007/978-94-009-1766-8.

[2] J. Zhu, J. Hou, Y. Zhang, M. Tian, T. He, J. Liu, V. Chen, Polymeric antimicrobial membranes enabled by nanomaterials for water treatment, J. Memb. Sci. 550 (2018) 173–197. doi:10.1016/j.memsci.2017.12.071.

[3] L.Y. Ng, A.W. Mohammad, C.P. Leo, N. Hilal, Polymeric membranes incorporated with metal/metal oxide nanoparticles: A comprehensive review, Desalination. (2013). doi:10.1016/j.desal.2010.11.033.

[4] Fanun, Microemulsions, CRC Press, 2008. doi:10.1201/9781420089608.

[5] H.-J. Lee, T.-H. Yoon, J.-H. Park, J. Perumal, D.-P. Kim, Characterization and fabrication of polyvinylsilazane glass microfluidic channels via soft lithographic technique, J. Ind. Eng. Chem. 14 (2008) 45–51. doi:10.1016/j.jiec.2007.06.002.

[6] B. Tüzün-Antepli, A.E. Elçin, Y.M. Elçin, Construction of micro-grooved PCL/nanohydroxyapatite membranes by non-solvent induced phase separation method and its evaluation for use as a substrate for

human periodontal ligament fibroblasts, Chem. Eng. Sci. 248 (2022) 117120. doi:10.1016/j.ces.2021.117120.

[7] L. Vogelaar, J.N. Barsema, C.J.M. van Rijn, W. Nijdam, M. Wessling, Phase Separation Micromolding—PSμM, Adv. Mater. 15 (2003) 1385–1389. doi:10.1002/adma.200304949.

[8] Y. Li, N. Koshizaki, W. Cai, Periodic one-dimensional nanostructured arrays based on colloidal templates, applications, and devices, Coord. Chem. Rev. 255 (2011) 357–373. doi:10.1016/j.ccr.2010.09.015.

[9] E. Haladjova, S. Rangelov, C. Tsvetanov, P. Simon, Preparation of polymeric nanocapsules via nano-sized poly(methoxydiethyleneglycol methacrylate) colloidal templates, Polymer (Guildf). 55 (2014) 1621–1627. doi:10.1016/j.polymer.2014.02.026.

[10] O.D. Velev, E.W. Kaler, Structured Porous Materials via Colloidal Crystal Templating: From Inorganic Oxides to Metals, Adv. Mater. 12 (2000) 531–534. doi:10.1002/(SICI)1521-4095(200004)12:7<531::AID-ADMA531>3.0.CO;2-S.

[11] D.S. Marques, U. Vainio, N.M. Chaparro, V.M. Calo, A.R. Bezahd, J.W. Pitera, K.-V. Peinemann, S.P. Nunes, Self-assembly in casting solutions of block copolymer membranes, Soft Matter. 9 (2013) 5557. doi:10.1039/c3sm27475f.

[12] L. Oss-Ronen, J. Schmidt, V. Abetz, A. Radulescu, Y. Cohen, Y. Talmon, Characterization of Block Copolymer Self-Assembly: From Solution to Nanoporous Membranes, Macromolecules. 45 (2012) 9631–9642. doi:10.1021/ma301611c.

[13] V. Pingitore, A. Gugliuzza, Fabrication of porous semiconductor interfaces by pH-driven assembly of carbon nanotubes on honeycomb structured membranes, J. Phys. Chem. C. (2013). doi:10.1021/jp405969b.

[14] A. Gugliuzza, M. Perrotta, E. Drioli, Controlled Bulk Properties of Composite Polymeric Solutions for Extensive Structural Order of Honeycomb Polysulfone Membranes, Membranes (Basel). 6 (2016) 27. doi:10.3390/membranes6020027.

[15] P. Bernardo, E. Drioli, G. Golemme, Membrane Gas Separation: A Review/State of the Art, Ind. Eng. Chem. Res. 48 (2009) 4638–4663. doi:10.1021/ie8019032.

[16] R. Castro-Muñoz, B.E. Barragán-Huerta, V. Fíla, P.C. Denis, R. Ruby-Figueroa, Current Role of Membrane Technology: From the Treatment of Agro-Industrial by-Products up to the Valorization of Valuable Compounds, Waste and Biomass Valorization. (2018). doi:10.1007/s12649-017-0003-1.

[17] J. Wu, Q. Fan, Y. Xia, G. Ma, Uniform-sized particles in biomedical field prepared by membrane emulsification technique, Chem. Eng. Sci. (2015). doi:10.1016/j.ces.2014.08.016.

[18] S. Zhao, Z. Liao, A. Fane, J. Li, C. Tang, C. Zheng, J. Lin, L. Kong, Engineering antifouling reverse osmosis membranes: A review, Desalination. 499 (2021) 114857. doi:10.1016/j.desal.2020.114857.

[19] M.F. Macedonio, F. E. Drioli, Progress of membrane engineering for water treatment, J. Membr. Sci. Res. (2019). doi:10.22079/jmsr.2019.108451.1265.

[20] A.E. Abdelhamid, M.M. Elawady, M.A.A. El-Ghaffar, A.M. Rabie, P. Larsen, M.L. Christensen, Surface modification of reverse osmosis membranes with zwitterionic polymer to reduce biofouling, Water Sci. Technol. Water Supply. 15 (2015) 999–1010. doi:10.2166/ws.2015.055.

[21] E. Jones, M. Qadir, M.T.H. van Vliet, V. Smakhtin, S. mu Kang, The state of desalination and brine production: A global outlook, Sci. Total Environ. (2019). doi:10.1016/j.scitotenv.2018.12.076.

[22] F. Giacalone, P. Catrini, A. Tamburini, A. Cipollina, A. Piacentino, G. Micale, Exergy analysis of reverse electrodialysis, Energy Convers. Manag. 164 (2018) 588–602. doi:10.1016/j.enconman.2018.03.014.

[23] E. Chabanon, D. Mangin, C. Charcosset, Membranes and crystallization processes: State of the art and prospects, J. Memb. Sci. (2016). doi:10.1016/j.memsci.2016.02.051.

[24] E. Favre, Membrane processes and postcombustion carbon dioxide capture: Challenges and prospects, Chem. Eng. J. (2011). doi:10.1016/j.cej.2011.01.010.

[25] L. Sun, Q. Chen, H. Lu, J. Wang, J. Zhao, P. Li, Electrodialysis with porous membrane for bioproduct separation: Technology, features, and progress, Food Res. Int. 137 (2020) 109343. doi:10.1016/j.foodres.2020.109343.

[26] D. Zarzo, Beneficial uses and valorization of reverse osmosis brines, in: Emerg. Technol. Sustain. Desalin. Handb., Elsevier, 2018: pp. 365–397. doi:10.1016/B978-0-12-815818-0.00011-4.

[27] Y.H. Teow, A.W. Mohammad, New generation nanomaterials for water desalination: A review, Desalination. 451 (2019) 2–17. doi:10.1016/j.desal.2017.11.041.

[28] J.J. Feria-Díaz, F. Correa-Mahecha, M.C. López-Méndez, J.P. Rodríguez-Miranda, J. Barrera-Rojas, Recent Desalination Technologies by Hybridization and Integration with Reverse Osmosis: A Review, Water. 13 (2021) 1369. doi:10.3390/w13101369.

[29] P. Loganathan, G. Naidu, S. Vigneswaran, Mining valuable minerals from seawater: A critical review, Environ. Sci. Water Res. Technol. 3 (2017) 37–53. doi:10.1039/c6ew00268d.

[30] G. Naidu, L. Tijing, M.A.H. Johir, H. Shon, S. Vigneswaran, Hybrid membrane distillation: Resource, nutrient and energy recovery, J. Memb. Sci. 599 (2020) 117832. doi:10.1016/j.memsci.2020.117832.

[31] M. Elimelech, W.A. Phillip, The future of seawater desalination: Energy, technology, and the environment, Science (80-.). 333 (2011) 712–717. doi:10.1126/science.1200488.

[32] C. Fritzmann, J. Löwenberg, T. Wintgens, T. Melin, State-of-the-art of reverse osmosis desalination, Desalination. 216 (2007) 1–76. doi:10.1016/j.desal.2006.12.009.

[33] G.L. Meerganz von Medeazza, “Direct” and socially-induced environmental impacts of desalination, Desalination. 185 (2005) 57–70. doi:10.1016/j.desal.2005.03.071.

[34] L.D. Lienhard, John H.; Thiel, Gregory P.; Warsinger, David M.; Banchik, Low Carbon Desalination: Status and Research, Development, and Demonstration Needs. Report of a workshop conducted at the Massachusetts Institute of Technology in association with the Global Clean Water Desalination Alliance., 2016. http://hdl.handle.net/1721.1/105755.

[35] A. Zhu, P.D. Christofides, Y. Cohen, Energy Consumption Optimization of Reverse Osmosis Membrane Water Desalination Subject to Feed Salinity Fluctuation, Ind. Eng. Chem. Res. 48 (2009) 9581–9589. doi:10.1021/ie900729x.

[36] R. Zhao, S. Porada, P.M. Biesheuvel, A. van der Wal, Energy consumption in membrane capacitive deionization for different water recoveries and flow rates, and comparison with reverse osmosis, Desalination. 330 (2013) 35–41. doi:10.1016/j.desal.2013.08.017.

[37] C. Thamaraiselvan, C.J. Arnusch, Integrated nanofiltration membrane process for water and wastewater treatment, in: Handb. Nanotechnol. Appl., Elsevier, 2021: pp. 147–168. doi:10.1016/B978-0-12-821506-7.00006-5.

[38] M. Baghbanzadeh, C.Q. Lan, D. Rana, T. Matsuura, Membrane Distillation, in: Nanostructured Polym. Membr., John Wiley & Sons, Inc., Hoboken, NJ, USA, 2016: pp. 419–455. doi:10.1002/9781118831779.ch11.

[39] M. Khayet, C. Cojocaru, Artificial neural network modeling and optimization of desalination by air gap membrane distillation, Sep. Purif. Technol. 86 (2012) 171–182. doi:10.1016/j.seppur.2011.11.001.

[40] G.W. Meindersma, C.M. Guijt, A.B. de Haan, Desalination and water recycling by air gap membrane distillation, Desalination. 187 (2006) 291–301. doi:10.1016/j.desal.2005.04.088.

[41] F. Kiefer, M. Spinnler, T. Sattelmayer, Multi-Effect Vacuum Membrane Distillation systems: Model derivation and calibration, Desalination. 438 (2018) 97–111. doi:10.1016/j.desal.2018.03.024.

[42] C.C. Ko, A. Ali, E. Drioli, K.L. Tung, C.H. Chen, Y.R. Chen, F. Macedonio, Performance of ceramic membrane in vacuum membrane distillation and in vacuum membrane crystallization, Desalination. 440 (2018) 48–58. doi:10.1016/j.desal.2018.03.011.

[43] Q. Ma, A. Ahmadi, C. Cabassud, Direct integration of a vacuum membrane distillation module within a solar collector for small-scale units adapted to seawater desalination in remote places: Design, modeling & evaluation of a flat-plate equipment, J. Memb. Sci. 564 (2018) 617–633. doi:10.1016/j.memsci.2018.07.067.

[44] Z. Xie, T. Duong, M. Hoang, C. Nguyen, B. Bolto, Ammonia removal by sweep gas membrane distillation, Water Res. 43 (2009) 1693–1699. doi:10.1016/j.watres.2008.12.052.

[45] F. GASCONSVILADOMAT, I. SOUCHON, V. ATHES, M. MARIN, Membrane air-stripping of aroma compounds, J. Memb. Sci. 277 (2006) 129–136. doi:10.1016/j.memsci.2005.10.023.

[46] A.E. Khalifa, Performances of air gap and water gap MD desalination modules, Water Pract. Technol. 13 (2018) 200–209. doi:10.2166/wpt.2018.034.

[47] M.. García-Payo, C.. Rivier, I.. Marison, U. von Stockar, Separation of binary mixtures by thermostatic sweeping gas membrane distillation, J. Memb. Sci. 198 (2002) 197–210. doi:10.1016/S0376-7388(01)00649-4.

[48] L. Francis, N. Ghaffour, A.A. Alsaadi, G.L. Amy, Material gap membrane distillation: A new design for water vapor flux enhancement, J. Memb. Sci. 448 (2013) 240–247. doi:10.1016/j.memsci.2013.08.013.

[49] F. Macedonio, C.A. Quist-Jensen, O. Al-Harbi, H. Alromaih, S.A. Al-Jlil, F. Al Shabouna, E. Drioli, Thermodynamic modeling of brine and its use in membrane crystallizer, Desalination. 323 (2013) 83–92. doi:10.1016/j.desal.2013.02.009.

[50] V. Calabrò, A. Basile, Economic analysis of membrane use in industrial applications, in: Adv. Membr. Sci. Technol. Sustain. Energy Environ. Appl., 2011. doi:10.1533/9780857093790.1.90.

[51] I. Ruiz Salmón, P. Luis, Membrane crystallization via membrane distillation, Chem. Eng. Process. Process Intensif. 123 (2018) 258–271. doi:10.1016/j.cep.2017.11.017.

[52] D. Singh, K.K. Sirkar, Performance of PVDF flat membranes and hollow fibers in desalination by direct contact membrane distillation at high temperatures, Sep. Purif. Technol. 187 (2017) 264–273. doi:10.1016/j.seppur.2017.06.012.

[53] C. Ren, H. Fang, J. Gu, L. Winnubst, C. Chen, Preparation and characterization of hydrophobic alumina planar membranes for water desalination, J. Eur. Ceram. Soc. (2015). doi:10.1016/j.jeurceramsoc.2014.07.012.

[54] M. Khayet, C. Cojocaru, C. García-Payo, Application of response surface methodology and experimental design in direct contact membrane distillation, Ind. Eng. Chem. Res. (2007). doi:10.1021/ie070446p.

[55] J. Chang, J. Zuo, L. Zhang, G.S. O'Brien, T.-S. Chung, Using green solvent, triethyl phosphate (TEP), to fabricate highly porous PVDF hollow fiber membranes for membrane distillation, J. Memb. Sci. 539 (2017) 295–304. doi:10.1016/j.memsci.2017.06.002.

[56] P. Termpiyakul, R. Jiraratananon, S. Srisurichan, Heat and mass transfer characteristics of a direct contact membrane distillation process for desalination, Desalination. (2005). doi:10.1016/j.desal.2004.11.019.

[57] S. ALOBAIDANI, E. CURCIO, F. MACEDONIO, G. DIPROFIO, H. ALHINAI, E. DRIOLI, Potential of membrane distillation in seawater desalination: Thermal efficiency, sensitivity study and cost estimation, J. Memb. Sci. 323 (2008) 85–98. doi:10.1016/j.memsci.2008.06.006.

[58] Y. Choi, G. Naidu, S. Jeong, S. Vigneswaran, S. Lee, R. Wang, A.G. Fane, Experimental comparison of submerged membrane distillation configurations for concentrated brine treatment, Desalination. (2017). doi:10.1016/j.desal.2017.06.024.

[59] D. Sun, M.-Q. Liu, J.-H. Guo, J.-Y. Zhang, B.-B. Li, D.-Y. Li, Preparation and characterization of PDMS-PVDF hydrophobic microporous membrane for membrane distillation, Desalination. 370 (2015) 63–71. doi:10.1016/j.desal.2015.05.017.

[60] H. Fan, Y. Peng, Application of PVDF membranes in desalination and comparison of the VMD and DCMD processes, Chem. Eng. Sci. 79 (2012) 94–102. doi:10.1016/j.ces.2012.05.052.

[61] D. Tong, X. Wang, M. Ali, C.Q. Lan, Y. Wang, E. Drioli, Z. Wang, Z. Cui, Preparation of Hyflon AD60/PVDF composite hollow fiber membranes for vacuum membrane distillation, Sep. Purif. Technol. 157 (2016) 1–8. doi:10.1016/j.seppur.2015.11.026.

[62] L. Zhao, X. Lu, C. Wu, Q. Zhang, Flux enhancement in membrane distillation by incorporating AC particles into PVDF polymer matrix, J. Memb. Sci. 500 (2016) 46–54. doi:10.1016/j.memsci.2015.11.010.

[63] H. Attia, M.S. Osman, D.J. Johnson, C. Wright, N. Hilal, Modelling of air gap membrane distillation and its application in heavy metals removal, Desalination. 424 (2017) 27–36. doi:10.1016/j.desal.2017.09.027.

[64] H. Attia, S. Alexander, C.J. Wright, N. Hilal, Superhydrophobic electrospun membrane for heavy metals removal by air gap membrane distillation (AGMD), Desalination. 420 (2017) 318–329. doi:10.1016/j.desal.2017.07.022.

[65] P.P. Zolotarev, V.V. Ugrozov, I.B. Volkina, V.M. Nikulin, Treatment of waste water for removing heavy metals by membrane distillation, J. Hazard. Mater. 37 (1994) 77–82. doi:10.1016/0304-3894(94)85035-6.

[66] K. Yao, Y. Qin, Y. Yuan, L. Liu, F. He, Y. Wu, A continuous-effect membrane distillation process based on hollow fiber AGMD module with internal latent-heat recovery, AIChE J. 59 (2013) 1278–1297. doi:10.1002/aic.13892.

[67] S. Leaper, A. Abdel-Karim, B. Faki, J.M. Luque-Alled, M. Alberto, A. Vijayaraghavan, S.M. Holmes, G. Szekely, M.I. Badawy, N. Shokri, P. Gorgojo, Flux-enhanced PVDF mixed matrix membranes incorporating APTS-functionalized graphene oxide for membrane distillation, J. Memb. Sci. (2018). doi:10.1016/j.memsci.2018.03.013.

[68] Y.C. Woo, Y. Kim, W.-G. Shim, L.D. Tijing, M. Yao, L.D. Nghiem, J.-S. Choi, S.-H. Kim, H.K. Shon, Graphene/PVDF flat-sheet membrane for the treatment of RO brine from coal seam gas produced water by air gap membrane distillation, J. Memb. Sci. 513 (2016) 74–84. doi:10.1016/j.memsci.2016.04.014.

[69] N.M. Mazlan, D. Peshev, A.G. Livingston, Energy consumption for desalination — A comparison of forward osmosis with reverse osmosis, and the potential for perfect membranes, Desalination. 377 (2016) 138–151. doi:10.1016/j.desal.2015.08.011.

[70] C.A. Quist-Jensen, A. Ali, S. Mondal, F. Macedonio, E. Drioli, A study of membrane distillation and crystallization for lithium recovery from high-concentrated aqueous solutions, J. Memb. Sci. (2016). doi:10.1016/j.memsci.2016.01.033.

[71] C.A. Quist-Jensen, A. Ali, E. Drioli, F. Macedonio, Perspectives on mining from sea and other alternative strategies for minerals and water recovery – The development of novel membrane operations, J. Taiwan Inst. Chem. Eng. 94 (2019) 129–134. doi:10.1016/j.jtice.2018.02.002.

[72] F. Macedonio, E. Drioli, Hydrophobic membranes for salts recovery from desalination plants, Desalin. Water Treat. 18 (2010) 224–234. doi:10.5004/dwt.2010.1775.

[73] F. Macedonio, L. Katzir, N. Geisma, S. Simone, E. Drioli, J. Gilron, Wind-Aided Intensified eVaporation (WAIV) and Membrane Crystallizer (MCr) integrated brackish water desalination process: Advantages and drawbacks, Desalination. 273 (2011) 127–135. doi:10.1016/j.desal.2010.12.002.

[74] Z. Cui, X. Li, Y. Zhang, Z. Wang, A. Gugliuzza, F. Militano, E. Drioli, F. Macedonio, Testing of three different PVDF membranes in membrane assisted-crystallization process: Influence of membrane

structural-properties on process performance, Desalination. 440 (2018) 68–77. doi:10.1016/j.desal.2017.12.038.

[75] S. Bensaadi, N. Nasrallah, A. Amrane, M. Trari, H. Kerdjoudj, O. Arous, M. Amara, Dialysis and photo-electrodialysis processes using new synthesized polymeric membranes for the selective removal of bivalent cations, J. Environ. Chem. Eng. 5 (2017) 1037–1047. doi:10.1016/j.jece.2017.01.014.

[76] A.L. Margolin, M.A. Navia, Protein Crystals as Novel Catalytic Materials, Angew. Chemie Int. Ed. 40 (2001) 2204–2222. doi:10.1002/1521-3773(20010618)40:12<2204::AID-ANIE2204>3.0.CO;2-J.

[77] B. Tang, G. Yu, J. Fang, T. Shi, Recovery of high-purity silver directly from dilute effluents by an emulsion liquid membrane-crystallization process, J. Hazard. Mater. 177 (2010) 377–383. doi:10.1016/j.jhazmat.2009.12.042.

[78] M. Rezaei, W.M. Samhaber, Wetting Behaviour of Superhydrophobic Membranes Coated with Nanoparticles in Membrane Distillation, Chem. Eng. Trans. 47 (2016) 373–378. doi:10.3303/CET1647063.

[79] M. Frappa, L. Xue, D. Enrico, M. Francesca, Membrane Crystallization and Membrane Condenser: Two Membrane Contactor Applications, J. Chem. Sci. Chem. Eng. 1 (2020) 7–17. doi:10.47890/JCSCE/2020/MFrappa/10082116.

[80] I. Ruiz Salmón, R. Janssens, P. Luis, Mass and heat transfer study in osmotic membrane distillation-crystallization for CO2 valorization as sodium carbonate, Sep. Purif. Technol. 176 (2017) 173–183. doi:10.1016/j.seppur.2016.12.010.

[81] R. Kieffer, D. Mangin, F. Puel, C. Charcosset, Precipitation of barium sulphate in a hollow fiber membrane contactor: Part II The influence of process parameters, Chem. Eng. Sci. 64 (2009) 1885–1891. doi:10.1016/j.ces.2009.01.013.

[82] E. Drioli, E. Curcio, A. Criscuoli, G. Di Profio, Integrated system for recovery of CaCO3, NaCl and MgSO4·7H2O from nanofiltration retentate, J. Memb. Sci. 239 (2004) 27–38. doi:10.1016/j.memsci.2003.09.028.

[83] S. Li, X. Li, D. Wang, Membrane (RO-UF) filtration for antibiotic wastewater treatment and recovery of antibiotics, Sep. Purif. Technol. 34 (2004) 109–114. doi:10.1016/S1383-5866(03)00184-9.

[84] R. Zheng, Y. Chen, J. Wang, J. Song, X.M. Li, T. He, Preparation of omniphobic PVDF membrane with hierarchical structure for treating saline oily wastewater using direct contact membrane distillation, J. Memb. Sci. (2018). doi:10.1016/j.memsci.2018.03.041.

[85] G. Di Profio, S. Tucci, E. Curcio, E. Drioli, Controlling Polymorphism with Membrane-Based Crystallizers: Application to Form I and II of Paracetamol, Chem. Mater. 19 (2007) 2386–2388. doi:10.1021/cm0701005.

[86] E. Curcio, E. Drioli, Membrane Distillation and Related Operations—A Review, Sep. Purif. Rev. 34 (2005) 35–86. doi:10.1081/SPM-200054951.

[87] J.C. Falkner, A.M. Al-Somali, J.A. Jamison, J. Zhang, S.L. Adrianse, R.L. Simpson, M.K. Calabretta, W. Radding, G.N. Phillips,, V.L. Colvin, Generation of Size-Controlled, Submicrometer Protein Crystals, Chem. Mater. 17 (2005) 2679–2686. doi:10.1021/cm047924w.

[88] A. McPherson, J.A. Gavira, Introduction to protein crystallization, Acta Crystallogr. Sect. F Struct. Biol. Commun. 70 (2014) 2–20. doi:10.1107/S2053230X13033141.

[89] I.K. Smatanová, Crystallization of biological macromolecules, Mater. Struct. 9 (2002) 14–15. doi:063.

[90] W. Li, B. Van der Bruggen, P. Luis, Integration of reverse osmosis and membrane crystallization for sodium sulphate recovery, Chem. Eng. Process. Process Intensif. 85 (2014) 57–68. doi:10.1016/j.cep.2014.08.003.

[91] C.M. Tun, A.G. Fane, J.T. Matheickal, R. Sheikholeslami, Membrane distillation crystallization of concentrated salts—flux and crystal formation, J. Memb. Sci. 257 (2005) 144–155. doi:10.1016/j.memsci.2004.09.051.

[92] G. Chen, Y. Lu, X. Yang, R. Wang, A.G. Fane, Quantitative Study on Crystallization-Induced Scaling in High-Concentration Direct-Contact Membrane Distillation, Ind. Eng. Chem. Res. 53 (2014) 15656–15666. doi:10.1021/ie501610q.

[93] E. Drioli, M.C. Carnevale, A. Figoli, A. Criscuoli, Vacuum Membrane Dryer (VMDr) for the recovery of solid microparticles from aqueous solutions, J. Memb. Sci. 472 (2014) 67–76. doi:10.1016/j.memsci.2014.08.047.

[94] E. Curcio, G. Di Profio, E. Drioli, A new membrane-based crystallization technique: tests on lysozyme, J. Cryst. Growth. 247 (2003) 166–176. doi:10.1016/S0022-0248(02)01794-3.

[95] S. SRISURICHAN, R. JIRARATANANON, A. FANE, Mass transfer mechanisms and transport resistances in direct contact membrane distillation process, J. Memb. Sci. 277 (2006) 186–194. doi:10.1016/j.memsci.2005.10.028.

[96] R.W. Schofield, A.G. Fane, C.J.D. Fell, Heat and mass transfer in membrane distillation, J. Memb. Sci. 33 (1987) 299–313. doi:10.1016/S0376-7388(00)80287-2.

[97] F. Laganà, G. Barbieri, E. Drioli, Direct contact membrane distillation: modelling and concentration experiments, J. Memb. Sci. 166 (2000) 1–11. doi:10.1016/S0376-7388(99)00234-3.

[98] J. Phattaranawik, Effect of pore size distribution and air flux on mass transport in direct contact membrane distillation, J. Memb. Sci. 215 (2003) 75–85. doi:10.1016/S0376-7388(02)00603-8.

[99] L. Martínez, J.M. Rodríguez-Maroto, Membrane thickness reduction effects on direct contact membrane distillation performance, J. Memb. Sci. 312 (2008) 143–156. doi:10.1016/j.memsci.2007.12.048.

[100] K.W. Lawson, D.R. Lloyd, Membrane distillation, J. Memb. Sci. 124 (1997) 1–25. doi:10.1016/S0376-7388(96)00236-0.

[101] J. Phattaranawik, R. Jiraratananon, A.. Fane, Heat transport and membrane distillation coefficients in direct contact membrane distillation, J. Memb. Sci. 212 (2003) 177–193. doi:10.1016/S0376-7388(02)00498-2.

[102] S. Bandini, C. Gostoli, G.C. Sarti, Role of heat and mass transfer in membrane distillation process, Desalination, Desalination. 81 (1991) 91–106.

[103] F. Macedonio, A. Ali, E. Drioli, 3.10 Membrane Distillation and Osmotic Distillation, in: Compr. Membr. Sci. Eng., Elsevier, 2017: pp. 282–296. doi:10.1016/B978-0-12-409547-2.12221-8.

[104] C. Wagner, Kinetik der Phasenbildung. Von Prof. Dr. M. Volmer. (Bd. IV der Sammlung „Die chemische Reaktion", herausgegeben von K. F. Bonhoeffer.) XII und 220 S. Verlag Th. Steinkopff, Dresden und Leipzig 1939. Preis geh. RM. 19,—, geb. RM. 20,—, Angew. Chemie. 52 (1939) 503–504. doi:10.1002/ange.19390523006.

[105] G. Di Profio, S. Tucci, E. Curcio, E. Drioli, Selective Glycine Polymorph Crystallization by Using Microporous Membranes, Cryst. Growth Des. 7 (2007) 526–530. doi:10.1021/cg0605990.

[106] Z. Ji, J. Wang, Z. Yin, D. Hou, Z. Luan, Effect of microwave irradiation on typical inorganic salts crystallization in membrane distillation process, J. Memb. Sci. 455 (2014) 24–30. doi:10.1016/j.memsci.2013.12.064.

[107] S. Meng, Y. Ye, J. Mansouri, V. Chen, Fouling and crystallisation behaviour of superhydrophobic nano-composite PVDF membranes in direct contact membrane distillation, J. Memb. Sci. 463 (2014) 102–112. doi:10.1016/j.memsci.2014.03.027.

[108] F. Edwie, T.-S. Chung, Development of simultaneous membrane distillation–crystallization (SMDC) technology for treatment of saturated brine, Chem. Eng. Sci. 98 (2013) 160–172. doi:10.1016/j.ces.2013.05.008.

[109] A. Ali, C. Quist-Jensen, F. Macedonio, E. Drioli, Application of Membrane Crystallization for Minerals' Recovery from Produced Water, Membranes (Basel). 5 (2015) 772–792. doi:10.3390/membranes5040772.

[110] K.L. Hickenbottom, T.Y. Cath, Sustainable operation of membrane distillation for enhancement of mineral recovery from hypersaline solutions, J. Memb. Sci. (2014). doi:10.1016/j.memsci.2013.12.043.

[111] P.K. Roy, S. Ray, A. Majumder, Study of Water Quality of Packaged and Municipal Supply Drinking Water With Performance Evaluation of Stand-Alone Filters, in: Bottled Packag. Water, Elsevier, 2019: pp. 63–82. doi:10.1016/B978-0-12-815272-0.00003-9.

[112] H. Takabatake, M. Taniguchi, M. Kurihara, Advanced technologies for stabilization and high performance of seawater ro membrane desalination plants, Membranes (Basel). 11 (2021) 1–20. doi:10.3390/membranes11020138.

[113] A. Al-Karaghouli, L.L. Kazmerski, Energy consumption and water production cost of conventional and renewable-energy-powered desalination processes, Renew. Sustain. Energy Rev. 24 (2013) 343–356. doi:10.1016/j.rser.2012.12.064.

[114] A. Panagopoulos, Process simulation and techno-economic assessment of a zero liquid discharge/multi-effect desalination/thermal vapor compression (ZLD/MED/TVC) system, Int. J. Energy Res. 44 (2020) 473–495. doi:10.1002/er.4948.

[115] D. Zhao, L.Y. Lee, S.L. Ong, P. Chowdhury, K.B. Siah, H.Y. Ng, Electrodialysis reversal for industrial reverse osmosis brine treatment, Sep. Purif. Technol. 213 (2019) 339–347. doi:10.1016/j.seppur.2018.12.056.

[116] S. Roy, S. Ragunath, Emerging membrane technologies for water and energy sustainability: Future prospects, constraints and challenges, Energies. 11 (2018) 2997. doi:10.3390/en11112997.

[117] R. Miladi, N. Frikha, S. Gabsi, Modeling and energy analysis of a solar thermal vacuum membrane distillation coupled with a liquid ring vacuum pump, Renew. Energy. 164 (2021) 1395–1407. doi:10.1016/j.renene.2020.10.136.

[118] N. Mir, Y. Bicer, Integration of electrodialysis with renewable energy sources for sustainable freshwater production: A review, J. Environ. Manage. 289 (2021) 112496. doi:10.1016/j.jenvman.2021.112496.

[119] M. Paul, S.D. Jons, Chemistry and fabrication of polymeric nanofiltration membranes: A review, Polymer (Guildf). 103 (2016) 417–456. doi:10.1016/j.polymer.2016.07.085.

[120] J.H. Tsai, F. Macedonio, E. Drioli, L. Giorno, C.Y. Chou, F.C. Hu, C.L. Li, C.J. Chuang, K.L. Tung, Membrane-based zero liquid discharge: Myth or reality?, J. Taiwan Inst. Chem. Eng. 80 (2017) 192–202. doi:10.1016/j.jtice.2017.06.050.

[121] F. Macedonio, E. Drioli, Advanced Membrane-Based Desalination Systems for Water and Minerals Extracted From the Sea, in: Desalin. Sustain., Elsevier, 2017: pp. 237–259. doi:10.1016/B978-0-12-809791-5.00006-7.

[122] E. Drioli, E. Curcio, G. di Profio, State of the Art and Recent Progresses in Membrane Contactors, Chem. Eng. Res. Des. 83 (2005) 223–233. doi:10.1205/cherd.04203.

[123] M. Essalhi, M. Khayet, Surface segregation of fluorinated modifying macromolecule for hydrophobic/hydrophilic membrane preparation and application in air gap and direct contact membrane distillation, J. Memb. Sci. 417–418 (2012) 163–173. doi:10.1016/j.memsci.2012.06.028.

[124] M.M. Puppolo, J.R. Hughey, B. Weber, T. Dillon, D. Storey, E. Cerkez, S. Jansen-Varnum, Plasma modification of microporous polymer membranes for application in biomimetic dissolution studies, AAPS Open. 3 (2017) 9. doi:10.1186/s41120-017-0019-4.

[125] J.H. Jhaveri, Z.V.P. Murthy, A comprehensive review on anti-fouling nanocomposite membranes for pressure driven membrane separation processes, Desalination. 379 (2016) 137–154. doi:10.1016/j.desal.2015.11.009.

[126] M. Frappa, A.E. Del Rio Castillo, F. Macedonio, A. Politano, E. Drioli, F. Bonaccorso, V. Pellegrini, A. Gugliuzza, A few-layer graphene for advanced composite PVDF membranes dedicated to water desalination: a comparative study, Nanoscale Adv. 2 (2020) 4728–4739. doi:10.1039/D0NA00403K.

[127] T. Zhang, C. Xiao, J. Zhao, X. Liu, D. Ji, H. Zhang, One-step facile fabrication of PVDF/graphene composite nanofibrous membrane with enhanced oil affinity for highly efficient gravity-driven emulsified oil/water separation and selective oil absorption, Sep. Purif. Technol. 254 (2021) 117576. doi:10.1016/j.seppur.2020.117576.

[128] F. Perreault, A. Fonseca De Faria, M. Elimelech, Environmental applications of graphene-based nanomaterials, Chem. Soc. Rev. (2015). doi:10.1039/c5cs00021a.

[129] S. Dervin, D.D. Dionysiou, S.C. Pillai, 2D nanostructures for water purification: Graphene and beyond, Nanoscale. (2016). doi:10.1039/c6nr04508a.

Chapter 3:

Exfoliation of 2D materials and related functionalization of PVDF membranes

Polymeric membranes used in desalination processes often have the disadvantage of low chemical resistance, limited lifetime, and membrane fouling. These issues have forced researchers to pursue new several materials, including polymeric and ceramic, as well as functionalize the membranes with innovative procedures. Several inorganic materials such as zeolites [1] and carbon nanotubes [2] have been employed for water desalination due to their subnanometer pores/channels (fig. 3.1). However, the high cost- and time-consuming process in preparing perfectly ordered subnanometer arrays of zeolites and carbon nanotubes has hindered their commercialization for water desalination [1].

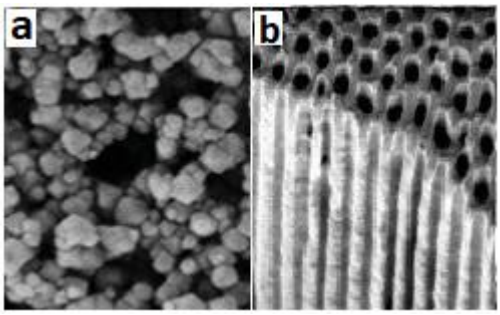

Figure 3.12 *SEM image of a) NaY zeolite nanoparticles and b) carbon nanotube. Reprinted with permission from [1,2].*

Graphene-based membranes [3,4], thermally rearranged polymers [5], two dimensional (2D) membranes based on zeolites, mixed-organic frameworks, bismuth chalcogenides [6,7], and others have been proposed and tested in Membrane Distillation systems. 2D materials are actively researched as they can achieve ion sieving via in-plane pores or stacked nanosheet channels. The hyper-thinness of 2D monolayers makes it possible to fabricate ultra-thin membranes with excellent mass transport and high water flow due to reduced resistance to mass transfer [8]. Several methods have been proposed for the production of exfoliated materials. Figure 3.2 shows the most common procedures providing in table 3.1 an overview about advantages and disadvantages of each single technique [9,10].

2D materials are already widely used in membrane processes such as nanofiltration (ie sieving of molecular and divalent ions with dimensions greater than 1 nm) [11], whilst their use in

membrane distillation has been still somewhat limited. Only in the recent years, a major focus has been given to the use of 2D materials-based membranes in MD applications.

In this chapter, a description of some manufacturing techniques to prepare polymeric membranes functionalized with 2D materials is proposed.

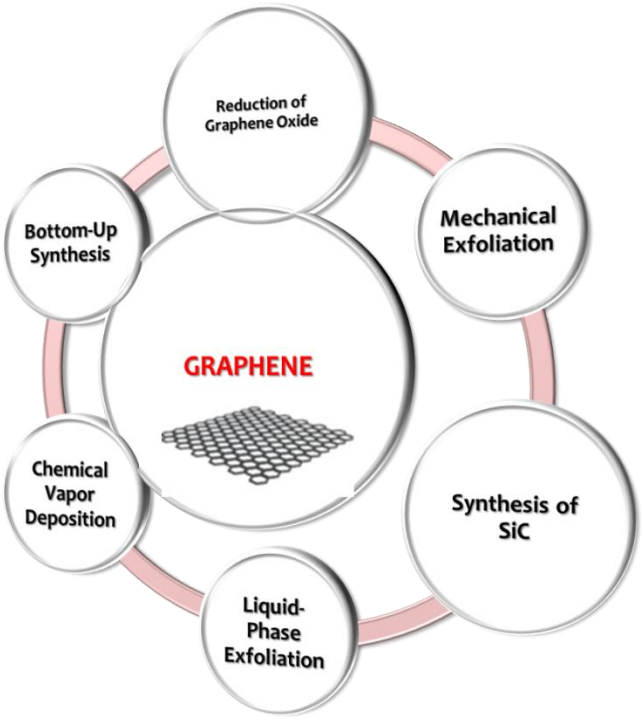

Figure 3.2 *Main exfoliation methods used for the graphene production. Modified from [9].*

Herein, the recent advances on 2D material-based membranes for water desalination are examined with particular emphasis for membrane technologies such as membrane distillation and membrane crystallization. A particular focus is on graphene and the dichalcogenic materials, examining aspects related to manufacturing cost and efficiency of the processes of interest

Table 3.1 *Main exfoliation methods with an overall production process in terms of quality, cost aspect (a low value corresponds to high cost of production), scalability, purity and yield, modified from [9].*

	Reduction of Graphene Oxide	Bottom-Up Synthesis	Chemical Vapor Deposition	Liquid-Phase Exfoliation	Mechanical Exfoliation
Quality	Low	High	High	High	High
Cost aspect	Average	None	None	Average	Average

Scalability	High	Low	Average	High	None
Purity	Low	Average	Average	Average	Average
Yield	High	Low	Low	Low	Low

3.1 Exfoliation procedures to get 2D materials

In the literature there are different liquid phase exfoliation techniques such as wet-jet milling, ultra-sonication, ball-milling and shear-exfoliation [12]. Hereafter, a brief description is given.

3.1.1 The wet-jet milling (WJM)

The wet-jet milling (WJM) is a high pressure hydraulic mechanism provided by a piston to push the sample into a series of 5 different perforated and interconnected discs, called the processor, where the jets are generated (fig.3.3) [12,13]. A pressure up to 250 MPa is usually operated. On an industrial level this technique is commonly used in the pulverization of drugs or paints. The pulverization is obtained from the shocks generated by the pressurized flows of the liquid dispersions of the particles [14]. Conversely, for the exfoliation of layered crystals, the shear force generated by the solvent as the sample passes through the disc is the main phenomenon promoting exfoliation.

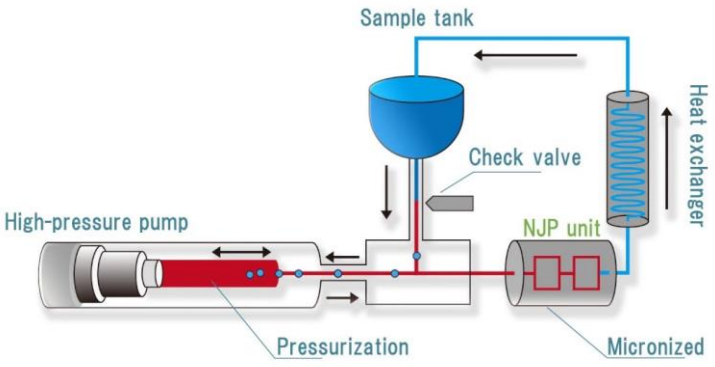

Figure 3.3 *Scheme of the wet-jet mill system. Reproduced from [13].*

An important factor that must be considered for the exfoliation of layered crystals is the selection of the solvent. Indeed, in order to exfoliate the layered crystals, it is necessary to minimize the

Gibbs free energy of the solvent / layered material mixture [15]. This condition can be achieved if the surface tension (γ) of the solvent is equivalent to the surface free energy of the material. For high-quality flakes with defined lateral dimension and thickness, a post-processing procedure is required to purify / separate the one-layer and fewer-layered 2D crystals from the thicker ones (> 10 layers) [12,16]. For this purpose, sedimentation-based separation (SBS) is used. Sedimentation occurs through the application of the centrifugal force proportional to the friction coefficient between the solvent and the particle itself, to the mass of the particle itself, the distance from the rotation axes, the square of the angular velocity, the buoyancy force, which is equal to the mass of the displaced solvent for the centrifugal acceleration, and the frictional force. Frictional force is the force acting on particles as they move with a sedimentation rate in a fluid. SBS is usually applied to particles or flakes dispersed in a solvent in a force field. Thick and large flakes settle faster than thin and small flakes due to higher sedimentation coefficients than small flakes. Therefore, by adjusting the experimental centrifugation parameters, it is possible to retain the flakes with desired lateral dimensions in dispersion. Among the various approaches to liquid phase exfoliation, micro fluidization is the most similar to WJM, as the whole fluid is forced through a spatial region where the flow becomes turbulent. In the case of microfluidization this region is a microchannel, while in the WJM it corresponds to the junctions of the channel before and after the nozzle. In this region, turbulent flow results in a high shear velocity, i.e. a velocity gradient orthogonal to the direction of the flow. The resulting shear stress applied to the scattered flakes induces the sliding of the 2D crystalline planes and initiates the exfoliation process. A more salient difference between the exfoliation process in the WJM and other liquid phase exfoliation (LPE) methods mentioned above is the large pressure drop over time experienced by the crystallites as the dispersion flows through the nozzle. In figure 3.4 the comparison between graphene flakes exfoliated with ultra-wave (fig.3.4a) and WJM (fig.3.4b). The WJM flakes show a higher lateral size and lower thickness (visible with the lighter colour of the flakes) than ultra-wave flakes. In chapter 5 a more details comparison between these two techniques will be illustrated and examined.

a) b)

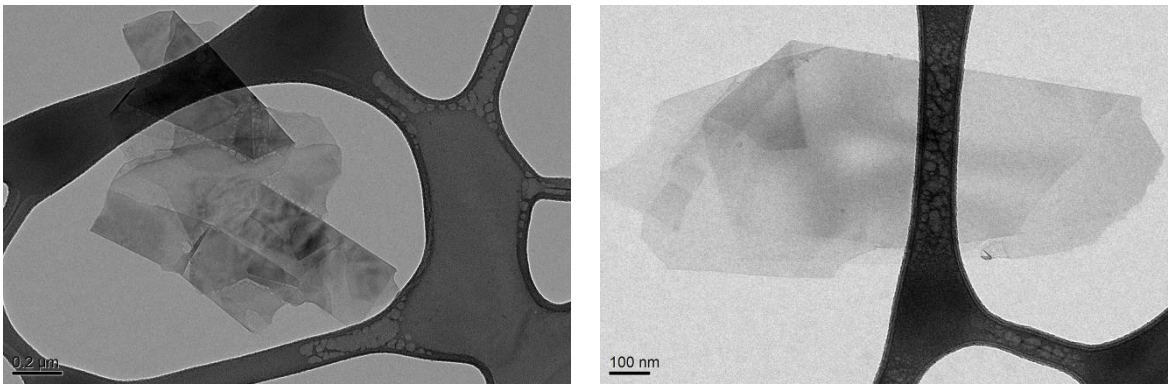

Figure 3.4: *Graphene flakes exfoliated a) with ultrawave and b) with WJM.*

The WJM process is currently exploited in the energy and (opto)electronics fields are extensive, covering a wide range of energy storage and energy production devices [17-19], sensors [20,21], high speed transistors [22], photodetectors [23,24], modulators and mode locking lasers [25,26], ceramic [27], pharmaceutical and food [28], industry to pulverise and homogenise the processed materials [29-31]. The WJM have been used for the exfoliation of layered materials, e.g., graphite, boron nitride and transition metal dichalcogenides [11,12,29,32,33].

3.1.2 Ultra-sonication

Ultrasound exfoliation (UW) is the most used LPE technique due to the ease and simplicity of the process. The creation of cavitation during ultra-sonication induces the exfoliation of layered crystals [34]. An ultrasonic wave is commonly used as an auxiliary method for liquid phase exfoliation. In the case of graphene exfoliation, UW is one of the most used methods (fig. 3.5). There are two main factors that play an important role in preparing graphene by ultrasound-assisted liquid phase exfoliation. The first is the phenomenon of cavitation [35]. In the ultrasonic treatment process, there will be microbubble formation, growth and cracks.

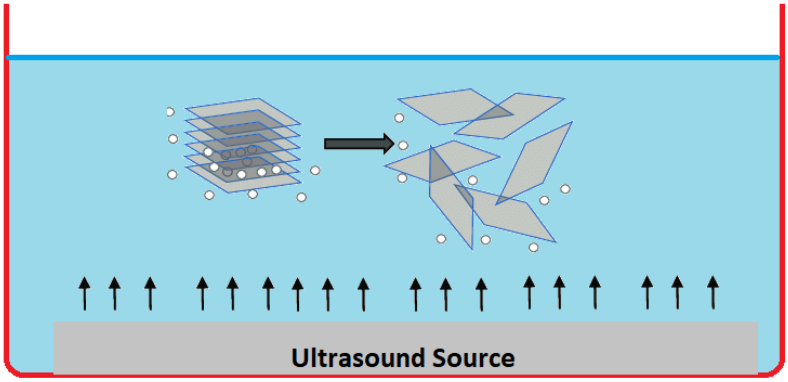

Figure 3.5 *Schematics of the exfoliation methods based on Bath ultra-sonication. Modified from [36].*

The bubbles in the liquid contract at high pressure and expand at low pressure. The bubbles burst violently as the pressure on the graphene surface changes, which causes the graphite dispersed in the solvent to shatter. The second is the pure force produced when the micro bubbles burst near the graphite (not in contact with the graphite) [37]. The solvent forms a microjet and pierces the graphite surface, thus forming a shear force to aid in the separation of the graphite layers. The ultrasonic wave will affect the size and thickness of the graphene layers. The size of lamellar graphene is an important parameter in the ultrasound-assisted liquid phase exfoliation process.

There are, however, significant drawbacks to currently used UW methods which typically rely on the following [37]:

(1) Chemical treatment processing (involving the use of harmful and polluting high-cost solvents or surfactants) to increase the gap between the graphite layers.

(2) Applying external fields such as cutting or ultrasound to exfoliate and diffuse the flakes in the solution;

(3) Purification of exfoliated materials from chemical residues.

Some of these aspects have been recently remedied by using green and non-toxic solvents in the production of graphene. In this respect, water is ideal and attractive, especially after graphene has been recently shown to be hydrophilic, as an environmentally friendly and low-cost dispersion medium [14,28]. Some studies reported on water-based UW still used surfactants, polymer stabilizers or some specialized ingredients as an exfoliating medium, which are considered necessary for the dispersion of flakes in water.

3.1.3 Ball-milling (BM)

A ball mill is a type of grinder used to grind and mix bulk material into QD / nanosize using different sized balls [15,38]. Reduction in impact size and friction occur when the ball falls near the top of a rotating hollow cylindrical shell. The size of the nanostructure can be varied by varying the number and size of the spheres, the material used for the spheres, the material used for the cylinder surface, the rotation speed and the choice of material to be milled (fig.3.6). Ball mills are commonly used to crush and grind materials into an extremely fine shape. The ball mill contains a hollow cylindrical shell that rotates around its own axis [39].

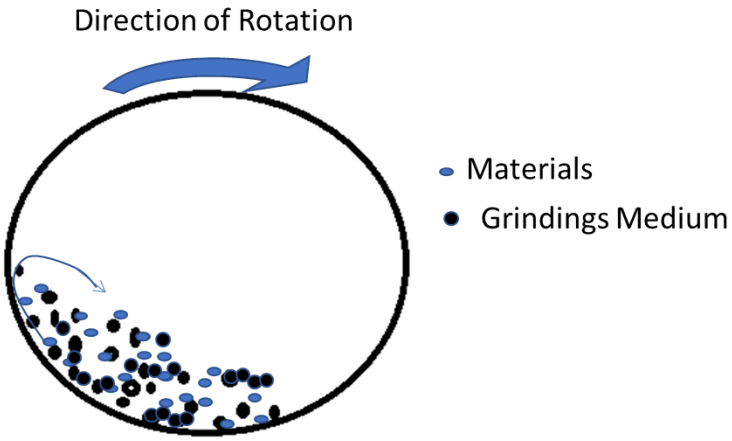

Figure 3.6 *Schematic diagram of a ball mill. Modified from [40].*

This cylinder is filled with balls made of stainless steel or rubber for the material it contains. Ball mills are classified as attritor, horizontal, planetary, high energy or agitator. During grinding, solvent is added to the planetary-rotary mill. The zirconia or metal container (vase) is filled with spheres of the same material. During the rotation of the vessel, the crash and friction between the spheres create shear forces that favour the exfoliation of the graphite. The scalability and repeatability of this method has been not yet demonstrated. The use of ball mills for organic synthesis is a strongly emerging research field [41]. As for the wide range of applications in organic chemistry, the highlights will only be presented in this tutorial review, which covers the past five years. In addition to classical organic synthesis, the ball grinding method is also applied in research areas on the border between inorganic and organic chemistry such as the synthesis of metal complexes, the formation of organic-metal frameworks and the synthesis of catalysts. From a pharmaceutical point of view, the assembly of co-crystals between pharmacologically active compounds initiated by grinding or grinding is a real field of research [38]. Contrary to the examples cited above and the reactions discussed here, the formation of co-crystals it rather

depends on the coordinative interactions between molecular dipoles than on the formation of covalent bonds.

3.1.4 Shear-exfoliation (SE)

In high shear exfoliation a shear force is applied to separate the sheets of the material to be exfoliated (e.g. graphene). The shear mixer has emerged as a new tool for the exfoliation of layered crystals [42]. The turbulence and shear forces produced by the reciprocal rotor / stator movement exfoliate the dispersed stratified crystals. To date, shear exfoliation appears to be a technique that still needs to be improved to meet demand on an industrial scale. The scalable method of high shear exfoliation has been not yet fully explored and there are only a few reports focused on shear mixing in environmentally friendly aqueous media to produce low-layer graphene dispersions. The highest concentrations recorded to date are approximately 1 mg / mL using processing times of up to 4 hours. Therefore, high shear exfoliation is still quite new techniques and, despite the apparent simplicity, many aspects are possible that influence the outcome of exfoliation in terms of quantity and quality [43,44].

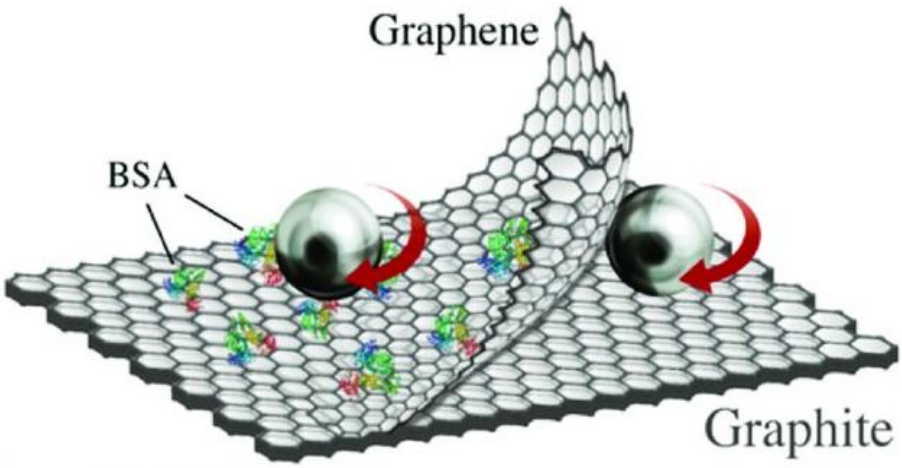

Figure 3.7 *Shear exfoliation of graphene. Adapted from [45] open access.*

These aspects include the properties of the graphite source material such as flake size, type of surfactant and its concentration, as well as mixing parameters (such as rotor speed and mixing time). Some of these aspects, such as the mixing parameters, have been studied more thoroughly, while other parameters have received less attention. In particular, the effect of flake size on the outcome of exfoliation has not gotten much attention and its effect is unclear. It is interesting to study it, as large graphite flakes with high crystallinity are typically used to obtain high quality, low-layer graphene. Furthermore, it is of great interest to reduce the amount of solvent and

surfactant residues since they limit the applicability of the material produced by decreasing for example the conductivity of the subsequent films.

3.1.5 Micro fluidization

A promising technique recently reported is micro-fluidization which consists in subjecting the layered crystals dispersion to high shear rate [46,47]. Microfluidization is used for production of micro and nanoscale size materials especially in pharmaceutical industry to make liposomal products, emulsion and in food industry to produce dairy products [48]. Processing time is limited to piston passages (70 passes) [49]. This technique uses only water / surfactant and the exfoliated flakes show structural defects, which increase proportionally with the piston passages. In particular, microfluidization has been used for boron nitride (h-BN) hexagonal flakes, high shear mixing to exfoliate bulk black phosphorus, MoS_2, h-BN, WS_2, $MoSe_2$, and $MoTe_2$, ball grinding for h -BN, and MoS_2 [47-51]. In pharmaceutical applications, Microfluidization has been also used to prepare unilamellar vesicles of defined size distribution, such as liposome (fig. 3.8). Microfluidization has been also used for the production of polymer nanosuspensions, in pharmaceutical applications to produce liposome nanoparticles for use in eye drops, to produce aspirin nanoemulsions, as well as in food applications for oil-in-water nanoemulsions. Another use has been for the de-agglomeration and dispersion of carbon nanotubes. However, the scale up for this technique from the laboratory scale to the market, to enable large-scale production of quality 2D crystals, still appears to be necessary.

A fluidized bed has been used for long time to improve mixing and transfer of heat and mass on a macro scale. Despite this, they have seen virtually no application in the context of microfluidics. However, experimental work has shown the potential that microfluidized beds (µFBs) could offer not only to overcome transport limits but also to provide a greater surface area per unit of volume that derives from the use of microparticles. Flows involving microparticles are typically characterized by non-negligible surface forces. A second major problem in µFBs is the possibility that particle-to-bed diameter ratios are greater than 0.1, leading to a significant influence of bed walls on particle packaging in the bed [49].

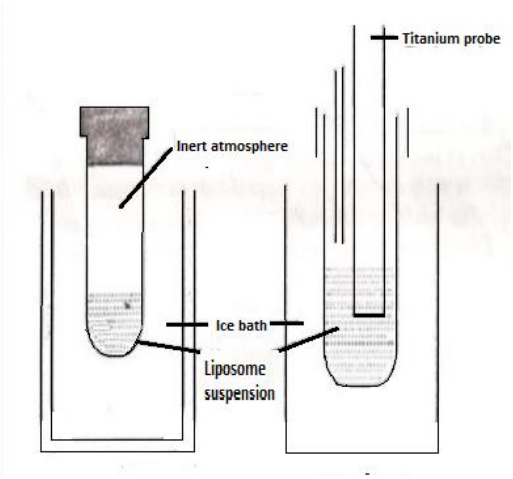

Figure 3.8 *Micro fluidization of liposome suspension. Modified from [52] open access.*

A major advantage of microfluidization over high-pressure homogenization is that it is less prone to clogging as it operates at a constant cutting speed. In addition, this method provides better reproducibility due to the fixed geometry.

3.1.6 Electrochemical exfoliation

Based on the different exfoliation electrode (EE), there are two types of electrochemical exfoliation: anodic and cathodic exfoliation. Anodic exfoliation utilizes platinum wire or foil as the cathode in a dilute solution of H_2SO_4 [18] or Na_2SO_4 [28] while the material to be exfoliated is positioned as an anode. Through this technique, materials such as graphene and MoS_2 are often exfoliated [53]. By applying a voltage to the working electrode material, oxidation of the electrolyzed water produces oxygen-containing radicals (OH and O) that collect around large crystals of the anode (fig. 3.9).

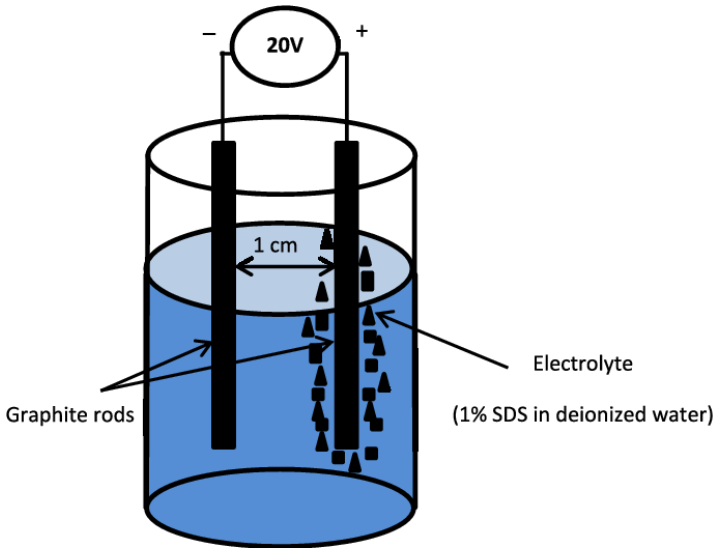

Figure 3.9 *Electrochemical exfoliation of the graphene. Reprinted with permission from [54].*

Oxygen radicals attack the edges of the loose crystals weakening the Van der Waals force between the two layers. In contrast to anodic exfoliation, cathodic exfoliation uses bulk MoS_2 crystals as cathodes and platinum strands or sheets as anodes in an organic solution of long-chain ammonium salts or an aqueous solution of inorganic salts (K_2SO_4 or KCl). As in the previous case, by applying a voltage, the expansion of the distance between the layers takes place at 0.89 nm. Subsequently, the migration and reduction of H^+ produces hydrogen bubbles according to the following equation:

$$H_2SO_4 \leftrightarrow SO_4^{2-} + H^+ + 2e^- \rightarrow H_2$$

which further expand the space between adjacent layers. Finally, the nanosheets are isolated and suspended in the electrolyte under the force of the gas eruption. Therefore, the selection of a suitable electrolyte to achieve cathode ion intercalation and gas generation are the main factors to achieve cathode exfoliation.

3.1.7 Top-down and Bottom-up method Mechanical Exfoliation

Mechanical exfoliation (ME) can be implemented according to top-down and bottom up approaches [55]. Top-down method allows the exfoliation of a single-layer from spout crystals VDW (*van der Waals heterostructures*). The top-down method can be achieved through different techniques between which: tape exfoliation, metal exfoliation, intercalation and exfoliation mediated by liquids [56,57]. The VDW link among the layers in the loose crystal is exceeded by

external mechanical forces. Tape exfoliation or thin metal movie mechanically scarps the loose crystals and produces single crystal flakes [12]. Single crystal flakes from the tape or metal exfoliation are often high purity and cleaning, which are mainly suitable for the manufacture of fundamental devices and characterizations of new 2D systems. For intercalation strategies, the ionic species are interspersed in the spaces between the layers. The intercalation creates expansion forces through the reaction and allows the separation of the layers in the liquid. Ultrasonic, or exfoliation mediated by liquids, uses a hard cavitation process to produce a high local temperature and extreme pressure, which breaks the flakes stacked in bulk crystal and tears layers [58]. Liquid phase preparations are superior in obtaining number of grams of nanophography. However, small submicrometric scales are often obtained with high defects and sometimes with modified chemical or physical properties. The monolayers prepared by fluid-mediated exhibitions are particularly useful for catalysis or other chemical applications [59].

Bottom-up method uses molecular precursors to form 2D crystal networks. During deposition, nucleation in different local positions leads to the continuous growth of the individual triangular domains, which later merge into a continuous monolayer thin film. The continuous thin film is usually polycrystalline and can cover a large area up to the wafer scale [60]. With tuned growth conditions, isolated triangular monocrystalline flakes up to a few hundred μm in the lateral dimension can be obtained. Controlling the number of strata through direct growth is particularly difficult due to the high barrier to nucleation [61].

3.1.8 Reduction of Graphene Oxide

Reduced graphene oxide (rGO) is an alternative form of graphene oxide (GO) that has been processed by various methods, which include chemical, thermal, etc. In order to minimize the amount of oxygen as the oxygen content makes GO more unstable [62]. In its usual oxidized state, GO exhibits reduced sensitivity due to oxygen functional groups, making it electrically insulating and not ideal for fabricating a conductance-based sensor. Typically the reduction process can be achieved by electrochemical reduction, chemical reduction and thermal reduction. Reduced GO prepared by chemical or thermal methods typically uses compounds such as hydrazine hydrate vapor, hydrogen sulfide, hydroquinone, dimethylhydrazine, $NaBH_4$ and aluminum powder [16,63-65]. The latter can restore conductivity by repeatedly removing oxygen and restoring the double bond aromatic carbon atoms. RGO does not convert GO to graphene in its pure form as at least few oxygen groups are present even after chemical and thermal exposure. Therefore, rGO exhibits

high conductivity, stability and the presence of defective sites that are chemically active making it a potential candidate for application as an active material in biosensors [66]. Reduced Graphene Oxide (rGO) has been commonly used to prepare composites with various materials, such as metal and metal oxides, using different techniques to improve the performance of the supercapacitor.

3.2 Functionalization of PVDF-based membranes with 2D materials

Factors of interest to improve membrane contactors research are the reduction of energy consumption, the difficulties faced with long-term operations, the simultaneous risk of wetting, scaling and fouling. Different methodologies have been developed to improve membrane performance such as the preparation of new types of membranes or of special coating on commercial membranes. This has been done to the improvement of the characteristics in terms of pore size, overall porosity, thickness and hydrophobic. In literature, new research in these fields have been developed such as the preparation of composite porous hydrophobic/hydrophilic membrane by using fluorinated surface modifying macromolecule (SMM) and polyethermide [67 nanoparticles (e.g., SiO2/Al2O3/ZnO) as fillers[68–70], zeolites, MoS2, CF4 plasma surface modification for enhance hydrophobicity [71,72] and preparation of nanotube-structured TiO2 surfaces with superomniphobic characteristics [73]. Another interesting way to enhance the membrane performance in the sector dedicated to the desalination of water is the functionalization of the membrane with the potential of 2D material [12,74,75]. A large variety of materials may be used for the preparation of advanced nanocomposite membranes such as graphene [76], transition metal dichalcogenides (TMDs) [77,78], metal organic frameworks (MOF) [79,80], Mxenes [81], Layered double hydroxides [82], layers silicates [83,84], etc.

3.2.1 Preparation of 2D Membranes

Several kinds of manufacturing techniques are proposed for the development of nanostructured membranes. Some of these (Lithographic techniques [85], Phase separation micro-molding combined technique [86,87], Techniques based on colloidal templates [88,89], Self-assembly copolymers [90] Breath figures [91], etc.) are mentioned in the Chapter 2 dedicated on the Membrane technology. Here particular attention has been done on the preparation techniques with a high degree of geometric order through two-dimensional (2D) and tridimensional (3D) space. Each approach brings advantages and limitations, with certain characteristics to the

membranes produced. Over the years, researchers have been tried to improve each technique in order to obtain increasingly efficient membranes [92].

a) *Deposition for filtration*: Pressure / vacuum filtration is one of the most common and effective deposition methods. The vertical downtown force, supplied by pressure / vacuum filtration, drives the 2D Nanosheets group in a layered interlocking structure on the substrate. The thickness is given by the thickness of the membrane that is supported, even if it can slightly vary with deposition. Furthermore, other ions, molecules or nanoparticles can be easily mixed and interspersed in the strikers, providing additional flexibility on the tuning of the membrane structure [93].

b) *Coating*: The coating is the creation of a thin layer on the surface of the membrane. Various coating methods have been reported to assemble 2D Nanosheets on membranes, including drop coating, sterile coating, spin coating and casting, etc. The success of a uniform coating is based on the smoothness of the substrate, the surface tension of the coating solutions, as well as the process of evaporation applied. Among the methods, spin-coating could provide centrifugal and cutting forces to control the assembly of Nanosheets, producing a well-intertoped ordered laminated structure. At present, this technique is also applied to prepare highly ordered labeled membranes [66,94].

c) *The level-by-layer self-assembly (LBL):* LBL refers to the deposit process alternately of different materials on the surface of the substrate. This approach is mainly based on the interactions between adjacent layers, including electrostatic bonding, hydrogen or even covalent interactions. The LBL method can accurately check the thickness of the selective layer by varying the number of deposition cycles and is useful for introducing the intercalay stabilization forces. Therefore, the resulting membranes can remain stable in aqueous or organic media. However, the implementation of this method requires the presence of material interactions and the preparation process takes time *[95,96].*

d) Honeycomb membranes: The honeycomb membranes possess a specific distribution of the pores on the surface of the partition walls and an enlarged porosity in addition to subtle dividing walls of a prescribed value. For the preparation of these particular structures it is based on the preparation of lithographic precision membranes according to a bf biospirated process [97]. The condensation water drops act as the imprinting agents on the polymer surface and with the

balance between solvent evaporation and humid air condensation in a 3D construction, bee nest membranes can be obtained in a single pass. After condensation, the dripping water drills grow and self-assemble in ordered arrays, producing a highly defined hexagonal geometry as a result of their imprinting action, different from what is observed for the separation techniques of conventional phases. The main limitation to produce commercially large-scale films is the lack of control over the long-range structural order through the surface of the films made: for this reason, a study of the behaviour of the dynamics of water droplets during self-assembly [98].

The scalability of membrane preparation methods is essential to implement practical applications. Coating and casting methods are scalable and industrially adaptable methods for thin lamellar flat sheet membranes. In addition, attaching 2D nanosheets to hollow fibers by filtration methods could facilitate the translation from the laboratory scale to the industrial scale. Note that all these methods are fundamentally based on a uniform suspension of nanosheets; accordingly, selecting appropriate solvents to match the hydrophilicity of the nanosheets and implementing necessary modifications to improve the dispersion are important pre-steps. Phase inversion techniques have various advantages such as low formation of defects, possibility to use green solvents, high possibility to control the final morphology (pore size, thickness, etc.) and symmetric structure. At industrial level, Phase inversion techniques are the most processes used for the membrane preparations [99-101].

3.2.2 Graphene

In the recent years, Graphene is became one of the materials most studied and used in different research fields. This is due to its unique proprieties such as excellent electronic conductivity, hydrophobic and anti-wetting nature, anti-fouling properties, great mechanical strength, low density and selective sorption of water vapours [102,103]. Graphene consists of single-atom-thick sheets of sp^2 bonded carbon. The combination of high-performance graphene with economical and relatively durable polymer membranes is a promising approach to support sustainable growth in industrial and research development [104]. The membrane with graphene few-layers presents ideal propriety for Membrane contactors process, such as narrow pore size, for great performance in terms of permeability and selectivity. Graphene is, in general, produced from exfoliation of graphite. The technique of exfoliation is fundamental for the quality of graphene in terms of number of layer, lateral size and thickness of the graphene flakes. In literature are reported different techniques for the graphene exfoliation such as Mechanical Exfoliation [105], Epitaxial

graphene out of SiC [106], direct graphene growth onto thin nickel [107], chemical vapor deposition (CVD) [108], etc. The most used is the LPE, which, in a liquid environment, allow the exfoliation of graphite by ultrasound or shear forces to break the van der Waals bond among the layers of graphite [15,109,110]. In the recent years, an innovative and advanced technique for high-quality graphene exfoliation has been developed. The mentioned technique is the wet-jet milling (MJW) that allows to prepare graphene with well-controlled thickness and lateral size in easy and scalable way [12,57]. Rouff et al. [111] prepared GO paper by filtering a GO solution through a microfiltration membrane. The obtained graphene layers has been studied by X-ray diffraction (XRD) pattern showing the layer-to-layer distance (d-spacing) of the GO paper has been about 0.83 nm. The d-spacing of a GO paper depends on the degree of oxidation. Moreover the study shows how increasing the degree of oxidation, the d-spacing could be increased to up to about 1nm. Li et al. [112] prepared graphene membranes in order to investigate the corrugation of GO nanosheets and found that GO nanosheets could be used with great result nanofiltration process with rejection rate of 67% for direct yellow. A direct transfer of graphene pattern has been investigated by Kim et al. [113] using plasma surface modification of polydimethylsiloxane (PDMS) with inductively coupled C_4F_8/O_2/Ar gas mixture plasma. Graphene has been coated on the modified PDMS and then directly transferred to the PET substrate. This technology allows obtaining a uniformity of the graphene on the membrane surface of about 85%.

Graphene in Membrane distillation Process

Graphene represent one of the most materials used in Membrane contactors process, especially in Membrane distillation (MD). An example of graphene-based membranes has been done from Gontarek et al. [70] in which powder of Graphene platelet has been dispersed in Solvent and confined in membrane matrix at different concentrations. The prepared membrane has been experimentally tested in MD and MCr. The results indicate that composite membranes are good in terms of trans-membrane fluxs with high rejection rate (of about 100%) and without wetting, fouling and thermal polarization phenomena. A different approach of functionalization of PVDF membrane with graphene layers has be proposed recently [114]. In figure 3.10 are shown trans-membrane flux of different kind of Graphene based membranes tested in direct contact membrane distillation. All the membrane with graphene and graphene oxide present a rejection rate over the 99.9%.

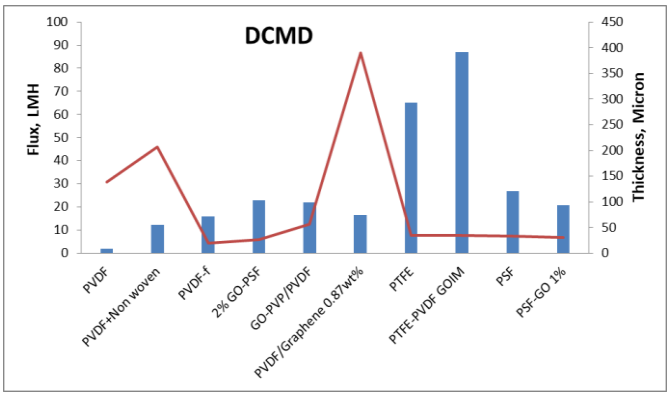

Figure 3.10 *Trans-membrane flux of graphene based membrane in DCMD; thickness of the membranes in micron.*

In this case Graphene is chemically anchored on membrane surface exploiting the π- π interactions created with PVDF surface. A recent study of graphene oxide functionalization for Membrane distillation was made by Zahirifar et al. [76]. In the specific, graphene oxide has been functionalized chemically with octadecylamine (ODA) in order to exploit the long hydrocarbon chain of ODA for reduces the surface energy and increases membrane hydrophobicity. The ODA-functionalized has been done by coating of Graphene oxide on PVDF membrane surface. The prepared membrane has been therefore applied for desalination in air gap membrane distillation in terms of water permeability and salt rejection. The results shows how the suitable amount of GO-ODA coated on PVDF membrane enhance significantly MD performance. This improvement has been attributed at the increase of hydrophobicity and roughness, reduced pore wetting and as well as low thermal conductivity of GO-ODA contribute. Moreover is present a decline of temperature polarization and heat diffusion across the membrane. Other example of Graphene application in MD process has been done by Bhadra et al. [115] that investigated desalination in DCMD. The membrane has been prepared by immobilization of graphene oxide on a PTFE membrane with an improvement in trans-membrane flux and high salt rejection. They argued that this improvement occurred because of selective sorption, non-capillary effects, reduced temperature polarization, and the introduction of functional groups by the graphene oxide. The potential of novel graphene quantum dots (GQDs)/polyvinylidene fluoride (PVDF) nanofibrous membranes for air gap membrane distillation (AGMD) have been studied by Jafari et al. [116]. In this work, AGMD experiments has been conducted with 3.5wt% NaCl solution for 8h, showing how the graphene may prevent the wetting and fouling in long time experiment. Moreover, the test indicate the high water flux of 17.6 kg/m^2 h and salt rejection of about 99.7% membrane containing 0.25 wt% GQDs compared to neat PVDF nanofibrous were partial wetting occurred after 4 h. A study on reduced Graphene oxide (rGO) on hydrophobic polyvinylidene fluoride (PVDF)

membranes has been successfully performed from Abdel-Karim et al. [117] in membrane distillation (MD). In this work, different degrees of reduction of graphene oxide (rGO) nanoplatelets have been incorporated as fillers in PVDF matrices in order to evaluate the effect of the oxygen content of the fillers in the MD performance. The term reduced Graphene oxide is utilized when the oxidized functional groups are removed, to obtain a graphene material. The MD results show how 0.5 wt% rGO in the mixed matrix membrane can enhance of about 169% the performance of PVDF membranes. Furthermore, continuous testing for up to 96 h showed a stable performance of the developed MMMs, without compromising the MD performance. Hongbin li et al. [118] proposed hydrophobic nanofibrous composites membrane for vacuum membrane distillation (VMD). This composite membrane are made of a hydrophobic polyvinylidene fluoride (PVDF) nanofibrous layer and a hydrophobic polypropylene (PP) nonwoven fabric (NWF) substrate. The PVDF layers have been directly fabricated on the surface of PP substrate by electrospinning technique and functionalized with GO. The GO functionalization allow to enhance the hydrophobicity and permeation water flux for VMD and add at the membrane the anti-wetting properties. A similar work where GO are used to functionalize the surface of a PVDF membrane has been developed by Qiu et al. [119] for improve the anti-fouling proprieties of the membrane. The surface modification has been done by dispersing graphene oxide (GO) on the channel surface forming a functional layer with the possibility of blockage of bulk pores. This may increase the mass transfer resistance and reduce the permeability. Respect to the membrane surface functionalized by nanoparticles such as SiO_2, GO has been mainly located on the pore surface of the membrane bulk. The membrane has been evaluated in direct-contact membrane distillation with anionic and cationic surfactants as the foulants, showing an improved antifouling behaviour and distillated flux compared to the pristine PVDF membrane. Qiu et al. attribute the enhanced results to the oxygen containing functional groups in GO and the healing of the membrane pore defects. This method guarantees an effective way to functionalize the membrane pore surface properties for anti-fouling separation without increasing mass transfer resistance.

3.2.3 MOF and Dichalcogenide Metals

Recently, given the growing scarcity of water, the research in order to improve the performance of water treatment focused on incorporating the two-dimensional (2D) nanomaterials into the membranes. This kind of material can add their property at the membranes such as atomic thickness, antibacterial property uniform pore diameter and surface charge characteristics. Other

to the most known Graphene oxide (GO), researchers found that the new 2D materials such as hexagonal boron nitride (h-BN) or Novel molybdenum disulfide (MoS_2). The first shows good mechanical stability, and is expected to improve the permeability of the membrane [120]. A modified interfacial polymerization (IP) reaction has been done to fabricate fouling-resistant membranes with few-layered amine functionalized-boron nitride BN(NH_2) nanosheets [121]. Membranes with BN(NH_2) nanosheets tested in nanofiltration to separate NOM from water revealed 59% enhancement in flux and 50% improvement in total fouling resistance, long-term operational stability and enhanced recoverability with no-leaching during filtration. Molybdenum disulfide (MoS_2) has been found promising in the field of membrane technology for displaying smooth surface without any oxygenated functional groups, reducing the resistance of water molecules to transport [78]. The pore structure of MoS_2 allow to achieve superior separation performance with a flux 3–5 times more compared to GO when prepared under the same conditions [122]. The exfoliated few-layers MoS_2 incorporated into PA membrane with negative charged show a good hydrophilicity that improve the permeability and selectivity of the NF and RO membranes. Similar to the oxidization of graphene nanosheets, the oxidation and exfoliation of molybdenum disulfide (O–MoS_2) allow to improve its proprieties and so to enhance the NF performance [123]. Compared to the MoS_2- TFN membrane, the O–MoS_2 TFN membrane has an unprecedented enhancement in permeability and selectivity with an excellent antifouling performance. The successful application of 2D O–MoS_2 nanosheets materials in NF membranes has opened up a new way for water desalination.

Novel thin layer of mesoporous silica nanoparticles (mMSN) is another simple way to optimize the membrane performance in water treatment. Wu et al. [124] introduce the mesoporous silica nanoparticles into polyamide membranes *via* interfacial polymerization of trimesoyl chloride (TMC) and piperazine (PIP) in the presence of mMSN. To prevent the reaction of amino groups with the acid chloride group of TMC during the polymerization, silica nanoparticles has been be chemically incorporated into the nanocomposite membrane *in situ.* This can improve the compatibility and the loading of silica nanoparticles with the polymer. The influence of the mMSN amount on the membrane performance allows to improve anti-fouling proprieties and a good long-term stability with an enhanced water flux. A novel two-dimensional material applied in order to optimize the membrane performance is the Mxene [125]. This material (with the formula of Mn+1XnTx), are usually produced by selectively etching the mainly group IIIA or IVA elements layers from Mn+1AXn phases (n = 1, 2, or 3), where M is a transition metal and X is carbon and/or

nitrogen. Each MXene layer prepared has been combined each other by hydrogen bonding and van der Waals force producing a two-dimensional lamellar membrane. The morphologies of the membranes present a narrow nanochannel between the neighboring MXene nanosheets, which makes MXene an ideal and promising material for water treatment and more. In general MXene membranes exhibit good removal rates maintaining exceptional water permeance. This is due to the water-transport pathways proprieties and the intercalated nanoparticles separate the slit pores between the MXene nanosheets, which provide greater interlayer distance and generate abundant nanochannels [125]. The mxenes have aroused the interest of the scientific community due to their particular characteristics, such as the high electronic conductivity, hydrophilicity, high surface area, active sites on the surface, metallic and antibacterial properties, and processability. These characteristics make them materials that can be used in the biomedical, energy, biosensor and catalysis fields. Some peculiar qualities such as low toxicity of degradation products, antibacterial properties and chemical functions have made it an interesting material in membrane processes of water purification [56.58-60]. Several studies have shown their effectiveness in removing metal ions, salts, dyes and radionuclides, killing E. coli and B. subtilis [62,63]. Furthermore, surface chemistry makes them able to be variously functionalized to impart further capacities. A study conducted by Tan et al 2018 in DCMD configuration on a PDVF coated membrane with Ti_3C_2Tx Mxene conferred a 56–64% reduction in flux decline compared to the uncoated membrane after 21 hours showing strong antifouling properties, however the Mxene membrane showed a more flow low non-modification. The mixene membrane showed interesting photothermal properties, showed a temperature rise of 43 ° C compared to pristine membranes after 1 min of sun exposure and a 12% saving of the energy input heater per unit of distilled volume [126].

Chaudhary et al. [127] has been developed a synthesis of 2D/2D interfaces between nickel/nickel oxide (Ni/NiO) hexagonal nanosheets with graphitic-carbon nitride ($g\text{-}C_3N_4$) by using an in-situ solid-state heat treatment. This new material might be enhancing the electrochemical activity for photo-electrochemical (PEC) water splitting. In particular has been studied the activity for oxygen evolution reaction (OER) and hydrogen evolution reaction (HER) with an enhancement in current density that facilitates the transfer of charge over their interfaces. Kaolin 2D nanosheets incorporated into membrane for ultrafiltration treatment has been developed and studied by Liu et al. [128]. The membranes has been prepared by stacking layer-by-layer the nanosheets with a cationic polyacrylamide cross-linking agent, assembled on a cellulose acetate supporting layer. The

kaolin membrane exhibited an ultrahigh flux of about 4000 $L.m^{-2}.h^{-1}.bar^{-1}$ which has been almost ten times greater than that of a commercial polyether sulfone (PES) ultrafiltration (UF) membrane. The membrane has been stable in terms of its pore size distribution (peak distribution at 20–35 nm) with a substantially reduced rate of fouling, and present an advantageous low cost making the 2D-kaolin membrane a potentially important development for water treatment.

Other interesting materials utilized for water treatment are represented by the metal organic frameworks. Exploiting the MOFs proprieties, such as with high porosity and surface area, incorporated into the polymeric membranes is possible to entrap the contaminants present in drinking water though the appropriate process. In literature is possible to find MOFs-base membrane utilized to remove arsenic, fluoride, and iron from drinking water [129]. MOF based membrane include continuous growth process where the membranes are formed in layer-by-layer deposition of MOF, electro-deposition, thin-film nano-composite and solvothermal [79]. The applications of MOFs allow good stabilities under various conditions, large scale production and cost-effective synthesis route. It is observed that, the stability of the MOFs can be enhanced by using carbon nano-tubes (CNT) for water purification from arsenic and fluoride [130].

Recently, as an alternative to the most used graphene, among the new few-layer materials, TMC (transition metals chalcogenide) have been emerged for their unique chemical-physical properties, such as the different electronic properties (metals, semi-metals, insulators and semi-conductors). Chalcogenide family are made of binary compounds consisting of a transition metal (M) and a chalcogenide element (X) of general formula MnXm, over 60 compounds are known, metals of group IV, V, VI, X and others have been reported [59]. MX_2 stoichiometries are common to have a sheet configuration stacked one above the other in sheets having thicknesses of three atoms with the metal in the center and above and below the chalcogenides [10]. The MX bond is covalent while the sheets are held together by weak interactions, which makes exfoliation feasible. TMD can have four crystalline polytypes, 2H, 1T, 1T ', in which the metal has trigonal or octahedral prismatic geometry [131].

The individually exfoliated TMCs have a flat honeycomb structure in the case of light chalcogenides or slightly wavy in the case of heavy ones. Similarly to TMD, there is a family of semimetal chalcogenides (SMC) with the difference that the transition metal is replaced by a semimetal. Their most common stoichiometry is M_2X_2 in layers of four atoms thickness, in X - M - M - X configuration [132]. Gugliuzza et al [133] successfully tested a Bi_2Se_3 / PVDF membrane in a distillation / crystallization experiment, obtaining a constant transmembrane flux over time with

improved salt rejection in both tests. Moreover the crystallization of NaCl shows an improved crystallization growth rate respect to the pristine PVDF membrane with a narrower crystal size distribution.

References

[1] A. Giwa, N. Akther, V. Dufour, S.W. Hasan, A critical review on recent polymeric and nano-enhanced membranes for reverse osmosis, RSC Adv. 6 (2016) 8134–8163. doi:10.1039/c5ra17221g.

[2] Jinghua Fang, Igor Levchenko, Zhao Jun Han, Samuel-Yick, Kostya Ken Ostrikov Carbon nanotubes on nanoporous alumina: From surface mats to conformal pore filling, Nanoscale Research Letters, 9(2014), 1, 390, http://dx.doi.org/10.1186/1556-276X-9-390

[3] A. Subramani, J.G. Jacangelo, Emerging desalination technologies for water treatment: A critical review, Water Res. 75 (2015) 164–187. doi:10.1016/j.watres.2015.02.032.

[4] A. Street, R. Sustich, J. Duncan, N. Savage, Nanotechnology Applications for Clean Water: Solutions for Improving Water Quality: Second Edition, 2014. doi:10.1016/C2012-0-00675-8.

[5] J.H. Kim, S.H. Park, M.J. Lee, S.M. Lee, W.H. Lee, K.H. Lee, N.R. Kang, H.J. Jo, J.F. Kim, E. Drioli, Y.M. Lee, Thermally rearranged polymer membranes for desalination, Energy Environ. Sci. 9 (2016) 878–884. doi:10.1039/C5EE03768A.

[6] A. Gugliuzza, F. Macedonio, A. Politano, E. Drioli, Prospects of 2D materials-based membranes in water desalination, Chem. Eng. Trans. (2019). doi:10.3303/CET1973045.

[7] J. Ni, X. Bi, Y. Jiang, L. Li, J. Lu, Bismuth chalcogenide compounds Bi2×3 (X=O, S, Se): Applications in electrochemical energy storage, Nano Energy. (2017). doi:10.1016/j.nanoen.2017.02.041.

[8] G. Liu, W. Jin, N. Xu, Two-Dimensional-Material Membranes: A New Family of High-Performance Separation Membranes, Angew. Chemie Int. Ed. 55 (2016) 13384–13397. doi:10.1002/anie.201600438.

[9] R. Raccichini, A. Varzi, S. Passerini, B. Scrosati, The role of graphene for electrochemical energy storage, Nat. Mater. 14 (2015) 271–279. doi:10.1038/nmat4170.

[10] C. Tan, X. Cao, X.J. Wu, Q. He, J. Yang, X. Zhang, J. Chen, W. Zhao, S. Han, G.H. Nam, M. Sindoro, H. Zhang, Recent Advances in Ultrathin Two-Dimensional Nanomaterials, Chem. Rev. (2017). doi:10.1021/acs.chemrev.6b00558.

[11] M. Frappa, A.E. Del Rio Castillo, F. Macedonio, A. Politano, E. Drioli, F. Bonaccorso, V. Pellegrini, A. Gugliuzza, A few-layer graphene for advanced composite PVDF membranes dedicated to water desalination: a comparative study, Nanoscale Adv. 2 (2020) 4728–4739. doi:10.1039/D0NA00403K.

[12] A.E. Del Rio Castillo, V. Pellegrini, A. Ansaldo, F. Ricciardella, H. Sun, L. Marasco, J. Buha, Z. Dang, L. Gagliani, E. Lago, N. Curreli, S. Gentiluomo, F. Palazon, M. Prato, R. Oropesa-Nuñez, P.S. Toth, E. Mantero, M. Crugliano, A. Gamucci, A. Tomadin, M. Polini, F. Bonaccorso, High-yield production of 2D crystals by wet-jet milling, Mater. Horizons. (2018). doi:10.1039/c8mh00487k.

[13] https://jokoh.com/en/, (n.d.).

[14] Z.H. Loh, A.K. Samanta, P.W. Sia Heng, Overview of milling techniques for improving the solubility of poorly water-soluble drugs, Asian J. Pharm. Sci. 10 (2015) 255–274. doi:10.1016/j.ajps.2014.12.006.

[15] A.E. Del Rio-Castillo, C. Merino, E. Díez-Barra, E. Vázquez, Selective suspension of single layer graphene mechanochemically exfoliated from carbon nanofibres, Nano Res. (2014). doi:10.1007/s12274-014-0457-4.

[16] J. Buha, R. Gaspari, A.E. Del Rio Castillo, F. Bonaccorso, L. Manna, Thermal Stability and Anisotropic

Sublimation of Two-Dimensional Colloidal Bi 2 Te 3 and Bi 2 Se 3 Nanocrystals, Nano Lett. 16 (2016) 4217–4223. doi:10.1021/acs.nanolett.6b01116.

[17] P. Lian, X. Zhu, H. Xiang, Z. Li, W. Yang, H. Wang, Enhanced cycling performance of Fe3O4–graphene nanocomposite as an anode material for lithium-ion batteries, Electrochim. Acta. 56 (2010) 834–840. doi:10.1016/j.electacta.2010.09.086.

[18] A. Ansaldo, P. Bondavalli, S. Bellani, A.E. Del Rio Castillo, M. Prato, V. Pellegrini, G. Pognon, F. Bonaccorso, High-power graphene–Carbon nanotube hybrid supercapacitors, ChemNanoMat. (2017). doi:10.1002/cnma.201700093.

[19] S.R.C. Vivekchand, C.S. Rout, K.S. Subrahmanyam, A. Govindaraj, C.N.R. Rao, Graphene-based electrochemical supercapacitors, J. Chem. Sci. 120 (2008) 9–13. doi:10.1007/s12039-008-0002-7.

[20] Z. Lou, S. Chen, L. Wang, K. Jiang, G. Shen, An ultra-sensitive and rapid response speed graphene pressure sensors for electronic skin and health monitoring, Nano Energy. 23 (2016) 7–14. doi:10.1016/j.nanoen.2016.02.053.

[21] Q. He, S. Wu, Z. Yin, H. Zhang, Graphene-based electronic sensors, Chem. Sci. 3 (2012) 1764. doi:10.1039/c2sc20205k.

[22] N.O. Weiss, H. Zhou, L. Liao, Y. Liu, S. Jiang, Y. Huang, X. Duan, Graphene: An Emerging Electronic Material, Adv. Mater. 24 (2012) 5782–5825. doi:10.1002/adma.201201482.

[23] F.H.L. Koppens, T. Mueller, P. Avouris, A.C. Ferrari, M.S. Vitiello, M. Polini, Photodetectors based on graphene, other two-dimensional materials and hybrid systems, Nat. Nanotechnol. 9 (2014) 780–793. doi:10.1038/nnano.2014.215.

[24] G. Konstantatos, M. Badioli, L. Gaudreau, J. Osmond, M. Bernechea, F.P.G. de Arquer, F. Gatti, F.H.L. Koppens, Hybrid graphene–quantum dot phototransistors with ultrahigh gain, Nat. Nanotechnol. 7 (2012) 363–368. doi:10.1038/nnano.2012.60.

[25] K.M.F. Shahil, A.A. Balandin, Graphene-multilayer graphene nanocomposites as highly efficient thermal interface materials, Nano Lett. (2012). doi:10.1021/nl203906r.

[26] S. Wang, W. Chen, Z.-Q. Yin, Y. Zhang, T. Zhang, H.-W. Li, F.-X. Xu, Z. Zhou, Y. Yang, D.-J. Huang, L.-J. Zhang, F.-Y. Li, D. Liu, Y.-G. Wang, G.-C. Guo, Z.-F. Han, Field test of wavelength-saving quantum key distribution network, Opt. Lett. 35 (2010) 2454. doi:10.1364/OL.35.002454.

[27] S. Cong, X. Liu, F. Guo, Membrane distillation using surface modified multi-layer porous ceramics, Int. J. Heat Mass Transf. (2019). doi:10.1016/j.ijheatmasstransfer.2018.10.011.

[28] F. Magesa, Y. Wu, Y. Tian, J.-M. Vianney, J. Buza, Q. He, Y. Tan, Graphene and graphene like 2D graphitic carbon nitride: Electrochemical detection of food colorants and toxic substances in environment, Trends Environ. Anal. Chem. 23 (2019) e00064. doi:10.1016/j.teac.2019.e00064.

[29] P. Cataldi, J.A. Heredia-Guerrero, S. Guzman-Puyol, L. Ceseracciu, L. La Notte, A. Reale, J. Ren, Y. Zhang, L. Liu, M. Miscuglio, P. Savi, S. Piazza, M. Duocastella, G. Perotto, A. Athanassiou, I.S. Bayer, Sustainable Electronics Based on Crop Plant Extracts and Graphene: A “Bioadvantaged” Approach, Adv. Sustain. Syst. 2 (2018) 1800069. doi:10.1002/adsu.201800069.

[30] F. Bonaccorso, A. Lombardo, T. Hasan, Z. Sun, L. Colombo, A.C. Ferrari, Production and processing of graphene and 2d crystals, Mater. Today. 15 (2012) 564–589. doi:10.1016/S1369-7021(13)70014-2.

[31] A.C. Ferrari, F. Bonaccorso, V. Fal’ko, K.S. Novoselov, S. Roche, P. Bøggild, S. Borini, F.H.L. Koppens, V. Palermo, N. Pugno, J.A. Garrido, R. Sordan, A. Bianco, L. Ballerini, M. Prato, E. Lidorikis, J. Kivioja,

C. Marinelli, T. Ryhänen, A. Morpurgo, J.N. Coleman, V. Nicolosi, L. Colombo, A. Fert, M. Garcia-Hernandez, A. Bachtold, G.F. Schneider, F. Guinea, C. Dekker, M. Barbone, Z. Sun, C. Galiotis, A.N. Grigorenko, G. Konstantatos, A. Kis, M. Katsnelson, L. Vandersypen, A. Loiseau, V. Morandi, D. Neumaier, E. Treossi, V. Pellegrini, M. Polini, A. Tredicucci, G.M. Williams, B. Hee Hong, J.H. Ahn, J. Min Kim, H. Zirath, B.J. Van Wees, H. Van Der Zant, L. Occhipinti, A. Di Matteo, I.A. Kinloch, T. Seyller, E. Quesnel, X. Feng, K. Teo, N. Rupesinghe, P. Hakonen, S.R.T. Neil, Q. Tannock, T. Löfwander, J. Kinaret, Science and technology roadmap for graphene, related two-dimensional crystals, and hybrid systems, Nanoscale. (2015). doi:10.1039/c4nr01600a.

[32] M. Frappa, A.E.D.R. Castillo, F. Macedonio, G. Di Luca, E. Drioli, A. Gugliuzza, Exfoliated Bi2Te3-enabled membranes for new concept water desalination: Freshwater production meets new routes, Water Res. 203 (2021) 117503. doi:10.1016/j.watres.2021.117503.

[33] A. Agresti, S. Pescetelli, B. Taheri, A.E. Del Rio Castillo, L. Cinà, F. Bonaccorso, A. Di Carlo, Graphene-Perovskite Solar Cells Exceed 18 % Efficiency: A Stability Study, ChemSusChem. 9 (2016) 2609–2619. doi:10.1002/cssc.201600942.

[34] X. Gu, Y. Zhao, K. Sun, C.L.Z. Vieira, Z. Jia, C. Cui, Z. Wang, A. Walsh, S. Huang, Method of ultrasound-assisted liquid-phase exfoliation to prepare graphene, Ultrason. Sonochem. 58 (2019) 104630. doi:10.1016/j.ultsonch.2019.104630.

[35] X. Li, X. Wang, L. Zhang, S. Lee, H. Dai, Chemically Derived, Ultrasmooth Graphene Nanoribbon Semiconductors, Science (80-.). 319 (2008) 1229–1232. doi:10.1126/science.1150878.

[36] B. Fu, J. Sun, G. Wang, C. Shang, Y. Ma, J. Ma, L. Xu, V. Scardaci, Solution-processed two-dimensional materials for ultrafast fiber lasers (invited), Nanophotonics. 9 (2020) 2169–2189. doi:10.1515/nanoph-2019-0558.

[37] A. V. Tyurnina, I. Tzanakis, J. Morton, J. Mi, K. Porfyrakis, B.M. Maciejewska, N. Grobert, D.G. Eskin, Ultrasonic exfoliation of graphene in water: A key parameter study, Carbon N. Y. 168 (2020) 737–747. doi:10.1016/j.carbon.2020.06.029.

[38] A. Stolle, T. Szuppa, S.E.S. Leonhardt, B. Ondruschka, Ball milling in organic synthesis: solutions and challenges, Chem. Soc. Rev. 40 (2011) 2317. doi:10.1039/c0cs00195c.

[39] J. Hu, J. Hou, S. Huang, L. Zong, X. Li, Z. Zhang, Y. Duan, J. Zhang, One-pot preparation of zwitterionic graphene nanosheets with exceptional redispersibility and its application in pickering emulsions, Carbon N. Y. (2020). doi:10.1016/j.carbon.2019.10.063.

[40] P. Khadka, J. Ro, H. Kim, I. Kim, J.T. Kim, H. Kim, J.M. Cho, G. Yun, J. Lee, Pharmaceutical particle technologies: An approach to improve drug solubility, dissolution and bioavailability, Asian J. Pharm. Sci. 9 (2014) 304–316. doi:10.1016/j.ajps.2014.05.005.

[41] D. Sumanth Kumar, B. Jai Kumar, H.M. Mahesh, Quantum Nanostructures (QDs): An Overview, in: Synth. Inorg. Nanomater., Elsevier, 2018: pp. 59–88. doi:10.1016/B978-0-08-101975-7.00003-8.

[42] S. Lund, J. Kauppila, S. Sirkiä, J. Palosaari, O. Eklund, R.-M. Latonen, J.-H. Smått, J. Peltonen, T. Lindfors, Fast high-shear exfoliation of natural flake graphite with temperature control and high yield, Carbon N. Y. 174 (2021) 123–131. doi:10.1016/j.carbon.2020.11.094.

[43] K.R. Paton, E. Varrla, C. Backes, R.J. Smith, U. Khan, A. O'Neill, C. Boland, M. Lotya, O.M. Istrate, P. King, T. Higgins, S. Barwich, P. May, P. Puczkarski, I. Ahmed, M. Moebius, H. Pettersson, E. Long, J. Coelho, S.E. O'Brien, E.K. McGuire, B.M. Sanchez, G.S. Duesberg, N. McEvoy, T.J. Pennycook, C. Downing, A. Crossley, V. Nicolosi, J.N. Coleman, Scalable production of large quantities of defect-free few-layer graphene by shear exfoliation in liquids, Nat. Mater. 13 (2014) 624–630.

doi:10.1038/nmat3944.

[44] E. Varrla, K.R. Paton, C. Backes, A. Harvey, R.J. Smith, J. McCauley, J.N. Coleman, Turbulence-assisted shear exfoliation of graphene using household detergent and a kitchen blender, Nanoscale. 6 (2014) 11810–11819. doi:10.1039/C4NR03560G.

[45] A.E. Niaraki Asli, J. Guo, P.L. Lai, R. Montazami, N.N. Hashemi, High-Yield Production of Aqueous Graphene for Electrohydrodynamic Drop-on-Demand Printing of Biocompatible Conductive Patterns, Biosensors. 10 (2020) 6. doi:10.3390/bios10010006.

[46] P.G. Karagiannidis, S.A. Hodge, L. Lombardi, F. Tomarchio, N. Decorde, S. Milana, I. Goykhman, Y. Su, S. V. Mesite, D.N. Johnstone, R.K. Leary, P.A. Midgley, N.M. Pugno, F. Torrisi, A.C. Ferrari, Microfluidization of Graphite and Formulation of Graphene-Based Conductive Inks, ACS Nano. 11 (2017) 2742–2755. doi:10.1021/acsnano.6b07735.

[47] Y. Zhang, Y.L. Ng, K.-L. Goh, Y. Chow, S. Wang, V. Zivkovic, Fluidization of fungal pellets in a 3D-printed micro-fluidized bed, Chem. Eng. Sci. 236 (2021) 116466. doi:10.1016/j.ces.2021.116466.

[48] H.M. Yurdacan, M. Murat Sari, Functional green-based nanomaterials towards sustainable carbon capture and sequestration, in: Sustain. Mater. Transitional Altern. Energy, Elsevier, 2021: pp. 125–177. doi:10.1016/B978-0-12-824379-4.00004-5.

[49] V. Zivkovic, M.N. Kashani, M.J. Biggs, Experimental and theoretical study of a micro-fluidized bed, in: 2013: pp. 93–96. doi:10.1063/1.4811875.

[50] Y.-F. Maa, C.C. Hsu, Performance of Sonication and Microfluidization for Liquid–Liquid Emulsification, Pharm. Dev. Technol. 4 (1999) 233–240. doi:10.1081/PDT-100101357.

[51] S.H. Osong, S. Norgren, P. Engstrand, Processing of wood-based microfibrillated cellulose and nanofibrillated cellulose, and applications relating to papermaking: a review, Cellulose. 23 (2016) 93–123. doi:10.1007/s10570-015-0798-5.

[52] R.T. Alhat Babita, Niosomal drug delivery system- promising drug carriers, Int. Res. J. Invent. Pharm. Sci. 1 (2013) 19–26.

[53] J. Zhu, J. Hou, A. Uliana, Y. Zhang, M. Tian, B. Van Der Bruggen, The rapid emergence of two-dimensional nanomaterials for high-performance separation membranes, J. Mater. Chem. A. 6 (2018) 3773–3792. doi:10.1039/c7ta10814a.

[54] N. Saidin, D.I.M. Zen, B.A. Hamida, S. Khan, H. Ahmad, K. Dimyati, S.W. Harun, A Q -switched thulium-doped fiber laser with a graphene thin film based saturable absorber, Laser Phys. 23 (2013) 115102. doi:10.1088/1054-660X/23/11/115102.

[55] A. Garciadiego, T. Luo, A.W. Dowling, Molecular design targets and optimization of low-temperature thermal desalination systems, Desalination. 504 (2021). doi:10.1016/j.desal.2021.114941.

[56] F. Liu, Mechanical exfoliation of large area 2D materials from vdW crystals, Prog. Surf. Sci. 96 (2021) 100626. doi:10.1016/j.progsurf.2021.100626.

[57] A.E. Del Río Castillo, C.D. Reyes-Vazquez, L.E. Rojas-Martinez, S.B. Thorat, M. Serri, A.L. Martinez-Hernandez, C. Velasco-Santos, V. Pellegrini, F. Bonaccorso, Single-step exfoliation and functionalization of few-layers black phosphorus and its application for polymer composites, FlatChem. (2019). doi:10.1016/j.flatc.2019.100131.

[58] A.P. Kauling, A.T. Seefeldt, D.P. Pisoni, R.C. Pradeep, R. Bentini, R.V.B. Oliveira, K.S. Novoselov, A.H. Castro Neto, The Worldwide Graphene Flake Production, Adv. Mater. (2018).

doi:10.1002/adma.201803784.

[59] M. Chhowalla, H.S. Shin, G. Eda, L.J. Li, K.P. Loh, H. Zhang, The chemistry of two-dimensional layered transition metal dichalcogenide nanosheets, Nat. Chem. (2013). doi:10.1038/nchem.1589.

[60] G.W. Murphy, Desalination by Photoelectrodialysis. II, J. Electrochem. Soc. 128 (1981) 1819–1821. doi:10.1149/1.2127739.

[61] Y.-H. Peng, A.A. Kashale, Y. Lai, F.-C. Hsu, I.-W.P. Chen, Exfoliation of 2D materials by saponin in water: Aerogel adsorption / photodegradation organic dye, Chemosphere. 274 (2021) 129795. doi:10.1016/j.chemosphere.2021.129795.

[62] S.W. Cranford, D.B. Brommer, M.J. Buehler, Extended graphynes: Simple scaling laws for stiffness, strength and fracture, Nanoscale. (2012). doi:10.1039/c2nr31644g.

[63] H.H. Huang, R.K. Joshi, K.K.H. De Silva, R. Badam, M. Yoshimura, Fabrication of reduced graphene oxide membranes for water desalination, J. Memb. Sci. (2019). doi:10.1016/j.memsci.2018.10.085.

[64] L. Stobinski, B. Lesiak, A. Malolepszy, M. Mazurkiewicz, B. Mierzwa, J. Zemek, P. Jiricek, I. Bieloshapka, Graphene oxide and reduced graphene oxide studied by the XRD, TEM and electron spectroscopy methods, J. Electron Spectros. Relat. Phenomena. 195 (2014) 145–154. doi:10.1016/j.elspec.2014.07.003.

[65] S. Yuan, Y. Li, Y. Xia, Y. Kang, J. Yang, M.H. Uddin, H. Liu, C. Selomulya, X. Zhang, Minimizing Non-selective Nanowrinkles of Reduced Graphene Oxide Laminar Membranes for Enhanced NaCl Rejection, Environ. Sci. Technol. Lett. 7 (2020) 273–279. doi:10.1021/acs.estlett.0c00143.

[66] X. Huang, K.L. Marsh, B.T. McVerry, E.M.V. Hoek, R.B. Kaner, Low-Fouling Antibacterial Reverse Osmosis Membranes via Surface Grafting of Graphene Oxide, ACS Appl. Mater. Interfaces. 8 (2016) 14334–14338. doi:10.1021/acsami.6b05293.

[67] M. Essalhi, M. Khayet, Surface segregation of fluorinated modifying macromolecule for hydrophobic/hydrophilic membrane preparation and application in air gap and direct contact membrane distillation, J. Memb. Sci. 417–418 (2012) 163–173. doi:10.1016/j.memsci.2012.06.028.

[68] E. Jones, M. Qadir, M.T.H. van Vliet, V. Smakhtin, S. mu Kang, The state of desalination and brine production: A global outlook, Sci. Total Environ. (2019). doi:10.1016/j.scitotenv.2018.12.076.

[69] J.M. Luque-Alled, A. Abdel-Karim, M. Alberto, S. Leaper, M. Perez-Page, K. Huang, A. Vijayaraghavan, A.S. El-Kalliny, S.M. Holmes, P. Gorgojo, Polyethersulfone membranes: From ultrafiltration to nanofiltration via the incorporation of APTS functionalized-graphene oxide, Sep. Purif. Technol. (2020). doi:10.1016/j.seppur.2019.115836.

[70] E. Gontarek, F. Macedonio, F. Militano, L. Giorno, M. Lieder, A. Politano, E. Drioli, A. Gugliuzza, Adsorption-assisted transport of water vapour in super-hydrophobic membranes filled with multilayer graphene platelets, Nanoscale. 11 (2019) 11521–11529. doi:10.1039/C9NR02581B.

[71] M.M. Puppolo, J.R. Hughey, B. Weber, T. Dillon, D. Storey, E. Cerkez, S. Jansen-Varnum, Plasma modification of microporous polymer membranes for application in biomimetic dissolution studies, AAPS Open. 3 (2017) 9. doi:10.1186/s41120-017-0019-4.

[72] X. Wei, B. Zhao, X.-M. Li, Z. Wang, B.-Q. He, T. He, B. Jiang, CF4 plasma surface modification of asymmetric hydrophilic polyethersulfone membranes for direct contact membrane distillation, J. Memb. Sci. 407–408 (2012) 164–175. doi:10.1016/j.memsci.2012.03.031.

[73] H. Kim, K. Noh, C. Choi, J. Khamwannah, D. Villwock, S. Jin, Extreme Superomniphobicity of

Multiwalled 8 nm TiO 2 Nanotubes, Langmuir. 27 (2011) 10191–10196. doi:10.1021/la2014978.

[74] A. Politano, M. Cattelan, D.W. Boukhvalov, D. Campi, A. Cupolillo, S. Agnoli, N.G. Apostol, P. Lacovig, S. Lizzit, D. Farías, G. Chiarello, G. Granozzi, R. Larciprete, Unveiling the Mechanisms Leading to H2 Production Promoted by Water Decomposition on Epitaxial Graphene at Room Temperature, ACS Nano. (2016). doi:10.1021/acsnano.6b00554.

[75] S. Leaper, A. Abdel-Karim, B. Faki, J.M. Luque-Alled, M. Alberto, A. Vijayaraghavan, S.M. Holmes, G. Szekely, M.I. Badawy, N. Shokri, P. Gorgojo, Flux-enhanced PVDF mixed matrix membranes incorporating APTS-functionalized graphene oxide for membrane distillation, J. Memb. Sci. (2018). doi:10.1016/j.memsci.2018.03.013.

[76] J. Zahirifar, S.M.A. Moosavian, A. Hadi, P. Khadiv-Parsi, J. Karimi-Sabet, Fabrication of a novel octadecylamine functionalized graphene oxide/PVDF dual-layer flat sheet membrane for desalination via air gap membrane distillation, Desalination. (2018). doi:10.1016/j.desal.2017.11.028.

[77] W. Hirunpinyopas, E. Prestat, S.D. Worrall, S.J. Haigh, R.A.W. Dryfe, M.A. Bissett, Desalination and Nanofiltration through Functionalized Laminar MoS2 Membranes, ACS Nano. (2017). doi:10.1021/acsnano.7b05124.

[78] L. Sun, Y. Ying, H. Huang, Z. Song, Y. Mao, Z. Xu, X. Peng, Ultrafast molecule separation through layered WS2 nanosheet membranes, ACS Nano. (2014). doi:10.1021/nn501786m.

[79] J. Zuo, T.-S. Chung, Metal–Organic Framework-Functionalized Alumina Membranes for Vacuum Membrane Distillation, Water. 8 (2016) 586. doi:10.3390/w8120586.

[80] S. Qiu, M. Xue, G. Zhu, Metal-organic framework membranes: From synthesis to separation application, Chem. Soc. Rev. (2014). doi:10.1039/c4cs00159a.

[81] C.E. Ren, K.B. Hatzell, M. Alhabeb, Z. Ling, K.A. Mahmoud, Y. Gogotsi, Charge- and Size-Selective Ion Sieving Through Ti3C2Tx MXene Membranes, J. Phys. Chem. Lett. (2015). doi:10.1021/acs.jpclett.5b01895.

[82] Y. Liu, N. Wang, Z. Cao, J. Caro, Molecular sieving through interlayer galleries, J. Mater. Chem. A. (2014). doi:10.1039/c3ta13792a.

[83] W. gwi Kim, J.S. Lee, D.G. Bucknall, W.J. Koros, S. Nair, Nanoporous layered silicate AMH-3/cellulose acetate nanocomposite membranes for gas separations, J. Memb. Sci. (2013). doi:10.1016/j.memsci.2013.03.044.

[84] J. Fu, S. Das, G. Xing, T. Ben, V. Valtchev, S. Qiu, Fabrication of COF-MOF Composite Membranes and Their Highly Selective Separation of H2/CO2, J. Am. Chem. Soc. (2016). doi:10.1021/jacs.6b03348.

[85] J. Prasek, J. Drbohlavova, J. Chomoucka, J. Hubalek, O. Jasek, V. Adam, R. Kizek, Methods for carbon nanotubes synthesis - Review, J. Mater. Chem. (2011). doi:10.1039/c1jm12254a.

[86] Z. Xiao, R. Zheng, Y. Liu, H. He, X. Yuan, Y. Ji, D. Li, H. Yin, Y. Zhang, X.M. Li, T. He, Slippery for scaling resistance in membrane distillation: A novel porous micropillared superhydrophobic surface, Water Res. (2019). doi:10.1016/j.watres.2019.01.036.

[87] L. Vogelaar, J.N. Barsema, C.J.M. van Rijn, W. Nijdam, M. Wessling, Phase Separation Micromolding—PSμM, Adv. Mater. 15 (2003) 1385–1389. doi:10.1002/adma.200304949.

[88] Y. Li, N. Koshizaki, W. Cai, Periodic one-dimensional nanostructured arrays based on colloidal templates, applications, and devices, Coord. Chem. Rev. 255 (2011) 357–373.

doi:10.1016/j.ccr.2010.09.015.

[89] E. Haladjova, S. Rangelov, C. Tsvetanov, P. Simon, Preparation of polymeric nanocapsules via nano-sized poly(methoxydiethyleneglycol methacrylate) colloidal templates, Polymer (Guildf). 55 (2014) 1621–1627. doi:10.1016/j.polymer.2014.02.026.

[90] Z.Q. Feng, F. Wu, L. Jin, T. Wang, W. Dong, J. Zheng, Graphene Nanofibrous Foam Designed as an Efficient Oil Absorbent, Ind. Eng. Chem. Res. 58 (2019) 3000–3008. doi:10.1021/acs.iecr.8b05646.

[91] Z. Zhen, Z. Li, X. Zhao, Y. Zhong, L. Zhang, Q. Chen, T. Yang, H. Zhu, Formation of Uniform Water Microdroplets on Wrinkled Graphene for Ultrafast Humidity Sensing, Small. (2018). doi:10.1002/smll.201703848.

[92] S. Wang, L. Yang, G. He, B. Shi, Y. Li, H. Wu, R. Zhang, S. Nunes, Z. Jiang, Two-dimensional nanochannel membranes for molecular and ionic separations, Chem. Soc. Rev. 49 (2020) 1071–1089. doi:10.1039/C9CS00751B.

[93] W. Ye, H. Liu, F. Lin, J. Lin, S. Zhao, S. Yang, J. Hou, S. Zhou, B. Van Der Bruggen, High-flux nanofiltration membranes tailored by bio-inspired co-deposition of hydrophilic g-C3N4 nanosheets for enhanced selectivity towards organics and salts, Environ. Sci. Nano. 6 (2019) 2958–2967. doi:10.1039/c9en00692c.

[94] F. Kotoka, I. Merino-Garcia, S. Velizarov, Surface modifications of anion exchange membranes for an improved reverse electrodialysis process performance: A review, Membranes (Basel). 10 (2020) 1–22. doi:10.3390/membranes10080160.

[95] M.S. Rahaman, H. Thérien-Aubin, M. Ben-Sasson, C.K. Ober, M. Nielsen, M. Elimelech, Control of biofouling on reverse osmosis polyamide membranes modified with biocidal nanoparticles and antifouling polymer brushes, J. Mater. Chem. B. 2 (2014) 1724–1732. doi:10.1039/c3tb21681k.

[96] W.S. Hung, C.H. Tsou, M. De Guzman, Q.F. An, Y.L. Liu, Y.M. Zhang, C.C. Hu, K.R. Lee, J.Y. Lai, Cross-linking with diamine monomers to prepare composite graphene oxide-framework membranes with varying d-spacing, Chem. Mater. (2014). doi:10.1021/cm5007873.

[97] A. Gugliuzza, M. Perrotta, E. Drioli, Controlled Bulk Properties of Composite Polymeric Solutions for Extensive Structural Order of Honeycomb Polysulfone Membranes, Membranes (Basel). 6 (2016) 27. doi:10.3390/membranes6020027.

[98] M.L. Perrotta, G. Saielli, G. Casella, F. Macedonio, L. Giorno, E. Drioli, A. Gugliuzza, An ultrathin suspended hydrophobic porous membrane for high-efficiency water desalination, Appl. Mater. Today. (2017). doi:10.1016/j.apmt.2017.04.009.

[99] https://www.gvs.com/it/, (n.d.).

[100] https://www.membrane.it/, (n.d.).

[101] https://www.lenntech.com/, (n.d.).

[102] H.P. Cong, J.F. Chen, S.H. Yu, Graphene-based macroscopic assemblies and architectures: An emerging material system, Chem. Soc. Rev. (2014). doi:10.1039/c4cs00181h.

[103] M.L. Perrotta, F. Macedonio, L. Giorno, W. Jin, E. Drioli, A. Gugliuzza, E. Tocci, Molecular insights on NaCl crystals formation approaching the PVDF membranes functionalized with graphene, Phys. Chem. Chem. Phys. (2020). doi:10.1039/d0cp00928h.

[104] T.C. Huang, Y.C. Liu, G.S. Lin, C.H. Lin, W.R. Liu, K.L. Tung, Fabrication of pebax-1657-based mixed-

matrix membranes incorporating N-doped few-layer graphene for carbon dioxide capture enhancement, J. Memb. Sci. (2020). doi:10.1016/j.memsci.2020.117946.

[105] K.S. Novoselov, A.K. Geim, S. V. Morozov, D. Jiang, Y. Zhang, S. V. Dubonos, I. V. Grigorieva, A.A. Firsov, Electric field in atomically thin carbon films, Science (80-.). (2004). doi:10.1126/science.1102896.

[106] J.M. Dawlaty, S. Shivaraman, M. Chandrashekhar, F. Rana, M.G. Spencer, Measurement of ultrafast carrier dynamics in epitaxial graphene, Appl. Phys. Lett. (2008). doi:10.1063/1.2837539.

[107] K.S. Kim, Y. Zhao, H. Jang, S.Y. Lee, J.M. Kim, K.S. Kim, J.H. Ahn, P. Kim, J.Y. Choi, B.H. Hong, Large-scale pattern growth of graphene films for stretchable transparent electrodes, Nature. (2009). doi:10.1038/nature07719.

[108] X. Li, W. Cai, J. An, S. Kim, J. Nah, D. Yang, R. Piner, A. Velamakanni, I. Jung, E. Tutuc, S.K. Banerjee, L. Colombo, R.S. Ruoff, Large-area synthesis of high-quality and uniform graphene films on copper foils, Science (80-.). (2009). doi:10.1126/science.1171245.

[109] F. Bonaccorso, A. Bartolotta, J.N. Coleman, C. Backes, 2D-Crystal-Based Functional Inks, Adv. Mater. (2016). doi:10.1002/adma.201506410.

[110] S.M. Notley, Highly concentrated aqueous suspensions of graphene through ultrasonic exfoliation with continuous surfactant addition, Langmuir. (2012). doi:10.1021/la302750e.

[111] D.A. Dikin, S. Stankovich, E.J. Zimney, R.D. Piner, G.H.B. Dommett, G. Evmenenko, S.T. Nguyen, R.S. Ruoff, Preparation and characterization of graphene oxide paper, Nature. (2007). doi:10.1038/nature06016.

[112] L. Qiu, X. Zhang, W. Yang, Y. Wang, G.P. Simon, D. Li, Controllable corrugation of chemically converted graphene sheets in water and potential application for nanofiltration, Chem. Commun. (2011). doi:10.1039/c1cc10720h.

[113] Y.G. Kim, C. Kim, J. Lee, H.W. Lee, K.H. Kwon, Direct transfer of graphene by control of polydimethylsiloxane surface energy, Thin Solid Films. (2020). doi:10.1016/j.tsf.2020.137847.

[114] G. Grasso, F. Galiano, M.J. Yoo, R. Mancuso, H.B. Park, B. Gabriele, A. Figoli, E. Drioli, Development of graphene-PVDF composite membranes for membrane distillation, J. Memb. Sci. (2020). doi:10.1016/j.memsci.2020.118017.

[115] M. Bhadra, S. Roy, S. Mitra, Desalination across a graphene oxide membrane via direct contact membrane distillation, Desalination. 378 (2016) 37–43. doi:10.1016/j.desal.2015.09.026.

[116] A. Jafari, M.R.S. Kebria, A. Rahimpour, G. Bakeri, Graphene quantum dots modified polyvinylidenefluride (PVDF) nanofibrous membranes with enhanced performance for air Gap membrane distillation, Chem. Eng. Process. - Process Intensif. (2018). doi:10.1016/j.cep.2018.03.010.

[117] A. Abdel-Karim, J.M. Luque-Alled, S. Leaper, M. Alberto, X. Fan, A. Vijayaraghavan, T.A. Gad-Allah, A.S. El-Kalliny, G. Szekely, S.I.A. Ahmed, S.M. Holmes, P. Gorgojo, PVDF membranes containing reduced graphene oxide: Effect of degree of reduction on membrane distillation performance, Desalination. (2019). doi:10.1016/j.desal.2018.11.014.

[118] H. Li, W. Shi, X. Zeng, S. Huang, H. Zhang, X. Qin, Improved desalination properties of hydrophobic GO-incorporated PVDF electrospun nanofibrous composites for vacuum membrane distillation, Sep. Purif. Technol. (2020). doi:10.1016/j.seppur.2019.115889.

[119] H. Qiu, Y. Peng, L. Ge, B. Villacorta Hernandez, Z. Zhu, Pore channel surface modification for enhancing anti-fouling membrane distillation, Appl. Surf. Sci. (2018). doi:10.1016/j.apsusc.2018.03.004.

[120] S. Abdikheibari, W. Lei, L.F. Dumée, N. Milne, K. Baskaran, Thin film nanocomposite nanofiltration membranes from amine functionalized-boron nitride/polypiperazine amide with enhanced flux and fouling resistance, J. Mater. Chem. A. (2018). doi:10.1039/c8ta03446j.

[121] S. Abdikheibari, W. Lei, L.F. Dumée, A.J. Barlow, K. Baskaran, Novel thin film nanocomposite membranes decorated with few-layered boron nitride nanosheets for simultaneously enhanced water flux and organic fouling resistance, Appl. Surf. Sci. (2019). doi:10.1016/j.apsusc.2019.05.217.

[122] S. Yang, K. Zhang, Few-layers MoS2 nanosheets modified thin film composite nanofiltration membranes with improved separation performance, J. Memb. Sci. (2020). doi:10.1016/j.memsci.2019.117526.

[123] S. Yang, Q. Jiang, K. Zhang, Few-layers 2D O–MoS2 TFN nanofiltration membranes for future desalination, J. Memb. Sci. (2020). doi:10.1016/j.memsci.2020.118052.

[124] H. Wu, B. Tang, P. Wu, Optimizing polyamide thin film composite membrane covalently bonded with modified mesoporous silica nanoparticles, J. Memb. Sci. (2013). doi:10.1016/j.memsci.2012.10.053.

[125] Y.A.J. Al-Hamadani, B.-M. Jun, M. Yoon, N. Taheri-Qazvini, S.A. Snyder, M. Jang, J. Heo, Y. Yoon, Applications of MXene-based membranes in water purification: A review, Chemosphere. (2020). doi:10.1016/j.chemosphere.2020.126821.

[126] Y.Z. Tan, H. Wang, L. Han, M.B. Tanis-Kanbur, M.V. Pranav, J.W. Chew, Photothermal-enhanced and fouling-resistant membrane for solar-assisted membrane distillation, J. Memb. Sci. 565 (2018) 254–265. doi:10.1016/j.memsci.2018.08.032.

[127] P. Chaudhary, P.P. Ingole, In-Situ solid-state synthesis of 2D/2D interface between Ni/NiO hexagonal nanosheets supported on g-C3N4 for enhanced photo-electrochemical water splitting, Int. J. Hydrogen Energy. (2020). doi:10.1016/j.ijhydene.2020.04.011.

[128] T. Liu, H. Zhou, N. Graham, W. Yu, K. Sun, 2D kaolin ultrafiltration membrane with ultrahigh flux for water purification, Water Res. (2019). doi:10.1016/j.watres.2019.03.050.

[129] D. Haldar, P. Duarah, M.K. Purkait, MOFs for the treatment of arsenic, fluoride and iron contaminated drinking water: A review, Chemosphere. (2020). doi:10.1016/j.chemosphere.2020.126388.

[130] C. Wang, X. Liu, J.P. Chen, K. Li, Superior removal of arsenic from water with zirconium metal-organic framework UiO-66, Sci. Rep. (2015). doi:10.1038/srep16613.

[131] D. Voiry, A. Mohite, M. Chhowalla, Phase engineering of transition metal dichalcogenides, Chem. Soc. Rev. (2015). doi:10.1039/c5cs00151j.

[132] P. Miró, M. Audiffred, T. Heine, An atlas of two-dimensional materials, Chem. Soc. Rev. (2014). doi:10.1039/c4cs00102h.

[133] F. Macedonio, A. Politano, E. Drioli, A. Gugliuzza, Bi 2 Se 3 -assisted membrane crystallization, Mater. Horizons. 5 (2018) 912–919. doi:10.1039/C8MH00612A.

Chapter 4:

Dry-wet phase inversion as porous membrane manufacturing procedure and membrane characterization methods.

4.1 Membrane preparation

As introduced briefly in Chapter 2, the membranes preparation might be done by different techniques depending on the final process. For membrane distillation/crystallization processes the using of hydrophobic porous membrane are necessary. The simplest method to produce membrane with the properly proprieties is the traditional phase inversion technique [1]. In the specific non-solvent phase inversion has been choose for the membrane preparation in this work. The 2D materials (such as graphene and bismuth telluride) were choice for the enhancement of the performance in MD/MCr. The 2D flakes have been incorporated in PVDF-based membranes during the membrane preparation. Before that, the 2D flakes have been exfoliated via the innovative Wet jet mill technique at high pressure by the colleagues from BeDImensional and dispersed in solvent (NMP).

Starting from the exfoliated solution, the membranes have been prepared by dry-wet phase inversion according to the procedure detailed in refs. Briefly, a fluorinated polymer (PVDF) in powder (PVDF powder (Solef 6020, Solvay Specialty Polymers S.p.A) has been slowly added at the exfoliated solution under mechanical stirring and controlled thermal conditions to prevent accumulations of polymer.

The 2D flakes concentration in the solvent establishes the final concentration of fillers in the membrane.

When all the polymer are well dissolved in solvent, the solutions have been casted on a glass with a casting knife and immersed in a coagulation bath in order to promote solid-liquid demixing and dried in oven with the same temperature used during the preparation. The membrane thickness depends on the thickness of the casting knife (Elcometer Instruments Inc. Manchester, England) and the time of immersion in the coagulation bath.

In this way membrane with Graphene and/or Bismuth Telluride with two different concentrations are prepared. In order to study the effect and the quality of 2D materials exfoliated via wet jet mill as filler, pristine PVDF membrane has been prepared with the same procedure.

In order to evaluate the quality of the flakes, they have been studied with TEM, Raman and AFM analysis establishing the thickness and the lateral size of 2D flakes exfoliated via Wet jet mill. The composite PVDF membranes have been characterized in order to analyse their physico-chemical properties in terms of morphology, and to measure their porosity, pore size distribution, mechanical proprieties, hydrophobic character and thickness. Moreover, the prepared membranes have been tested in Membrane distillation and Membrane Crystallization analysing the effective enhancement of the performance due to the functionalization.

The preparation of a polymeric membrane by phase inversion can be explained through the schematic phase diagram of a ternary system. Ternary systems for the preparation of polymer membranes comprise a mixture of three components: a polymer, a solvent and a non-solvent. This ternary system is completely miscible over a certain composition range but shows a miscibility gap over another composition range, which shows an isothermal phase diagram of the ternary components. This, as shown in Fig. 1, includes two main regions in the diagram, the homogeneous phase region, or a phase region, (which is outside the binodal line) and the two-phase liquid-liquid region (which is found within the binodal line) [2]. The pure components are represented at the corners of the triangle, while the boundary lines between any two corners of the triangle represent mixtures of two components, and any point within the triangle diagram represents a mixture of all three components. The main elements of the ternary phase diagram are binodal and spinodal curves, a critical point, connecting lines and a glassy region shown in Fig. 4.1. If a non-solvent (such as water) is added to a homogeneous solution consisting of a binary mixture of polymer and solvent, a ternary system will be created whose composition of the final solution will be calculated according to the ternary diagram. Thus, if the solvent is removed from the polymer solution (this occurs by precipitation by immersion), the composition of the mixture of the casting solution will change. The composition of the yield system will reach the demix gap, and then two produced phases will begin to form a polymer rich phase at the upper limit of the demix gap and a low polymer phase at the lower limit of the demix gap. The concentration of the polymer in the polymer-rich phase will be sufficiently high to be considered solid; this occurs at a certain composition of the ternary mixtures. At this point the membrane structure is more or less formed. A further exchange of solvent and non-solvent will lead to the final composition of the membrane, the porosity of which is determined by the concentration of the polymer in the mixture of the solid phase and the liquid phase rich in solvent. The region between the binodal line and the spinodal line is a metastable region. There are believed to be two types of typical mechanisms in

the membrane formation process by the immersion precipitation method, which results in two different types of membrane morphology. One is instant liquid-liquid demixing, which means that the membrane forms immediately upon immersion in the non-solvent bath. The other is the delayed start of liquid-liquid demixing, in which case it takes some time for the membrane to form. The composition path may change as shown in line 3 depending on the time elapsed after the dive. Under conditions of rapid demixing, membranes with a very thin top layer and a substrate with many macro voids can be expected. This is due to the rapidity with which the polymeric macromolecules will tend to reorganize during demixing. Conversely, for membranes obtained by delayed demixing, the macromolecules will tend to rearrange themselves in a more orderly way, creating a very dense and thick top layer, and the substrate will have an open or closed cell structure.

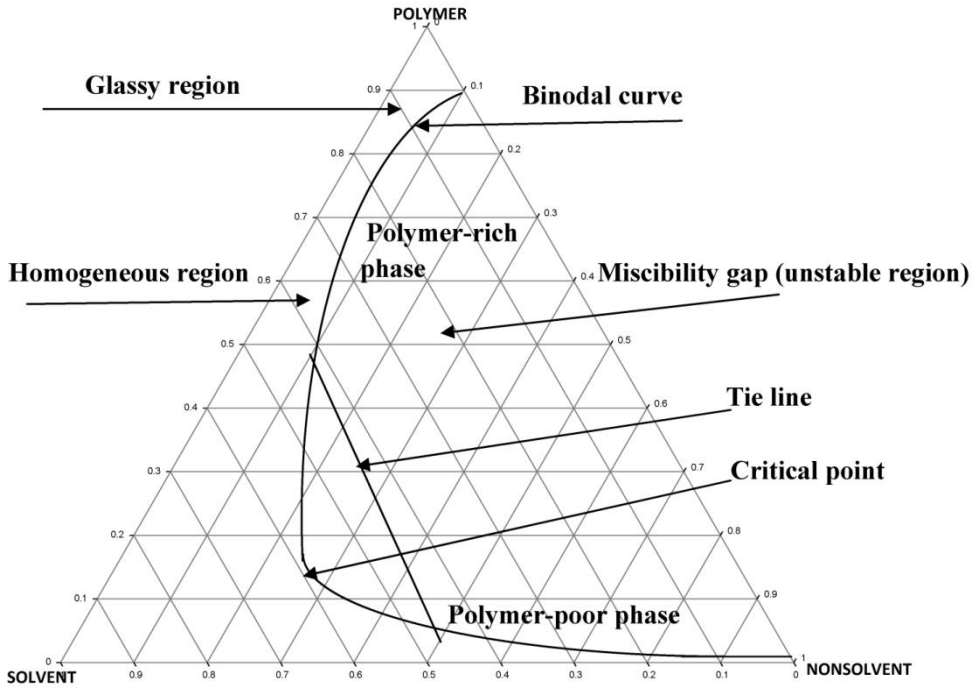

Figure 4.1 *Typical schematic phase diagram of a ternary system.*

The main important step for membrane formation from such ternary systems is always to prepare a homogeneous (thermodynamically stable) polymer solution. This will often represent a point on the polymer / solvent axis. However, it is also possible to add non-solvent to a binary mixture such that all components of the polymer solution are still miscible (homogeneous region) before the binodal curve is reached. In a ternary system consisting of a polymer / solvent / non-solvent, the types of demixing that can occur are as follows:

Liquid-liquid phase separation

The addition of a certain amount of non-solvent can induce the demixing process when the polymer solution becomes thermodynamically unstable. When the binodal is reached, liquid-liquid demixing will take place. The free enthalpy of the polymer solution decreases by separating into two equilibrium liquid phases. De-mixing can occur in two ways: (1) nucleation and growth of second-phase droplets and (2) instant spinodal de-mixing. The composition area surrounds the spinodal demixing gap where phase separation (inversion) occurs by nucleation and growth.

Crystallization or gelation

Many polymers, in fact, are partially crystalline. Crystallization can occur if the solution temperature is below the melting point of the polymer. Gelling is a phenomenon of considerable importance during the preparation of the membrane to form the skin layer (upper layer). When gelation occurs, a dilute or more viscous polymer solution transforms into a system of infinite viscosity, that is, a gel. At the start of demixing, the free enthalpy of the solution is reduced by the polymer molecules to form ordered structures. On the one hand, single crystals can be formed at low polymer concentrations. On the other hand, at higher polymer concentrations, very small crystalline regions could function as a physical crosslinking between polymer molecules and the result is a thermoreversible gel.

4.2 Membrane Characterization

4.2.1 TEM (Transmission electron microscopy)

Transmission electron microscopy (TEM) is an imaging technique in which an electron beam is focused on a sample causing an enlarged version to appear on a fluorescent screen or a layer of photographic film placed beyond the sample. It is based on the Louis-Victor de Broglie equivalence principle to convert an electron beam into an electron wave, whose wavelength is enormously shorter than that of a light wave, in order to examine much finer details than those visible optically, i.e. at much higher magnifications (a normal optical microscope only reaches 1000 magnifications). As shown in fig. 4.2, TEM essentially consists of a high vacuum column in which are housed: a source of electrons (usually a tungsten filament heated to a very high temperature); a series of magnetic lenses that focus the electron beam making it fall on the sample (an ultra-thin preparation housed on a conductive metal grid); a detection system that transforms into images

the phenomena of deflection undergone by the electrons as they pass through the sample. Samples must always be ultra-thin (thicknesses less than 1 μm) due to the high absorption that electrons undergo when they pass through any material and are prepared either as foils, if of metallic consistency, or as thin wedge edges of a larger grain etched by acids or an ion beam, if solid non-conductive, or as deposits on the grid hardened by liquid nitrogen, if organic substances.

The TEM examination highlights the single elementary cells, their repetition on a plane, the presence of extensive structural defects (growth steps and spirals, dislocations and faults, etc.) and also, in particular light conditions, point defects.

Many physical techniques rely on the interaction between high-energy electrons and atoms in a solid, resulting in many types of possible interactions. In TEM a thin sample is illuminated with electrons, the primary electrons. Any electron microscope, of any type, must have a source of high-energy primary electrons: an electron gun. Figure 4.2 shows the scheme of a TEM.

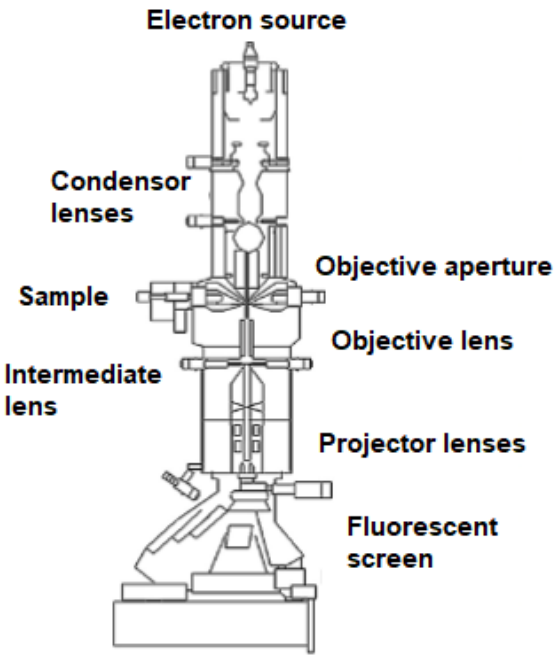

Figure 4.2 *Schematic diagram of transmission electron microscope.*

The gun's function is to produce a thin beam of precisely controlled energy (i.e. velocity) electrons all from a small source region. A thermionic electron gun works as follows: Select the acceleration potential (kV). Increase the current flowing through the filament until it reaches the knee of the emission curve (saturation), obtaining the best compromise between the beam current emitted (as high as possible) and the useful life of the filament (as long as possible). The filament current controls the temperature of the filament and thus the number of electrons emitted or "beam current". We generally want a large number of electrons emitted from a small region of the

filament. After an inner shell excitation, an atom has energy higher than its ground state. He can relax and lose some of this energy in several ways. The bias potential controls the size of the electron-emitting region of the filament and thus affects both the size of the source and the current of the beam. If the polarization is too high, no region of the filament will emit and the beam is said to be squashed. The main reason for altering the bias is to change the brightness of the beam. Diffraction at an aperture limits the resolution of many optical systems. Use simulation to show that the size of the central illumination disc varies inversely with the size of the aperture (W). TEM allows to observe the intimate structure of materials at magnifications up to 50 million times, with a spatial resolution of 0.05 ÷ 0.1 nm.

Theoretically, the maximum resolution, *d*, that one can obtain with a light microscope has been limited by the wavelength of the photons (λ) that are being used to probe the sample and the numerical aperture NA of the system.

$$d = \frac{\lambda}{2nsin\alpha} \tag{4.1}$$

where n is the index of refraction of the medium in which the lens is working and α is the maximum half-angle of the cone of light that can enter the lens (see numerical aperture). Like all matter, electrons have both wave and particle properties (as theorized by Louis-Victor de Broglie), and their wave-like properties mean that a beam of electrons can be focused and diffracted much like light can. The wavelength of electrons is related to their kinetic energy via the de Broglie equation, which says that the wavelength is inversely proportional to the momentum. Taking into account relativistic effects (as in a TEM an electron's velocity is a substantial fraction of the speed of light, c) the wavelength is

$$\lambda_e = \frac{h}{\sqrt{2m_0E(1+\frac{E}{2m_0c^2})}} \tag{4.2}$$

where, *h* is Planck's constant, m0 is the rest mass of an electron and E is the kinetic energy of the accelerated electron.

Transmission electron microscopy (TEM) analysis has been performed by drop-casting the 2D material dispersion onto ultrathin C-film on holey carbon 400 mesh Cu grids, from Ted Pella Inc (Redding, CA, USA). TEM images have been captured by a JEOL JEM-1011 transmission electron microscope (Peabody, MA, USA), operated at an acceleration voltage of 100 kV.

4.2.2 Raman Spectroscopy

The Raman effect concerns Anelastic Light Scattering. Scattering is a general expression to indicate a class of two-photon processes between electro-magnetic radiation and condensed matter. The scattering of light arises through the modulation of the dielectric constant of the system by internal excitations (in a molecular approach, the polarizability). The dielectric constant is sensitive to any change of the electronic state of the matter and this permits coupling with essentially all types of excitations: rotational and vibrational excitations for the molecules, phonons in solids, but also plasmons, excitons, magnons. Hereafter we shall deal with mainly with Raman scattering by molecular vibrational excitations and phonons. Raman has been able to observe the weak Raman Effect by using the most intense light source available at the time, the sun. He focused a large telescope on the sun and placed a green filter in the intense beams of sunlight. When he used a yellow filter to observe this beam of green light passing through a solution of chloroform, he could see a weak yellow light. The origin of the yellow light has been the Raman Effect. A small amount of the green light from the sun had inelastically scattered from the chloroform molecules and shifted its energy so that the photons fell within the yellow part of the spectrum. A photon with energy

$E_0 = hv_0$

collides with a molecule. *h* is known as the Planck constant. If the collision is perfectly elastic, the photon will be deflected but its frequency will remain unchanged (Rayleigh). If a fraction of the energy of the incident radiation is exchanged during the impact (inelastic), the molecule uses part of the energy (ΔE) acquired by the photon to make a vibrational transition and / or rotational.

• If the molecule gains the energy ΔE, the photon diffuse will have a frequency:

$v = v_0 - \Delta E/h$ (Stokes radiation)

• If the molecule loses the ΔE energy, the scattered photon will have a frequency:

$v = v_0 + \Delta E/h$ (anti-Stokes radiation)

For Raman spectroscopy, the as-prepared dispersions are diluted 1:30 in NMP and drop-cast onto a Si wafer (LDB Technologies Ltd.) covered with 300 nm thermally grown SiO2. Raman measurements are carried out by a Renishaw via spectrometer using a 50× objective (numerical aperture 0.75), a laser with a wavelength of 514.5 nm with an incident power of ~5 mW. A total of ca. 30 points per sample are measured to perform the statistical analysis.

4.2.3 XPS (X-ray photoelectron spectroscopy)

X-ray photoelectron spectroscopy (XPS) is a surface-sensitive quantitative spectroscopic technique based on the photoelectric effect that can identify the elements that exist within a material (elemental composition) or are covering its surface, as well as their chemical state, and the overall electronic structure and density of the electronic states in the material. XPS is a powerful measurement technique because it not only shows what elements are present, but also what other elements they are bonded to. The technique can be used in line profiling of the elemental composition across the surface, or in depth profiling when paired with ion-beam etching. It is often applied to study chemical processes in the materials in their as-received state or after cleavage, scraping, exposure to heat, reactive gasses or solutions, ultraviolet light, or during ion implantation.

XPS belongs to the family of photoemission spectroscopies in which electron population spectra are obtained by irradiating a material with a beam of X-rays. Chemical states are inferred from the measurement of the kinetic energy and the number of the ejected electrons. XPS requires high vacuum (residual gas pressure p ~ 10−6 Pa) or ultra-high vacuum (p < 10−7 Pa) conditions, although a current area of development is ambient-pressure XPS, in which samples are analysed at pressures of a few tens of millibar.

When laboratory X-ray sources are used, XPS easily detects all elements except hydrogen and helium. The detection limit is in the parts per thousand range, but parts per million (ppm) are achievable with long collection times and concentration at top surface.

XPS is routinely used to analyse inorganic compounds, metal alloys [1], semiconductors [2], polymers, elements, catalysts [3,4,5,6], glasses, ceramics, paints, papers, inks, woods, plant parts, make-up, teeth, bones, medical implants, bio-materials [7], coatings [8], viscous oils, glues, ion-modified materials [9] and many others. Somewhat less routinely XPS is used to analyse the hydrated forms of materials such as hydrogels and biological samples by freezing them in their hydrated state in an ultrapure environment, and allowing multilayers of ice to sublime away prior to analysis.

XPS involves the detection of photoelectrons emitted from a sample as a result of irradiation of the sample by single-energy X-ray photons. XPS or electron spectroscopy for chemical analysis (ESCA) has become a relatively simple and increasingly routine technique for the compositional and chemical state analysis of surfaces. The basic principle of XPS is the photoelectric effect discovered by Hertz in 1887 [7, 8] and extended to surface analysis by K. Siegbahn and his research

group at Uppsala University, Sweden, during the mid-1960s. Siegbahn won the Nobel Prize in Physics in 1981 for his work in XPS and coined the acronym ESCA [9]. Both XPS and ESCA are commonly used to describe this technique.

XPS is useful for quantitative analysis of surface composition and can detect all elements with the exception of hydrogen and helium through the detection of the binding energies of the photoelectrons. Small variations in binding energies of the photoelectron lines as well as Auger lines, satellite peaks, and multiple splitting can be used to identify chemical states. XPS is initiated by irradiating a sample with monoenergetic soft X-rays, most commonly Mg Kα (1253.6 eV with a line width ≈ 0.7 eV) or Al Kα (1486.6 eV with a line width ≈ 0.85 eV). In many modern instruments the Al Kα X-ray line is further narrowed (to ≈ 0.35 eV) using a monchrometer.

X-ray photoelectron spectroscopy analysis has been accomplished using a Kratos Axis UltraDLD spectrometer (Manchester, UK) on samples drop-cast onto gold-coated silicon wafers. The X-ray photoelectron spectroscopy (XPS) spectra have been acquired using a monochromatic Al Kα source operating at 20 mA and 15 kV.

4.2.4 XRD (X-ray Diffraction)

X-ray diffraction (XRD) is a method used for studying the structure, composition, and physical properties of materials by analysing their crystal structures. With XRD, it is also possible to identify crystalline materials.

XRD is commonly applied in materials science but it also benefits many fields of industry in product development and improvement of production processes of different materials.

X-ray diffraction (XRD) is used for determining the properties of the crystallographic structure (i.e. crystal structure) of crystalline materials. Crystal structure means the order of the particles (atoms, ions or molecules) in a crystalline matter, where they are arranged into regular arrays of repeating unit cells. Sodium chloride and diamond are examples of crystalline matter, but all solid materials have some kind of a crystal structure. The components of this structure are usually crystal planes that are atoms which have settled as planes on top of each other with certain distances. These distances can be measured with XRD. Diffraction phenomenon

XRD is based on a phenomenon called diffraction. In diffraction, a regular array of scatterers produces a regular array of spherical waves of radiation when the radiation hits them and is reflected from them. This is called elastic scattering. In almost all directions, the reflected waves cancel each other out, which are called destructive interference. However, in a few specific directions the waves add constructively and therefore amplify each other, which are called

constructive interference. These specific directions appear as bright spots called reflections on the formed diffraction pattern. This phenomenon can be represented with Bragg's law: $2d\sin\theta = n\lambda$, where d is the distance between diffracting (wave reflecting) planes or objects, θ is the angle of the reflected radiation, n is an integer representing the amount of scatterers, and λ is the wavelength of the radiation used. In conclusion, the diffraction patterns result from waves of electromagnetic radiation reflecting from a regular array of scatterers.

Diffraction can be applied to the atomic level of different materials, when X-rays are used as the electromagnetic radiation to produce the diffraction pattern. X-rays are a good tool in determining crystal structures because the wavelength (λ) of X-rays is often the same order of magnitude as the distance of the spaces (d) between the crystal planes in the material. In XRD, the X-rays scatter from the atoms in the crystal structure primarily because they interact with the electrons in the atoms. The diffraction pattern produced by the diffracted X-rays is different for every substance because of the unique order of the atoms or molecules in them. The intensities and scattering angles of the X-rays diffracted from the material are measured with an X-ray analyzer. The final result of the measurement is a diffractogram, which is a plot having the X-ray intensity on the y-axis and the angle between the incident and the diffracted X-ray beam on the x-axis. When the angles where the constructive interference happens and the reflections occur are measured and the wavelength of the used X-rays (λ) is known, the distances between the crystal planes or atoms in the material (d) can be calculated using the mathematical formula of Bragg's law.

Many kinds of information can be obtained from the diffractogram. Because every crystalline matter produces its own kind of diffraction pattern and thus diffractogram, different materials can be identified by comparing the obtained diffractogram with commonly used databases of diffractograms of different materials. It is also possible to determine the individual components and their relative amounts in a material which consists of several different phases or substances. The lattice parameters of particles in a crystalline structure can be determined with XRD, because it is possible to measure the dimensions, shapes and geometries of the particles in the material. Additionally, the crystallite size and strain can be measured with XRD, because the width of the bright spots in the diffraction pattern depends on the crystallite size of the matter and microstrain in the sample. Thus, information about the size and strain of the crystallites can be obtained from the broadening of the peaks in the diffractogram. Single crystals can also be investigated to determine the three-dimensional structure of their molecules with the help of single crystal

diffraction (SCD). This analysis requires a single crystal from the sample which can be produced by varying conditions like solvent or evaporation rate.

XRD measurements have been acquired with a PANalytical Empyrean using Cu K radiation. The samples for XRD have been prepared by depositing the samples onto Si/SiO2 substrates.

4.2.5 AFM (Atomic Force Microscopy)

AFM is an instrument that allows you to obtain very high resolution images of the surface of a sample, and whose operation is based on a microscopic probe placed near the sample under examination. The first AFM has been invented by Gerd Binnig, Calvin Quate and Christoph Gerber in 1986. This type of microscope gives the possibility to directly observe even single molecules with the great advantage of understanding how they behave, perform their functions, interact with other molecules and respond to external stimuli. Obviously, for this, the AFM must be able to work on very small scales, therefore we speak of micrometric and nanometric scales (from 10-6 to 10-9 meters approximately). The operating principle, unlike optical or electronic microscopes, does not use lenses to form the image, but uses a very thin tip located on the end of a flexible lever (cantilever), which scans the surface of the sample. During the scan, weak interaction forces between tip and sample are established known as van der Waals forces, which determine a deflection of the lever from which it is possible to trace the surface topography Furthermore, the AFM is a very versatile instrument, being able to work in air, in vacuum or in liquid allowing to obtain the topography of both hard samples such as crystals and metal alloys and soft samples such as polymers or biological materials. In addition to the tip already mentioned, the AFM consists of a piezoelectric scanner, a computer and an optical lever system, as shown in Figure 4.3. The optical lever consists of a laser and a photodiode which allows to detect lever deflections up to 0.01. The operating mode of an optical lever is as follows:

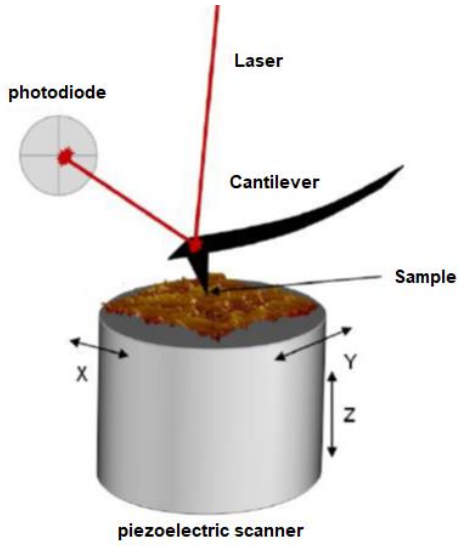

Figure 4.3 *Components of an AFM.*

The laser is reflected from the rear of the lever towards the photodiode which converts light energy into electrical energy and amplifies the incoming signal by means of a photomultiplier. The photodiode consists of two quadrants between which the difference in output current is measured. This difference is proportional to the deflection of the lever. In conditions of zero deflection, this difference is taken as a reference and set equal to zero.

Thanks to this system, the movements of the lever are amplified several times; for a lever of length l and a photodetector placed at a distance of 2L, the "gain of the optical lever" is equal to 2L/l. Using the piezoelectric scanner, the tip-sample distance is checked and the sample is moved under the tip to obtain an image of the surface.

The AFM is able to work in three different ways with reference to the interaction forces between tip and sample:

Contact mode

In this mode the lever is kept a few Å from the sample surface and the interatomic force between the latter and the tip will be of the repulsive type; tip and sample are in close contact so that the distance between them can be imagined as virtually incompressible. This mode is used in the case of slightly rough and hard samples.

No contact mode

In this mode the lever is held a few tens of Å from the surface, in the zone of attractive interactions, and is made to vibrate close to its resonant frequency with amplitude ranging from a few tens to hundreds of Å. Since the force is of an attractive type, the lever must be more rigid to

avoid any contact between the tip and the surface. This mode provides information on long range forces and is used for delicate samples such as polymers.

Tapping mode

Also referred to as intermittent contact, it is a resonant mode like No Contact, but the lever is vibrated at frequencies higher than the resonant frequency (~ 100 kHz) so that the tip makes intermittent contact with the surface. In this mode, the tip-sample interaction cyclically passes from repulsive to attractive. This mode allows to obtain high resolution topographic images of the sample without damaging it, overcoming problems related to friction, adhesion and electrostatic forces between tip and sample. The continuous lifting of the tip allows in fact not to drag material along the sample making it ideal for studying biological samples. Due to its characteristics, the tapping mode has been chosen in this thesis to acquire the images of the prepared membranes.

For atomic force microscopy analysis, the graphene dispersion is diluted 1:30 in NMP. 100 µL of the dilutions are drop-cast onto Si/SiO2 wafers and dried at 50°C overnight. AFM images are acquired with a Bruker Innova® AFM in tapping mode using silicon probes (frequency = 300 kHz, spring constant = 40 Nm^{-1}). Thickness statistics is performed by measuring ~100 flakes from the AFM images. Statistical analyses are fitted with log-normal distributions. Statistical analyses are performed in WSxM Beta 4.0 software.

4.2.6 SEM (Scanning electron microscopy)

The scanning electron microscope, indicated by the abbreviation SEM (Scanning Electron Microscope), provides information on the appearance, nature and properties of surfaces and underlying layers of usually solid samples, presenting an important advantage, namely a high depth of field, which allows you to focus on a large area of the sample, with an average resolution of 2¸5 nanometers (referred to the signal "generated" by the secondary electrons). However, since normal optical devices do not deflect electrons, electrostatic or magnetic lenses are used which, by acting on the electrical charge of the electrons, cause them to deflect. The electron microscope is essentially composed of an electronic source of convenient intensity (generally an incandescent filament that emits electrons due to the thermoelectronic effect) and a device that gives strong accelerations to the emitted electron beam, subjecting them to a high voltage in a range that goes from 20 to 100 thousand volts. The accelerated electron beam passes through a capacitor (electrostatic or magnetic), affects the sample, which is in turn re-emitted by the sample. The secondary electron beam emitted from the sample is collected by a detector and analysed through

the use of a computer, as shown in Figure 4.4. Naturally, what described takes place in the ultra-high vacuum ensured by a system of pumps.

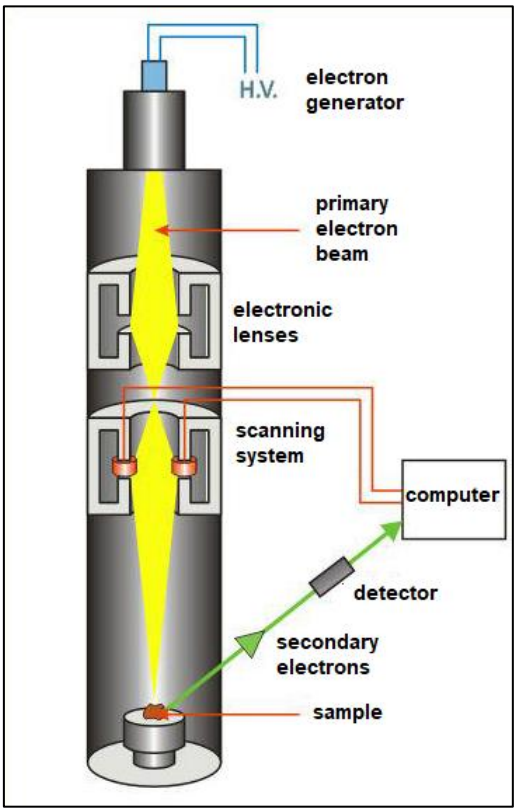

Figure 4.4 *Operation scheme of a SEM.*

Under these conditions, the wavelength of the electrons ranges from 0.1 to 0.005 Å (1 angström = 10^{-10} meters) so as to be a few tens of thousands of times smaller than visible light.

While not reaching the theoretical limits, the electron microscope provides up to 150,000 - 200,000 magnifications, with a resolving power of the order of one millionth of a millimeter (millimicron).

Membrane morphology has been inspected using scanning electron microscope (SEM, Zeiss-EVO MA10, Oberkochen, Germany). Small samples specimens have been broken in liquid nitrogen and placed in a sample holder. An ultra-thin coating of electrically-conducting gold (Au) has been deposited by using a sputter coating for SEM and the morphology of the membranes has been analysed in high vacuum.

4.2.7 Contact angle

By contact angle we mean the angle between the free surface of a liquid and the surface on which it has been deposited. By means of it, it is therefore possible to measure the wettability, that is, the relationship between the interfacial tensions of the separation surfaces. The three-phase

equilibrium configuration can occur in two different forms: it can take place through a contact line (a drop suspended on a liquid surface) or one of the three phases can spread completely between the other two, as shown in figure 4.5.

An empirical estimation of hydrophobicity is performed by contact angle value measurements. This value depends mainly on the material used for fabrication of the membrane and membrane topography, as mentioned. The resistance of the membrane to wetting stands as long as the pressure feed does not exceed the breakthrough pressure, well-known as bubble point pressure as well. This pressure corresponds to the required force to let water enter in the pore and wet the membrane. It can be calculated according to the following Laplace equation [3]:

$$\Delta P = \frac{4\sigma\cos\theta}{r} \qquad (4.3)$$

where σ is the surface tension of water in N/m, θ is the contact angle and r is the pore size of the membrane.

As evident, the pore of the membrane is a critical parameter in the regulation mass transfer and prevent wetting phenomena. Herafter, a discussion of some aspects concerning the role of pore size in reduced resistance to transport and controlled mutual liquid-membrane interaction is proposed. It is regarded as a boundary condition of the liquid/pore wall interface and as the result of balanced cohesive attraction of the liquid phase with the solid surface. The ideal case is a totally smooth membrane of the same solid material. In this case the contact angle depends only on the kind of material of the membrane and type of liquid in contact with them. t would on an ideal, flat surface of the same solid material (the intrinsic contact angle, Fig 4.5 A). The real case (fig. 4.5 B) can exist in two states: the Cassie–Baxter state, in which the liquid phase bridges the peaks of a surface and rests on top of air gaps, and the Wenzel state, in which the liquid is in full contact with the uneven surface [4].

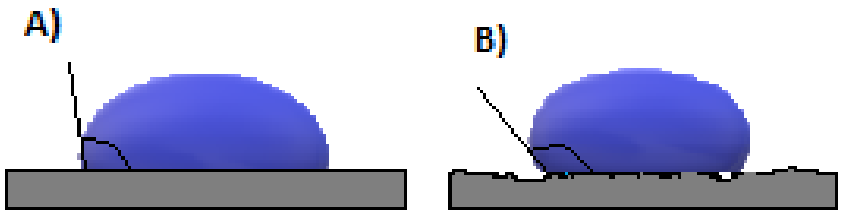

Figure 4.5 *A) The ideal case of membrane surface, B) the real case with a rough surface of the membrane.*

According to Wenzel's theory, is possible to calculate the roughness *r* as the ratio between the intrinsic contact angle, ϑi, and the apparent contact angle, ϑa, as:

$$r = \frac{cos\theta_a}{cos\theta_i} \quad (4.4)$$

Where the intrinsic contact angle is the contact angle which a liquid would make with an ideal (i.e. rigid, flat, chemically homogeneous, insoluble and non-reactive) solid surface:

$$cos\theta_i = \sigma_{sf} - \sigma_{sl}\sigma_{lf} \quad (4.5)$$

with σ_{lf}, σ_{sl}, and σ_{sf} are the liquid-fluid, solid-liquid, and solid-fluid interfacial tensions, respectively. The apparent contact angle is the angle between the apparent solid surface and the tangent to the liquid-fluid interface.

In the case of a rough surface, so $r>1$, the apparent contact angle will be larger than the intrinsic contact angle if $\vartheta i>90°$, and smaller if $\vartheta i<90°$.

In the case of increase surface roughness, vapor may be trapped underneath the liquid producing a composite interface. This case of heterogeneous wetting can be described by Cassie–Baxter equation, studied in 1944 to measure equilibrium contact angle, ϑ^{CB}. Considering the interface components 1 and 2, ϑ^{CB} can be measured as:

$$\cos\theta^{CB} = f_1\cos\theta_1 + f_2\cos\theta_2 = f_1\cos\theta_1 + (1 - f_1)\cos\theta_2 \quad (4.6)$$

where f is the liquid/solid contact area fractions of solid and ϑ is the equilibrium contact angles of the same liquid on each of the flat surfaces of these components. Fig.4.6 A) show the special case when vapor air remains trapped under the drop while the Fig.4.6 B) shows the case of absence of air trapped under the drop (Wenzel mode). It is suggested that the contact line model is a better approach to predict the superhydrophobicity of surfaces.

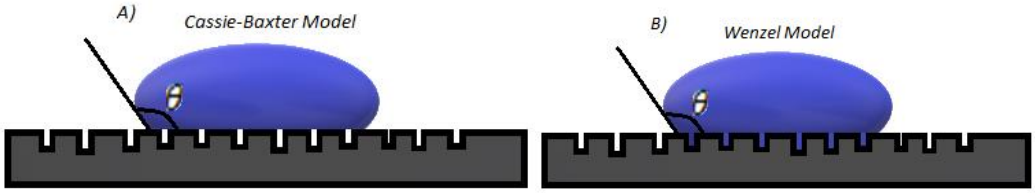

Figure 4.6 *A) Membrane roughness substrate with air trapped under the drop, described by Cassie-Baxter model; Membrane Roughness with water fill the pore described by Wenzel model.*

The pore volume for hollows fibers is determined by the following:

$$Vf = n_p\pi\varepsilon(d_o^2 - d^2)L \quad (4.7)$$

where n_p is the number of pore in the membrane, L is fiber length, di is inner diameter of fiber and d_o is fiber outer diameter.

The wetting can be one of the main limits of membrane contactors application because it can cause loss of separation capacity of the membrane [5]. The wetting of the membrane pores involves a complex of physical and chemical interactions related to topography and chemistry aspects of the membrane. Anti-wetting can be the result of high degree of surface roughness and high surface tension at liquid-membrane interface [6].

The hydrophobicity of the composite membranes has been characterized by measuring water contact angle using CAM 200-KSV instrument LTD (Helsinki, Finland).

4.2.8 Mechanical Proprieties

The mechanical properties of a membrane aim to study the behaviour of the material under external stress. The analysis of the material will be at a macroscopic level. The mechanical properties of a material can be classified into static and dynamic properties. Strain-strain measurements are the most widely used mechanical tests for the mechanical characterization of a material. A typical measurement is shown in Figure 4.7.

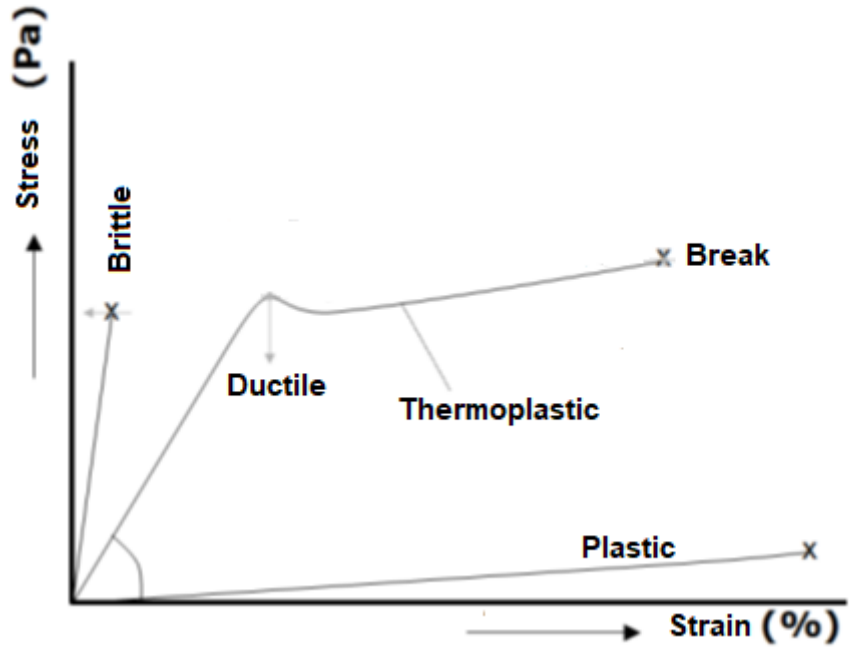

Figure 4.7 *Classical stress-strain measurement, x indicates the breaking point of the material.*

Stress-strain experiments give indications on how fragile or soft a sample can be, by means of Young's modulus, i.e. the slope of the initial part of the curve, information on the toughness and weakness of a material can be obtained respectively from the maximum elongation and from tension to break. Figure 4.7 shows guidelines on how to read a stress-strain curve, and what differences between the curves indicate. It must be emphasized that the mechanical properties of polymers with a glass transition temperature close to room temperature can be greatly influenced

by the variation of temperature. For example, a material with high modulus and small maximum elongation, that is hard and brittle, if the temperature is increased it could have low modulus and great elongation, becoming soft and tenacious. Obviously different structures will have different forms of elongation, and it will therefore be possible to recognize if a polymer is crystalline, elastomeric or amorphous. The line that joins the words rigid and ductile in Figure 4.7 marks the threshold between two types of deformations, the elastic and the plastic. The elastic deformation depends on internal “movements” in the same polymer chain; in fact there is a change in the bond angles and their stretching. This type of deformation is reversible, and the polymer that is deformed in this area returns to its original length as soon as the application of the effort is suspended. The plastic zone is attributed to the sliding of the polymer chains between them. Contrary to what happens in the elastic zone, a deformation of this type is irreversible [7,8]. The mechanical properties of the membranes, during the normal conditions of application of the membranes, are not directly relevant, but they can provide important details on the normal properties of the materials used. The main parameters to set concern three aspects: preload, Young's modulus and complete experiment. The preload phase is used to reduce the error on the position of the sample. When it is positioned between the clamps, in fact, it is not sure to have the sample perfectly stretched: in the central part it may have a slight hump. The preload, force and speed parameters mean that the actual measurement begins only after the transducer has measured a force greater than the limit imposed by us. This value should usually be less than 5% - 10% of the sample's breaking strength. At this stage, the speed must also be set based on the selected preload force. With reference to Young's modulus, the speed with which the terminals must be separated in the period in which it is determined must be set. The extremes of the voltage range in which to consider the tangent to the curve to calculate (graphically) the Young's modulus must also be identified. This setting is very delicate since it will significantly affect each value obtained, and it is not uncommon for the software, if not carefully instructed, to consider instead of the tangent to the curve a line that intersects the graph in several points, thus losing the physical meaning of the measurement. In these cases, action is taken at the end of the measurement to set the correct interval. The other parameters to be set are the distance between the clamps, the speed with which they return to the initial position and the speed with which the machine must measure the breaking force.

Mechanical properties (i.e., tensile stress and elongation at break) have been investigated through the tensile elongation testing. The membranes have been cut to a predetermined length of 5 cm

and clamped to a tensile stress-strain meter Roell/Zwick universal testing machine, single-column model Z2.5 (Genova, Italy).

4.2.9 Pore size and Pore size distribution

The porometer is an instrument capable of determining the size of the pores present in the analysed sample. The technique used by this instrument is capillary flow porometer, also known as the liquid ejection technique, which uses the pressure of a gas to force a liquid out of the interconnected pores in a sample. By means of the pressure exerted it is thus possible to ascertain the size of the pores. In fact, the pressure at which the pores empty is inversely proportional to their size, where large pores need less pressure, while small pores need a greater pushing force. The largest pore to be emptied defines the so-called "bubble point". The measurement will end when all the pores are emptied of the liquid. This measurement is carried out in a first test where the sample, wetted by the liquid, will define the "wetting" measurement, a second measurement instead provides for the dry sample from the liquid thus having a "dry" measurement on the same sample. From the complete data set various parameters such as flow-related pore size, pore size distribution and gas permeability can be calculated. The Capillary Flow Porometer-CFP 1500 AXEL model has been used in this work.

A large number of small sized pores are preferable to control wetting phenomena without adding resistance to transport through membrane. Small pore size can induce capillary forces that prevent direct contact of two phases in contact with membrane [7]. A larger pore size suffers severe absorption causing flux decline with pressure due to wetting, whereas smaller pores can leave the membrane in completely dry state under higher *pressure*. Therefore wetting membrane with a large pore size is extremely sensitive to variations in the supply pressure, with consequent serious deterioration in performance. It is interesting to observe the relation between the transmembrane pressure difference and the pore size according to the Laplace equation (eq. 4.8). It is evident how the mass transfer resistance of the membrane decreases with increasing pore size, even if the risk of wetting is increased. Mass transfer resistance represent a key issue for the membrane contactor technology due to a lower driving force in the process. To limit this inconvenient a simple solution is to make thin membrane thickness without affecting the mechanical resistance and, hence, the durability of the membrane. So, a suitable pore size should be provided preventing insufficient mechanical stability and wetting. In an ideal case with a pore with a narrow size and a high surface tension, the capillary forces raise the liquid with a height given by:

$$h = 4\sigma cos\theta\rho gr \quad (4.8)$$

where *h* is the height of the liquid lifted in the capillary, *ρ* is the density of the liquid and *g* is the acceleration of gravity. In case of hydrophobic propriety (i.e. contact angle $\theta > 90°$) the liquid will be depressed below the surface of the surrounding liquid do not wet the tube.

Another important aspect is related to the uniformity of the pore distribution, which is determinant to reproduce the same event throughout the entire membrane surface. The pore size distribution of the membrane is well described by the most common form of the two-parameter log-normal distribution function (*f*(*d*))[8]:

$$f(d) = \frac{1}{\ln(d_g)r\sqrt{2\pi}} \exp\left[-\frac{1}{2}\left(\frac{\ln\left(\frac{r}{D}*\right)}{\ln(\sigma)}\right)^2\right] \quad (4.9)$$

where D^*, d_g are the geometric mean diameter and the geometric standard deviation that can explain the uniformity of pore size, respectively. A low value of σ_g indicates pore size almost close to the average pore size (narrow pore size), whereas with high value of σ_g the pore sizes vary widely from the average value. Moreover a high σ_g, indicate generally a more easier partial wetting than the membrane with narrower pore distribution [9].

These two parameters can be measured from the Levenberg–Marquardt algorithm, which correlates them with the rejection coefficient of a solute *R*(*a*) and the pore size distribution parameters [10]:

$$\sum_{i=1}^{N}\{R(a_i)|_{Exp.} - R(a_i)|_{Cal.}\}2|_{MIN} \rightarrow (D^*, \sigma_g) \quad (4.10)$$

Where $R(a_i)$ is usually calculated with concentrations of solute molecule in the C_f and in the permeate C_p by the following:

$$R(a) = \frac{C_f - C_p}{C_f} \quad (4.11)$$

The pore distribution depends on many factors including manufacturing, materials and fabrication conditions [11,12].

In general, two shapes of pore size distribution exist as shown in fig. 4.8. The first case (fig. 4.8A) is an asymmetric pore size distribution while the second (fig. 4.8B) is a normal distribution where the shape of pore size is symmetric, and the distribution has a Gaussian shape distribution.

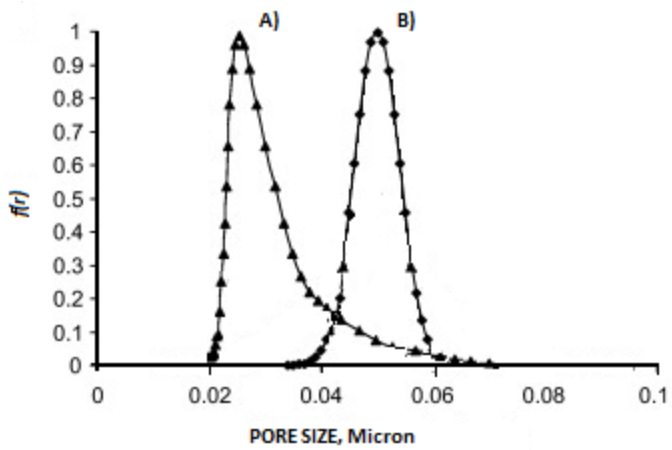

Figure 4.8 *Pore size distribution for A) asymmetric porous and B) symmetric porous distribution.*

In literature is possible to find various physical methods for pore size and pore size distribution determination, such as:

- Microscopic method: Through microscopy observation and, consequently, image processing is possible to obtain directly a visual information on the membrane morphology, such as surface pore shape and size, their distributions, pore density, surface porosity, cross-sectional structure, and so on. However, it has been not possible to obtain an indication of pore length or tortuosity and the quality of information is directly proportional to the quality of microscopy [13].
- Bubble pressure and gas transport method: Bubble and gas pressure transport method: the combination of the bubble pressure and solvent permeability method can evaluate the pore size and distribution by measuring the pressure needed to force a liquid through a swollen solvent membrane. First, the flow of gas through a dry membrane is measured as a function of pressure. This measurement leads to a straight curve that clarifies the linear relationship between pressure and gas flow. Then, the gas flow is then measured again through a solvent-wetted membrane. Usually, two immiscible liquids with different surface tension are selected. The difference of surface tension allows one liquid to better wet the membrane than the other liquid. The interfacial tension between the two liquids is low and this allows to measure very small pores without need to apply high pressure [14].
- Mercury porosimetry: the intrusion of mercury under controlled pressure into the porous structure of the material [15]. Intrusion pressure values are directly converted into the corresponding pore radius by using the Washburn equation, while intruded mercury

volume corresponds to the pore volume. The Washburn equation for a liquid that will penetrate a distance L into the capillary pore can be calculated by:

$$L = \sqrt{\frac{\sigma r t cos\theta}{2\mu}} \quad (4.12)$$

Where μ is the dynamic viscosity. Higher pressure corresponded to a small pore size.

- Liquid-vapor equilibrium method (BJH): The method of Barrett, Joyner, and Halenda is a procedure for calculating pore size distributions from experimental isotherms using the Kelvin model of pore filling. It applies only to the mesopore and small macropore size range. When the dimension of pore size tends to decrease, a decrease in the pressure tend is also observed, so increasing the condensation of the vapors within pores. This phenomenon can be related to capillary condensation.

$$\frac{\rho RT}{M} \ln\left(\frac{P_c}{P_o}\right) = -2\sigma\cos(\frac{\theta}{r_P}) \quad (4.13)$$

where ρ is the condensate density and Po is the vapor saturation pressure at a planar surface

- Liquid-solid equilibrium method (thermoporometry): This method is based on the liquid—solid phase transformations in porous materials providing the relationships between the size of the pores. The solidification takes place in the membrane pores. The relationship between the solid = liquid interphase extension energy σ_{ls} a and the temperature is given by:

$$(To - Ts) = \Delta Ts = \frac{2}{r}\frac{\sigma_{ls}}{\Delta S} \quad (4.14)$$

where ΔS is the fusion volumic entropy of a liquid film adhering to the solid matrix of the porous material which does not undergo a change of state.

- Permporometry (Gas-liquid equilibrium method): The method is based on the well-known phenomenon of capillary condensation of liquids in micropores. It is known that the vapor pressure of a liquid is dependent on the radius of curvature of its sur face, as mentioned by the Kelvin equation (eq.4.13).

- Gas Permeability method: This method is based on the gas permeability of porous media in a membrane structure. In this way is possible to obtain only the average pore size, rather the pore size distribution. The gas permeability coefficient K for porous membrane can be given generally by

$$K = K_n + \frac{B}{\mu}\Delta P \quad (4.15)$$

Where K_n is the Knudsen permeability coefficient, μ is the viscosity of the permeant gas, B is the geometric factor of a membrane, and ΔP is the mean pressure of the gas on both sides of a membrane.

Pore size and pore size distribution have been determined through porometer (Capillary Flow Porometer-CFP 1500 AXEL, Porous Materials Inc., Ithaca, NY, USA).

4.2.10 Porosity

Number and pore size contribute to form the overall volume of void spaces per total membrane volume. Well expressed as overall porosity (ε). This parameter describes the open space, which permeating component can pass through [9]. A larger void space should allow to a better mass transfer due to a less resistance to transport. One possibility to estimate porosity is to measure the pressure loss across the membrane at a given air flow rate [16]. Porosity is high when the slope of pressure loss versus increasing air flow is flat (Fig. 4.9).

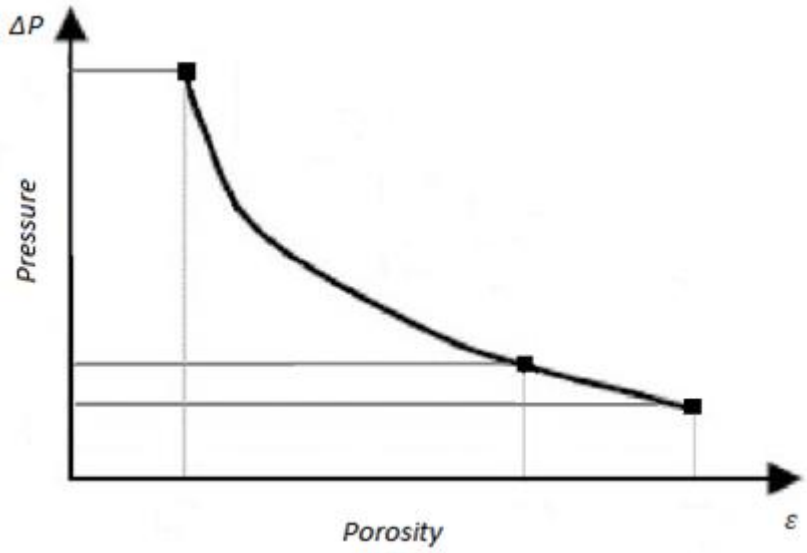

Figure 4.9 *Pressure drop in function of porosity.*

. It can be calculated in different way such as:

$$\varepsilon = \left(1 - \frac{\rho_{bulk}}{\rho_{particle}}\right) * 100 = \left(\frac{V_p}{V_b}\right) * 100 \quad (4.16)$$

Where ρ_{bulk} is the density of the bulk, $\rho_{particle}$ is the density of the particle which is equal to the mass of the sample divided by volume of the sample, V_p is the pore volume and V_b is the bulk volume of sample.

A correlation of porosity with mass transfer coefficient can be expressed by following [16,17]:

$$k = \frac{D\varepsilon}{\delta\tau} \quad (4.17)$$

Where *K* is the mass transfer coefficient and *D* is the diffusion coefficient.

Membrane porosity is another factor significantly affects system performance. In fact, the wetting ration x* of membranes have been influenced by porosities (ε).

The degree of wetting is generally expressed with the term of wetting ratio (x^*). It is defined as the ratio of the volume of liquid in the pore (V_w) and pore volume of membrane (V_f). The wetting ratio can be expressed as the following:

$$x^* = \frac{Vw}{Vf} \tag{4.18}$$

When the membrane present a high porosity, x* of the membrane is more significant compared to the lower porosity membrane under the same operating conditions. When the porosity increases will enhance the membrane mass transfer coefficient.

The overall porosity has been measured by filling them with FC-40.

4.2.11 Energy Dispersive X-ray Analysis (EDX)

Energy Dispersive X-ray Analysis or EDX spectroscopy indicates a type of analytical instrumentation that exploits the emission of X-rays generated by an accelerated electron beam, incident on the sample (fig. 4.10). For this type of spectroscopy a common SEM-EDX scanning electron microscope (SEM) has been used. The operating principle is based on an emitter consisting of a tungsten or lanthanum hexaboride filament, brought over 1000 ° C by electric heating, which acts as a source of electrons for the thermionic effect. This electron beam thus generated is first accelerated by a potential difference of 0.3-30 KV and then subsequently passed through an electromagnetic collimator to be deflected, so as to generate the scan, and finally collimated towards the sample. . All this is carried out under vacuum by an ion pump, at about 10^{-4}-10^{-6} mbar, to increase the average free path of the electrons and avoid secondary diffusion phenomena caused by the interactions that electrons can have with air. Finally, through the use of a computer and a screen, the classic image generated by the SEM is provided. A JEOL JXA-8230 SEM has been used.

Figure 4.10 *EDX instrument.*

4.3 Membrane Distillation

Thermally-driven MD experiments have been executed accordingly with the Direct Contact (DC) configuration using salt solutions 0.6 M (35 g/L NaCl and 35 g/L with mixture salts). In the first moment only NaCl has been used as salt in the 0.6M solutions while in the second moment different salts has been introduced in the 35 g/L NaCl solutions. In this way we tried to reproduce in the laboratory a solution more and more similar to sea water. Moreover, different concentration of NaCl solutions (2 and 4 M) and different flow rates have been also utilized to prove durability and stability of the novel membranes with high concentrated NaCl solutions. On the permeate side, distillated water has been used in counter-current respect the feed side. Retentate and distillate streams have been converged toward the membrane module containing the membrane, where the liquid water has been evaporated (Fig. 4.11).

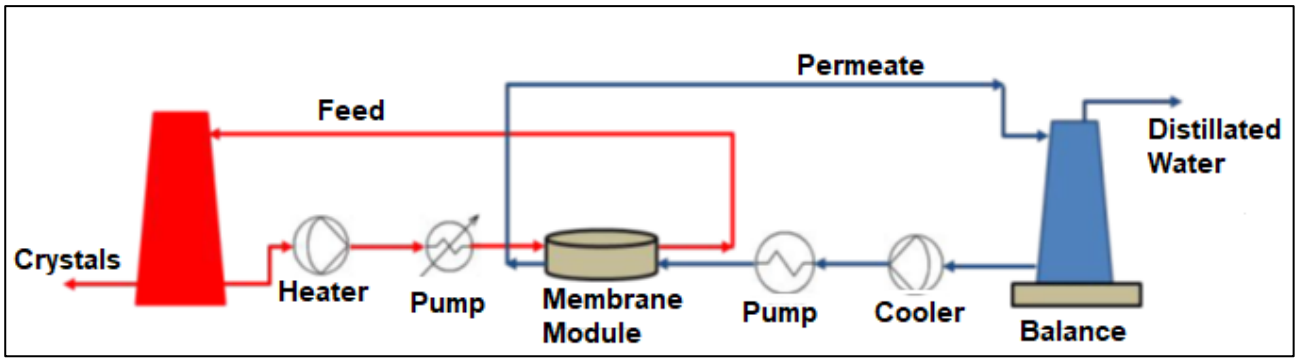

Figure 4.11 *Schematic drawing of a membrane distillation/crystallization (MD/MCr) plant.*

On the retentate side, a pump has been taking and sending the heated feed to the membrane module. Also on the distillate side, a second pump ensured the counter-current recycle of the cold stream in order to remove from the solution the vapour diffusing through the membrane pores. The transmembrane fluxes J ($L*m^{-2}h^{-1}$) have been estimated by evaluating the weight variations in the distillate tanks according to the relation:

$$J = \frac{Q}{A*t} = B(P_{fm} - P_{pm}) \qquad (4.19)$$

Where Q is the permeate volume (L) collected during time t (h), A is the effective area of the membrane (m^2), P_{fm} and P_{pm} are vapor pressures of feed and permeate, respectively, at the corresponding membrane surface temperatures T_{fm} and T_{pm}. The salt conductivity of the feed and permeate streams have been measured by using a conductive meter at the beginning and the ending of each tests (Eutech Instruments PC 2700). The temperature polarization has been measured with the τ coefficient and expressed as the ratio between the difference of T_{m1} and T_{m2}, which are the temperatures at the hot and cold membrane surfaces, respectively, and the difference between T_{b1} and T_{b2}, which are the temperatures in the feed and permeate bulk solutions, respectively.

$$B = \left[\frac{3\tau\delta_m}{2\varepsilon r}\left(\frac{\pi RT}{8M}\right)^{\frac{1}{2}} + \frac{\tau\delta_m}{\varepsilon}\frac{P_a}{PD}\frac{RT}{M}\right]^{-1} \qquad (4.20)$$

Where ε is the porosity, δ_m is the membrane Thickness, $\tau$is the tortuosity, P_a is a conversion factor, R is the Universal gas constant, M is the molecular weight, r is the average pore size, P is the vapor pressure and D is the module diameter.

The thermal conductivity of the materials is calculated assuming the thermal conductivity of single type of few layers and related percentage in the nanocomposite membranes.

Thermal conduction has been considered as a heat loss mechanism through the membrane material and the vapor that fills the pore and has been expressed as

$$Q_m = h_m \Delta T_m \tag{4.21}$$

where

$$h_m = \varepsilon * h_{mg} + (1-\varepsilon) h_{ms} = \frac{k_g * \varepsilon + k_m(1-\varepsilon)}{\delta} \tag{4.22}$$

Here, h_{ms} and h_{mg} represent the heat transfer coefficients of the vapor within the membrane pores and the solid membrane material, respectively; k_g and k_m the thermal conductivity of vapor and membrane.

Total heat transfer across the membrane has been estimated as

$$Q = Q_v + Q_m \tag{4.23}$$

Where

$$Q_v = h_v * \Delta T_m = J * \Delta H_v \tag{4.24}$$

is the heat of vaporization. On the other hand, the heat transfer by convection in the feed f and permeate p boundary layers can be expressed as:

$$Q = h_f * \Delta T_f = h_f (T_f - T_{fm}) \tag{4.25}$$

$$Q = h_p * \Delta T_p = h_p (T_p - T_{pm}) \tag{4.26}$$

Therefore, the overall heat transfer coefficient of the MD process is given by:

$$\frac{1}{U} = \frac{1}{h_f} + \frac{1}{h_m + h_v} + \frac{1}{h_p} = \frac{1}{h_f} + \frac{1}{\frac{k_g * \varepsilon + k_m(1-\varepsilon)}{\delta} + \frac{J * \Delta H_v}{T_{fm} - T_{pm}}} + \frac{1}{h_p} \tag{4.27}$$

Where each h and each T represent the corresponding heat transfer coefficients and temperatures either at feed (f) side or permeate (p) side or at membrane surface (m).

Finally, the total heat transferred across the membrane is expressed as:

$$Q = U * \Delta T \tag{4.28}$$

while the thermal efficiency in MD can be specified as the ratio of latent heat of vaporization to the total - latent and conduction - heat.

For DCMD, the thermal efficiency is, hence, expressed as:

$$Thermal\ efficiency = \frac{J * \Delta H}{U * \Delta T} * 100 \tag{4.29}$$

4.4 Membrane Crystallization

Membrane crystallization experiments have been executed, as MD tests, in Direct Contact (DC) configuration using a higher concentrated NaCl solution (5 M) respect the MD as feed and distillate water as permeate.

The procedure for MCr tests is almost the same of MD tests. Feed and permeate have been recirculated in the plant with a flowrate of 250 and 100mL*min^{-1} respectively; and with a temperature of 34±0.2 °C at the feed side and 11±0.2°C at the permeate side, respectively. Samples of the feed solution of almost 5 mL have been accurately extracted from the retentate side and observed using an optical microscope (Nikon Eclipse LV100ND, Nikon Eclipse LV100ND, Firenze, Italy) in order to determine crystal size distribution and growth rate at different stages of experimentation for all the analysed conditions. In particular, samples containing NaCl crystals have been removed from the retentate solution after regular intervals of 30 min from onset of crystallization and each experiment has been continued for 60 min to follow the growth of the crystals. Therefore, each crystallization experiment required a time equal to the sum (1) of the time necessary to reach supersaturation and the first clearly visible crystals, plus (2) the 60 min required to observe the growth of the crystals. The evolution of the particle size distribution as a function of time allowed the evaluation of the quality (in terms of coefficient of variation (*CV*) and length to width ratio). Coefficient of variation (*CV*) is a parameter indicating the dispersion of a distribution around the average crystal size. CV has been calculated using the following equation:

$$CV = \frac{PD_{84\%} - PD_{16\%}}{2 * PD_{50\%}} * 100 \qquad (4.30)$$

Where CV is expressed as percentage and PD is the crystal length at the indicated percentage.

Growth and nucleation rate (G^C and B^0) have been estimated on the basis of the Randolph-Larson model [18] as follows:

$$\ln(n) = \frac{-L}{G^C t} + \ln(n^0) \qquad (4.31)$$

Where n is the crystal population density, L is the crystal size, t is retention time and n^0 is population density at L equal to zero. A plot of $ln(n)$ versus L is a straight line whose intercept is $ln(n^0)$ and whose slope is $-1/G^C t$. Thus, from a given product sample of known slurry density and retention time, it is possible to obtain the nucleation rate and growth rate for the conditions tested when the sample satisfies the assumptions of the derivation and yields a straight line. The evolution of particle size distribution as a function of time allows for the evaluation of the nucleation rate according to the following equation:

$$B^0 = n^0 G^C \quad (4.32)$$

References

[1] A. Gugliuzza, M.C. Aceto, E. Drioli, Interactive functional poly(vinylidene fluoride) membranes with modulated lysozyme affinity: A promising class of new interfaces for contactor crystallizers, Polym. Int. (2009). doi:10.1002/pi.2681.

[2] X. Wang, L. Zhang, D. Sun, Q. An, H. Chen, Formation mechanism and crystallization of poly(vinylidene fluoride) membrane via immersion precipitation method, Desalination. 236 (2009) 170–178. doi:10.1016/j.desal.2007.10.064.

[3] M. Mortazavi, K. Tajiri, Liquid water breakthrough pressure through gas diffusion layer of proton exchange membrane fuel cell, Int. J. Hydrogen Energy. (2014). doi:10.1016/j.ijhydene.2014.03.238.

[4] R. Chunbo, D. Guqiao, L. Weichang, D. Yan, H. Wentao, Wetting on nanoporous alumina surface: Transition between Wenzel and Cassie states controlled by surface structure, Langmuir. (2008). doi:10.1021/la801461j.

[5] D.L. Mejia Mendez, C. Castel, C. Lemaitre, E. Favre, Membrane distillation (MD) processes for water desalination applications. Can dense selfstanding membranes compete with microporous hydrophobic materials?, Chem. Eng. Sci. 188 (2018) 84–96. doi:10.1016/j.ces.2018.05.025.

[6] M. Rezaei, D.M. Warsinger, J.H. Lienhard V, M.C. Duke, T. Matsuura, W.M. Samhaber, Wetting phenomena in membrane distillation: Mechanisms, reversal, and prevention, Water Res. 139 (2018) 329–352. doi:10.1016/j.watres.2018.03.058.

[7] A. Hernández, J.I. Calvo, P. Prádanos, F. Tejerina, Pore size distributions in microporous membranes. A critical analysis of the bubble point extended method, J. Memb. Sci. (1996). doi:10.1016/0376-7388(95)00025-9.

[8] S. Atchariyawut, C. Feng, R. Wang, R. Jiraratananon, D.T. Liang, Effect of membrane structure on mass-transfer in the membrane gas-liquid contacting process using microporous PVDF hollow fibers, J. Memb. Sci. (2006). doi:10.1016/j.memsci.2006.08.029.

[9] S. Boributh, S. Assabumrungrat, N. Laosiripojana, R. Jiraratananon, A modeling study on the effects of membrane characteristics and operating parameters on physical absorption of CO2 by hollow fiber membrane contactor, J. Memb. Sci. (2011). doi:10.1016/j.memsci.2011.06.029.

[10] J. Ren, R. Wang, H.Y. Zhang, Z. Li, D.T. Liang, J.H. Tay, Effect of PVDF dope rheology on the structure of hollow fiber membranes used for CO2 capture, J. Memb. Sci. (2006). doi:10.1016/j.memsci.2006.04.003.

[11] A. Figoli, S. Simone, A. Criscuoli, S.A. Al-Jlil, F.S. Al Shabouna, H.S. Al-Romaih, E. Di Nicolò, O.A. Al-Harbi, E. Drioli, Hollow fibers for seawater desalination from blends of PVDF with different molecular weights: Morphology, properties and VMD performance, Polymer (Guildf). (2014). doi:10.1016/j.polymer.2014.01.035.

[12] a. Gugliuzza, E. Drioli, PVDF and HYFLON AD membranes: Ideal interfaces for contactor applications, J. Memb. Sci. 300 (2007) 51–62. doi:10.1016/j.memsci.2007.05.004.

[13] S. ichi Nakao, Determination of pore size and pore size distribution. 3. Filtration membranes, J. Memb. Sci. (1994). doi:10.1016/0376-7388(94)00128-6.

[14] I.G. Wenten, K. Khoiruddin, A.N. Hakim, N.F. Himma, Chapter 11 - The Bubble Gas Transport Method BT - Membrane Characterization, 2017. doi:https://doi.org/10.1016/B978-0-444-63776-5.00011-5.

[15] P.S. Liu, G.F. Chen, General Introduction to Porous Materials, in: Porous Mater., 2014. doi:10.1016/b978-0-12-407788-1.00001-0.

[16] B. Lauterböck, K. Moder, T. Germ, W. Fuchs, Impact of characteristic membrane parameters on the transfer rate of ammonia in membrane contactor application, Sep. Purif. Technol. (2013). doi:10.1016/j.seppur.2013.06.010.

[17] S.B. Iversen, V.K. Bhatia, K. Dam-Johansen, G. Jonsson, Characterization of microporous membranes for use in membrane contactors, J. Memb. Sci. (1997). doi:10.1016/S0376-7388(97)00026-4.

[18] F. Macedonio, E. Drioli, Hydrophobic membranes for salts recovery from desalination plants, Desalin. Water Treat. 18 (2010) 224–234. doi:10.5004/dwt.2010.1775.

Chapter 5:

Preparation of nanocomposite PVDF membranes using 2D materials dispersant liquid phases

The design of breakthrough membranes is one of the most important challenges for the development of advanced membrane distillation (MD) and crystallization (MCr) operations, which are mainly dedicated to the production of clean water and recovery of salts contained in saline streams. In this chapter the preparation and characterization of polymeric membranes functionalized with 2D materials will be discussed concerning the request of intrinsic features materials suitable for MD and MCr.

An advanced procedure to exfoliate 2D materials along with a combined membranes fabrication methodology will be examined. Structural, morphological and chemical properties will be screened and structure-properties relationships will be explained.

5.1 Wet-jet milling exfoliation of 2D materials and their confinement in polymeric matrix

In the following sections a combined procedure, including exfoliation of 2D materials via wet-jet milling techniques and confinement of few layer materials in porous hydrophobic polymeric network, will be discussed

5.1.1 Preparation of 2D materials dispersant liquid phases

Wet Jet Milling is an exfoliation technique for producing few layers with an improved lateral dimension and a high surface-to-area ratio. 2D materials (Bi_2Te_3 (BT), Bi_2Se_3 (BS) and graphene (G)) exfoliated in dispersant NMP at a concentration of 0.65 and 10 g/L for Bi_2Te_3 and graphene, and 1 g/L Bi_2Se_3, respectively [1,2]. The procedure has been described in details in Chapter 3. Briefly, graphite or bismuth telluride powder is dispersed in NMP, in a mass ratio of 1:100, and placed in the container with a mechanical stirrer. The successive exfoliation step of the dispersed flakes occurred when the mixtures are exposed to hydrodynamic forces, *i.e.*, high shear rates (10^8 s^{-1}) and cavitation, produced through high-pressure (250 MPa) compression of the dispersant fluid phase [3-5]. The resulting shear stress applied to the dispersed flakes induces sliding of the 2D crystal planes and initiates the exfoliation process. For graphite, it has been shown that shear rates in excess of 104 s^{-1} are sufficient for the exfoliation process to occur [4].

5.1.2 Membranes preparation

Nanostructured membranes have been prepared by from dispersing high-exfoliated materials at a predefined stoichiometric ratio through a combination of WJM e dry-wet phase inversion (Table 5.1).

Table 5.1. *List of functional membranes prepared in this work.*

Name of Membrane	Acronym filler	Filler Dispersed in NMP
PVDF	-	No Filler
PVDF-BT (7%)	BT	Bi_2Te_3
PVDF-BT (0.5%)	BT	Bi_2Te_3
PVDF-G (7%)	G	Graphene
PVDF-G (0.5%)	G	Graphene
PVDF-BT-G 1-1	BT-G	Bi_2Te_3 and Graphene (1:1)

In particular, PVDF powder has been added at 12 wt.% under mechanical stirring at 30 °C to 2D materials dispersant liquid phases. After removing bubble air, each mixture has been uniformly casted on a glass plate by using a casting knife regulated on 250µm.

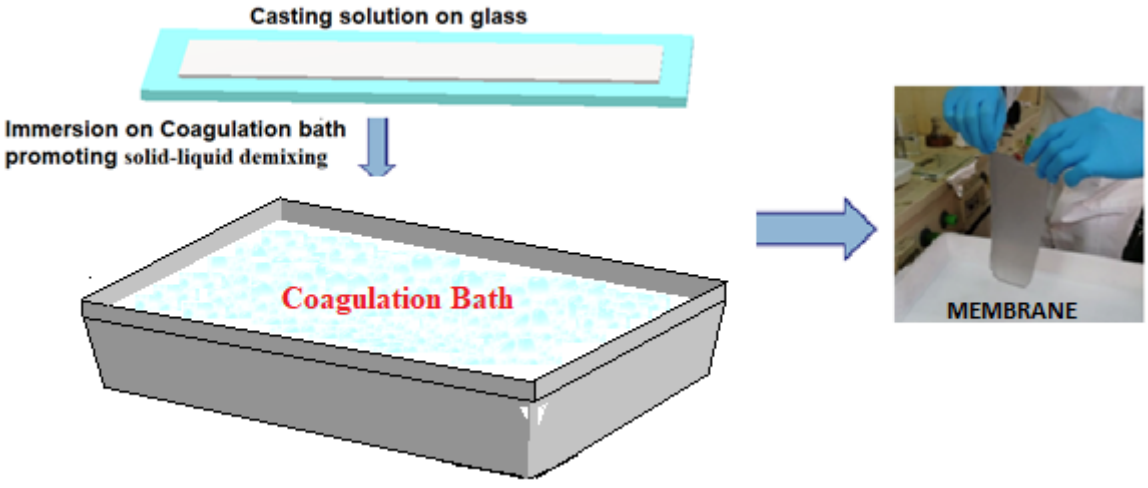

Figure 5.1 *Schematic representation of membrane preparation methodology.*

The casting solutions have been successively coagulated in a soft bath containing IPA in order to promote the precipitation of the polymer through soli-liquid demixing and the formation of flat porous membranes with particulate-like morphology. The latter have been washed in milli-Q

water, air-dried at room temperature overnight and annealed at 30°C for 1 h before using. The final concentration of each nanofiller with respect to the polymer was 0.5 % and 7.0 %. Moreover, a membrane with graphene and bismuth telluride in a ratio of 1:1 have been prepared in order to evaluate the effects of the mixed materials on the membrane performance. The final concentration for each filler was 0.5% with respect to the polymer.

5.2 Characterization of 2D exfoliated materials

TEM images for selected graphene and bismuth telluride flakes exfoliated via WJM are shown in Figure 5.2a, b, respectively. The graphene and bismuth telluride samples have been taken from liquid dispersant (0.65g/L) and diluted 1:50. The grids have been stored under vacuum at room temperature to remove the solvent residues so TEM analyses have been performed. They confirmed the presence of few layers of Bi_2Te_3 and graphene in the solvent residues. Graphene flakes appear to be larger and more regular than Bi_2Te_3 flakes, which show instead irregular and wrinkled geometries. In particular, graphene and Bi_2Te_3 flakes have a lateral size of about 490 and 200 nm, respectively. Moreover, the darkest contrast of Bi2Te3 flakes with respect to graphene flakes is characteristics of a thicker structure.

a) b)

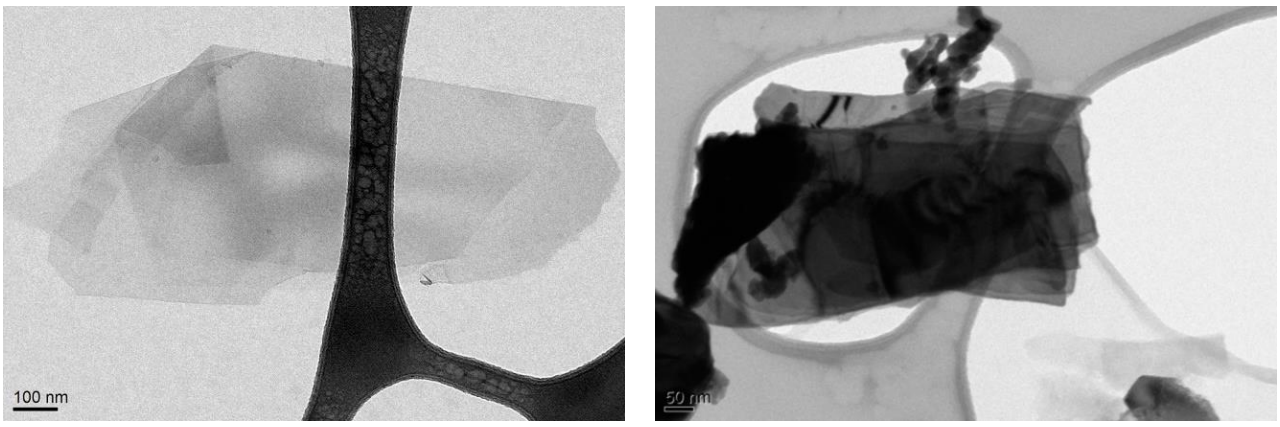

Figure 5.2 *TEM micrographs collected onto (a) graphene (0.65 g/L) flakes and (b) bismuth telluride (0.65g/L) crystals after WJM exfoliation.*

The topographic image of exfoliated graphene by WJM have been also examined by AFM and compared to that obtained by graphene flakes exfoliated via Ultra Wave (UW), Figure 5.3 a and b. The homogeneous surface shows some flakes dispersed on the membrane surfaces. Moreover is

clearly evident how the flakes exfoliated via WJM present a higher lateral size than the flakes exfoliated via UW, confirming how observed from TEM analysis.

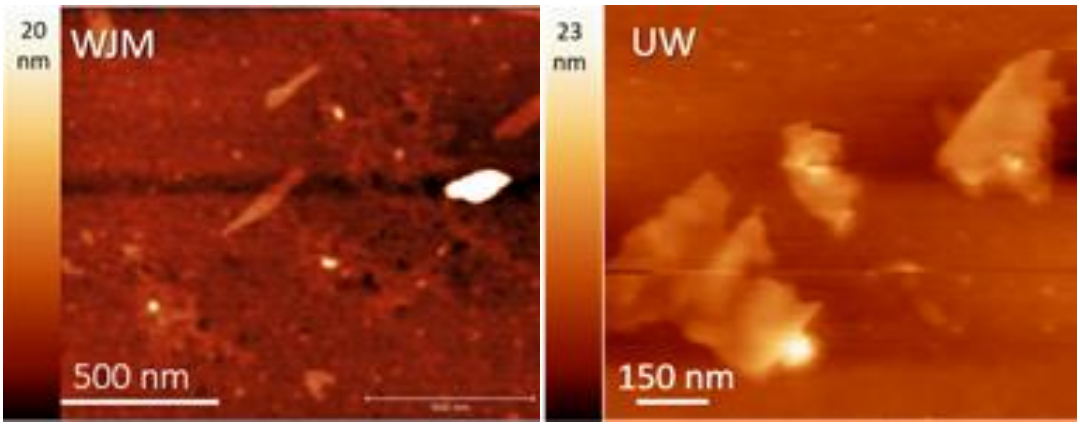

Figure 5.3 *AFM image of graphene exfoliated via WJM (a) and UW (b).*

The Raman spectrum of exfoliated graphene shows enhanced (I(D)/I(G)) ratio, while the deconvolution of the band 2D bands evidences a predominant $2D_1/2D_2$ ratio, confirming an enrichment in few layers graphene (Figure 5.4a). The Raman spectra of Bi_2Te_3 in bulk and exfoliated state exhibit typical Raman-active modes of the chalcogenide compound (A^1_{1g}, E^2_g, A^2_{1g}) (Figure 5.4b).

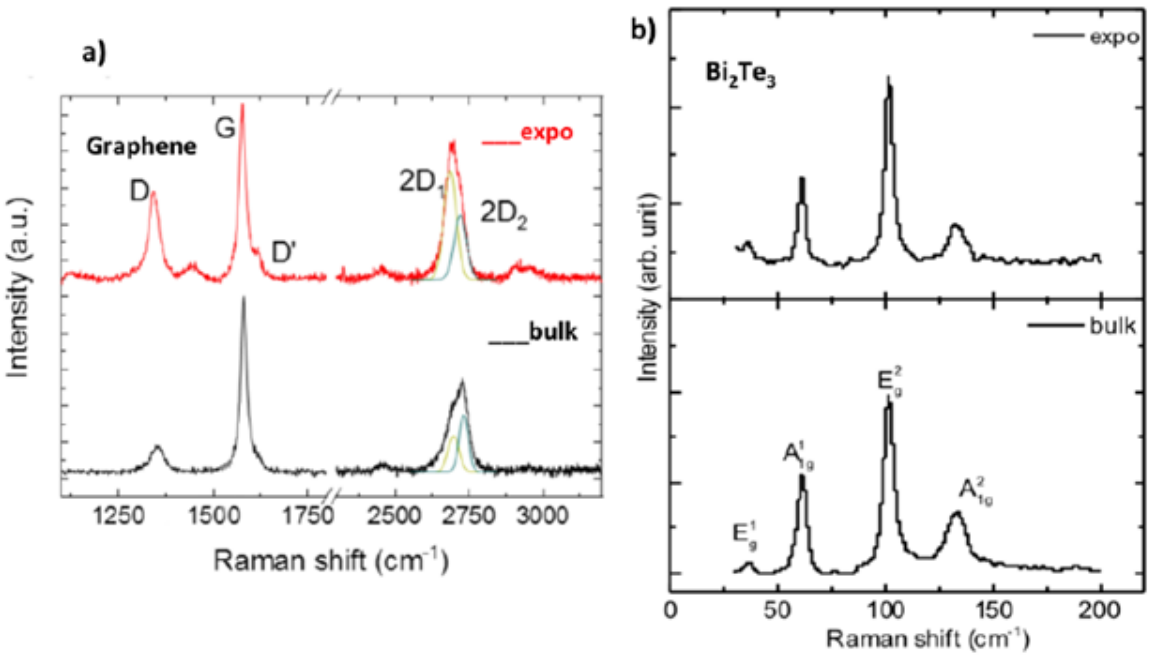

Figure 5.4 *Raman spectra related to graphene (a) and bismuth telluride (b) at the bulk and exfoliated state (0.65 g/L).*

5.3 Characterization of 2D materials-based PVDF membranes

The presences of 2D flakes in membranes have been confirmed by X-ray diffraction analysis (XRD) where the typical peaks corresponding to 2D fillers have been observed (Figure 5.5e, c). In particular, Figure 5.5 shows the comparison between XRD patterns of the pristine PVDF membrane (without filler), few layer materials and PVDF membrane with 2D materials. Due to large contribution of PVDF peaks, XRD patterns of membranes uploading the highest content of few layer materials have been examined. When the concentration of 2D materials inside the membrane is low (0.5%), XRD analysis is no able to relieve the presence of 2D materials in PVDF matrix due to the weak signals.

X-ray diffraction pattern (XRD) confirms further the presence of few layers BT and G in membranes (Figure 5.5 e, c). In spite of predominant signals of PVDF (peaks depicted in blue), all of the detected peaks are indexed to the standard diffraction pattern of Bi_2Te_3 (JCPDS 15-0863) with main peaks (depicted in red) originated from the (015), (1010), and (0015) planes [6] while the graphene is identified with a detectable peak at (C002, depicted in green) [7].

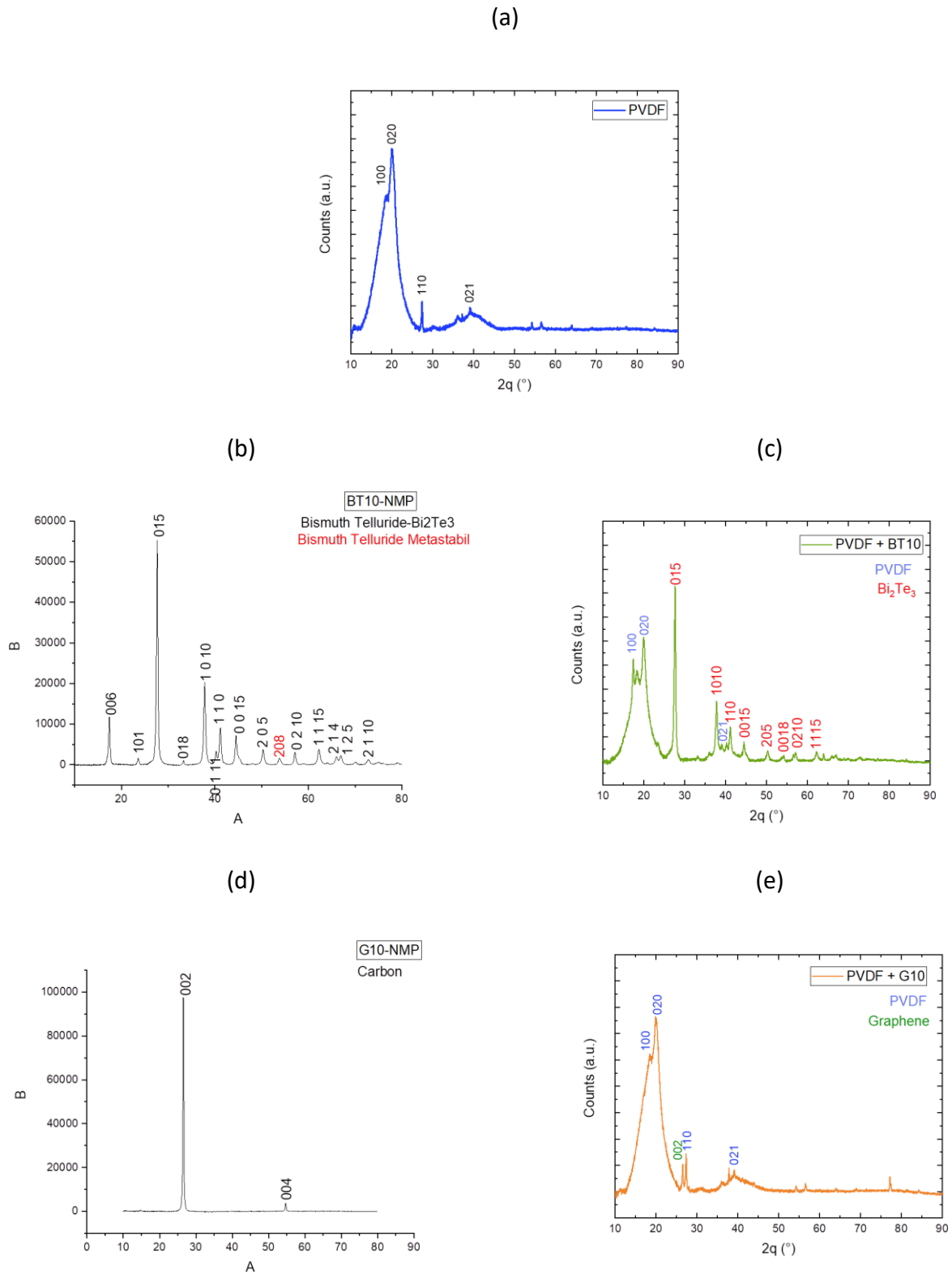

Figure 5.5 *XRD patterns for (a) pristine PVDF, (b) Bi2Ti3 flakes and (c) PVDF-BT (7%) membrane, (d) Graphene flakes, (e) PVDF-G (7%) membrane.*

X-ray photoelectron spectroscopy (XPS) measurements have been also carried in order to check the presence of 2D materials in PVDF membranes (Fig. 5.6). In PVDF membranes containing few layers graphene higher contribution of C 1s have been detected around 290 eV. Contributions of bismuth (~200 eV) and telluride (~600 eV) have been detected for the PVDF membrane filled with bismuth telluride. Weak contributions of oxygen have been also detected for both the nanocomposite membranes.

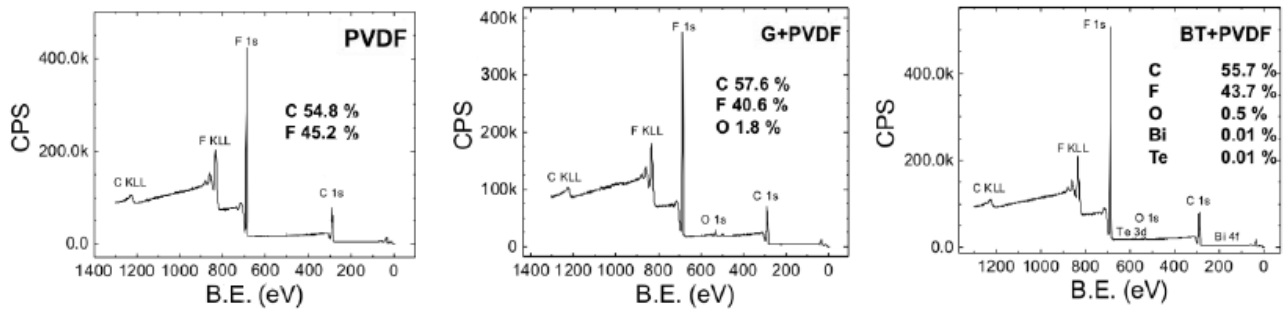

Figure 5.6 *XPS spectra collected on pristine PVDF, PVDF-G (0.5%) and PVDF-BT (7%) membranes.*

AFM topographic images show the polymeric structure of pristine PVDF, PVDF-G (0.5%), PVDF-BT (0.5%) and PVDF-BT-G 1: 1 membranes respectively (Fig. 5.7). The typical spherulitic structure of the semicristalline PVDF can be appreciated for all membranes. The pores are clearly free gaps frozen in polymer matrices.

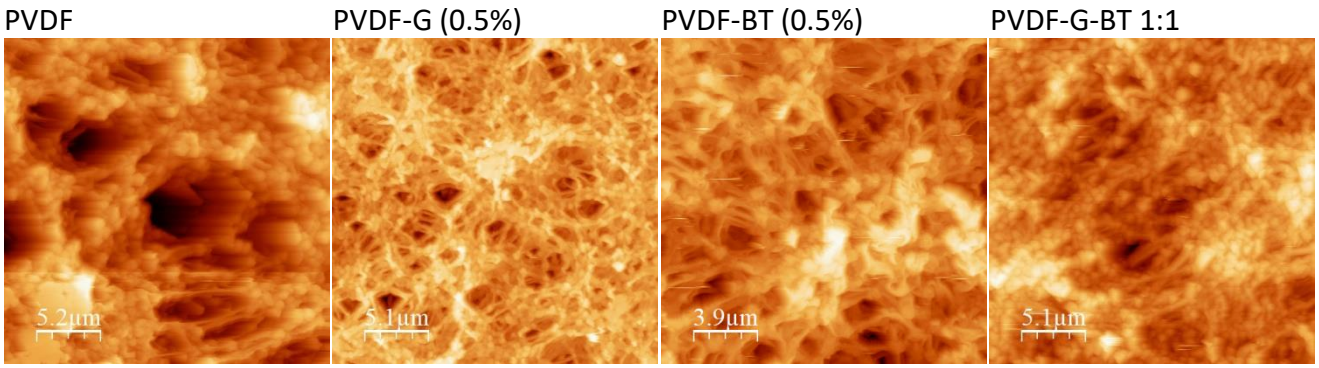

Figure 5.7 *AFM images of pristine PVDF, PVDF-G (0.5%), PVDF-BT(0.5%) and PVDF - BT-G 1: 1 membranes, respectively.*

Due to the fact that few layer materials are randomly and in a discrete way entrapped in the polymer matrix, they are not intercepted easily by AFM. Differently, SEM micrographs reveal their

presence in entangled polymer chains, characterized by a particulate-like morphology visibly (Figure 5.8)

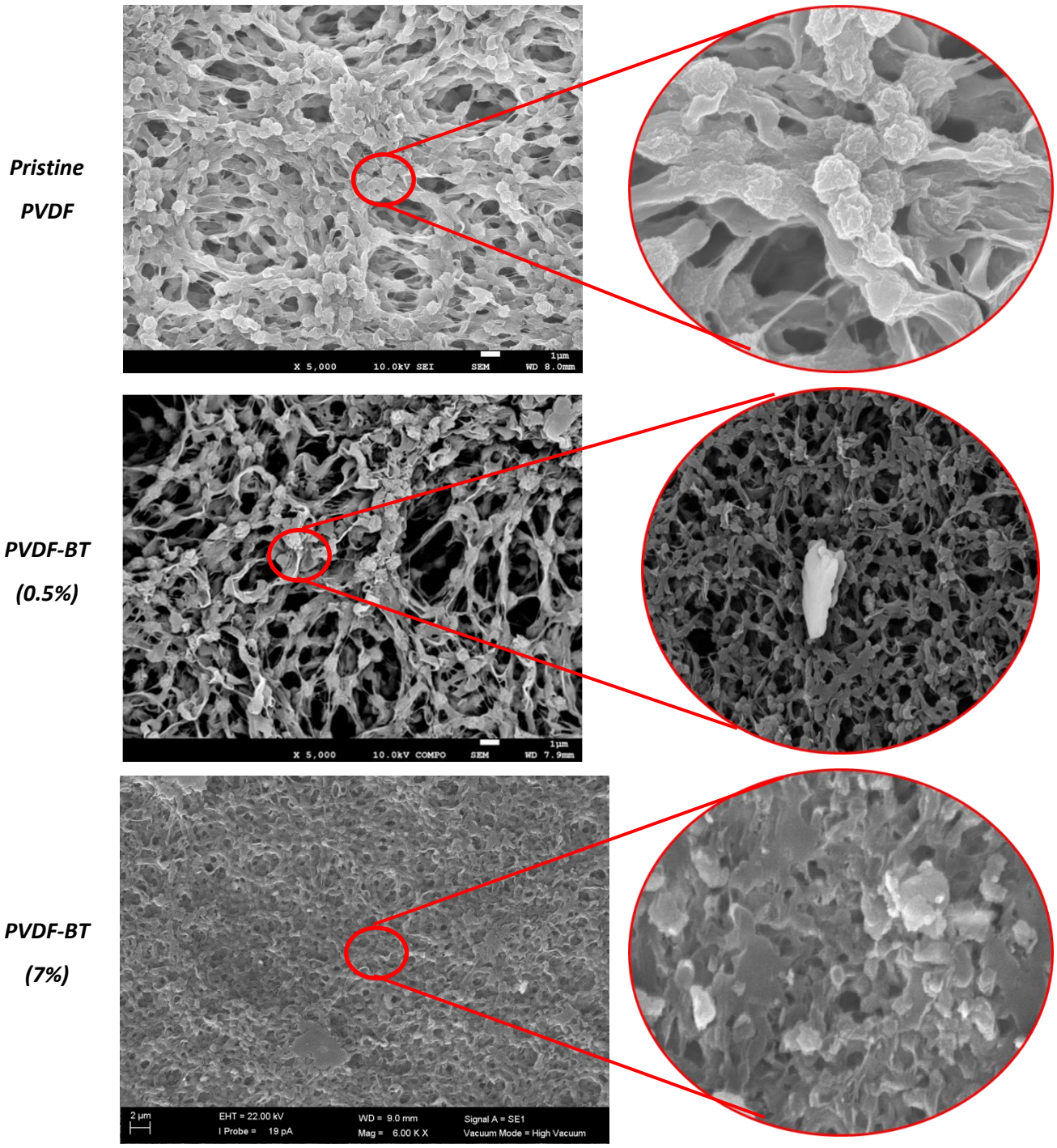

PVDF-G(0.5%)

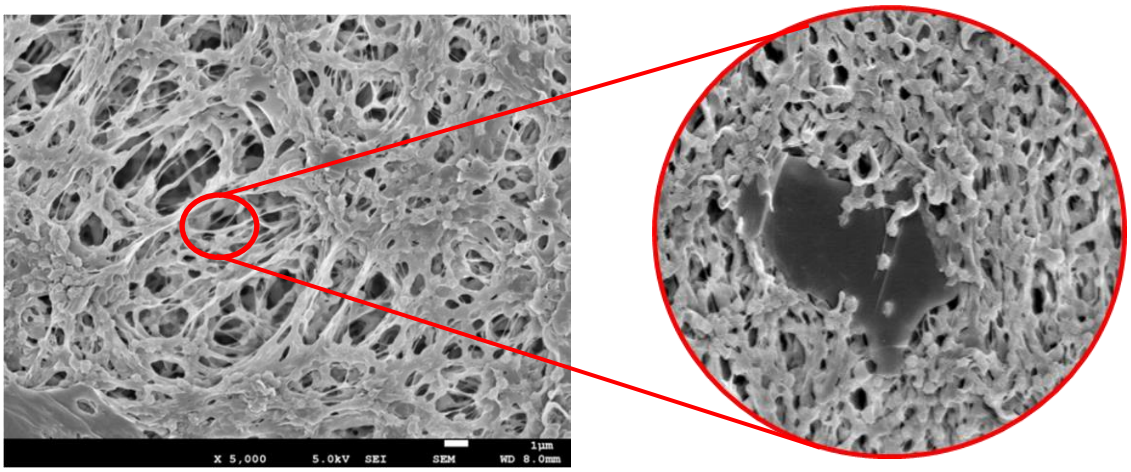

Figure 5.8 *SEM images collected on the top surface of the pristine PVDF at two different magnitudes (enlargements at 5.000 and 20.000X).*

SEM micrographs display also few layers bismuth telluride and graphene entrapped in the PVDF polymeric networks. Figure 5.8 shows the graphene flakes entrapped in the PVDF network at two different magnitudes.

Except for membrane containing 0.5 % of graphene (0.24µm), comparable mean pore size are have been measured for all membranes with bubble point values ranging from 0.5 to 0.8 μm. Low concentration of filler tends to limit the presence of larger pore size, whereas higher concentrations of filler generate bigger free gaps. Generally, graphene flakes reduce pore size and porosity of the membrane respect to PVDF membrane [7]. In figure 5.9 are shown the comparison between the pore size distribution achieved with pristine PVDF and PVDF-G(0.5%) membranes. Both membranes show a narrow pore size distribution. All the prepared membranes with 2D materials present a narrow pore size distribution. The overall of voids distributed through the membrane gives raise the overall porosity, which results in larger values for membranes filled with BT. In the case of Bi_2Te_3 (7%), the membrane displays porosity around 77±1% while PVDF-BT (0.5%) shows a porosity of 75%. The membranes with graphene show the lowest porosity with values of 56 ± 7 and 58 ± 3, respectively for PVDF-G(0.5%) and PVDF-G(7%)).

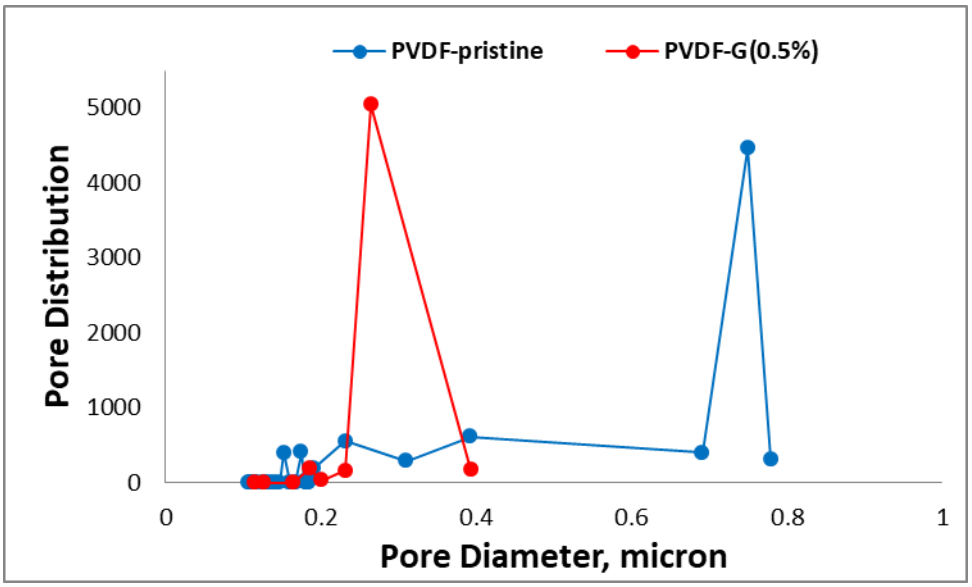

Figure 5.9 *Pore size distribution of pristine PVDF and PVDF-G(0.5%).*

This aspect is more evident in the pristine PVDF membrane have been a larger pore is shown, confirming how obtained on pore size measurement (bubble point diameter of 0.73µm).

Table 5.2 *Main characteristics of PVDF-based membranes.*

Membrane	Pore size (µm)	Bubble point (µm)	Porosity (%)	Thickness (µm)
PVDF	0.48±0.09	0.73 ±0.05	63±5	57±2
PVDF-G (0.5%)	0.24±0.05	0.43±0.01	56 ± 7	62 ± 3
PVDF-G(7%)	0.50±0.08	0.83 ± 0.08	58 ± 3	63 ± 3
PVDF-BT(0.5%)	0.5±0.2	0.66±0.03	75±1	68±1
PVDF-BT(7%)	0.40±0.06	0.71±0.02	77±1	100±5
PVDF-(G:BT) 1:1	0.38±0.05	0.48±0.01	55±3	65±5

Values of contact angle with pure water of 139 ± 3 ° have been estimated for the pristine PVDF while values of 128 ± 8° have been measured on PVDF-BT0.5; PVDF-BT07 membrane and PVDF-(BT-G) membranes have also revealed good wetting resistance with contact angle values of 130 ± 2° and 136 ± 4 °, respectively. PVDF-G(0.5%) exhibits also a good wetting resistance with a contact angle of 136±1 [8] (Fig. 5.10).

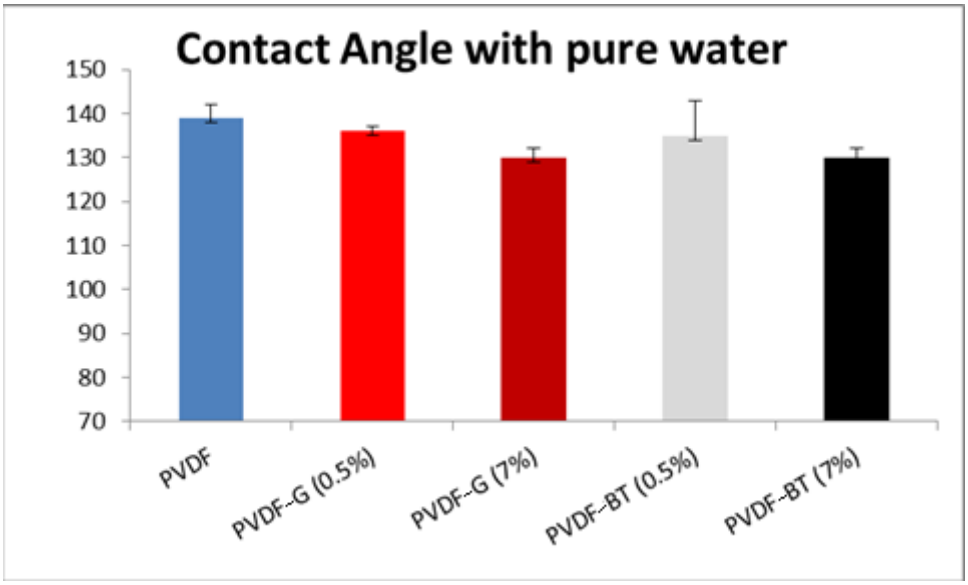

Figure 5.10 *Contact angles for the PVDF-based prepared membranes.*

The wetting resistance of the prepared membranes have been also evaluated with sodium chloride solution at different concentration. For these tests the concentration of salt in seawater (0.6M) and the concentration close to supersaturation level (5M) have been considered in order to simulate the composition of the streams used in MD and MCr tests. The figure 5.11 shows the trend of contact angles with increasing NaCl concentration for pristine PVDF, PVDF-G (0.5%) and PVDF-BT(0.5%). Pristine PVDF membrane shows the highest value with pure water (139°), whereas a decrease down to 122° is observed with 5M NaCl droplets. The highest decrease has been detected for PVDF-BT(0.5%) with a reduction of the contact angle value of 14%. On contrary PVDF-G(0.5%) shows an reduction only of 5% with a contact angle of 129°. In the overall, the membranes filled with G exhibit a better resistance to wetting events.

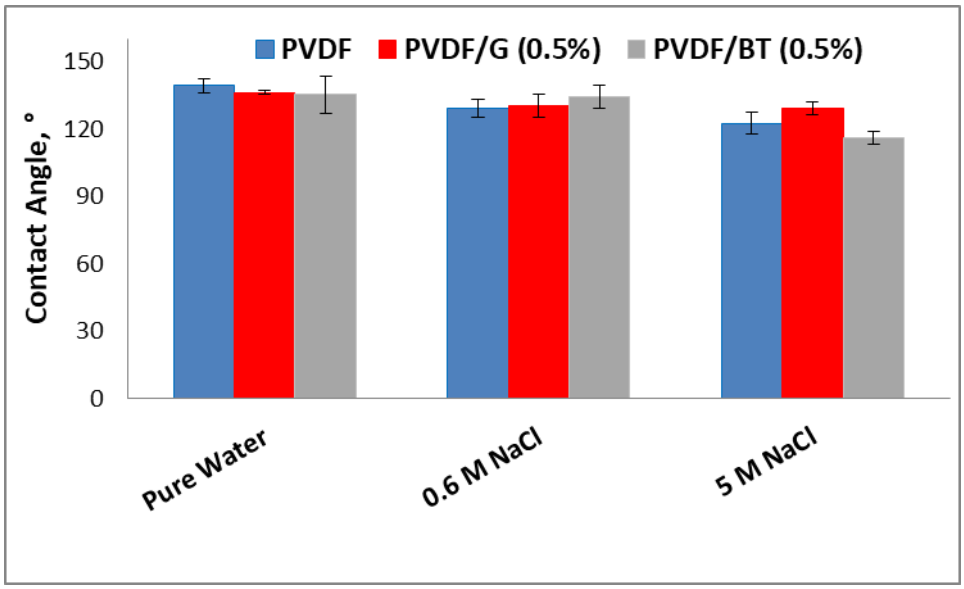

Figure 5.11 *Contact angles trend with the increase of sodium chloride concentration.*

The wetting resistance has been also evaluated with time by the first 30 minutes of contact. Each droplet has been covered with a clear cup so that effects of evaporation have been limited. Figure 5.12 shows the contact angle trends with 0.6M NaCl for the three tested membranes. In tables 5.3 are summarized the values achieved at the beginning and the end of the contact angle test with pure water and 0.6M NaCl solution.

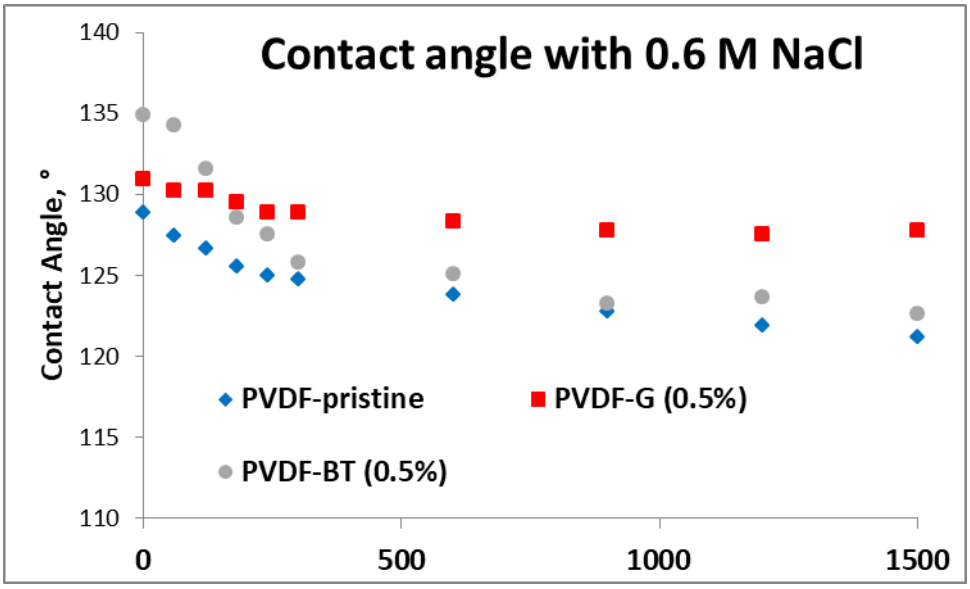

Figure 5.12 *Contact angles trend with 0.6M NaCl droplet.*

PVDF-G (0.5%) showed the highest wetting resistance when 0.6M NaCl has been used for the test with the contact angle decreased from 130° to 124°. On contrary PVDF-BT(0.5%) showed the

higher wetting resistance when only pure water has been used for the test with a decrease from 135° to 131°.

Table 5.3. Contact angle after 30minutes for pristine PVDF, PVDF-G(0.5%) and PVDF-BT(0.5%).

	Contact angle with Pure Water		**Contact angle with 0.6 M NaCl**	
	T= 0	T= 30 min	T= 0	T= 30 min
pristine PVDF	139±3	127±2	129±4	121±3
PVDF-G (0.5%)	136±1	125±3	130±5	124±6
PVDF-BT (0.5%)	135±8	131±6	134±5	122±6

Histograms reported in Figure 5.13a shows that the inclusion of 2D materials exfoliated via WJM into the PVDF matrix improves the resistance at break in comparison to the pristine PVDF membrane (elongation at break of 32.6±6%). A low elongation at break indicates low ductility so the material will be less likely to warp and break. Instead High ductility indicates that a material will be more likely to deform and not break. This property is a fundamental requisite for membrane durability and processing because is mayor the possibility to resist at external stress during the processes. The highest resistance at break has been estimated for PVDF-G (0.5%) and PVDF-BT (7%) membranes with values of 88±5 and 84.3±8 %, respectively. An increase of 170 and 159% has been measured with respect to pristine PVDF. The enhanced mechanical resistance obtained with WJM exfoliated few layers has been further confirmed by the Young modulus, which appears to be more contained when the 2D fillers are embedded in the polymer matrix, especially for the membrane PVDF-BT (7%) with a value of 59.33N/mm^2 (Figure 5.13b). In the literature, contradictory results can be found - worsening or enhancing of elastic moduli - depending on the effect of the average lateral size, directional alignment, degree of dispersion in polymer matrix, and the thickness of the 2D nanofillers on the final properties of polymeric matrices [9,10]. The 2D nature of the nanoflakes is the major reason for enhancement of mechanical proprieties due to major specific surface area of 2D flakes and improved mechanical interlocking/adhesion at the filler-matrix interface [11,12].

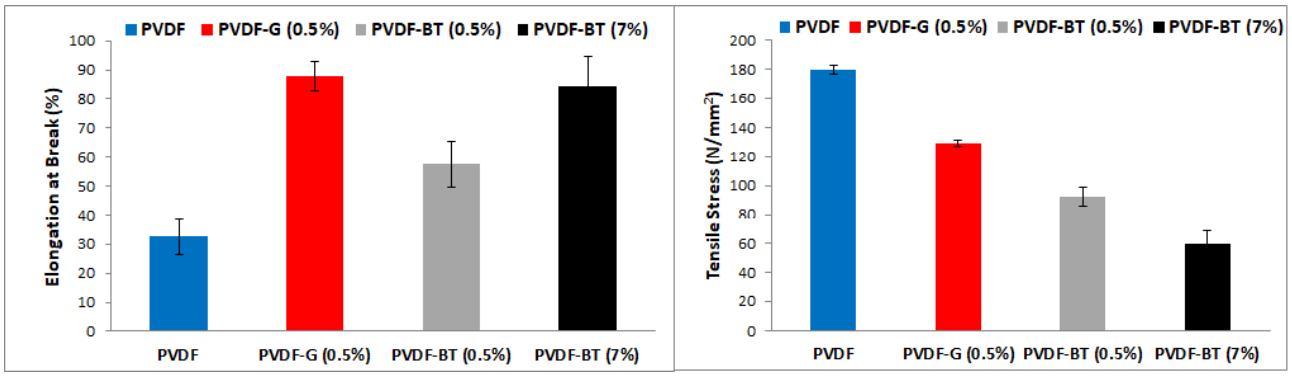

Figure5.13 *Elongation at break (a) and tensile stress (b) estimated for pristine PVDF, PVDF-G (0.5%), PVDF-BT (0.5%) and PVDF-BT (7%) membranes.*

The mechanical performance of PVDF membranes functionalized with graphene has been also evaluated in comparison to that of membranes functionalised with graphene exfoliated via traditional UW [3] at a comparable concentration of nanofiller (0.5 and 7 %, respectively). This has been done to evaluate the quality of the exfoliated materials via WJM with respect to a more traditional method (i.e. UW). Figures 5.14a and b show the results obtained with pristine PVDF membrane, PVDF with graphene exfoliated via WJM and UW (denominated PVDF-GUW) at two concentrations.

It has been proved that the inclusion of graphene (0.5%) exfoliated via WJM into the PVDF matrix improves the resistance at break by up to 175% compared to the pristine membrane (PVDF), whereas the resistance at the break increases by 166% for the composite membranes with graphene exfoliated via UW at the same concentration (0.5%), when compared to the pristine PVDF membrane. Moreover, when the graphene percentage in the WJM membranes has increased up to 7.0% an improvement of 38% can be obtained while a drastic reduction in the elongation at break (-73%) is estimated for PVDF-GUW at 10% nanofiller. Therefore, the largest size of graphene flakes improved the elastic behaviour of the composite membranes with respect to both the pristine PVDF membrane and composite membranes prepared with PVDF-GUW.

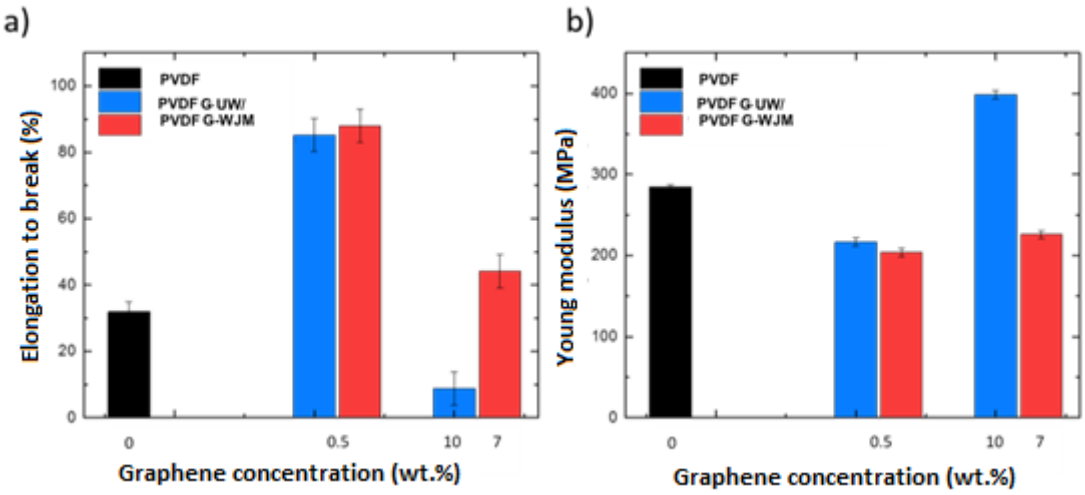

Figure 5.14 *Young module and elongation at break estimated for the pristine PVDF membranes and graphene-WJM (0.5 and 7.0 wt.% derived from dispersions at 0.65 and 10 g/L, in red) and graphene-UW membranes (0.5 and 5 wt.%, in blue) [3].*

5.4 Summary

For the first time, ultrathin porous PVDF-based membranes have been successfully prepared with the combination of no-solvent phase inversion and high-exfoliation Wet Jet Mill techniques. The aims of the prepared membranes were to enhance the productivity and the efficiency for membrane distillation/crystallization processes. Graphene and bismuth telluride flakes exfoliated via WJM have been utilized in this challenge. As explained in this Chapter, the PVDF-based membranes with 2D flakes, compared with pristine PVDF, have a good resistance to wetting and improved mechanical resistance. The internal morphological structures (pore size and porosity) of the prepared membranes changes based on the type of flakes and its concentration. The flakes exfoliated via WJM respect the same flakes exfoliated via traditional technique (UW) present a higher lateral size and lower thickness, thus resulting in a higher surface area.

Reference

[1] E. Gontarek, F. Macedonio, F. Militano, L. Giorno, M. Lieder, A. Politano, E. Drioli, A. Gugliuzza, Adsorption-assisted transport of water vapour in super-hydrophobic membranes filled with multilayer graphene platelets, Nanoscale. 11 (2019) 11521–11529. doi:10.1039/C9NR02581B.

[2] F. Bonaccorso, A. Bartolotta, J.N. Coleman, C. Backes, 2D-Crystal-Based Functional Inks, Adv. Mater. (2016). doi:10.1002/adma.201506410.

[3] M. Frappa, A.E. Del Rio Castillo, F. Macedonio, A. Politano, E. Drioli, F. Bonaccorso, V. Pellegrini, A. Gugliuzza, A few-layer graphene for advanced composite PVDF membranes dedicated to water desalination: a comparative study, Nanoscale Adv. 2 (2020) 4728–4739. doi:10.1039/D0NA00403K.

[4] A.E. Del Rio Castillo, V. Pellegrini, A. Ansaldo, F. Ricciardella, H. Sun, L. Marasco, J. Buha, Z. Dang, L. Gagliani, E. Lago, N. Curreli, S. Gentiluomo, F. Palazon, M. Prato, R. Oropesa-Nuñez, P.S. Toth, E. Mantero, M. Crugliano, A. Gamucci, A. Tomadin, M. Polini, F. Bonaccorso, High-yield production of 2D crystals by wet-jet milling, Mater. Horizons. (2018). doi:10.1039/c8mh00487k.

[5] A.E. Del Río Castillo, C.D. Reyes-Vazquez, L.E. Rojas-Martinez, S.B. Thorat, M. Serri, A.L. Martinez-Hernandez, C. Velasco-Santos, V. Pellegrini, F. Bonaccorso, Single-step exfoliation and functionalization of few-layers black phosphorus and its application for polymer composites, FlatChem. (2019). doi:10.1016/j.flatc.2019.100131.

[6] Y. Hosokawa, K. Tomita, M. Takashiri, Growth of single-crystalline Bi2Te3 hexagonal nanoplates with and without single nanopores during temperature-controlled solvothermal synthesis, Sci. Rep. 9 (2019) 10790. doi:10.1038/s41598-019-47356-5.

[7] S. Charpentier, L. Galletti, G. Kunakova, R. Arpaia, Y. Song, R. Baghdadi, S.M. Wang, A. Kalaboukhov, E. Olsson, F. Tafuri, D. Golubev, J. Linder, T. Bauch, F. Lombardi, Induced unconventional superconductivity on the surface states of Bi2Te3 topological insulator, Nat. Commun. 8 (2017) 2019. doi:10.1038/s41467-017-02069-z.

[8] A. Gugliuzza, A. Politano, E. Drioli, The advent of graphene and other two-dimensional materials in membrane science and technology, Curr. Opin. Chem. Eng. 16 (2017) 78–85. doi:10.1016/j.coche.2017.03.003.

[9] S. Dervin, D.D. Dionysiou, S.C. Pillai, 2D nanostructures for water purification: Graphene and beyond, Nanoscale. (2016). doi:10.1039/c6nr04508a.

[10] K.K. Sadasivuni, D. Ponnamma, J. Kim, S. Thomas, Graphene-based polymer nanocomposites in electronics, 2015. doi:10.1007/978-3-319-13875-6.

[11] A. Gugliuzza, F. Macedonio, A. Politano, E. Drioli, Prospects of 2D materials-based membranes in water desalination, Chem. Eng. Trans. (2019). doi:10.3303/CET1973045.

[12] A. Abdel-Karim, J.M. Luque-Alled, S. Leaper, M. Alberto, X. Fan, A. Vijayaraghavan, T.A. Gad-Allah, A.S. El-Kalliny, G. Szekely, S.I.A. Ahmed, S.M. Holmes, P. Gorgojo, PVDF membranes

containing reduced graphene oxide: Effect of degree of reduction on membrane distillation performance, Desalination. (2019). doi:10.1016/j.desal.2018.11.014.

Chapter 6:

PVDF membranes functionalized with wet-jet milling exfoliated 2D materials for enhanced Membrane Distillation

Water desalination is considered a reliable and sustainable path for managing natural resources and providing solutions to water scarcity [1,2]. As a greener technology, membrane distillation (MD) allows eco-sustainable recovery of fresh water from saline streams [3–7] as well as being suitable for the conservation of ecosystems and biodiversity [8]. Herein, we propose new membranes functionalized with 2D materials, whose preparation has been described in Chapter 5, for equipping Membrane Distillation devices. The intrinsic characteristics of the membranes - porosity, pore size, hydrophobicity, mechanical resistance, etc. make them ideal for MD processes [9–18]. The focus of the present research is the evaluation of the effects of confined few layers graphene (G) and bismuth telluride (BT), exfoliated by WJM, on the productivity of membrane distillation through an optimized use of the thermal energy. In particular, bismuth telluride has been exploited for the first time in frontier processes for water desalination.

This work demonstrates as an adequate combination of cooperative functions allocated in a single membrane allows producing fruitful water desalination through the realization of a renewed ultra-fast and energy-efficient membrane distillation. In this regard, comparative analyses are also proposed to examine the real progress beyond the state of the art in the field of mass and thermal energy trade-offs.

6.1 Membrane Distillation Tests

6.1.1 Effects of few layers graphene on mass transfer through PVDF membranes

All membranes resumed in table 6.1 have been tested in membrane distillation operations by using a direct contact configuration and choosing NaCl 0.6M stream as a model solution.

For each kind of membranes, circular sample specimens have been allocated in a circular module with a diameter of 3.8 cm. as displayed in Figure 6.1. Details of working conditions used for each process are reported in the chapter 5

Table 6.1 *Membranes tested in MD with related morphological characteristics.*

Name of Membrane	Filler Dispersed in NMP	Pore size (µm)	Porosity (%)	Thickness (µm)
PVDF	No Filler	0.48±0.09	63±5	57±2
PVDF-G (0.5%)	Graphene	0.24±0.05	56 ± 7	62 ± 3
PVDF-G (7%)	Graphene	0.50±0.08	58 ± 3	63 ± 3
PVDF-BT (0.5%)	Bi_2Te_3	0.5±0.2	75±1	68±1
PVDF-BT (7%)	Bi_2Te_3	0.40±0.06	77±1	100±5
PVDF-BT-G 1-1	Bi_2Te_3 and Graphene (ratio 1:1)	0.38±0.05	55±3	65±5

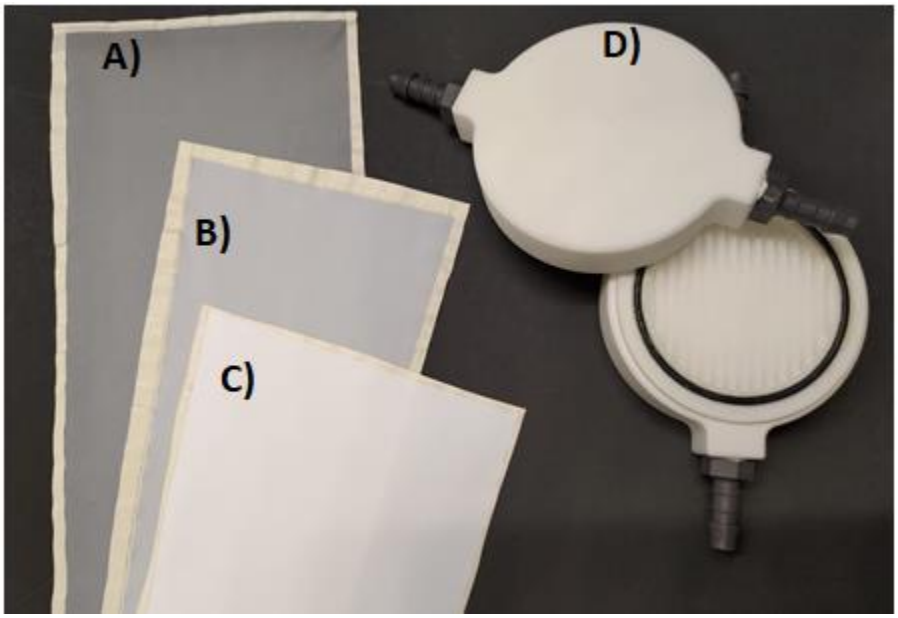

Figure 6.1 *Picture of three prepared membrane and membrane module for flat sheet membrane: A) PVDF-G(7%), B) PVDF-G(0.5%), C) pristine PVDF) and D) membrane module.*

Figure 6.2 shows the flux measured through PVDF-G (0.5 and 7 %) and pristine PVDF membranes as a function of the temperature. In this case NaCl is used as feed solution – at a concentration of 0.6 M corresponding to TDS 35 g/L of seawater. As expected, a general increase in the flux is observed with temperature; however, higher mass transfer is detected for membranes filled with Graphene flakes (FLG) according to the sequence PVDF-G (0.5%) > PVDF-G (7%) > pristine PVDF. Considering that the membranes exhibit more or less comparable porosity and thickness but a smaller mean pore size for PVDF-G (0.5%) membrane, it is reasonable to suppose an involvement of the nanofiller in the diffusion of water through the membranes [4,7,19].

When an inert gas, (i.e. nitrogen), has been used through the membranes, a transport dependence on the pore size has been detected as a consequence of the different resistance opposed to the mass transfer. In fact, Fig. 6.2a shows how the pristine PVDF membranes permeated similarly to the PVDF-G(7%) but much more than the PVDF-G(0.5%) ones. On contrary when only water vapor is present (as in MD process) PVDF-G(0.5%) allow the passage of more water vapor molecules. In fact the flux reported in fig. 6.2 shows a higher flux for PVDF-G(0.5%) than PVDF-G(7%) and pristine PVDF. For the latter, the lowering in the flux has been also ascribed to the effect of a minor driving force; that is, a lower difference in the vapour partial pressure (ΔP) across the membrane (table 6.2).

a)

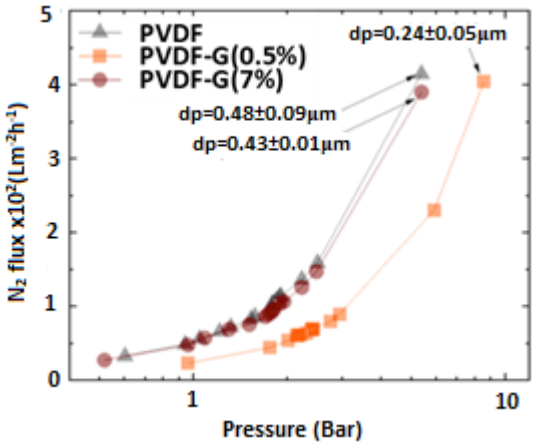

b)

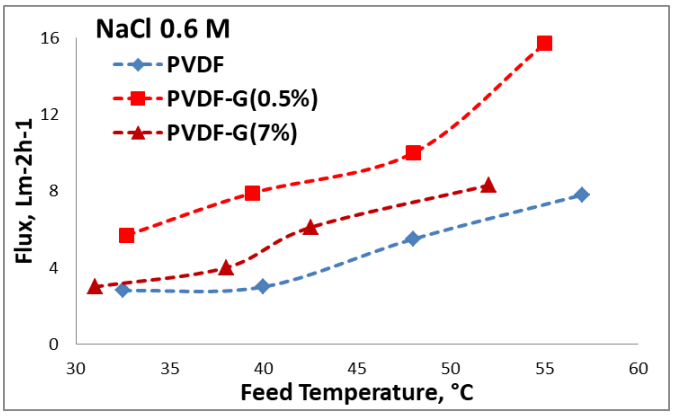

Figure 6.2 *(a) N2 Flux vs pressure at 20°C and water flux at 40 °C; (B)Flux vs Tfeed estimated at 100 mLmin^{-1} for pristine PVDF and PVDF-G membranes in NaCl 0.6 M solutions.*

Table 6.2 shows the MD transport coefficients (B) (defined in Chapter 4 eq. 4.20) calculated for the two PVDF-G membranes [20]. For PVDF-G(0.5%), the transport coefficient decrease linearly with increasing driving force (ΔP). As expected, the reduction of resistance to mass transfer promotes a higher flux. On contrary, when the graphene concentration in the membrane network increases the trend is fluctuating independently of the difference of partial pressure applied across the membranes. This behaviour suggests there is no inertia of graphene towards water vapour but rather an involvement of the flakes in the water diffusion process.

The literature refers to the aptitude of graphene to interact with water molecules [21] through adsorption of water on the edge of graphene. Raman spectroscopy (Chapter 5) yields indication of

the presence of defects due to the edges of the WJM few layers (Fig. 5.4), while XPS analysis indicates the state of oxidation of around 1.2% for WJM few layer graphene (Fig. 5.6).

Table 6.2. *MD mass transport coefficient estimated for PVDF-G(0.5%) and PVDF-G(7%) at different difference of partial pressure (ΔP).*

PVDF-G (0.5%)		**PVDF-G (7%)**	
ΔP (Pa)	**Bx 10-4 (L $m^{-2}h^{-1}Pa^{-1}$)**	**ΔP (Pa)**	**Bx 10-4 ($Lm^{-2}h^{-1}Pa^{-1}$)**
3628	8.5	3044	5.9
5683	8.0	5008	4.5
10040	6.8	6750	5.7
14296	6.5	11517	4.6

Total salt rejection (100%) has been achieved in all the cases, providing clear evidence about the good membrane waterproofness. Total rejection can be generally observed for membranes filled with WJM few layer graphene, independently of relatively low liquid entry pressure (LEP), which is around 1 bar for all membranes. Really, functionalised graphene PVDF membranes show contact angle values higher than 130°. More specifically, PVDF-G (0.5%) and PVDF-G (7%) membrane surfaces show contact angle values of 136±1° and 129±2° against a value of 144±2 ° measured for the pristine PVDF membrane. This results in a very good resistance to undesired wetting and efficient stop to ion diffusion through the membranes (Table 6.2).

Experiments have been carried out with time, yielding indication about constant and stable fluxes and confirming a good resistance to fouling phenomena [22] (Figure 6.3). Figure 6.3 shows an increase in productivity of 180% for PVDF-G (0.5%) in contact with NaCl 0.6 M as the temperature raises from 40 to 55 °C, leading to an increase in the flux up to 99.7% as compared to the pristine PVDF.

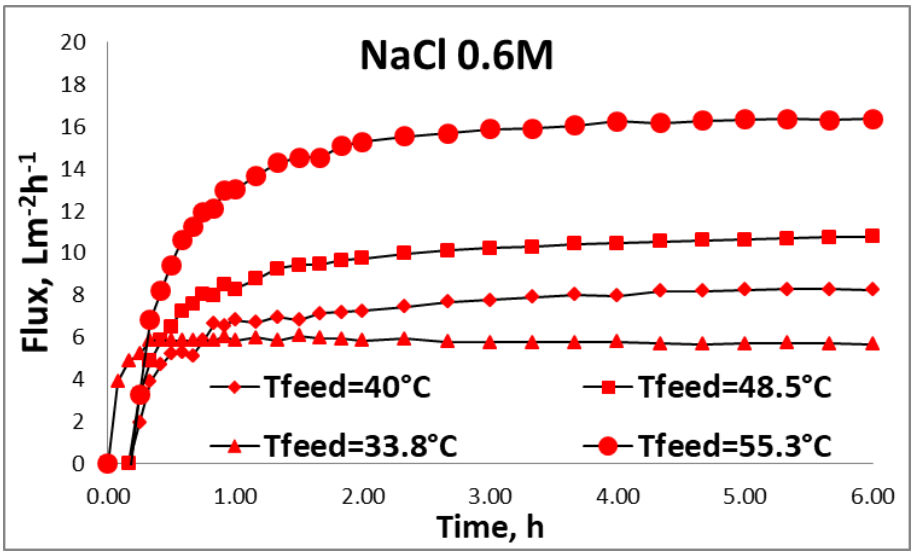

Figure 6.3 *Flux with time estimated at different Tfeed and 100 mLmin^{-1} for PVDF-G(0.5%) membrane when NaCl 0.6 M is used.*

Summarizing, the confinement of low amounts of exfoliated graphene in membranes appears to be a good compromise for enhancing the MD productivity without undergoing all in all important thermal polarization effects due to the high thermal conductivity of graphene

The relative flux (F/F_0) indicated a decline in water transfer of around 30% over the last 13 h of operation for the PVDF-G(0.5%) membrane (fig.6.4). This undesired event was due of the feed concentration [23].

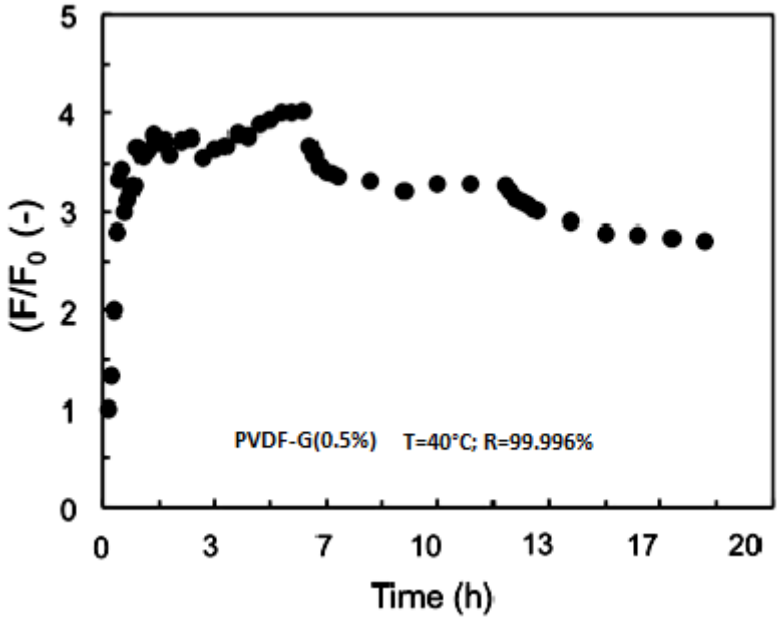

Figure 6.4 *Relative flux (F/F_0) estimated with time for PVDF-G(0.65) at T_{feed} = 40 °C and 100 mL min^{-1}.*

To establish the capability of PVDF-G(0.5%) of productivity, experiments at four different flow rates have been carried out as well (from 100 to 400mL/min, NaCl 0.6M solution, T_{feed}= 58 °C, $T_{permeate}$= 14°C). As expected, a further increase in the flux up to 28.4 $Lm^{-2}h^{-1}$ is achievable when working at 55°C under a flow rate of 400 $mLmin^{-1}$, as shown in figure 6.4. Amplifying flow rate in MD test, a better fluid-dynamics aspect is promoted in the boundary layers on membrane surface. In this way a reduction of thermal polarization phenomena can be achieved, detecting a flux increase from 18.4 $Lm^{-2}h^{-1}$ when working at ~ 60 °C and a flow rate of 100 $mLmin^{-1}$ to 28.4 $Lm^{-2}h^{-1}$ when working at ~ 55 °C and a flow rate of 400 $mLmin^{-1}$. In this case, a further increase of ~ 80 % of the flux can be obtained

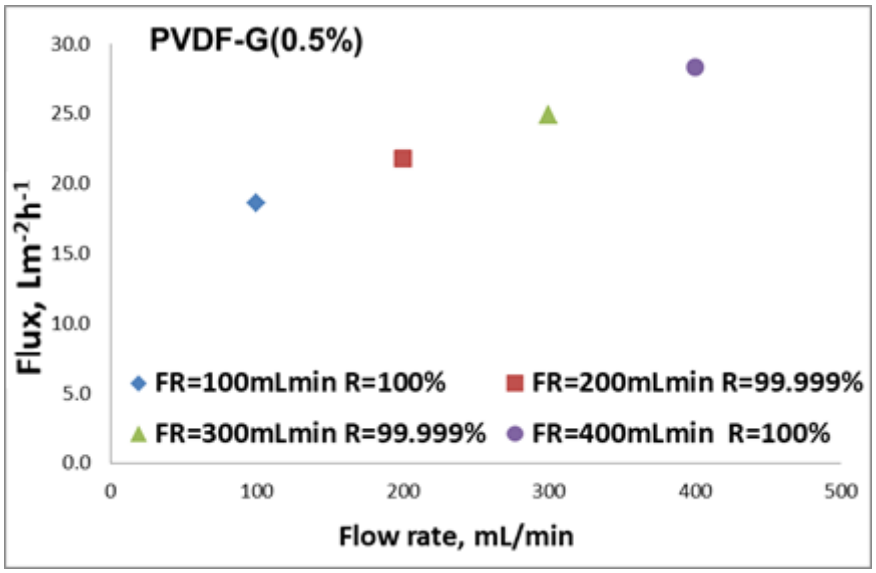

Figure 6.5 *Flux dependence of feed Flow Rate.*

These membranes have been tested under harsher conditions as well. The mass transfer has been evaluated with time by using hypersaline NaCl solutions at 2 M and 4 M (Figure 6.5). These values have been chosen to study the behaviour of membranes prepared and the wetting resistance with solutions having a concentration higher than the concentration of sea water (0.6 M). The higher salinity might be favours the wetting phenomena due to its nature tend to decrease the surface tensions.

The fluxes continue to increase with temperature, even if higher viscosity of the solutions together with reduced water activity cause a loss in the mass transfer. With this regard, it is instructive to compare the performance of PVDF-G membranes with that of other perfluorinated membranes discussed in literature. PVDF-G0.5 exhibits at 48.8°C and with a NaCl solution 4 M a flux of 7 Lm^{-}

$^{2}h^{-1}$ and a rejection value of 99.999 % (Figure 4.3) against a flux of 5 $Lm^{-2}h^{-1}$ and a rejection of 99.0 % estimated at 50 °C for polypropylene membranes layered with a PTFE (Thickness = 35 µm; mean pore size = 0.22 µm porosity = 82 %) [24]. At 65.8 °C and with a NaCl solution of 4 M, PVDF-G0.5 membrane permeates water vapour with a flux of 15.7 $Lm^{-2}h^{-1}$ and a rejection of 99.994 % (Figure 4.3 c) against a flux of 12 $Lm^{-2}h^{-1}$ and a rejection of 99.90 % estimated at 60 °C for a porous superhydrophobic PVDF membrane micro-pillared with CF4 (Thickness = 264 µm; mean pore size= 0.124 µm porosity = 79 %) [25].

a)

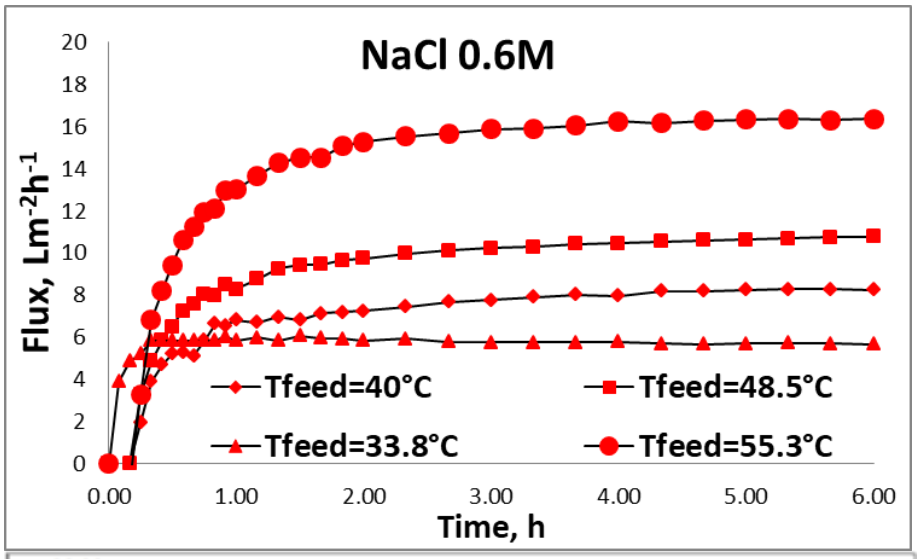

b)

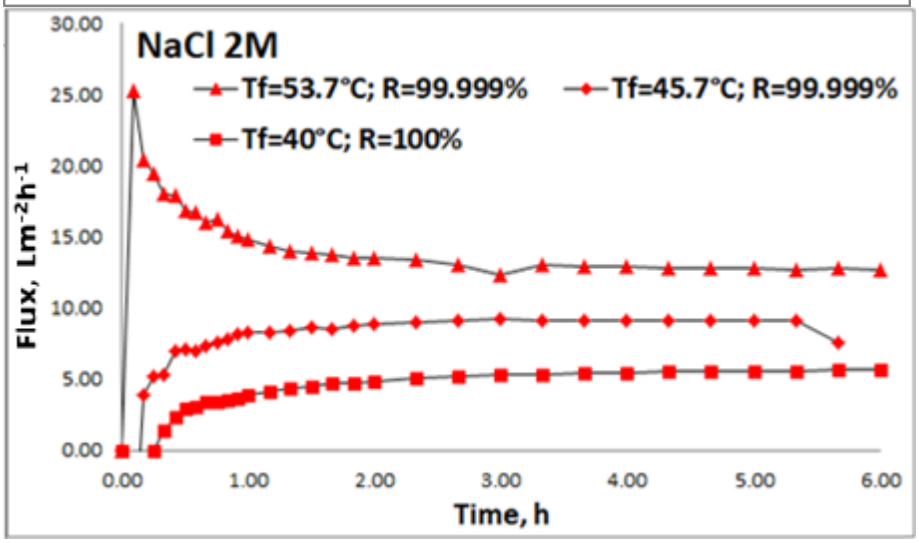

c)

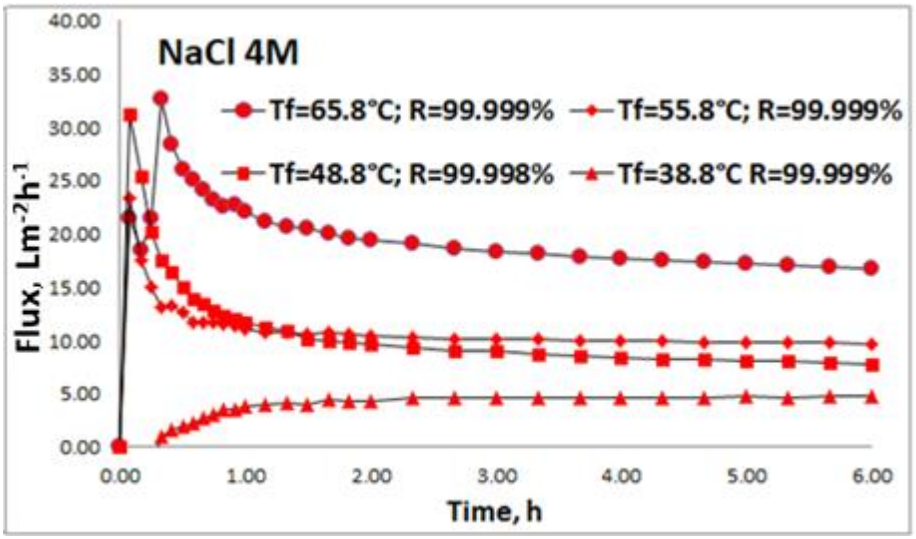

Figure 6.6 *Permeation capacity of PVDF-G(0.5%) membrane under different working conditions: (a) effect of NaCl concentration (0.6, 2 and 4 M) on the flux at 40 °C (a); effect of the temperature on the flux when NaCl 2M (b) and 4 M (c) are used. (T_{feed} of ~ 55 °C and T_{perm} of 20 °C and a flow rate of 100 and 83 mL min^{-1} at feed and permeate side).*

Despite the higher NaCl concentration, the waterproofness continues to be preserved with rejection values always around 99.999 %. However, as expected, a gradual reduction of the mass transfer is detected with the increase of NaCl concentration (2M and 4M) as shown in figure 6.5. It has been chosen to perform MD tests 6 hours long, at different operative conditions (such as different feed temperature and feed concentrations) to understand the behaviour of the prepared membranes. The experimental data reported in figure 6.6 have been done utilizing the same membrane for a total of 72 hours. The testing of the membrane for a so long period proved the stability of the hydrophobic character of the prepared membrane. As can be observed from figure 6.6, in each test steady state conditions have been achieved after 2-2.5 hours, thus justifying the choice to have test 6 hours long. For what concern fouling issue in the prepared and tested membranes, this has been also evaluated and results are reported in figure 6.4 that refers to a test 20 hours long. More specifically, when 2 M solutions are used a reduction of the flux of 31% is appreciated against the flux estimated with NaCl 0.6 M at 40°. With concentration of 4 M the reduction of the flux is of 43%. The higher salt concentration decreases the water activity and so decreases the water vapour pressure. This is expected to cause lower driving force for evaporation with respect to the NaCl 0.6 M solution. However, the increase in temperature results in a proportional increase in the driving force despite the high salt concentrations as shown in Figures 6.6b and 6.6c for concentrations of 2M and 4M respectively. To evaluate the effect of the lateral size of few layers WJM graphene, flux-rejection trade-offs have been compared taking in account the results obtained with PVDF-G and membranes prepared with graphene exfoliated via

ultrasonication (UW) at the same concentration [19]. A plot of rejection *versus* flux has been generated considering membranes worked in plants having a Direct Contact Membrane Distillation (DCMD) configuration and coming in contact with NaCl 0.6 M (35 g/L) (Figure 6.6). PVDF-G (0.5%) membranes - with an effective graphene concentration in membrane of 0.5 % - exhibit an increase in the flux of 38 % and a rejection value of 100 % as compared to membranes containing graphene nanoplatelts (GNPs) exfoliated via UW (GNPs: a thickness of ∼1.8 nm but a lateral size of 120 nm)[19]. Also, PVDF-G (7%) membranes exhibit higher flux and salt rejection (F = 9.05 $Lm^{-2}h^{-1}$ and R = 99.996 %) as compared to GNPs- UW membranes containing GPNs at 10 % (F = 0.3 $Lm^{-2}h^{-1}$ and R = 99.984 %) [26]. These results are not unexpected because a larger lateral size of few-layers provides a greater surface area and subsequently higher contact points between water molecules and nanofiller. A more accessible interface between penetrant and defective flakes supports water diffusion in full agreement with indication provided by the MD mass transport coefficients (*B*) (Table 6.2). To concern the performance of PVDF-G with respect to other tailor-made membranes operated under similar conditions [27–29], further assessment have been done (Figure 6.7). Compared to electrospun membranes based on clay and having an average thickness of 300 µm and an overall porosity of ~ 82 %, PVDF-G membranes show a better flux-rejection ratio with a flux increase of 217 % and a salt rejection of 100 %. Also, an increase in flux of 6 % and a rejection of 100 % against 99.99 % is estimated with respect to supported nonwoven fabric flat-sheet membranes with a thickness of 200 to 215 µm and an overall porosity of ~ 48 to 55 %. A better performance is further appreciated for PVDF-G (0.5%) membranes when compared to the ones functionalized with nanoparticles (NPs, thickness = ~70 µm and overall porosity = ~ 68 %) and processed at 70 °C. Membranes filled with PVDF-G show an increase in flux higher than 13.3 % and a salt rejection of 100 % (Figure 6.6).

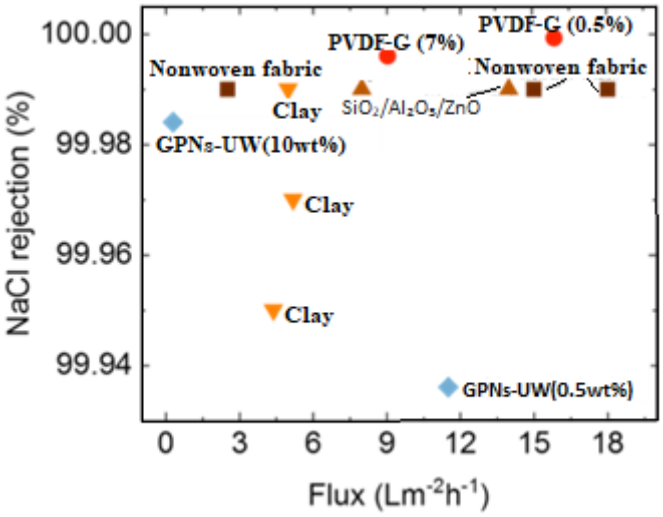

Figure 6.7 *Comparative productivity-efficiency trade-off of membranes based on PVDF enhanced with different fillers, i.e., graphene (obtained by WJM, red circles and UW in blue diamond's [19]), clay (orange triangles)* [30]*, nonwoven fabric (dark brown squares)* [31]*, nanoparticles (NPs) at 70°C (brown triangles)* [29]*. Working conditions: feed: NaCl solution 35 g/L (0.6 M); Tfeed: ~ 55 °C (except for the nanoparticles Tfeed = 70 °C).*

6.1.2 Bismuth Telluride (Bi_2Te_3) enabled PVDF membranes

After graphene flakes, analysed in the previous paragraph, the effect of Bismuth Telluride (Bi_2Te_3, BT) few layers on water vapor transfer has been also evaluated. In the same way of PVDF-G, the membranes functionalized with BT have been put in contact with synthetic seawater (0.6 M NaCl). A Comparative study between graphene and bismuth telluride in membrane process have been also done. A binary mixture with graphene and bismuth telluride has been further prepared to study the behaviour of both materials in the same membrane network.

Figure 6.7 shows a comparison of fluxes measured through PVDF-BT(0.5%), pristine PVDF and PVDF-BT-G(1:1) at different temperature and under a flow rate of 100 mL/min with 0.6M NaCl solution. All the membranes show a salt rejection ranging from 99.99 to 100 %. It is interesting to observe how the PVDF-BT (0.5%) membrane presents a higher ability to transfer water vapor than the pristine PVDF membrane at the same operating conditions. Moreover, the membrane enabled with Bismuth telluride shows a trans-membrane flux higher than the membrane enabled with graphene and with the binary mixture. The first reason of this result could be justified by the highest porosity of *PVDF-BT(0.5%) (75%±1) respect PVDF-G(0.5%) (56%±7)* as reported in table 6.1. Although the morphological parameter of the membranes is important, it should be noted that

PVDF-BT (0.5%) shows greater sensitivity to temperature increase, allowing higher flows than PVDF-G (0.5%). This implies more passages and space for water vapor to pass through. Considering the results obtained at feed temperature of about 50°C, PVDF-BT(0.5%) increase the flux of about 200% than pristine PVDF membrane. The membrane containing BT in mixture with G (1:1) continues to exhibit a constant increase in the mass transfer when compared to the pristine PVDF membrane (ε= *65 %, δ = 58* μ*m*), even if it exhibits a lower porosity (ε= *55 %*) and a bit higher thickness (δ= *65* μ*m*). It is also quite interesting to observe how the difference between the two nanocomposite membranes –PVDF-BT(0.5%) and PVDF-(BT-G) (0.5%) - becomes larger at high temperature, leading to an increase in the flux of 93 % at 48 °C and 137 % at 55 °C for membranes wherein only the chalcogenide compound is confined.

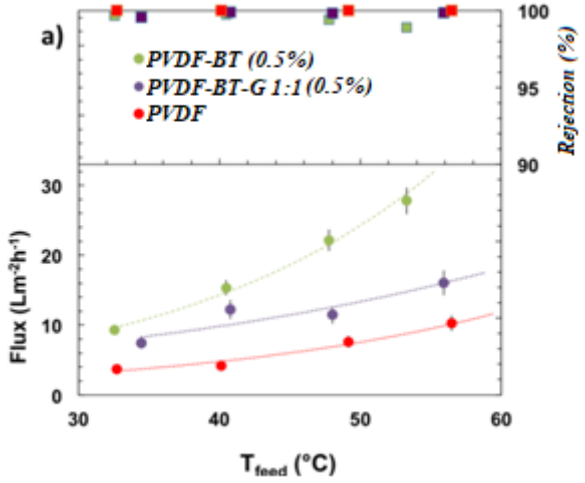

Figure 6.8 *Flux and rejection values estimated at different ΔT for PVDF, PVDF-(BT-G 0.5%) (1:1) and PVDF-BT(0.5%) membranes: Tfeed, 32-55 °C.*

Figure 6.8 yields indication about the stability of the flux with time at different temperatures through PVDF-BT(0.5%).

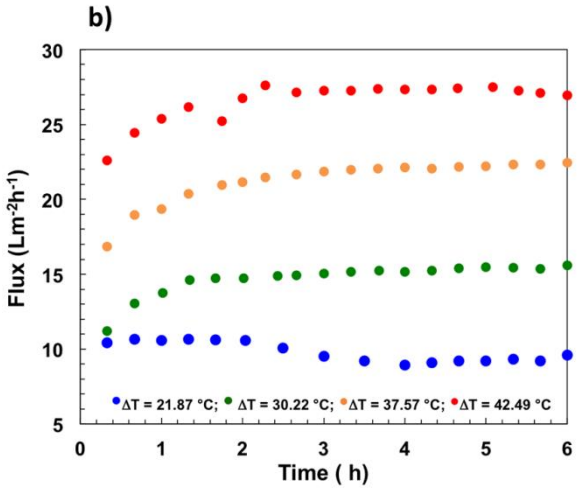

Figure 6.9 *Flux in function of time (h) at different feed Temperature for PVDF-BT(0.5%) membranes: Flow rate at the feed side, 100 mLmin^{-1}; Conc: 35g/L NaCl.*

When a larger content of Bi_2Te_3 (7.0 %) is confined in the polymeric matrix, the flux tends to increase slightly than PVDF-BT(0.5%) at high feed temperature. In fact, At 55 °C PVDF-BT(7%) allow to reaching values of 31.8 Lm^{-2}h^{-1} at ~ and under a flow rate of 100 mLmin^{-1}, slightly higher than the flux of about 27 Lm^{-2}h^{-1} achieved with PVDF-BT(5%), as shown in figure 6.9.

The relative flux (*Fi/F0*) confirms stability and durability of Bi_2Te_3-enabled PVDF membrane at longer operational time as well (Fig.6.10). No decline is observed but rather the flux is kept constant with rejection factors higher than 99.99%. This yields clear indication about a good resistance of these novel membranes to wetting and fouling events. When a larger content of Bi_2Te_3 (7.0%) is confined in the polymeric matrix, the flux tends to increase slightly reaching values of 31.8 Lm $^{-2}$h $^{-1}$ at ~ 55 ◦C and under a flow rate of 100 mL min $^{-1}$. Moreover, PVDF-BT(7%) has been tested in continuous for 1400minutes showing a stable trans-membrane flux over time without show wetting phenomena. In fact, the rejection values ranging from 99.993 to 99.996 %

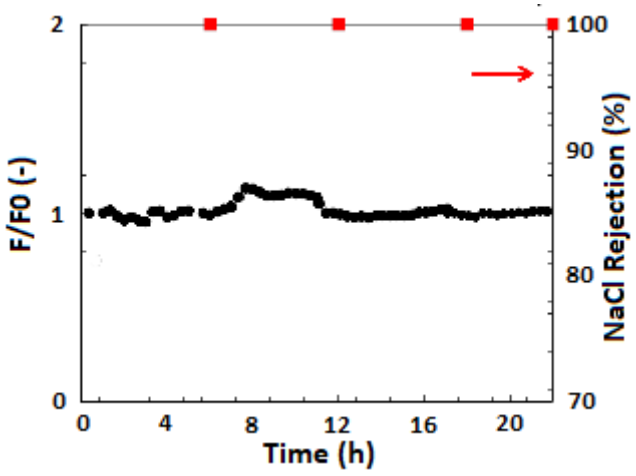

Figure 6.10 *Relative flux (Fi/F0) with time estimated for PVDF-BT (7%) membrane at Tfeed = 58 ◦C; FR= 100 mL min $^{-1}$; Conc: NaCl, 35 g/L.*

Under harsh fluid dynamics, the membrane exhibits a great thermal stability and mechanical robustness reaching fluxes of 74 Lm^{-2}h^{-1}. Also, a good resistance to wetting continues to be appreciated with rejection values ranging from 99.92 to 99.99 %.

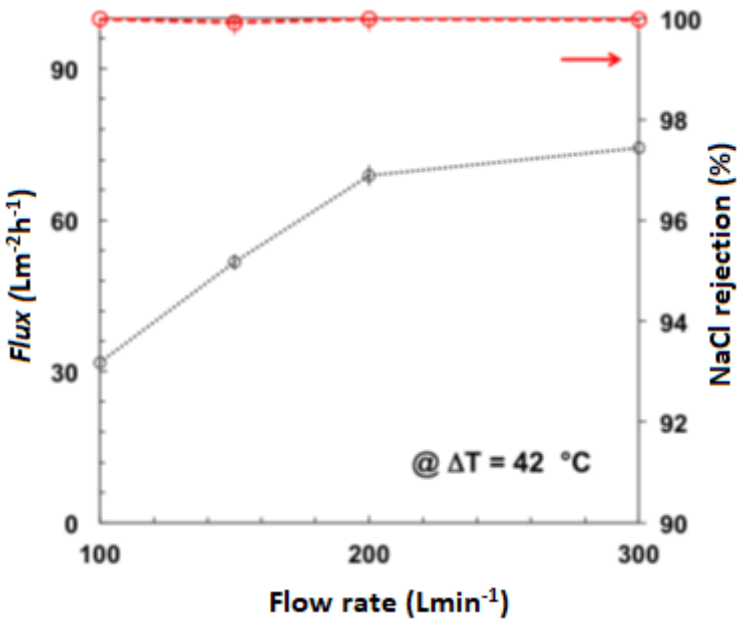

Figure 6.11 *Flux measured through PVDF-BT(7%) membrane as a function of the difference of the volume of fluid per unit time (Flow rate) at Tfeed 58.8 °C and with synthetic seawater (NaCl 35 g/L). Each experiment has been carried out for 6 h.*

Undoubtedly, higher flow rates reduce the residence time of dirtying agents that could deposit on the membrane, i.e. salts contained in the feed). Improved mixing of the feed solution is achieved along with a reduced thermal boundary layer and temperature polarization.

To better appreciate the influence of bismuth telluride in MD process, a comparative analysis has been done with PVDF-based membranes tested under similar working conditions. The gain in productivity is interestingly higher than that estimated for other kinds of nanocomposite membranes, as shown in Table 6.3.

Table 6.3. *Comparative flux estimated for nanocomposite PVDF membranes in DCMD configuration at different temperature and flow rate using NaCl ≈ 35 g/L.*

Membrane	**Tfeed** *[°C]*	**Flow rate** *[mLmin^{-1}]*	**Flux** *[Lm^{-2}h^{-1}]*	**Reference**
PVDF/MWC	60	150	30.8	[32]
PVDF-HFP/G	60	200	23	[33]
PVDF-BT (7%)	58.	200	69	In this work
PVDF/ZnO	60	250	9.68	[18]
PVDF-BT (7%)	58.8	300	74	In this work
PVDF/rGO	90	350	7	[34]

PVDF/PS/ZnO	70	400	15.79	[12]
PVDF/CF4 plasma	62.4	600	38	[35]
PVDF/TiO2	80	720	42	[36]
PVDF/SiO2	60	750	34.2	[37]
PVDF/GNP	80	833	8.27	[16]

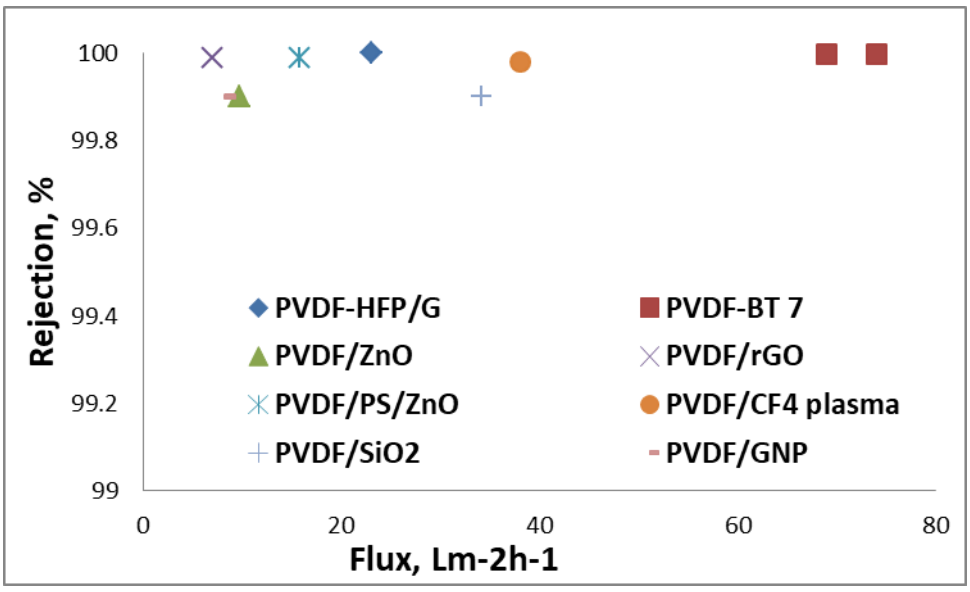

Figure 6.12 *Flux vs Rejection estimated for nanocomposite PVDF membranes in DCMD configuration at different temperature and flow rate using NaCl ≈ 35 g/L.*

Multiwalled carbon nanotubes immobilized in PP-PVDF membranes yielded about a flux of 30.8 $Lm^{-2}h^{-1}$ when worked at 60 °C and with a flow rate of 150 $mLmin^{-1}$ [38]. Electro-spinned PVDF HFP membranes filled with graphene has been demonstrated to exhibit a flux close to 23 $Lm^{-2}h^{-1}$ at 60 °C and with a flow rate of 200 $mLmin^{-1}$ (Woo et al., 2016) as well as hollow fiber PVDF/ZnO membranes worked at 60 ° at a flow rate of 250 $mLmin^{-1}$ have produced a flux of 9.68 $Lm^{-2}h^{-1}$ [18] against 69 $Lm^{-2}h^{-1}$ estimated for PVDF-BT(7%) around 58 °C at 200 $mLmin^{-1}$. PVDF membranes functionalized with polystyrene/ZnO nanoparticles have yielded flux of 17.79 $Lm^{-2}h^{-1}$ at a temperature and flow rate of 70 °C and 400 $mLmin^{-1}$ [12].

Moreover, membranes functionalized with *r*GO have showed flux of 7 $Lm^{-2}h^{-1}$ when contacting NaCl solutions (0.6 M) at 90 °C and with a flow rate of 350 $mLmin^{-1}$ [34]. Also, PVDF/membrane filled with graphene nanoplatelets has yielded a flux of 8.27 $Lm^{-2}h^{-1}$ when operated at 80 °C under a flow rate of 833 $mLmin^{-1}$ [16]. Flux of 38 $Lm^{-2}h^{-1}$ has been obtained with CF_4 plasma-modified superhydrophobic PVDF membranes at 62.4 °C and flow rate of 600 $mLmin^{-1}$ [35]. Depositions of TiO2 particles on PVDF have rendered a flux of 42 $Lm^{-2}h^{-1}$ at 80 °C and 720 $mLmin^{-1}$ [36]. Flux of 34.2 $Lm^{-2}h^{-1}$ has been obtained at 60 °C and 750 $mLmin^{-1}$ with PVDF/SiO_2 membranes [37]. For

PVDF-BT(7%) membranes, we calculate a 74 $Lm^{-2}h^{-1}$ at a lower temperature (T_{feed} = 58.8 °C) and with a flow rate of 300 $mLmin^{-1}$. From this comparison, BT seems to be more beneficial for higher flux at milder working conditions.

6.2 Energetics aspects concerning membranes filled with bismuth telluride

Undoubtedly, MD is a somewhat complex process and its performance depends on the interplay of various factors, including morphological and thermal properties. In this case, thickness and pore size are somewhat comparable and are not primary for governing the mass transfer. On the other hand, the highest porosity of PVDF-BT(0.5%) could justify the largest mass transfer but it does not rationalize fully the amplification of the flux observed at higher temperature. Another issue is the susceptibility of the flux to wetting and/or fouling events.

According to equations reported in Chapter 4 (eq. 4.25 and 4.26), heat flow has been estimated for each single membrane taking in account morphological features of the membrane, thermal conductivity and flux. Figure 6.12 shows the amount of thermal energy (*Q*) transmitted through pristine and membranes containing nanofiller at different content. As expected, the amount of heat transmitted through the membranes increases with rising temperature [39,40], even if reduced heat dissipation is appreciated for membranes filled with bismuth telluride only (Fig.6.13).

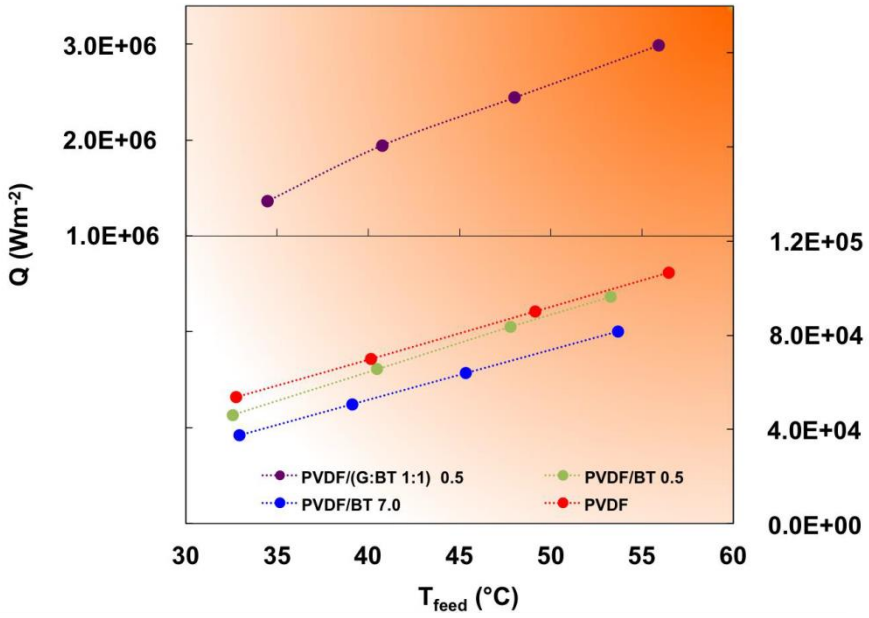

Figure 6.13 *Heat flow estimated for all membranes within the overall range of temperature and at flow rate of 100 $mLmin^{-1}$.*

Compared to the pristine PVDF membrane, PVDF-BT(0.5%) yields heat flow values less than 140 % at 32 °C, while a reduction of 2 % is found at 53 °C. A further lessening of heat dissipation around 190 % at 32 °C and 170 % at 53 °C is obtained with a thicker PVDF-BT (7%) membrane (δ= 100 μm). Based on equations 4.25-4.26, a higher thickness reduces the heat transfer coefficient of thermal conduction via membrane material, but also it renders longer the passage for water vapor [41]. It is however important to remark that membranes filled with Bi_2Te_3 shows the highest trans-membrane fluxes with a pronounced exponential trend at higher temperature. Heat flow is positively proportional to the overall membrane thermal conductivity, which depends in turn on thermal conductivity of materials and related porosity.

A thermal conductivity of 0.5 to 1.6 $Wm^{-1}K^{-1}$ in bulk and of 0.1 to 0.3 $Wm^{-1}K^{-1}$ in stacked films has been estimated for Bi_2Te_3 at room temperature against 0.17-0.21 $Wm^{-1}K^{-1}$ of PVDF [42]. While considering the role of morphological parameters of the membranes and the increase in thermal conductivity of materials with temperature, it is important to point out that Bi_2Te_3 is one of the best thermoelectric materials with the highest thermoelectric figure of merit, ZT (~1.1-1.2) of any material around room temperature. When exfoliated, it could maximize a Seebeck effect (an electromotive force (emf) that develops across two points of an electrically conducting material when there is a temperature difference between them) [43]. So, in membranes with widespread distribution of Bi_2Te_3 (Figure 6.14) synergistic effects may reasonably enhance the ability of the Bi_2Te_3-enabled membranes to restore the driving force thus maximizing the productivity especially when the feed temperature is increased while the temperature at the cold side is fixed. Figure 6.8 shows indeed an important widening of the gap between the fluxes measured at temperature higher than 40 °C.

The beneficial effect of the chacolgenide compound seems to be contrasted in PVDF-(BT-G) 0.5 (Figure 6.13). Few layer graphene with a thermal conductivity of 5000 $Wm^{-1}K^{-1}$ [42] causes a heat loss higher than one order of magnitude as compared with the other membrane-types (Figure 6.14). This large heat dissipation is expected to sacrifice the driving force, even if the mass transfer continues to control the overall MD transport. Recently, Perrotta et al. (2020) [4] have been discussed on the defective graphene ability to accelerate water uptake from saline stream. As mentioned, the productivity of this membrane is better than that measured through the pristine PVDF membrane, in spite of the fact that the morphological features should be not in favour to a large mass transfer. This confirms how complex effects govern the performance of a MD process and it could be misdealing to identify only one factor as affecting the final performance of the

separation. PVDF-(BT-G) membrane is not however satisfactory from energetics point of view, while the choice to incorporate Bi_2Te_3 becomes crucial to make MD process ultrafast and energetically efficient simultaneously. Bi2Te3-enabled membranes show the best capability to promote water vapor transfer while contrasting heat conduction. According to equation 4.23, a superior thermal efficiency is subsequent for the MD process (Figure 6.14). An increase of 65% is estimated for PVDF-BT(7%) when the difference of the temperature (ΔT) across the membrane is increased; the intensification is of 40 % for PVDF-BT (0.5%) against the 34 % for the pristine PVDF membrane. As expected, a loss of thermal efficiency is assessed for the membrane containing the mixture of few layers bismuth telluride and graphene.

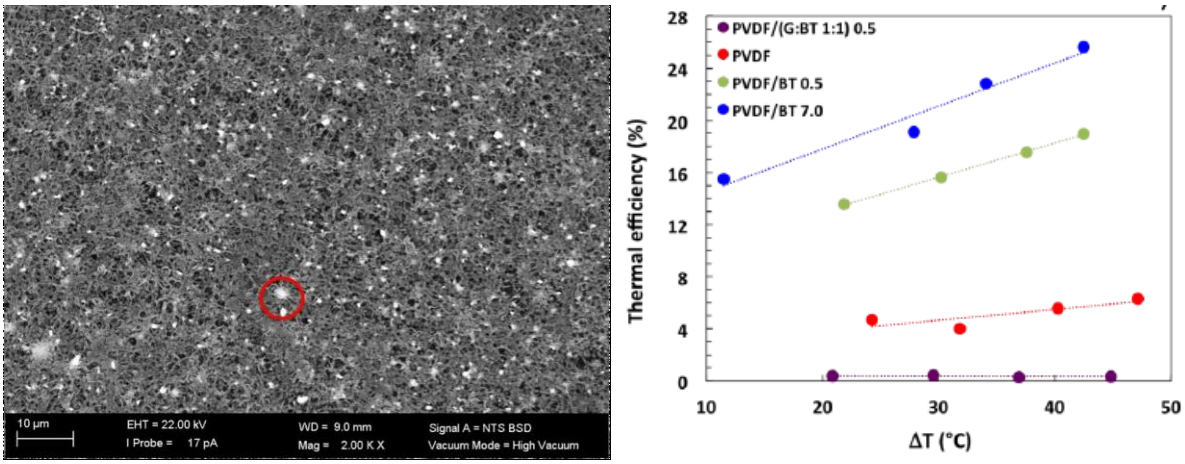

Figure 6.14 *BSE micrograph collected onto the surface of PVDT/BT(7%) membrane; Thermal efficiency estimated for all membranes within the overall range of temperature at flow rate of 100 mLmin^{-1}.*

In other words, a lower resistance to mass transfer and a higher resistance to heat flow are coupled in membranes filled entirely with bismuth telluride. Values of thermal efficiency up to 19 and 25.6 % are calculated at 53 °C for systems containing 0.5 and 7.0 % of the chalcogenide compound against a value of 6% estimated for pristine PVDF worked under same conditions (Figure 6.13).

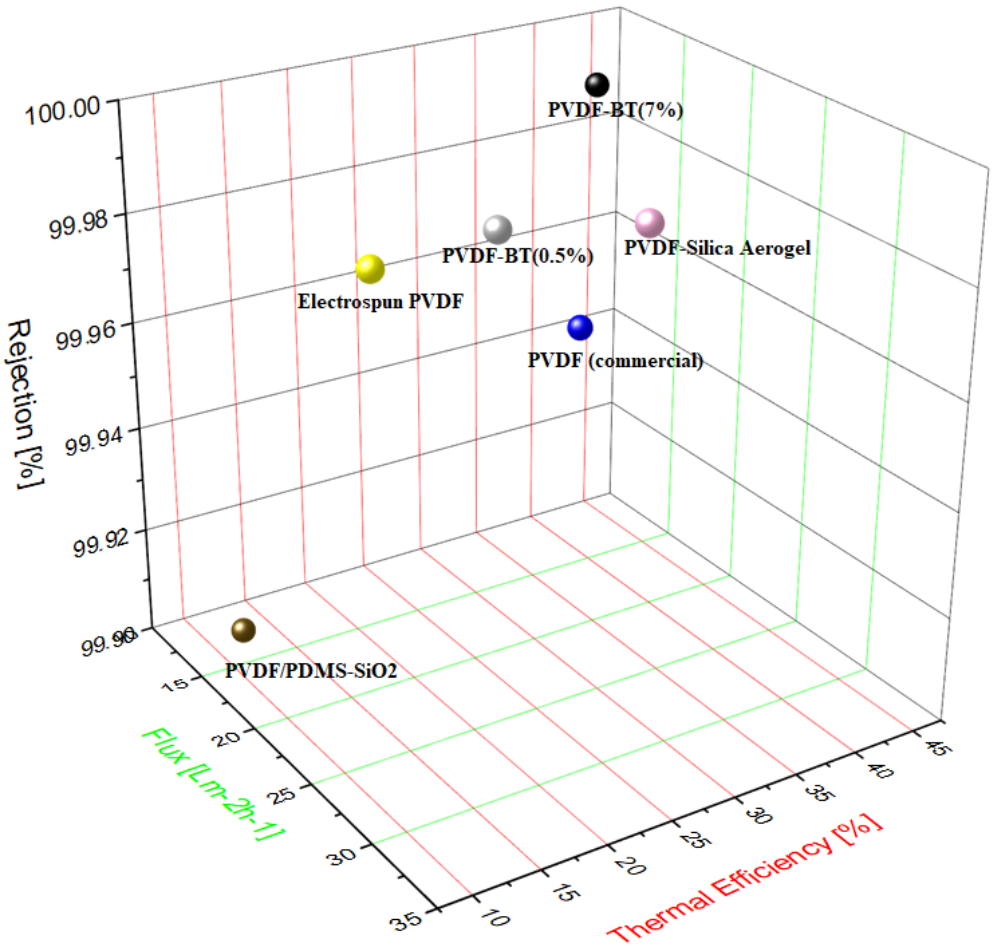

Figure 6.15 *Thermally efficiency vs Flux vs Rejection estimated for some PVDF membrane-types.*

It should be recalled that an increase in thermal efficiency implies a minor use of thermal energy and, hence, major sustainability. Compared to other PVDF membrane-types [11,44–46], productivity and thermal efficiency trade-off appears to be somewhat competitive for PVDF-BT membranes if examined from mass and energy transfer point of views (Table 6.4). A suitable balance between water flux and thermal efficiency is obtained in the same membrane after 6h-MD test and with NaCl 35 g/L [47–49].

Table 6.4. *Comparative Flux and Thermal efficiency estimated for some PVDF membrane-types.*

Membrane	**$T_{feed}/T_{permeate}$** *[°C]*	**Flux** *[$Lm^{-2}h^{-1}$]*	**Thermal Efficiency** *[%]*	**Rejection** [%]	**Reference**
PVDF (Hollow Fiber)	60.7/29.8	0.64	28.92	*n.a.*	[44]
PVDF (commercial)	60/20	20.5	~ 33*	99.96	[11]
PVDF/PDMS–SiO2	73/25	12.4	12.9	99.9	[17]
Electrospun PVDF	50/25	25.99	11.82	99.99	[39]
PVDF-Silica aerogel	65/20	12.5	42.81*	99.99	[50]
PVDF-BT(0.5%)	53/11	27.8	19.0**	99.995	**In this work**
PVDF-BT(7%)	53/11	31.8	25.6**	99.998	**In this work**

6.3 Summary

Graphene-based PVDF membranes at different concentration percentage of nanofiller (0.5 and 7 %), bismuth Telluride-PVDF membranes at different concentration percentage of nanofiller (0.5 and 7 %) exfoliated via WJM have been evaluated in Membrane Distillation process. Moreover the cited membranes have been also compared with a membrane containing a mixture of 0.5% Graphene and 0.5% Bismuth telluride and with pristine PVDF membrane. When graphene platelets and Bi_2Te_3 are blended in PVDF matrix, the results achieved show an enhancement of trans membrane flux with 35g/L NaCl solution as feed. This results have been emphasized whit Bi_2Te_3-enabled membranes at high concentration (7%) that gave a clear evidence to increase effectively mass transfer reducing heat loss simultaneously (T_{feed}=58.8°C, FR=300mLmin^{-1}, Flux=74Lm^{-2}h^{-1}). High salt rejection has been achieved with all the membranes especially with PVDF-G(0.5%) where a total salt rejection has been detected. Moreover, membranes enabled with graphene flakes exfoliated via WJM compared with membranes enabled with graphene exfoliated via UW (under same operating conditions), has been achieved an increase in productivity of 38% and of 99.7% with respect to pristine membranes fabricated using the same procedure. The mixture of G and BT in PVDF membrane enhanced the flux in MD compared with PVDF-mixture but with lower thermal efficiency. This result is due to the high thermal conductivity of Graphene (5000 Wm^{-1}K^{-1}).

The combination of PVDF membranes and 2D exfoliated via WJM in a single device makes MD process highly productive and energetically efficient. High quality freshwater can be produced reducing energy and working in more eco-sustainable way.

References

[1] M. Elimelech, W.A. Phillip, The future of seawater desalination: Energy, technology, and the environment, Science (80-.). 333 (2011) 712–717. doi:10.1126/science.1200488.

[2] S.S. Ray, S.-S. Chen, D. Sangeetha, N.C. Nguyen, H.-T. Nguyen, Sustainable Desalination Process and Nanotechnology, in: 2018: pp. 185–228. doi:10.1007/978-3-319-70166-0_6.

[3] E. Drioli, A. Ali, F. Macedonio, Membrane distillation: Recent developments and perspectives, Desalination. 356 (2015) 56–84. doi:10.1016/j.desal.2014.10.028.

[4] M.L. Perrotta, F. Macedonio, E. Tocci, L. Giorno, E. Drioli, A. Gugliuzza, Graphene stimulates the

nucleation and growth rate of NaCl crystals from hypersaline solution via membrane crystallization, Environ. Sci. Water Res. Technol. (2020). doi:10.1039/C9EW01124B.

[5] J.-H. Tsai, M.L. Perrotta, A. Gugliuzza, F. Macedonio, L. Giorno, E. Drioli, K.-L. Tung, E. Tocci, Membrane-Assisted Crystallization: A Molecular View of NaCl Nucleation and Growth, Appl. Sci. 8 (2018) 2145. doi:10.3390/app8112145.

[6] A. Gugliuzza, M.C. Aceto, E. Drioli, Interactive functional poly(vinylidene fluoride) membranes with modulated lysozyme affinity: A promising class of new interfaces for contactor crystallizers, Polym. Int. (2009). doi:10.1002/pi.2681.

[7] F. Macedonio, A. Politano, E. Drioli, A. Gugliuzza, Bi 2 Se 3 -assisted membrane crystallization, Mater. Horizons. 5 (2018) 912–919. doi:10.1039/C8MH00612A.

[8] C.J. Vörösmarty, P.B. McIntyre, M.O. Gessner, D. Dudgeon, A. Prusevich, P. Green, S. Glidden, S.E. Bunn, C.A. Sullivan, C.R. Liermann, P.M. Davies, Global threats to human water security and river biodiversity, Nature. 468 (2010) 334–334. doi:10.1038/nature09549.

[9] M.L. Perrotta, G. Saielli, G. Casella, F. Macedonio, L. Giorno, E. Drioli, A. Gugliuzza, An ultrathin suspended hydrophobic porous membrane for high-efficiency water desalination, Appl. Mater. Today. (2017). doi:10.1016/j.apmt.2017.04.009.

[10] A. Deshmukh, C. Boo, V. Karanikola, S. Lin, A.P. Straub, T. Tong, D.M. Warsinger, M. Elimelech, Membrane distillation at the water-energy nexus: limits, opportunities, and challenges, Energy Environ. Sci. 11 (2018) 1177–1196. doi:10.1039/C8EE00291F.

[11] J. Vanneste, J.A. Bush, K.L. Hickenbottom, C.A. Marks, D. Jassby, C.S. Turchi, T.Y. Cath, Novel thermal efficiency-based model for determination of thermal conductivity of membrane distillation membranes, J. Memb. Sci. 548 (2018) 298–308. doi:10.1016/j.memsci.2017.11.028.

[12] R. Roshani, F. Ardeshiri, M. Peyravi, M. Jahanshahi, Highly permeable PVDF membrane with PS/ZnO nanocomposite incorporated for distillation process, RSC Adv. 8 (2018) 23499–23515. doi:10.1039/C8RA02908C.

[13] L.N. Nthunya, L. Gutierrez, S. Derese, E.N. Nxumalo, A.R. Verliefde, B.B. Mamba, S.D. Mhlanga, A review of nanoparticle-enhanced membrane distillation membranes: membrane synthesis and applications in water treatment, J. Chem. Technol. Biotechnol. 94 (2019) 2757–2771. doi:10.1002/jctb.5977.

[14] S. Lee, A.P. Straub, Opportunities for high productivity and selectivity desalination via osmotic distillation with improved membrane design, J. Memb. Sci. 611 (2020) 118309. doi:10.1016/j.memsci.2020.118309.

[15] B. Meng, G. Liu, Y. Mao, F. Liang, G. Liu, W. Jin, Fabrication of surface-charged MXene membrane and its application for water desalination, J. Memb. Sci. 623 (2021) 119076. doi:10.1016/j.memsci.2021.119076.

[16] J. Ravi, M.H.D. Othman, Z.S. Tai, T. El-badawy, T. Matsuura, T.A. Kurniawan, Comparative DCMD performance of hydrophobic-hydrophilic dual-layer hollow fibre PVDF membranes incorporated with different concentrations of carbon-based nanoparticles, Sep. Purif. Technol. 274 (2021) 118948. doi:10.1016/j.seppur.2021.118948.

[17] Z. Li, Y. Peng, Y. Dong, H. Fan, P. Chen, L. Qiu, Q. Jiang, Effects of thermal efficiency in DCMD and the preparation of membranes with low thermal conductivity, Appl. Surf. Sci. 317 (2014) 338–349. doi:10.1016/j.apsusc.2014.07.080.

[18] N.H. Mat Radzi, A.L. Ahmad, Effect of ZnO nanoparticles loading in double-layer polyvinylidene fluoride membrane for desalination via direct contact membrane distillation, Asia-Pacific J. Chem. Eng. 16 (2021). doi:10.1002/apj.2552.

[19] E. Gontarek, F. Macedonio, F. Militano, L. Giorno, M. Lieder, A. Politano, E. Drioli, A. Gugliuzza, Adsorption-assisted transport of water vapour in super-hydrophobic membranes filled with multilayer graphene platelets, Nanoscale. 11 (2019) 11521–11529. doi:10.1039/C9NR02581B.

[20] A. Ali, C.A. Quist-Jensen, F. Macedonio, E. Drioli, Optimization of module length for continuous direct contact membrane distillation process, Chem. Eng. Process. Process Intensif. 110 (2016) 188–200. doi:10.1016/j.cep.2016.10.014.

[21] M.X. Wang, Z.H. Huang, W. Lv, Q.H. Yang, F. Kang, K. Liang, Water vapor adsorption on low-temperature exfoliated graphene nanosheets, in: J. Phys. Chem. Solids, 2012. doi:10.1016/j.jpcs.2011.10.048.

[22] D.H. Seo, S. Pineda, Y.C. Woo, M. Xie, A.T. Murdock, E.Y.M. Ang, Y. Jiao, M.J. Park, S. Il Lim, M. Lawn, F.F. Borghi, Z.J. Han, S. Gray, G. Millar, A. Du, H.K. Shon, T.Y. Ng, K. Ostrikov, Anti-fouling graphene-based membranes for effective water desalination, Nat. Commun. (2018). doi:10.1038/s41467-018-02871-3.

[23] M. Frappa, A.E. Del Rio Castillo, F. Macedonio, A. Politano, E. Drioli, F. Bonaccorso, V. Pellegrini, A. Gugliuzza, A few-layer graphene for advanced composite PVDF membranes dedicated to water desalination: a comparative study, Nanoscale Adv. 2 (2020) 4728–4739. doi:10.1039/D0NA00403K.

[24] Y. Guan, J. Li, F. Cheng, J. Zhao, X. Wang, Influence of salt concentration on DCMD performance for treatment of highly concentrated NaCl, KCl, MgCl2 and MgSO4 solutions, Desalination. (2015). doi:10.1016/j.desal.2014.10.005.

[25] Z. Xiao, R. Zheng, Y. Liu, H. He, X. Yuan, Y. Ji, D. Li, H. Yin, Y. Zhang, X.M. Li, T. He, Slippery for scaling resistance in membrane distillation: A novel porous micropillared superhydrophobic surface, Water Res. (2019). doi:10.1016/j.watres.2019.01.036.

[26] A. Chogani, A. Moosavi, M. Rahiminejad, Numerical Simulation of Salt Water Passing Mechanism Through Nanoporous Single-Layer Graphene Membrane, Chem. Prod. Process Model. (2016). doi:10.1515/cppm-2015-0068.

[27] J.A. Prince, G. Singh, D. Rana, T. Matsuura, V. Anbharasi, T.S. Shanmugasundaram, Preparation and characterization of highly hydrophobic poly(vinylidene fluoride) – Clay nanocomposite nanofiber membranes (PVDF–clay NNMs) for desalination using direct contact membrane distillation, J. Memb. Sci. 397–398 (2012) 80–86. doi:10.1016/j.memsci.2012.01.012.

[28] D. Hou, H. Fan, Q. Jiang, J. Wang, X. Zhang, Preparation and characterization of PVDF flat-sheet membranes for direct contact membrane distillation, Sep. Purif. Technol. 135 (2014) 211–222. doi:10.1016/j.seppur.2014.08.023.

[29] J. Zhang, Z. Song, B. Li, Q. Wang, S. Wang, Fabrication and characterization of superhydrophobic poly (vinylidene fluoride) membrane for direct contact membrane distillation, Desalination. (2013). doi:10.1016/j.desal.2013.05.018.

[30] J.A. Prince, G. Singh, D. Rana, T. Matsuura, V. Anbharasi, T.S. Shanmugasundaram, Preparation and characterization of highly hydrophobic poly(vinylidene fluoride) - Clay nanocomposite nanofiber membranes (PVDF-clay NNMs) for desalination using direct contact membrane distillation, J. Memb. Sci. (2012). doi:10.1016/j.memsci.2012.01.012.

[31] D. Hou, G. Dai, J. Wang, H. Fan, L. Zhang, Z. Luan, Preparation and characterization of PVDF/nonwoven fabric flat-sheet composite membranes for desalination through direct contact membrane distillation, Sep. Purif. Technol. (2012). doi:10.1016/j.seppur.2012.08.031.

[32] S. Ragunath, S. Roy, S. Mitra, Carbon nanotube immobilized membrane with controlled nanotube incorporation via phase inversion polymerization for membrane distillation based desalination, Sep. Purif. Technol. 194 (2018) 249–255. doi:10.1016/j.seppur.2017.11.053.

[33] Y.C. Woo, L.D. Tijing, W.-G. Shim, J.-S. Choi, S.-H. Kim, T. He, E. Drioli, H.K. Shon, Water desalination using graphene-enhanced electrospun nanofiber membrane via air gap membrane distillation, J. Memb. Sci. 520 (2016) 99–110. doi:10.1016/j.memsci.2016.07.049.

[34] A. Abdel-Karim, J.M. Luque-Alled, S. Leaper, M. Alberto, X. Fan, A. Vijayaraghavan, T.A. Gad-Allah, A.S. El-Kalliny, G. Szekely, S.I.A. Ahmed, S.M. Holmes, P. Gorgojo, PVDF membranes containing reduced graphene oxide: Effect of degree of reduction on membrane distillation performance, Desalination. (2019). doi:10.1016/j.desal.2018.11.014.

[35] C. Yang, X.-M. Li, J. Gilron, D. Kong, Y. Yin, Y. Oren, C. Linder, T. He, CF4 plasma-modified superhydrophobic PVDF membranes for direct contact membrane distillation, J. Memb. Sci. 456 (2014) 155–161. doi:10.1016/j.memsci.2014.01.013.

[36] A. Razmjou, E. Arifin, G. Dong, J. Mansouri, V. Chen, Superhydrophobic modification of TiO2 nanocomposite PVDF membranes for applications in membrane distillation, J. Memb. Sci. 415–416 (2012) 850–863. doi:10.1016/j.memsci.2012.06.004.

[37] L.N. Nthunya, L. Gutierrez, A.R. Verliefde, S.D. Mhlanga, Enhanced flux in direct contact membrane distillation using superhydrophobic PVDF nanofibre membranes embedded with organically

modified SiO 2 nanoparticles, J. Chem. Technol. Biotechnol. 94 (2019) 2826–2837. doi:10.1002/jctb.6104.

[38] S. Ragunath, S. Roy, S. Mitra, Carbon nanotube immobilized membrane with controlled nanotube incorporation via phase inversion polymerization for membrane distillation based desalination, Sep. Purif. Technol. (2018). doi:10.1016/j.seppur.2017.11.053.

[39] I. Janajreh, R. Hashaikeh, M.N. Hussain, Evaluation of Thermal Efficiency of Membrane Distillation under Conductive Layer Integration, Energy Procedia. 105 (2017) 4935–4942. doi:10.1016/j.egypro.2017.03.985.

[40] K.S.S. Christie, T. Horseman, S. Lin, Energy efficiency of membrane distillation: Simplified analysis, heat recovery, and the use of waste-heat, Environ. Int. 138 (2020) 105588. doi:10.1016/j.envint.2020.105588.

[41] M. Frappa, A.E.D.R. Castillo, F. Macedonio, G. Di Luca, E. Drioli, A. Gugliuzza, Exfoliated Bi2Te3-enabled membranes for new concept water desalination: Freshwater production meets new routes, Water Res. 203 (2021) 117503. doi:10.1016/j.watres.2021.117503.

[42] A. Gugliuzza, A. Politano, E. Drioli, The advent of graphene and other two-dimensional materials in membrane science and technology, Curr. Opin. Chem. Eng. 16 (2017) 78–85. doi:10.1016/j.coche.2017.03.003.

[43] Y. Lan, A.J. Minnich, G. Chen, Z. Ren, Enhancement of Thermoelectric Figure-of-Merit by a Bulk Nanostructuring Approach, Adv. Funct. Mater. 20 (2010) 357–376. doi:10.1002/adfm.200901512.

[44] Y. Park, S. Lee, Analysis of thermal energy efficiency for hollow fiber membranes in direct contact membrane distillation, Environ. Eng. Res. 24 (2018) 347–353. doi:10.4491/eer.2018.253.

[45] H. Li, L. Peng, Y. Luo, P. Yu, Enhancement in membrane performances of a commercial polyamide reverse osmosis membrane via surface coating of polydopamine followed by the grafting of polyethylenimine, RSC Adv. 5 (2015) 98566–98575. doi:10.1039/c5ra20891b.

[46] H. Li, W. Shi, X. Zeng, S. Huang, H. Zhang, X. Qin, Improved desalination properties of hydrophobic GO-incorporated PVDF electrospun nanofibrous composites for vacuum membrane distillation, Sep. Purif. Technol. (2020). doi:10.1016/j.seppur.2019.115889.

[47] A. Gugliuzza, A. Basile, Membranes for Clean and Renewable Power Applications, 2014. doi:10.1016/c2013-0-16316-7.

[48] S. Manju, N. Sagar, Renewable energy integrated desalination: A sustainable solution to overcome future fresh-water scarcity in India, Renew. Sustain. Energy Rev. 73 (2017) 594–609. doi:10.1016/j.rser.2017.01.164.

[49] M. Heihsel, M. Lenzen, F. Behrendt, Desalination and sustainability: a triple bottom line study of Australia, Environ. Res. Lett. 15 (2020) 114044. doi:10.1088/1748-9326/abbd63.

[50] K. Li, K. Wang, Y. Zhang, H. Liu, J. Wang, A polyvinylidene fluoride (PVDF)–silica aerogel (SiAG)

insulating membrane for improvement of thermal efficiency during membrane distillation, J. Memb. Sci. (2020). doi:10.1016/j.memsci.2019.117632.

Chapter 7

Membranes filled with few layers materials for enhanced NaCl crystallization

This Chapter illustrates the potentiality of membranes functionalized with exfoliated few layers (Graphene (G) and Bismuth Telluride (BT)) in crystallization process. More specifically, the intent is to produce high-quality crystals for size and shape in shortened crystallization time. With this regard, a comparative study is also including pristine PVDF membranes. The membranes performance has been evaluated in terms of capability to yield more uniform crystals through controlled nucleation and growth rate kinetics.

7.1 Membrane Crystallization Implementation

The crystallization tests have been performed as explained in Chapter 4.For crystallization tests, NaCl solutions 5M have been used at Temperature 36°C and flow rate of 250mL/min. On permeate side the temperature was 10°C and flow rate of 100mL/min. MCr tests have been performed with 5M NaCl solution in direct contact configuration.

7.1.1 Nucleation and growth rate of NaCl crystals

Membranes with the best MD performance have been selected for implementing MCr operations. Table 7.1 resumes main characteristics of the membranes examined in this chapter. Figure 7.1 shows the trend of trans-membrane flux with time for the pristine and PVDF membranes functionalized with 2D materials. The feed concentration used for the crystallization tests was 5M. This value was chosen as it is close to the saturation concentration of the NaCl solutions (above to 5.3M).

Table 7.1 *Membranes tested in MCr with the main characteristics.*

Name of Membrane	Filler Dispersed in NMP	Pore size (μm)	Porosity (%)	Thickness (μm)
PVDF	No Filler	0.52±0.09	82±4	71±2
PVDF-G (0.5%)	Graphene	0.24±0.05	56 ± 7	62 ± 3
PVDF-BT (0.5%)	Bi_2Te_3	0.5±0.2	75±1	68±1
PVDF-BT (7%)	Bi_2Te_3	0.40±0.06	77±1	100±5

pristine PVDF membrane exhibits a trans-membrane flux of 5.7 $L \cdot m^{-2}h^{-1}$ due to higher porosity and mean pore size thus yielding a larger mass transfer through the membrane Among the PVDF membranes functionalized with 2D materials, PVDF-BT (7%) presents the highest trans-membrane flux (average flux of 3.9 $L \cdot m^{-2}h^{-1}$). This result is due to the higher porosity (77%) and mean pore size (0.5µm) of PVDF-BT(7%) membrane than the ones achieved with other membranes. These aspects allow a more mass transport during the process despite the higher thickness [1]. For similar considerations, the other two membranes PVDF-BT (0.5%) and PVDF-G(0.5%) exhibit an average flux of 2.7 $L \cdot m^{-2}h^{-1}$ and 1.6 $L \cdot m^{-2}h^{-1}$, respectively. All the membranes showed a percentage of rejection equal or higher than 99.9% with the highest value obtained with PVDF-G (0.5%); in this case, the rejection is equal to 99.99%. The high values of rejection obtained in the tests guarantee that, at least in the experimental time, the salts infiltration through the membrane pores has been negligible and that the analyzed membranes preserved the crucial requisite of hydrophobicity. MD experiments carried out in similar conditions have confirmed the good resistance of membranes to wetting.

Contact angle values measured with 5M NaCl solution (Chapter 5) confirm the highest resistance PVDF-G (0.5%) to wetting as well. Also, PVDF-BT (0.5%) with the lowest contact angle yields the lowest value of rejection in MCr test (99.86%).

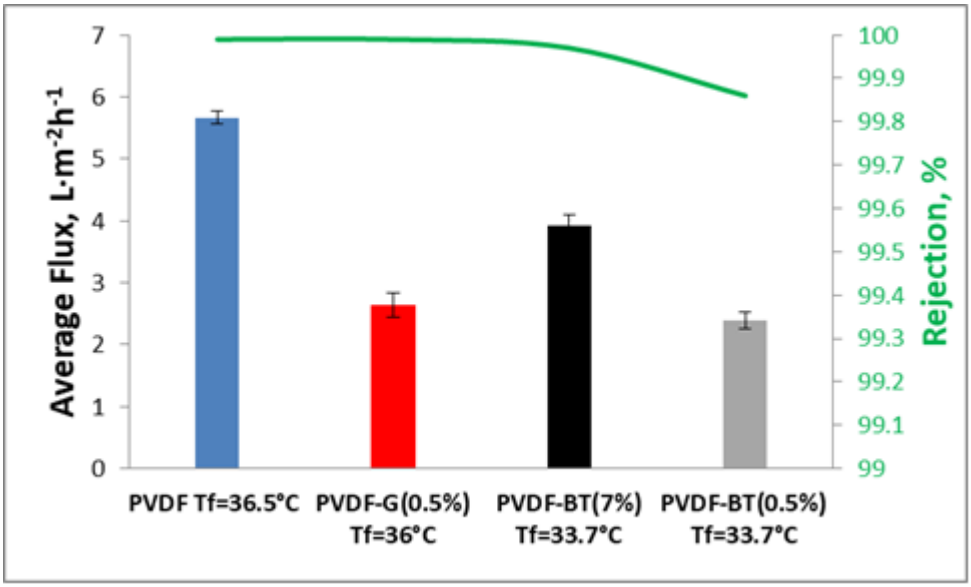

Figure 7.1 *Average flux for PVDF-based membranes functionalized with 2D materials at (0.5 %) and PVDF-BT (7%).*

As an effect of a continuous removal of pure water from the feed side, the saturation of the saline solution has been induced, thus resulting in the formation of sodium chloride crystals different for number, size and shape depending on the membranes worked (Figure7.2).

As mentioned in Chapter 4, the main factor for study the achieved crystals are nucleation rate (B^0), Coefficient of variation (*CV*), crystal size diameter (*dm*) and crystals growth rate (G^c). A massive nucleation of small crystals has been obtained with PVDF-BT(0.5%) with a value of B^0 = 1060979 and *dm* =9.56µm. Slightly less numerous but larger and differently sized crystals have been obtained with PVDF (where B^0=490593, *dm*=20.6µm and *CV*=77.1%). Less numerous and small (B^0=337756 and *dm* =13.38µm) but more uniform (*CV*=47%) crystals have been obtained with PVDF-BT (7%) an relatively few but larger and more uniform crystals have been obtained with PVDF-G(0.5%) (where B^0=280475, *dm* =18.92µm and *CV*=36.7%).

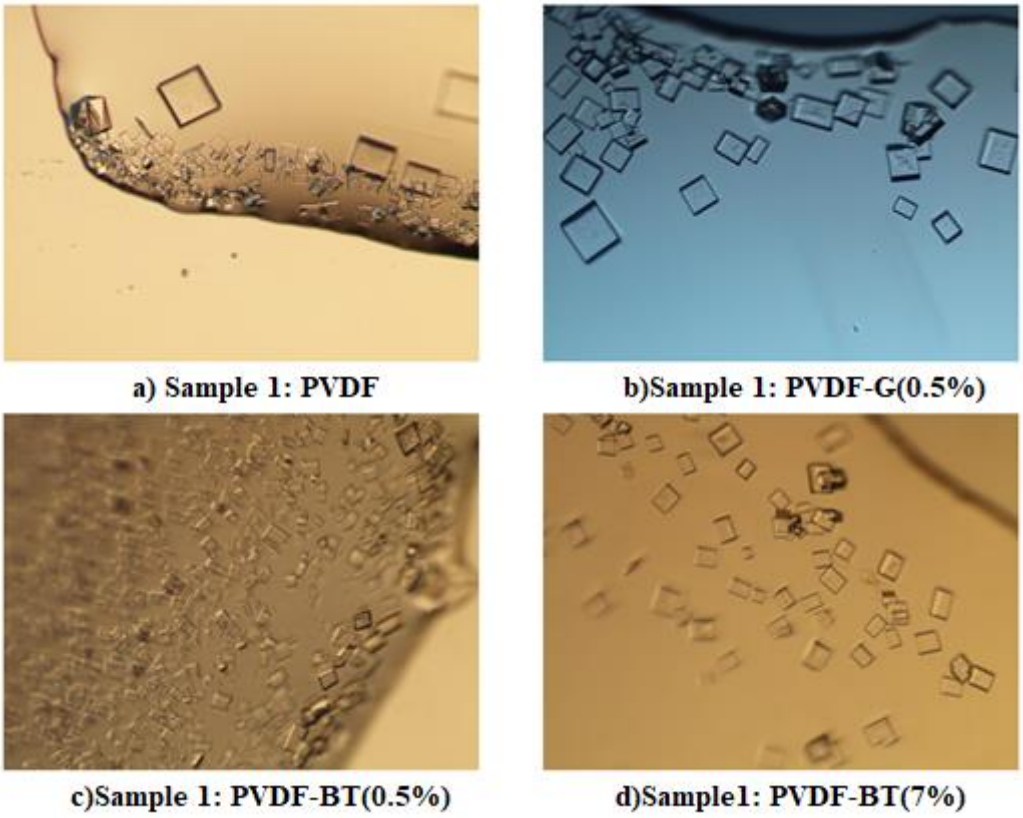

Figure 7.2 *Pictures collected on the first sample of NaCl crystals obtained with the different analysed membranes: (a) PVDF, (b) PVDF-G(0.5%), (c) PVDF-BT(0.5%) and (d) PVDF-BT(7%).*

Figure 7.3 clearly shows the growth in size, from the first sample to the last one collected during crystallization, of NaCl. In this case, pictures collected with the PVDF-BT (0.5%) membrane are reported.

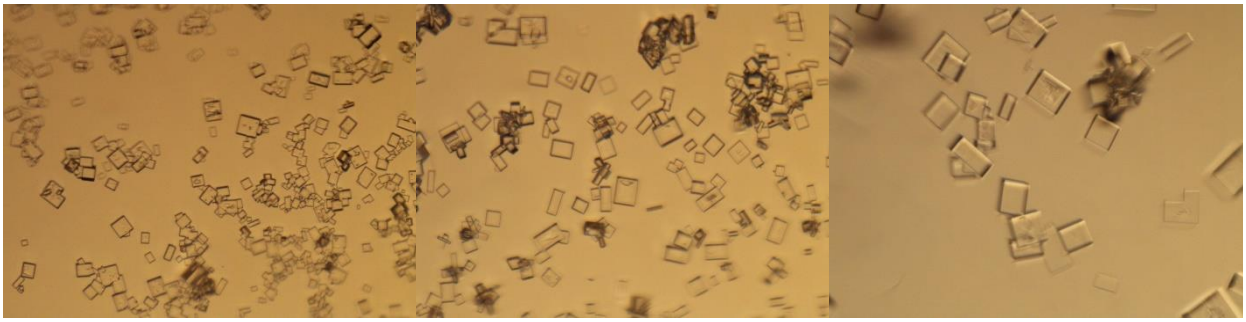

(a) (b) (c)

Figure 7.3. *Pictures collected on the first sample of NaCl crystals obtained with the different analysed membranes: with PVDF-BT (0.5%) membrane (magnification20X): after (a) 140, (b) 170 and (c) 200 min.*

Figure 7.4 yields a clear indication about crystals size distribution and shape uniformity based on the number of crystals in function of their length/width ratio obtained with the different membranes. The most part of crystals shows cubic block-like lattice in accordance with the expected geometry of the NaCl crystals. This structure is predominant with PVDF-BT (0.5%).

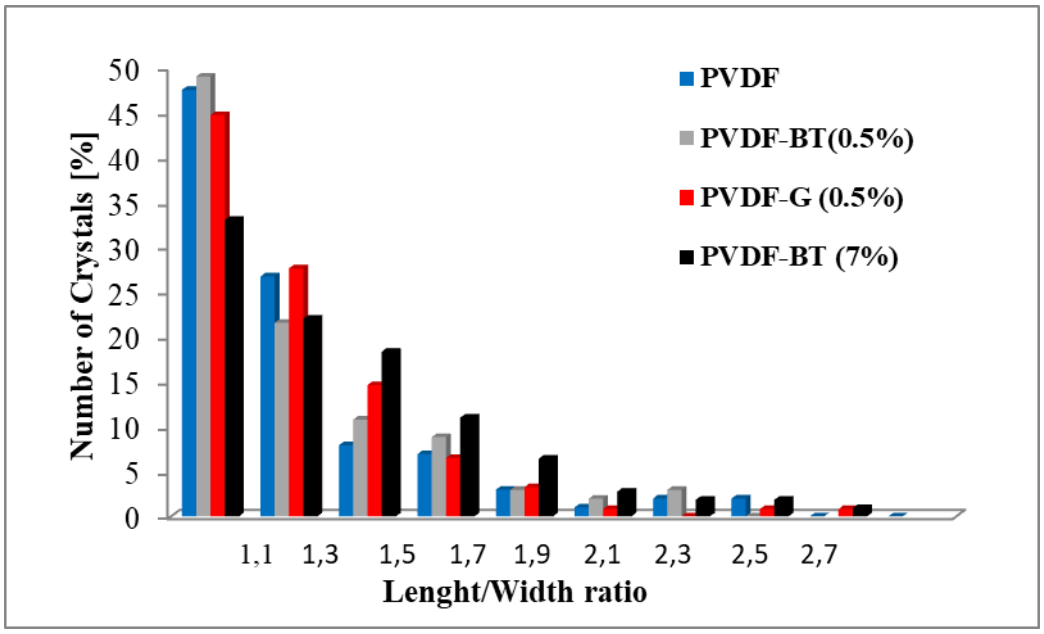

Figure 7.4 *Number of crystals [%] in function on Length/width ratio for the functionalized PVDF-based membranes.*

CV, G^c and B^0 values estimated for each NaCl structure lattice obtained with the various membranes are resumed in Table 7.2. As mentioned, the results indicate a more uniform distribution of NaCl crystals with the PVDF-G (0.5%) membrane, which exhibits CV values ranging from 36.7 to 44.2% (Table 7.2) within the 60 minutes of crystals growth observation, i.e., from sample 1 to sample 3. PVDF-BT(0.5%) shows also good CV values, with decreasing CV from sample 1 - time with clearly visible crystals in the feed solution - to sample 3 - 60 minutes later. This trend is due to the fact that the most part of crystals have been growing as proved by decreasing values of B^0 and increasing values of middle diameter *dm* - from sample 1 to sample 3. The worst CV values have been obtained with the PVDF-BT (7%) membrane due to the simultaneous presence of low values of G^c and high values of B^0 – successive nucleation. This indicates that the formation of new crystals takes place in the solution rather than the growth of those previously formed, causing a wider crystal size distribution at the third observation (CV=65.4%).

***Table 7.2**: NaCl crystal parameters obtained with PVDF-based membranes.*

	CV [%]	B^0 -	G^c [mm·min^{-1}]	d_m [□m]	CV [%]	B^0 -	G^c [mm·min^{-1}]	d_m [□m]
	PVDF				**PVDF-G (0.5%)**			
Sample 1	77.1	490593	0.0000298	20.6	36.7	280475	0.0000385	18.92
Sample 2	48.4	257598	0.0000524	42.5	43.8	199025	0.0000456	23.25
Sample 3	53.8	149088	0.0000795	65.1	44.2	374721	0.0000251	17.27
	PVDF-BT (0.5%)				**PVDF-BT (7%)**			
Sample 1	54.2	1060979	0.0000317	9.56	46.0	337756	0.0000239	13.38
Sample 2	44.4	1633024	0.0000315	12.08	29.5	343006	0.0000245	13.93
Sample 3	43.1	811706	0.0000388	16.82	65.4	392031	0.0000212	16.70

For what concerns NaCl size (Fig.7.5A), crystals of comparable dimension have been obtained (after one hour of growth) with the three membranes filled with 2D materials. PVDF-G (0.5%), PVDF-BT (0.5%) and PVDF-BT (7%) have showed crystal size of 16.27 µm, 16.82µm and 16.70 µm, respectively. Larger NaCl crystals (65.1 µm) have been instead measured in the case of pristine PVDF membrane due to the highest crystal growth (G^c 7.95 *10^{-5} mm min^{-1}), as shown in figure 7.5B. Also, a wider distribution with high *CV* values has been with this membrane-type.

A) B)

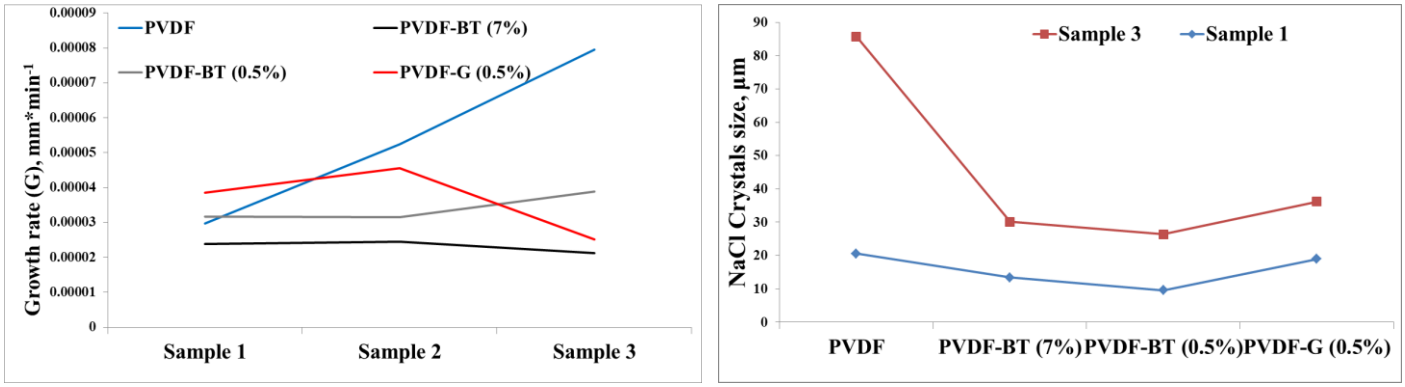

Figure 7.5 *A) Crystal size comparison in sample 1 and sample 3 and B)Crystal Growth rate for all the prepared membranes.*

To summarise, the presence of fillers in PVDF-based membranes reduces averagely the time for detection of the first clearly visible crystals in comparison with pristine PVDF membrane, from 285 minutes to 140 minutes in the case of PVDF-BT (0.5%), with a nucleation reaching the peak of crystals number as depicted in Figure 7.6.

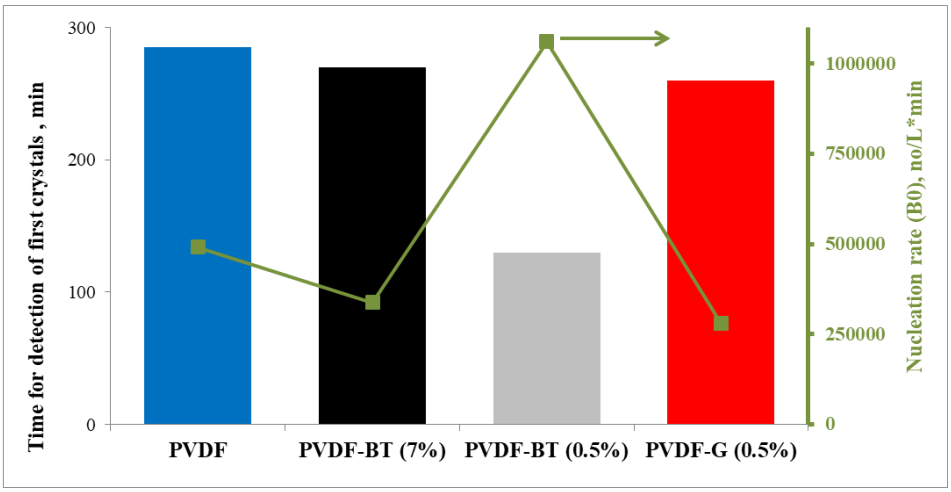

Figure 7.6 *Time for detection of the first crystals and nucleation rate for the pristine PVDF membrane and PVDF functionalized membranes.*

These experimental results are in full agreement with the findings reported by Perrotta et al. [2,3]. The authors suggest that well-established interactions are established at the graphene–solution interface, thereby stimulating water sequestration from ion–water clusters and promote ion–ion aggregation. Moreover, it has been proven that PVDF composite membranes with Bi_2Se_3 promote the capture of water molecules by adsorption favouring a faster achievement of the saturation conditions [4]. It has been proposed that the rapid water removal produces a shrinking of the ionic core preceding the crystallization, in analogy to theoretical predictions crystallization from aqueous solutions [5]. In this study, the sudden formation of crystals observed with PVDF-BT (0.5%) reduced the experimental test, shortening the detection of crystals to 140 min of experiment against 285 min needed for pristine PVDF while for PVDF-BT(7%) and PVDF-G(0.5%) were necessary 270 and 260 min, respectively. A significant increase in BT concentration increases the mass transfer through the membrane but it does not affect the nucleation time. Similar trend has been observed in a previous work of Perrotta et al. [6] where the increase of Graphene concentration in the PVDF membranes allows achieving the lowest nucleation rate value despite the higher flux estimated than the membrane with lower graphene concentration [6].

Compared to conventional crystallizers, the membrane crystallization process offers the possibility of working continuously with solutions with a high concentration of salts and the possibility of low operating temperatures. Furthermore, MCr offers better fluid distribution, heterogeneous nucleation and a high surface / volume ratio. Another very important advantage for the crystallization processes is the possibility of dissociating the nucleation from the growth as well as having an easy control of the removal of the solvent which therefore means having controlled

supersaturation. However, although membrane crystallization offers numerous advantages, this type of technology also has some drawbacks. The main disadvantage is related to the membrane itself, which adds a resistance to the mass transfer and thus reduces the flow of water through the membrane, i.e. lowers the evaporation rate. Another important drawback is the scaling phenomena on the top of the membrane which can lead to a reduction of the flow or even to the complete block of the membrane. To evaluate the advancement of 2D materials membranes-assisted NaCl crystallization beyond to the state of the art, a comparison in terms of CV and flux including the results achieved in this work and others crystallization experiments obtained with PVDF membranes and discussed in literature has been proposed (Table 7.3). All of the fluxs are comparable each other except for DL-PVDF-PAN that shows the highest trans-membrane flux (8 L/m^2h) and AD40H_022 that exhibits the lowest trans-membrane flux (1.5 L/m^2h). However, it is relevant to observe that the feed concentration in the case of DL-PVDF-PAN is lower than the other tests so causing a higher driving force and justify the higher mass transfer [7]. Considering the CV values, the membranes studied in this work (PVDF-G (0.5%) and PVDF-BT (7%)) show a coefficient of variation in general lower than the other membranes. The only exception is 26.7% as achieved for the membrane with graphene powder PVDF GP 5, prepared with the same procedure described in this article but with 10 times higher graphene concentration.

***Table 7.3**: Membrane Assisted Crystallization performances in literature.*

Membrane code	Feed	Feed flow rate [L/h]	Temperature feed [°C]	Lower CV [%]	Flux [L/m^2h]	Ref.
AD40H_010	5.3 M NaCl	15	34	35	1.78	[8]
AD40H_045	5.3 M NaCl	15	34	38.7	2.54	[8]
AD40H_022	5.3 M NaCl	15	34	34.4	1.5	[8]
DL-PVDF-PAN	27wt% NaCl	0.06	60	n.a	8	[9]
PVDF	5M NaCl	6	21.96	40	4	[4]

PVDF/Bi_2Se_3	5M NaCl	6	21.96	36	3.9	[4]
PVDF–GP 0.5	5M NaCl	0.17m/s	36.5	32.2	3.8	[6]
PVDF–GP 5	5M NaCl	0.17m/s	36.5	26.7	6	[6]
PVDF–GP10	5M NaCl	0.17m/s	36.5	35.8	5.5	[6]
PVDF-G (0.5%)	5M NaCl	15	42	27.5	2.7	**This work**
PVDF-BT (0.5%)	5M NaCl	15	42	43	2.7	**This work**
PVDF-BT(7%)	5M NaCl	15	42	29.5	3.9	**This work**

7.2 Summary

Subsequently the results obtained in MD, the membranes functionalized with 2D nanofillers have been evaluated in MCr for the crystallization of sodium chloride starting from 5M NaCl aqueous solutions. The suitability of operation has been evaluated in terms of enhancing productivity and quality of obtained crystals. Under the same operating conditions, PVDF-BT(7%) membrane exhibited flux higher than the other 2D composite membranes, (3.9 $Lm^{-2}h^{-1}$) while PVDF-BT(0.5%) and PVDF-G(0.5%) showed an average flux of 2.7 $Lm^{-2}h^{-1}$and 1.6 $Lm^{-2}h^{-1}$, respectively. The confinement of graphene and bismuth telluride in polymeric hydrophobic matrices has produced a more uniform NaCl crystals dispersion (especially in the case of PVDF-G (0.5%) membrane) and reduced the time for detection of the first clearly visible crystals (from 285 min in the case of pristine PVDF membrane to 140 min in the case of PVDF-BT (0.5%)). Moreover, the high rejection together with a good trans-membrane flux confirmed the interesting performance of the process, without any wetting phenomena, at least during the crystallization tests.

References

[1] Z. Cui, J. Pan, Z. Wang, M. Frappa, E. Drioli, F. Macedonio, Hyflon/PVDF membranes prepared by NIPS and TIPS: Comparison in MD performance, Sep. Purif. Technol. 247 (2020) 116992.

doi:10.1016/j.seppur.2020.116992.

[2] M.L. Perrotta, F. Macedonio, E. Tocci, L. Giorno, E. Drioli, A. Gugliuzza, Graphene stimulates the nucleation and growth rate of NaCl crystals from hypersaline solution via membrane crystallization, Environ. Sci. Water Res. Technol. 6 (2020) 1723–1736. doi:10.1039/C9EW01124B.

[3] M.L. Perrotta, F. Macedonio, L. Giorno, W. Jin, E. Drioli, A. Gugliuzza, E. Tocci, Molecular insights on NaCl crystals formation approaching the PVDF membranes functionalized with graphene, Phys. Chem. Chem. Phys. (2020). doi:10.1039/d0cp00928h.

[4] F. Macedonio, A. Politano, E. Drioli, A. Gugliuzza, Bi 2 Se 3 -assisted membrane crystallization, Mater. Horizons. 5 (2018) 912–919. doi:10.1039/C8MH00612A.

[5] M. Mucha, P. Jungwirth, Salt Crystallization from an Evaporating Aqueous Solution by Molecular Dynamics Simulations, J. Phys. Chem. B. 107 (2003) 8271–8274. doi:10.1021/jp034461t.

[6] M.L. Perrotta, F. Macedonio, E. Tocci, L. Giorno, E. Drioli, A. Gugliuzza, Graphene stimulates the nucleation and growth rate of NaCl crystals from hypersaline solution via membrane crystallization, Environ. Sci. Water Res. Technol. (2020). doi:10.1039/C9EW01124B.

[7] G. Di Profio, S.M. Salehi, E. Curcio, E. Drioli, 3.11 Membrane Crystallization Technology, in: Compr. Membr. Sci. Eng., Elsevier, 2017: pp. 297–317. doi:10.1016/B978-0-12-409547-2.12247-4.

[8] Z. Cui, X. Li, Y. Zhang, Z. Wang, A. Gugliuzza, F. Militano, E. Drioli, F. Macedonio, Testing of three different PVDF membranes in membrane assisted-crystallization process: Influence of membrane structural-properties on process performance, Desalination. 440 (2018) 68–77. doi:10.1016/j.desal.2017.12.038.

[9] F. Edwie, T.-S. Chung, Development of hollow fiber membranes for water and salt recovery from highly concentrated brine via direct contact membrane distillation and crystallization, J. Memb. Sci. 421–422 (2012) 111–123. doi:10.1016/j.memsci.2012.07.001.

[10] M. Frappa, A.E. Del Rio Castillo, F. Macedonio, A. Politano, E. Drioli, F. Bonaccorso, V. Pellegrini, A. Gugliuzza, A few-layer graphene for advanced composite PVDF membranes dedicated to water desalination: a comparative study, Nanoscale Adv. 2 (2020) 4728–4739. doi:10.1039/D0NA00403K.

Chapter 8

PVDF membranes filled with a MOF compound: an explorative study about its potential use in MD and MCr operations

Organic metal structures (MOFs) are a class of nanoporous materials composed of central metal clusters or ions and organic ligands, which possess a large specific surface area, high porosity, low thermal conductivity and ordered nanopores [1–3]. In recent years, MOFs have attracted significant interest by acting as unique nanofillers for mixed matrix membranes in the field of liquid separation. However, in the field of MD, there have been only a few studies on the use of MOFs as novel additives to improve membrane MD performance [4–7].

In the framework of collaborative activities with the Nanjing Tech University (China), [MIL-140B] has been synthetized and used to functionalize PVDF membrane according to dry-wet phase inversion. This Zr-based MOF present high hydrophobic properties and, hence, is suitable for functionalizing membranes dedicated to MD applications.

The MOF-functionalized membranes have been characterized and compared with PVDF-based membranes in terms of porosity, hydrophobicity, pore size, thickness and surface analysis. Moreover, the prepared membranes functionalized with MOF have been tested in MD and MCr processes under working conditions used for other membranes filled with few layers 2D materials. Preliminary results have been achieved and analysed in term of trans-membrane flux and salt rejection for MD while crystals analysis have been done for MCr tests.

The performance of the functional membranes has been also compared to those of the other 2D materials-based membranes developed within this research work.

8.1 Preparation of MOF-enabled Membranes

PVDF membranes functionalized with MOF ([MIL-140B]) have been prepared by dry-wet procedure described in Chapter 5. On contrary with the previous membranes, the MOF has been synthetized and kindly provided from Nanjing Tech University (China). The MOF has been dispersed in N-Methyl-2-pyrrolidone at a concentration of 0.6g/L. To better disperse MOF in NMP, the solution has been stirred for 1h. After this, the preparation has continued with the addiction of 12 wt.% of PVDF powder under mechanical stirring. Then, the solution has been casted on a glassy support by a casting knife regulated on 250 µm and immersed in a coagulation bath (IPA) to

promote solid-liquid demixing. The final MOF concentration in the membranes has been 0.5% with respect to the polymer (Table 8.1). As for the other membrane filled with 2D materials, the prepared membranes have been washed in milli-Q water, air-dried at room temperature overnight and dried at 30°C for 1 h.

8.2 Characterization of membrane filled with MOF

The main structural proprieties of PVDF membranes functionalized with ([MIL-140B] are reported in table 8.1. Table 8.1 reports the characteristics of pristine PVDF membrane as well in order to compare the effects of the nanofiller on morphological properties of the membranes. The PVDF-MOF0.5 membrane shows porosity comparable with the ones achieved with pristine PVDF (64±1 *vs* 63±5 %, respectively), while it results slightly thicker with a thickness of 63±3 μm against 57±2 μm measured for the pristine PVDF membrane.

Table 8.1: *Main characteristics of PVDF membranes filled with MOF MIL-140B).*

Membrane	Filler Dispersed in NMP	Pore size (μm)	Bubble point (μm)	Contact Angle (°)	Porosity (%)	Thickness (μm)
PVDF	No Filler	0.48±0.09	0.73 ±0.05	139±3	63±5	57±2
PVDF-MOF (0.5%)	MIL-140B	0.18±0.05	0.41±0.02	126±5	64±1	63±3

The membrane containing 0.5% of MOF exhibits a mean pore size of 0.18±0.05μm with a bubble point of 0.41±002 μm, resulting smaller than that estimated for pristine PVDF (0.48 μm). The pore size distribution results however with a narrower than pristine PVDF, even if a cluster of bigger pores are present in the same range of the pristine membrane (Figure 8.1).

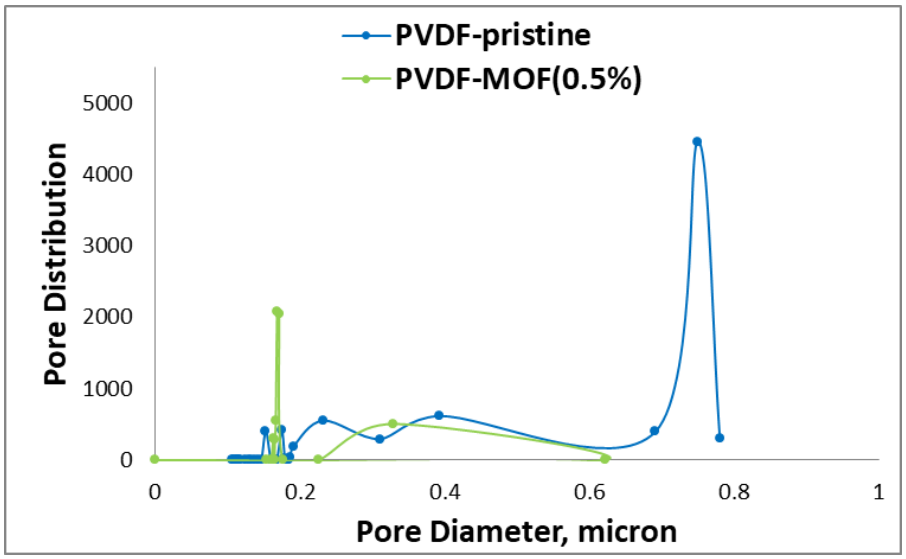

Figure 8.1 *Pore size distribution of pristine PVDF and PVDF-MOF(0.5%).*

The presence of MOF has been confirmed by BSE analysis showing MOF particles entrapped in PVDF network (Figure 8.2). Moreover, from SEM images is possible to observe the structure of PVDF membrane, the same achieved with the membrane functionalized with 2Dmaterials.

SEM

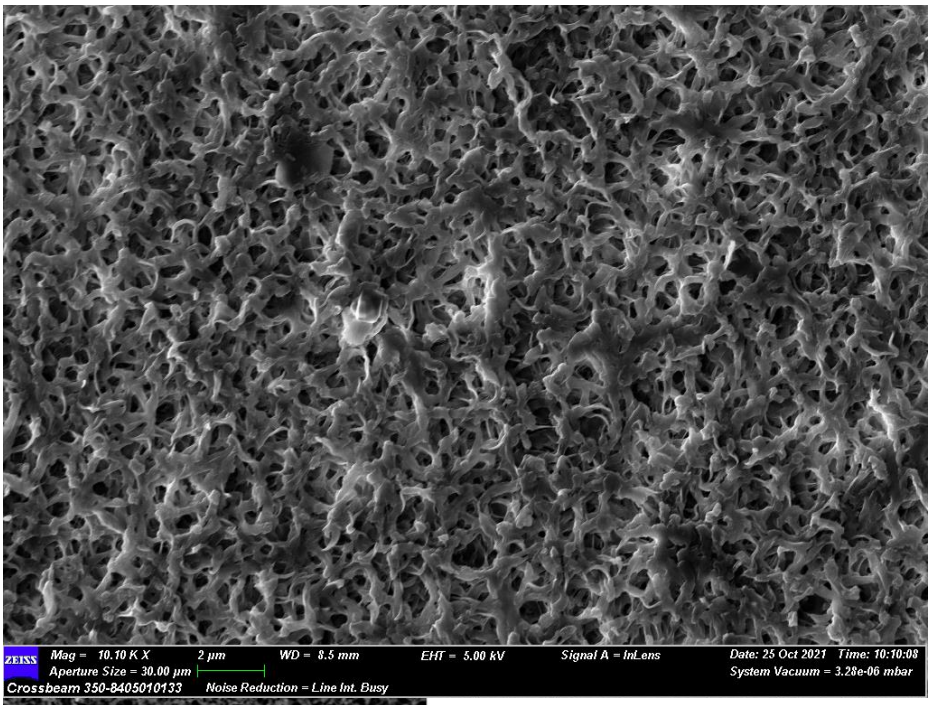

BSE

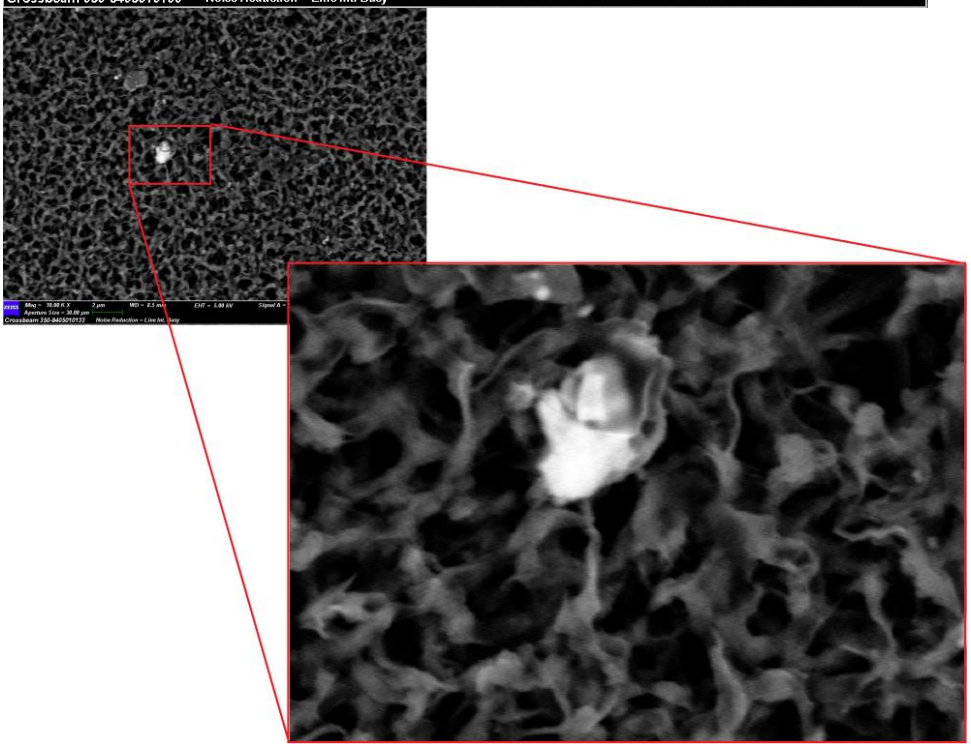

Figure 8.2 *SEM and BSE images collected on the top surface of the PVDF with MOF flakes at 0.5% at two different magnitudes (enlargements at 5.000 and 15.000X).*

An analysis of MOF entrapped in PVDF gives information about the presence of zirconium, which is distinctive element of the nanonfiller (Fig. 8.3, table 8.2).

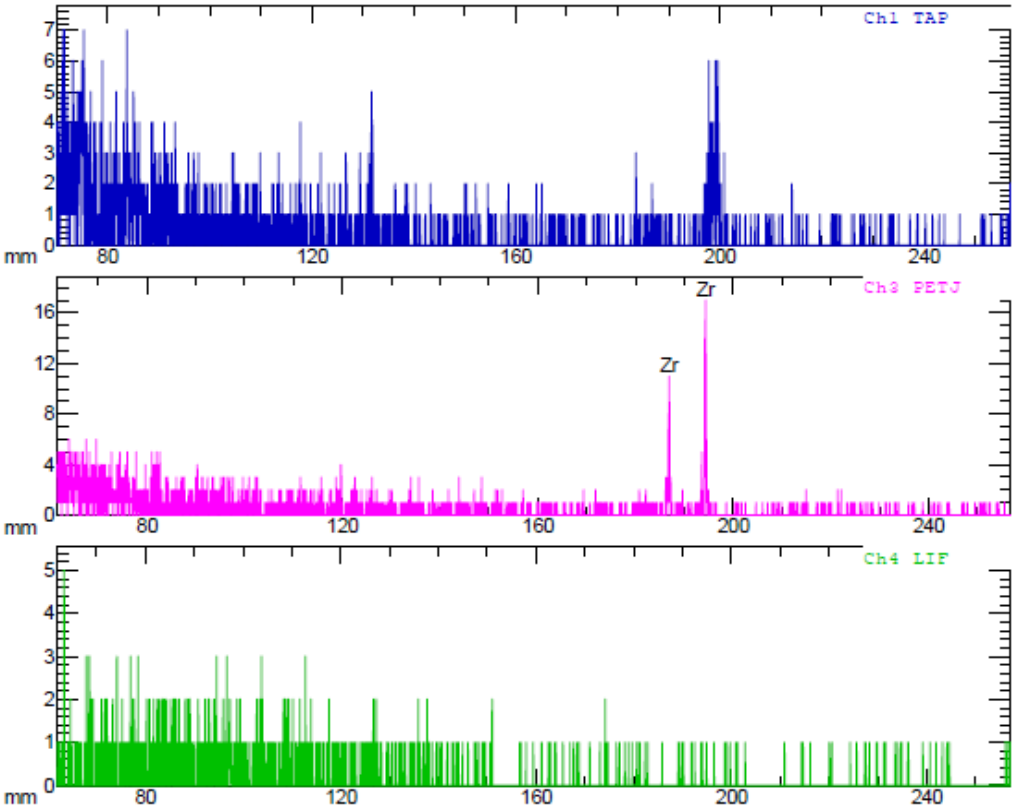

Figure 8.3 *EDX Analysis of the MOF composition.*

Table 8.2: *SEM Analysis of the MOF composition: Percentage Mass and Atom present in MOF.*

Element	Mass (%)	Atom (%)	K(%)
Zr	100.000	100.000	8.894
Total	100.000	100.000	8.894

The surface proprieties have been analysed with pure water, resulting in contact angle values of 125.8±5° (Fig. 8.4). Despite the waterproofness is lower than that estimated for pristine PVDF (139±3 °), the membrane continues to exhibit a suitable hydrophobic character.

The wetting resistance has been also evaluated with 0.6 M NaCl. A plateau has been reached with stable contact angle values of 117±1° with longer time (fig. 8.4).

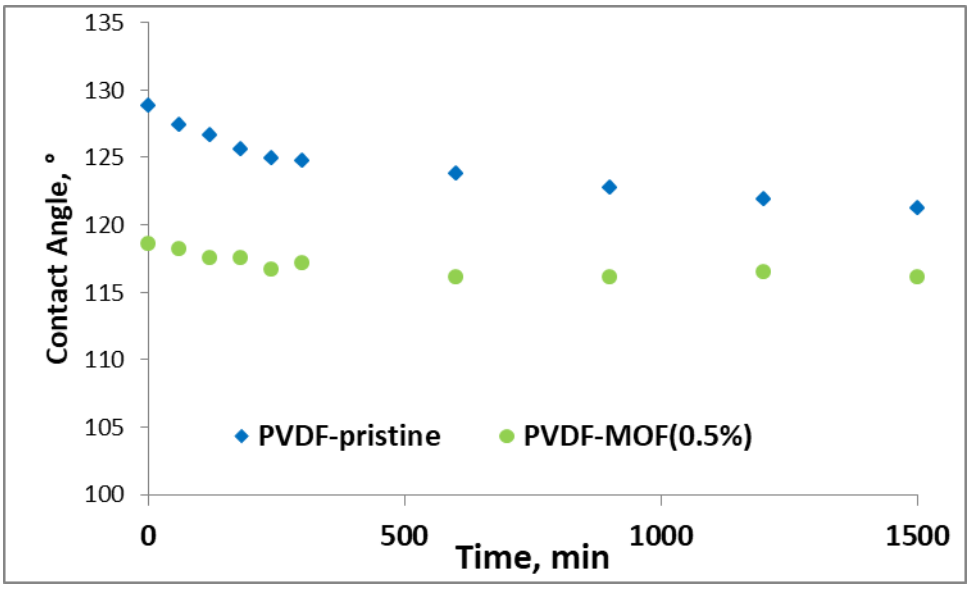

Figure 8.4 *Contact angles trend during the time with 0.6M NaCl droplet.*

8.3 MOF-enabled Membranes for Water Desalination via Membrane Distillation

The effects of MOF materials on the water vapor transfer through the membranes have been investigated in MD direct contact configuration using synthetic seawater (NaCl 35 g/L). Figure 8.5 shows the average fluxes measured at two different feed temperatures (50 and 70°C) under a flow rate of 100 mL/min on the feed side. It can be observed how the PVDF-MOF membrane presents a salt rejection of about 99.99**%.** In comparison with the pristine PVDF membrane, the PVDF-MOF(0.5%) shows a lower flux with same operating condition (1.8 $Lm^{-2}h^{-1}$ and 8 $Lm^{-2}h^{-1}$ for PVDF-MOF and pristine PVDF membrane, respectively). Considering that porosity and thickness values are more or less comparable, (ε = 64 and 63%; δ= 63 and 57 μm, respectively) this result could be justified by the lowest pore size of the PVDF-MOF membrane, which implies less free pathways for the water vapor.

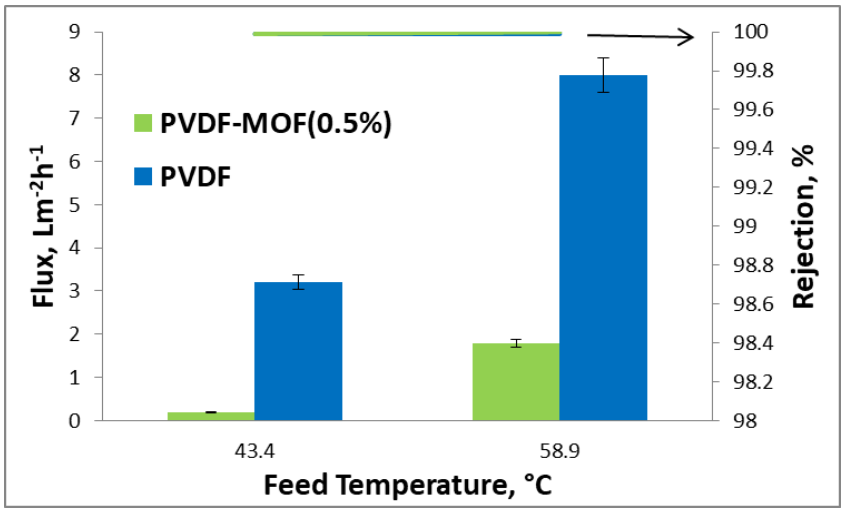

Figure 8.5 *Average Flux at two feed temperature for pristine PVDF and PVDF-MOF(0.5%), FR=100mL/min, Conc: 35 g/L.*

In table 8.3 are reported the mass transfer coefficient *B* calculated for pristine PVDF and PVDF-MOF(0.5%) membranes with the related different of partial pressure (*ΔP)* for MD tests**.** As expected, the low trans-membrane flux with PVDF-MOF(0.5%) corresponds to a low value of transport coefficient *B*, yielding indication about a higher resistance to mass transfer through the functionalized membrane.

Table 8.3 *MD mass transport coefficient estimated for PVDF-MOF(0.5%) and pristine PVDF membranes at different difference of partial pressure (ΔP).*

PVDF-MOF (0.5%)		**PVDF**	
ΔP (Pa)	**B 10^{-4} (L $m^{-2}h^{-1}Pa^{-1}$)**	**ΔP (Pa)**	**B 10^{-4} (L $m^{-2}h^{-1}Pa^{-1}$)**
6726.2	0.22	6111.7	6.7
17168.4	1.0	10455.5	7.8

The use of MOF materials in MD is however still little explored in the literature [1,6,8-9]. Table 8.4 reports a comparative analysis, even if it has to be stressed the use of different operating conditions, which can affect the final result. Considered that the flow rate used with PVDF-MOF in this work is the lowest, it is interesting that the productivity-selectivity trade-off could be competitive with that reported for MOF/PVDF (PV-5) [6] and 1% AlFu MOF/PVDF [9].

Table 8.4: *Membranes functionalized with MOF tested in MD with related operating conditions.*

Membrane	**Tfeed** *[°C]*	**Flow rate** *[mLmin^{-1}]*	**Flux** *[Lm^{-2}h^{-1}]*	**Rejection [%]**	**Reference**
PVDF-HFP/AlFu-2	50	500	22.7	99.9	[1]
PVDF-HFP/AlFu-0.1	50	500	17.0	99.9	[1]
PVDF	48	1500	1.83	99.98	[6]
MOF/PVDF (PV-5)	48	1500	3.26	99.98	[6]
Pristine PTFE	50	500	43.5	99.9	[8]
PTFE-PS/AlFu MOF	50	500	45.1	99.9	[8]
1% AlFu MOF/PVDF	50	450	8.04	99.9	[9]
1% AlFu MOF/PVDF	70	450	15.64	99.9	[9]
PVDF-MOF(0.5%)	58.9	100	1.8	99.99	In this work

8.3.1 Summary

The inclusion of MOF in PVDF-based membrane has been prepared via non-solvent phase inversion technique. The prepared membrane has been characterized to study the morphological proprieties and then, evaluated in Membrane Distillation process. A comparison with pristine PVDF membrane has been done to study the effect of MOF in membrane-matrix. The inclusion of MOF tends to reduce the pore size and porosity of the membrane respect the pristine PVDF. This aspect induced the reduction of flux in MD compared to pristine PVDF. However, a salt rejection of 99.99% has been achieved.

8.4 MOF-enabled Membranes for Crystallization test

PVDF-MOF membranes have been also tested in Membrane Crystallization devices. The MCr tests have been performed with a supersatured NaCl solution (5M) in direct contact configuration. Despite the highest feed temperature used for the MCr test with PVDF-MOF(0.5%) respect the ones used with pristine PVDF (Tfeed=44.6°C and 36.5°C, respectively), PVDF-MOF(0.5%) exhibits a lower trans-membrane flux (1.3 Lm^{-2}h^{-1}) (fig. 8.6). Again, this is due to the lowest mean pore size of the PVDF-MOF membrane, which is responsible for additional resistance to mass transfer. The percentage of rejection was of 99.995%. Pristine PVDF membrane exhibits a trans-membrane flux of 5.7 L·m^{-2}h^{-1} (as shown in fig. 7.1).

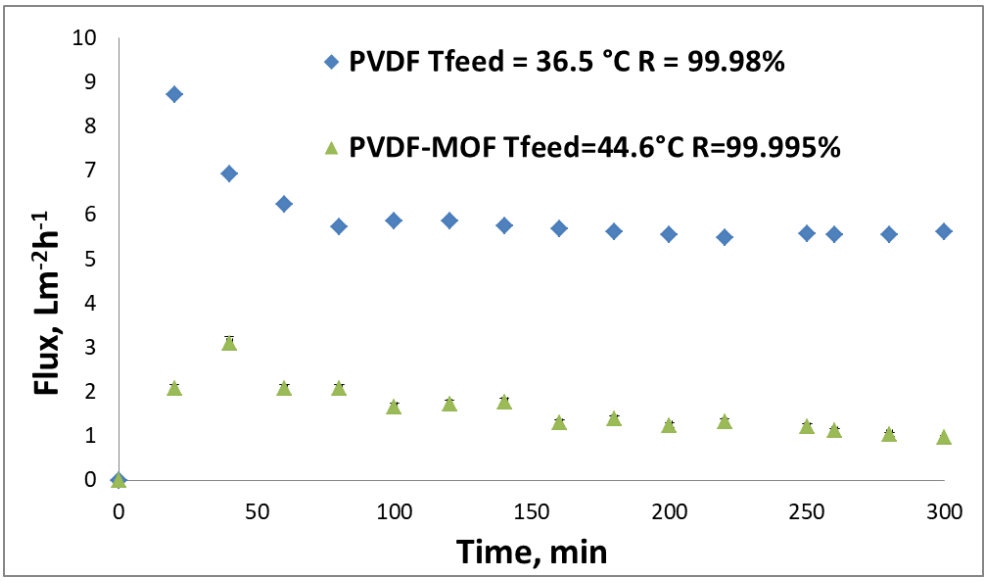

Figure 8.6 *Trend of the flux as a function of time for PVDF-based membranes functionalized with Graphene and MOF at 0.5 %.*

The continuous removal of pure water as permeate from the feed solution with PVDF-MOF induced the saturation of the sodium chloride with formation of the first crystals after 680 minutes, while for pristine PVDF membrane 285 minutes have been necessary to detect the first visible crystals (Fig.8.7). These results are in agreement with the fluxes estimated for the two membranes.

Summarizing, PVDF-MOF provides a lower number of crystals due to a lower nucleation rate with B^0 from 115170 to 148879 for PVDF-MOF(0.5%) (from 149088 to 490593 for pristine PVDF, respectively) with a smaller size from 18.36 µm to 22.06 µm for PVDF-MOF(0.5%) (from 42.5 to 65.1 µm for pristine PVDF respectively) and a G^c from 0,0000107 to 0,0000142 mm·min^{-1} for PVDF-MOF(0.5%) and from 0.0000298 to 0.0000795mm·min^{-1} for pristine PVDF, respectively.

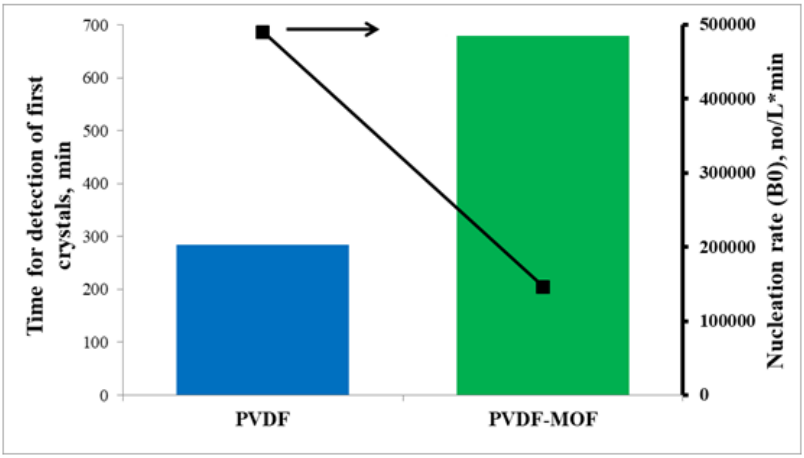

Figure 8.7 *Time for detection of the first crystals (histograms) and nucleation rate (black line) for the PVDF-MOF and pristine PVDF membrane.*

Figure 8.8 shows the comparison from sample 1 to sample 3 of NaCl crystals obtained with PVDF-MOF(0.5%) and pristine PVDF. The time elapsed between sample 1 to sample 3 was 60 minutes.
In agreement with the results reported in Table 8.4, it is possible to observe a lower number of crystals for PVDF-MOF(0.5%), but much more uniform in size and shape. In figure 8.8, the magnitude for each membrane was dissimilar due the different crystal size (Magnitude 20X for PVDF-MOF(0.5%) and Magnitude 10X for pristine PVDF).

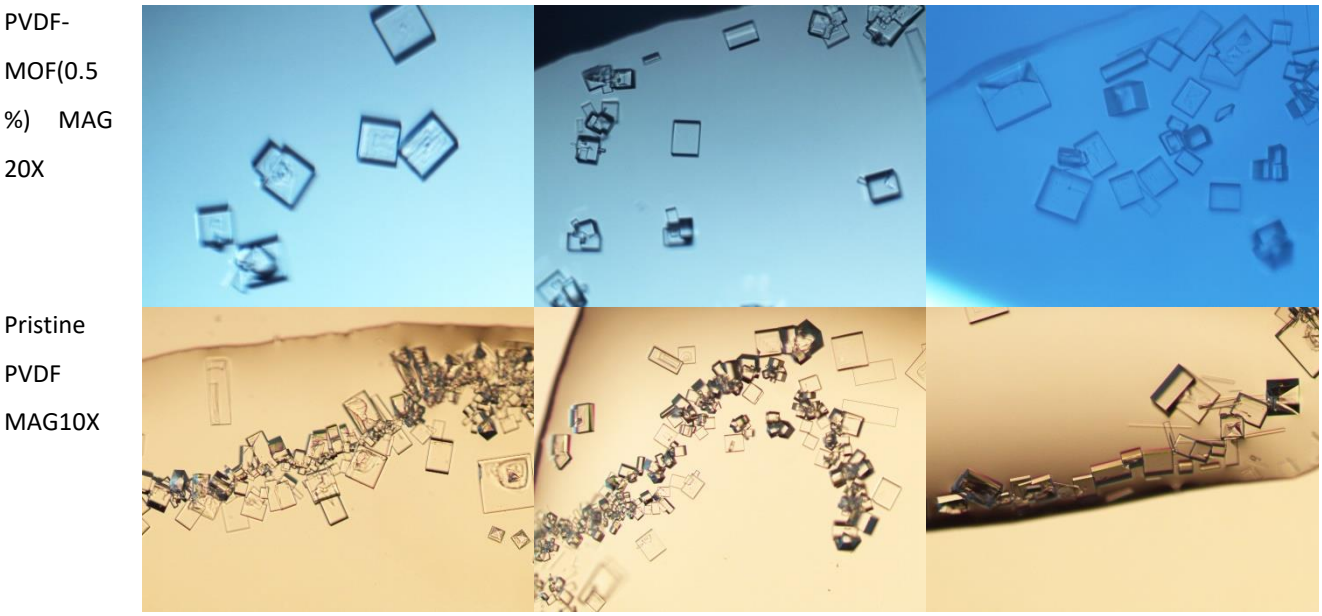

Figure 8.8 *Pictures collected during the crystallization test with PVDF-MOF membrane at three different times.*

Also, the NaCl crystals achieved with the functional membrane exhibit a predominant cubic shape according to the expected lattice structure of NaCl.

Table 8.5*: NaCl crystal parameters obtained with PVDF-MOF and pristine PVDF membranes.*

	B^0	G^C [mm·min^{-1}]	d_m [µm]	CV	B^0	G^C [mm·min^{-1}]	d_m [µm]	CV
	PVDF-MOF				**PVDF**			
Sample 1	146363,4	0,0000130	19.72	40.91	490593	0.0000298	20.6	77.1
Sample 2	148879,7	0,0000107	18.36	29.61	257598	0.0000524	42.5	48.4

Sample 3	115170,5	0,0000142	22.06	46.67	149088	0.0000795	65.1	53.8

A good uniformity in distribution with *CV* values ranging from 29.61 to 46.67% is obtained with functionalized membranes (Table 8.5). From sample 1 to sample 2 has been observed a slight decrease of growth rate G^C with a slightly increase of nucleation rate B^0, as an effect of secondary nucleation. The result is a general decrease in crystals size. On contrary from sample 2 to sample 3 the crystals size increase due to higher growth rate (G^C) (table 8.5). Nucleation and growth rate are more marked for pristine PVDF, leading to a more inhomogeneous crystal distribution.

8.4.1 Summary

The PVDF-based membrane with MOF has been tested in MCr with a solution of 5M NaCl as feed in direct contact configuration. In terms of trans-membrane flux, PVDF-MOF(0.5%) has shown the same trend of MD test. The flux achieved with MOF-enabled membrane was lower than the ones achieved with pristine PVDF membrane. This result in a slower nucleation of NaCl crystals with the first crystals observed after 680 minutes, while with pristine PVDF the appearance of the first detectable crystals is after 285 minutes. On contrary the quality of obtained crystals with PVDF-MOF(0.5%) appears to be better than that estimated for pristine PVDF membranes. A coefficient of variation is lower with PVDF-MOF(0.5%), so that a more uniformity of crystals in size and shape can be obtained.

8.5 Explorative tests with mixtures of salts

For each category of membranes filled with 2D materials, MD test with mixtures of mono and bivalent salts have been also implemented. All properties of the membranes are resumed in table 8.6 for convenience. The mean pore size is comparable for all membranes, whereas higher porosity is estimated for PVDF-MOF0.5 and a lower thickness for PVDF-BS0.7 membrane.

A direct contact configuration has been used choosing NaCl 0.6M stream and related mixtures of $MgCl_2$, and Na_2SO_4 as model solutions. For this test Bismuth Selenide (Bi_2Se_3 (BS)) has been used in place of Bi_2Te_3 at a concentration of 0.7%.

The membranes have been evaluated at two different flow rates (100 and 200 mL/min) with a feed and permeate temperatures of about 50°C and 10°C, respectively.

Table 8.6 *Membranes tested in MD with salt mixture as feed with related morphological characteristics.*

Name of Membrane	Filler Dispersed in NMP	Pore size (μm)	Porosity (%)	Thickness (μm)
PVDF-G (0.5%)	Graphene	0.24±0.05	56 ± 7	62 ± 3
PVDF-MOF (0.5%)	MOF	0.18±0.05	64±1	63±3
PVDF-BS (0.7%)	Bi_2Se_3	0.17±0.3	54±3	50±2

In table 8.7 are reported the composition of salt mixture solution used for MD tests. The composition proposed has been choose from the Mediterranean Seawater composition reported in Chapter 1. The concentration total of mixture was 35 g/L

Table 8.7: *Salt mixture composition used for MD tests.*

Salt Mixture	
Salt	**Weight (g/Kg)**
NaCl	29,535
$MgCl_2*6H_2O$	8,129
Na_2SO_4	1,658
H_2O	960,678

Before the test with salt mixture all the membranes have been tested with 0.6M NaCl as shown in figure 8.9. PVDF-G(0.5%) shows the higher flux of 6.0 $Lm^{-2}h^{-1}$ respect the PVDF-BS(0.7%) and PVDF-MOF(0.5%) with 2.0 and 0.4 $Lm^{-2}h^{-1}$, respectively. All the three membranes showed a rejection of salt over 99.992%, but the highest flux is estimated for PVDF-G0.5 membrane. Considering that this membrane has porosity slightly lower than that of PVDF-MOG0.5 but comparable with the one of PVDF-BS0.7, it is plausible that graphene flakes can be involved in diffusion process. Indeed, MOF has additional intrinsic porosity, but it is not enough to provide free pathway to penetrant diffusion. Also, PVDF-BS0.7 exhibits a lower thickness and therefore minor resistance to the mass transfer; its flux is higher than that estimated for PVDF-MOF0.5 but continues to be lower than that measured through PVDF-G0.5.

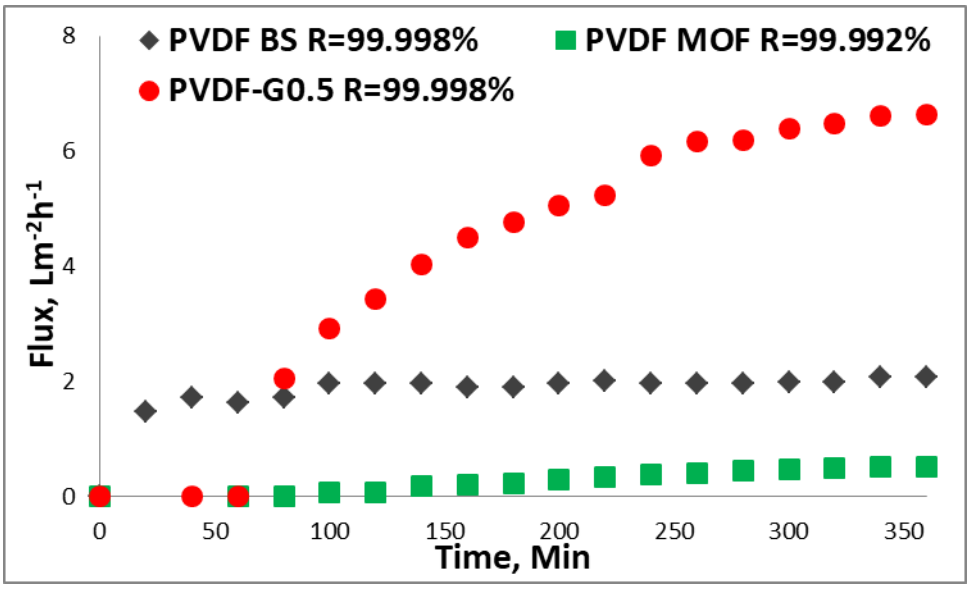

Figure 8.9 *Trans-membrane fluxs for PVDF-based membranes; Feed temperature 50°C, FR=100ml/min.*

A similar trend has been achieved when a salt mixture has been used as feed. PVDF-G(0.5%) shows the highest flux of 6.9 $Lm^{-2}h^{-1}$, while increasing the flow rate to 200mL/min the flux reaches a value of 9.3 $Lm^{-2}h^{-1}$. However PVDF-G(0.5%) shows the lowest percentage of rejection of 99.94%. The flux for PVDF-BS(0.7%) and PVDF-MOF(0.5%) increase with the flow rate from 1.9 to 4.4 $Lm^{-2}h^{-1}$ and from 0.2 to 0.6 $Lm^{-2}h^{-1}$. Both the membranes show rejection values over 99.99%.

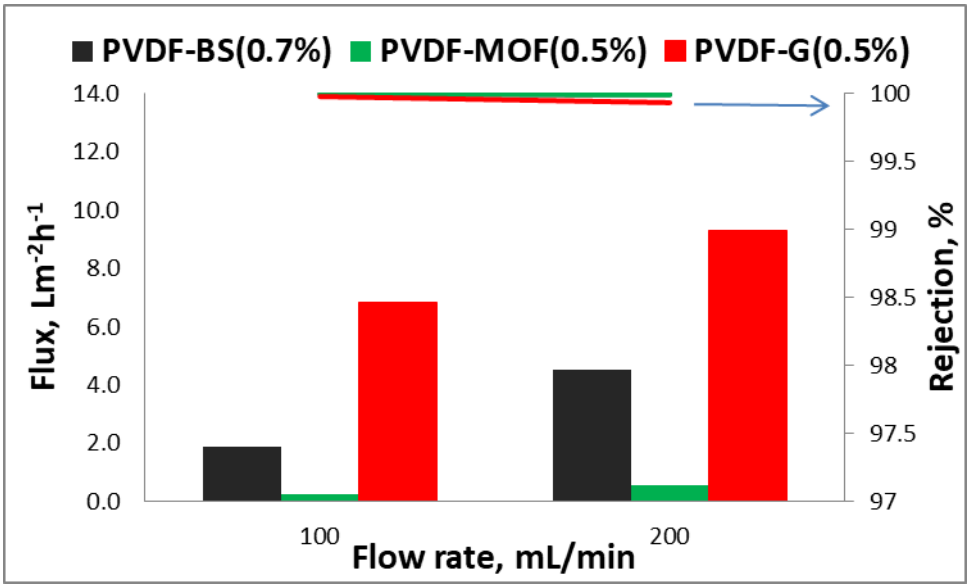

Figure 8.10 *Tests with salt mixture at two different flow rates.*

8.5.1 Summary

MD test with mixtures of mono and bivalent salts have been performed with PVDF-G(0.5%), PVDF-MOF(0.5%) and PVDF-BS(0.7%). The tests have been performed at two different flow rates with the same feed and permeate temperature for all membranes. By increasing the flow rate, an increase in the trans-membrane flux has been obtained with all the membranes. PVDF-G(0.5%) showed the highest trans-membrane flux, suggesting a combination of the membrane morphological features with graphene-assisted transport.

References

[1] X.-Q. Wu, N.R. Mirza, Z. Huang, J. Zhang, Y.-M. Zheng, J. Xiang, Z. Xie, Enhanced desalination performance of aluminium fumarate MOF-incorporated electrospun nanofiber membrane with bead-on-string structure for membrane distillation, Desalination. 520 (2021) 115338. doi:10.1016/j.desal.2021.115338.

[2] E. Elsayed, R. AL-Dadah, S. Mahmoud, P.A. Anderson, A. Elsayed, P.G. Youssef, CPO-27(Ni), aluminium fumarate and MIL-101(Cr) MOF materials for adsorption water desalination, Desalination. 406 (2017) 25–36. doi:10.1016/j.desal.2016.07.030.

[3] R. Ananthoji, J.F. Eubank, F. Nouar, H. Mouttaki, M. Eddaoudi, J.P. Harmon, Symbiosis of zeolite-like metal-organic frameworks (rho-ZMOF) and hydrogels: Composites for controlled drug release, J. Mater. Chem. 21 (2011) 9587–9594. doi:10.1039/c1jm11075f.

[4] J. Zuo, T.-S. Chung, Metal–Organic Framework-Functionalized Alumina Membranes for Vacuum Membrane Distillation, Water. 8 (2016) 586. doi:10.3390/w8120586.

[5] M.R.S. Kebria, A. Rahimpour, G. Bakeri, R. Abedini, Experimental and theoretical investigation of thin ZIF-8/chitosan coated layer on air gap membrane distillation performance of PVDF membrane, Desalination. 450 (2019) 21–32. doi:10.1016/j.desal.2018.10.023.

[6] F. Yang, J.E. Efome, D. Rana, T. Matsuura, C. Lan, Metal–Organic Frameworks Supported on Nanofiber for Desalination by Direct Contact Membrane Distillation, ACS Appl. Mater. Interfaces. 10 (2018) 11251–11260. doi:10.1021/acsami.8b01371.

[7] J.E. Efome, D. Rana, T. Matsuura, F. Yang, Y. Cong, C.Q. Lan, Triple-Layered Nanofibrous Metal–Organic Framework-Based Membranes for Desalination by Direct Contact Membrane Distillation, ACS Sustain. Chem. Eng. 8 (2020) 6601–6610. doi:10.1021/acssuschemeng.9b06791.

[8] Z. Huang, G. Yang, J. Zhang, S. Gray, Z. Xie, Dual-layer membranes with a thin film hydrophilic MOF/PVA nanocomposite for enhanced antiwetting property in membrane distillation, Desalination. 518 (2021) 115268. doi:10.1016/j.desal.2021.115268.

[9] D. Cheng, L. Zhao, N. Li, S.J.D. Smith, D. Wu, J. Zhang, D. Ng, C. Wu, M.R. Martinez, M.P. Batten, Z. Xie, Aluminum fumarate MOF/PVDF hollow fiber membrane for enhancement of water flux and thermal efficiency in direct contact membrane distillation, J. Memb. Sci. 588 (2019) 117204. doi:10.1016/j.memsci.2019.117204.

Conclusions

The main goal of this thesis has been to prepare hydrophobic porous membranes for enhancing perfomance in Membrane Distillation and Membrane-Assisted Crystallization processes. To raise the performance and efficiency of the membranes, 2D materials exfoliated via Wet Jet Milling procedure have been chosen. The polymeric membranes have been prepared via non-solvent phase inversion including 2D materials, graphene and bismuth compounds, at two different concentrations in polymer networks. Moreover, a Zr-based MOF has been utilized a third comparative nanofiller. Targets and benefits obtained by applying polymerisable bicontinuous microemulsion (PBM) membranes to an membrane bio-reactor (MBR) technology are summarised here below:

- PVDF-based membranes including 2D materials (Graphene, Bismuth Telluride, Zr-MOF) have been mainly prepared by combined WJM_NIPS procedures.
- The inclusion of 2D materials has been evaluated with XRD, XPS SEM and BSE analyses.
- 2D materials exfoliated via WJM have been also analysed before being entered in membranes by TEM, AFM and Raman spectroscopy.
- Membrane morphology has been analysed with SEM, AFM and porometer
- Wetting resistance has been assessed with pure water and sodium chloride solution at different concentrations.
- Effects of 2D materials on mechanical properties have been investigated and compared with those measured for pristine PVDF
- Membrane distillation process in direct contact configuration has been implemented by using NaCl alone or in mixture with bivalent salt ($35 gL^{-1}$) solution under different operating conditions. Effects on water flux amplification and therma efficiency have been investigated and discussed
- MCr operations have been carried out by using supersaturation NaCl solution (5 M) and 2D materials effect on crystal nucleation, growth rate have been investigated by evaluation the impact on crystal quality.
- Comparative analyses as well as durability and reproducibility of the performance have accompanied all investigations through the overall research.

Based on the results of the research, we can conclude that 2D materials can accelerate the flux through the membranes, reducing under particular circumstance thermal energy consumption. It is possible to amplify the productivity by working under condition softer than those traditionally reported in literature. Also, better-quality minerals may be achieved through controlled kinetics, thereby obtaining a major control of number, size and shape of the crystals.

Nomenclature

a

Exponent of pore size

A

Effective area of the membrane (m^2)

AGMD

Air gap membrane distillation

AFM

Atomic Force Microscopy

B

Membrane distillation transport coefficient

B^0

Nucleation rate

BM

Ball-milling

BS

Bismuth selenide

BT

Bismuth Telluride

CPC

Concentration polarization coefficient

CV

Coefficient of Variation (%)

DCMD

Direct contact membrane distillation

D_h

Hydraulic diameter (m)

D_{ij}

Diffusivity

D_{KA}

Knudsen diffusion coefficient

D_{WA}

Molecular diffusion coefficient

ECTFE

Ethylene Chlorotrifluoroethylene

ED

Electrodialysis

EDX

Energy Dispersive X-ray Analysis

EE

Electrochemical exfoliation

EIPS

Evaporation of the solvent

FD

Freeze desalination

FO

Forward Osmosis

FR

Flow rate

G

Graphene

G^c

Crystal Growth rate

GO

Graphene Oxide

GS

Membrane gas separation

EU

European Union

h_f

Feed side heat transfer coefficient (W/m^2 K)

h_m

Heat transfer coefficients of the vapor within the membrane

H_v

Enthalpy of vapor

IC

Desalination by ion exchange

J

Flux (kg/m^2 h)

K

Thermal conductivity (W/m K)

Kb

Boltzmann's constant

L

Length (m)

LEP

Liquid entry pressure

LGMD

Liquid Gap Membrane Distillation

M_i

Molecular weight

MBR

Membrane bio-reactor

MCr

Membrane Crystallization

MD

Membrane Distillation

ME

Mechanical exfoliation

MED

Multi-effect distillation

MGMD

Material gap membrane distillation

MF

Microfiltration

MOF

Metal organic framework

MSF

Multi-stage flash distillation

MVC

Mechanical vapour compression

M_w

Molecular weight (kg/mol)

n^*

Critical size of crystals

N

rate of mass transfer

NF

Nanofiltration

NIPS

Non-solvent-induced phase inversion

P

Pressure (Pa)

PAN

Polyacrylonitrile

PBM

Polymerisable bicontinuous microemulsion

PD

Permeation desalination

PE

Polyethylene

PES

Polyethersulfone

PGMD

Permeate Gap Membrane Distillation

PVDF

Polyvinylidene fluoride

PP

Polypropylene

PTFE

Polytetrafluoroethylene

PSμM

Phase separation micro-molding

Q

Heat flux (J/s)

R

Universal gas constant (8.3143 J/K mol)

r

Pore size of membrane

R_c

Resistance due to concentration

Re

Reynolds number

R_f

Resistance due to fouling

R_{fb}

Feed side boundary layer resistance

rGO

Reduced graphene oxide

R_m

Resistance due to membrane

RO

Reverse osmosis

R_{pb}

Permeate side boundary layer resistance

S

Supersaturation

SD

Solar distillation

SE

Shear-exfoliation

SEM

Scanning electron microscopy

SGMD

Sweep gas membrane distillation

t

Time

TCV

Thermal Vapor Compression

TEM

Transmission electron microscopy

T_f

Feed side bulk temperature (°C)

T_{fm}

Feed side membrane surface temperature (°C)

TIPS

Thermally Induced Phase Separation

T_p

Permeate side bulk temperature (°C)

TPC

Temperature polarization coefficient

T_{pm}

Permeate/distillate side membrane surface temperature (°C)

TSGMD

Thermostatic sweeping gas membrane distillation

UV

Ultrafiltration

UW

Ultrawave exfoliation

Q

Heat transfer rate

V

Permeate volume (L)

VC

Vapor compression distillation

VIPS

Vapor Induced Phase Separation

VMD

Vacuum membrane distillation

WHO

World Health Organization

WJM

Wet Jet Milling

XPS

X-ray photoelectron spectroscopy

XRD

X-ray Diffraction

Greek letter

Y_{ln}

log mean average pressure (Pa)

x

Mole fraction of NaCl

ε

Porosity

σ

Interfacial energy

τ

Tortuosity

δ

Membrane thickness (m)

γ_L

Liquid surface tension

v_0

Molecular volume

ϑ

The liquid/solid contact angle.